August 2016

The Spectral Variability of Astronomical PAHs

Matthew Shannon
The University of Western Ontario

Supervisor
Els Peeters
The University of Western Ontario

Graduate Program in Astronomy

A thesis submitted in partial fulfillment of the requirements for the degree in Doctor of Philosophy

Thesis advisor: Professor Els Peeters Matthew J. Shannon

Abstract

Polycyclic aromatic hydrocarbons (PAHs) are highly abundant molecules found throughout the universe. Illuminated by ultraviolet photons, they can emit up to 10% of the total power output of star-forming galaxies and are involved in many important physical and chemical processes (e.g., gas heating). They produce prominent emission bands between 3-20 μm which vary strongly in intensity and spectral profile. The origins of these variations are not fully understood, which limits the use of PAHs as (ubiquitous) diagnostic tracers of physical conditions.

To characterize their variability, we studied the relative intensities and profiles of the 10-20 μm PAH bands in a varied sample of objects, including several extended Galactic sources. Our overarching conclusion is that charge is the dominant parameter in determining the strengths and/or shapes of the 10-20 μm bands. While some bands are due to a single charge state, others exhibit mixed contributions–the mixing ratios of which determine the overall band shape and thus drive the profile variations.

We also investigate the nature of the surprisingly strong PAH emission observed in lines of sight toward the Galactic bulge. These sight lines are not associated with any known stellar sources. We use forbidden emission lines and spectral energy distributions to determine the physical conditions and relate these to the observed variability of the PAH emission bands, hypothesizing about possible origins of the excitation.

Keywords: Astrochemistry, interstellar medium, spectroscopy, molecules, dust, lines and bands

Authorship statement

The following authors contributed to Chapter 2: M. J. Shannon, D. J. Stock, E. Peeters.

EP pointed out the unusual nature of the 15-20 μm bands and suggested a large-sample analysis of their properties. EP reduced spectral cubes which we used in our analysis. MJS analyzed the spectra and prepared the figures and manuscript text. MJS determined relationships between the PAH bands based on these results. MJS, EP and DJS interpreted these results in the context of charge and molecular structure. DJS provided regular feedback and guidance, and manuscript suggestions, as did EP. DJS also introduced a new method for separating the 12.7 μm PAH emission from the 12.8 μm [Ne II] line with which it typically blends, which we have made use of here and in subsequent papers.

The following authors contributed to Chapter 3: M. J. Shannon, D. J. Stock, E. Peeters.

MJS introduced the seed for the paper by showing that profile variations of the 12.7 μm emission band in select reflection nebulae could be decomposed by two competing spatially independent components, whose relative strengths determined the resulting band profile. EP reduced the spectral cubes which we used for this analysis. MJS performed the Gaussian-based fitting of the PAH band profiles and prepared the results and figures. MJS also suggested the use of the structural similarity index (commonly used in image analysis) as a way of quantifying the relationships between our spectral maps. MJS estimated the ionization states of the individual components and prepared the manuscript text. DJS prepared extinction maps and provided frequent advice and discussion about the project, in addition to manuscript feedback. EP provided manuscript feedback and regular useful discussions, as well as suggesting that we examine the 12.7/11.2 ratio and extinction in our discussion. EP also gave useful advice on how best to structure the paper.

The following authors contributed to Chapter 4: M. J. Shannon, E. Peeters, J. Cami.

The premise of examining the background emission in lines of sight toward the Galactic bulge was put forward by JC. MJS acquired and reduced the data, measured the spectroscopic cubes and photometric images, and prepared correlation plots and tables. MJS was responsible for identifying and discussing relationships between structure observed in the multiwavelength imaging and corresponding trends in our spectroscopic data. MJS prepared the figures and manuscript text and performed the modelling of spectral energy distributions. EP and JC gave regular feedback and guidance on how to interpret the results and possible ways of using these data. EP and JC also provided useful manuscript comments.

To my family. You were truly inspirational.

Acknowledgments

Thank you to my parents, Judy and James, who have always supported and believed in me. To my grandparents, Sid and Sara, who have been loving, nurturing and generous as long as I've known them. To my wife, Erin, who has always encouraged me and been there in times of need. Thank you to my extended family, old and new. Your support has meant a great deal.

Thank you to my advisor, Els Peeters. At every step of the way you've helped guide me, teach me, scold me (not that often) and mentor me on how to be a scientist. Thank you Dave Stock, your guidance and patience has helped tremendously.

Thank you to everyone in the department, professor, staff and student, of which there are too many to name. I appreciate each and every interaction.

Contents

Listing of tables

Listing of figures

Listing of acronyms

AGB	Asymptotic Giant Branch
FIR	Far-Infrared
HII	H^+
IR	Infrared
IRS	Infrared Spectrograph
ISM	Interstellar Medium
MIR	Mid-Infrared
MRN	Mathis, Rumpl, and Nordsieck (1977)
NIR	Near-Infrared
NGC	New General Catalogue
OGLE	Optical Gravitational Lensing Experiment
PAH	Polycyclic Aromatic Hydrocarbon
PDR	Photodissociation Region
PNe	Planetary Nebulae
RNe	Reflection Nebulae
SAGE	Surveying the Agents of Galaxy Evolution (Meixner et al., 2006)
SINGS	Spitzer Infrared Nearby Galaxies Survey (Kennicutt et al., 2003)
SNR	Signal-to-Noise Ratio
SSIM	Structural Similarity Index (Wang et al., 2004)
UIR	Unidentified Infrared (Bands)
VSG	Very Small Grain (Berné et al., 2007)
YSO	Young Stellar Object

The interstellar medium is anything not in stars.

Donald Osterbrock

1 Introduction

1.1 Stellar life cycles

The dust and gas that pervades the space between stars is known as the interstellar medium (ISM). The ISM includes many diverse environments, from hot ionized gas, to vast expanses of warm wispy clouds of atomic hydrogen, to cold dense cores in molecular clouds where stars are being formed. The interstellar materials themselves are products of stellar evolution, originating in the cores and circumstellar environments of aging stars. To understand the properties and compositions of the interstellar molecules and grains we look to the process of stellar evolution.

Stars begin life as the hydrogen gas in cold ($T \sim 20K$) dense clouds (Fig. 1.1). The natural flow of material in the cloud can allow the formation of locally "over-dense" regions under the influence of gravity. These may also be formed by an external agent, such as the impact of a shockwave from a supernova. If the density of material in any particular region of the cloud is sufficiently great (typically defined by the Boner-Ebert mass), barring any external influence the material will inevitably collapse gravitationally. The gravitational pressure is opposed by the thermal pressure of the gas, resulting in a temporary equilibrium. The gas however continues to radiate and therefore cools, which decreases the thermal pressure against collapse. As a result, the gas becomes denser, which causes the temperature to increase. This quasi-static cycle repeats, which is known as the Kelvin-Helmholtz mechanism, until the gas becomes sufficiently hot to permit a new source of pressure against collapse: energy released from nuclear fusion. While this collapse occurs, the surrounding environment

of gas and dust is slowly swept away by the interior radiation. Some material accretes during this process, in the form of a circumstellar disk. Once nuclear fusion of hydrogen has turned on in the core, the protostar has become a star on the main sequence evolutionary track. Its location is dependent almost entirely on its initial mass and metallicity. The star will stably burn hydrogen for millions to billions of years via the proton-proton chain or CNO cycle mechanisms.

Once the central reservoir of hydrogen has been fully consumed, the star's core will contract and its outer layers expand, and it leaves the main sequence. The central core of helium is inert, but the heating of the adjacent material spurs nuclear fusion of the shell material. Shell burning progresses until the temperature of the central helium core becomes sufficiently hot to trigger helium burning. In low mass stars, there is a latent period with a degenerate helium core before fusion is triggered suddenly, which is known as a helium flash. If the star is of an intermediate or high mass, this cycle of core burning, periods of inertness, shell burning, and core burning of new elements will continue until there is simply not enough external pressure to heat the latest inert core to fusion temperatures. The star has an onion-like structure of elemental layers. These metals can be cycled to the surface of the star (and later expelled into the surrounding environment) by convective flows. In the late phase of asymptotic giant branch evolution, strong convective events known as dredge-ups transport large amounts of interior products to the outer surface. Pulsations in the stellar atmosphere expel these products into space. High-mass stars exhibit outflow velocities on the order of 2000 km/s, whereas low and intermediate mass stars have typical outflows around 10-30 km/s (Tielens, 2008). If the star is very high mass, internal pressure cannot withstand gravity and a type II supernova will occur, violently ejecting the outer layers of the star at typical velocities of 30000 km/s. As the material enters the interstellar medium, it cools and complex molecules and grains can form. The chemistry of the resulting species is dependent on which elements are brought to the outer layers of the star by convection, as well as, to a lesser degree, the metallicity of the nascent gas.

Eventually, amorphous dust grains will form in the expelled material driven by the stellar wind. The type of dust produced (whether carbonaceous or silicate) is dependent on the relative abundances of carbon and oxygen. CO is an extremely stable molecule–thus, if there is more carbon than oxygen in the local environment, all oxygen will be incorporated into CO, and the leftover carbon can be used to form carbonaceous species. Conversely, an overabundance of oxygen relative to carbon will lead to silicate dust. Over time, these metals will be incorporated into the formation of new stars, or new molecules in situ in the local ISM. The remaining stellar cores of low and intermediate mass stars will become white dwarfs,

which will slowly cool over great periods of time. Without the influence of an external source, such as a wandering nearby star whose atmosphere may be slowly stripped away by the white dwarf, the white dwarf will be forever dormant. The entire process has reprocessed hydrogen into metals, enriching the ISM for future stars.

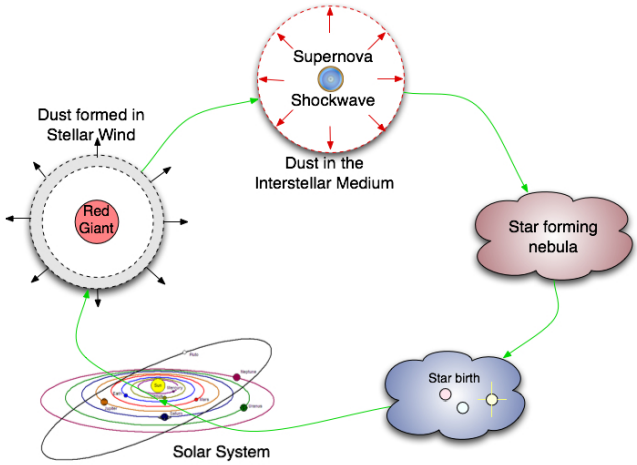

Figure 1.1: The cycle of stellar evolution. Stars form in cold molecular clouds, quietly burn hydrogen on the main sequence, and eventually eject material (including dust, atoms, and molecules) into the interstellar medium. These metal-rich ejecta can then be incorporated into successive generations of stars. "The lifecycle of dust in galaxies" by E. L. Gomez, used with permission.

1.2 Polycyclic aromatic hydrocarbons

An important family of molecules formed in the late phases of stellar evolution is polycyclic aromatic hydrocarbons (PAHs). It is also thought that they may form in situ in the interstellar medium (see Section 1.2.4).

PAHs are composed of interlocking aromatic carbon rings (Fig. 1.2). Each six-membered ring in the lattice forms bonds with its neighbours. Each interior carbon atom in the PAH has three neighbouring carbon atoms, which together form covalent bonds in the form of (three) σ bonds. However, since carbon has four valence electrons, the fourth electron forms out-of-plane π bonds with the adjacent atoms. The π-bonded electron clouds are not associated with any particular atom in the lattice–they are delocalized (and hence aromatically bonded). Aromatic C-H bonds are more stable to photodestruction than non-aromatic bonds, such as the aliphatic bonds of a linear carbon chain.

Carbon atoms situated on the perimeter of the PAH molecule have only two adjacent carbon atoms with which to bond, leading to two σ bonds and one π bond. The fourth unbonded electron generally attracts a free-floating hydrogen atom due to the overwhelming

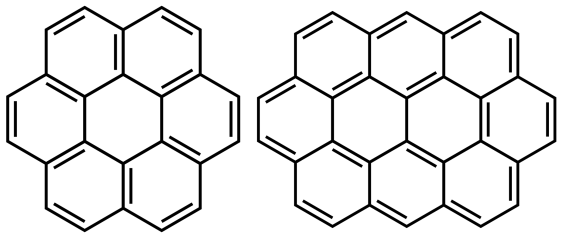

Figure 1.2: Two PAH molecules are illustrated: coronene, $C_{24}H_{12}$, and ovalene, $C_{32}H_{14}$. Each vertex in the diagram represents a carbon atom, with aromatic hydrogen attached to peripheral carbon atoms (not shown). Typical PAHs observed in space contain $50 - 100$ carbon atoms, larger than those shown above but of a similar structure. "The structure of Coronene" and "The structure of Ovalene, a polycyclic aromatic hydrocarbon, or PAH" by Inductiveload, released into the public domain (https://en.wikipedia.org/wiki/File:Coronene.svg, https://en.wikipedia.org/wiki/File:Ovalene.svg).

abundance of hydrogen, creating a third σ bond. Observations show that functional groups other than hydrogen (such as CH_3) exist in much fewer numbers ($< 2\%$, Tielens 2008). It is generally assumed then that a typical polycyclic aromatic hydrocarbon is coated with peripheral hydrogen atoms.

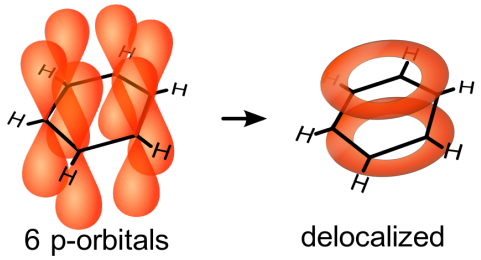

Figure 1.3: Depiction of π-bonding of p-orbitals leading to electron delocalization in aromatic molecules. "Orbital hybridization in benzene rings" by Vladsinger is licensed under CC BY-SA 3.0 (https://en.wikipedia.org/wiki/File:Benzene_Orbitals.svg).

1.2.1 Physical characteristics

PAHs are extremely common on Earth, being byproducts of incomplete combustion; they are a common pollutant and carcinogen. In space, they are also highly abundant: PAH emission measurements in conjunction with theoretical emission models imply abundances of 3×10^{-7} relative to hydrogen, making them the most abundant polyatomic molecule after CO (Tielens, 2008). Typical astronomical PAHs have between 50-100 carbon atoms (denoted by N_C), as smaller PAHs are less stable to photodestruction. PAH clusters, which consist of vertically stacked PAHs ($N_C \sim 400$) have similar abundances relative to hydrogen. Due to their planar structure, astronomical PAHs are generally on the order of 10-20Å in diameter (Tie-

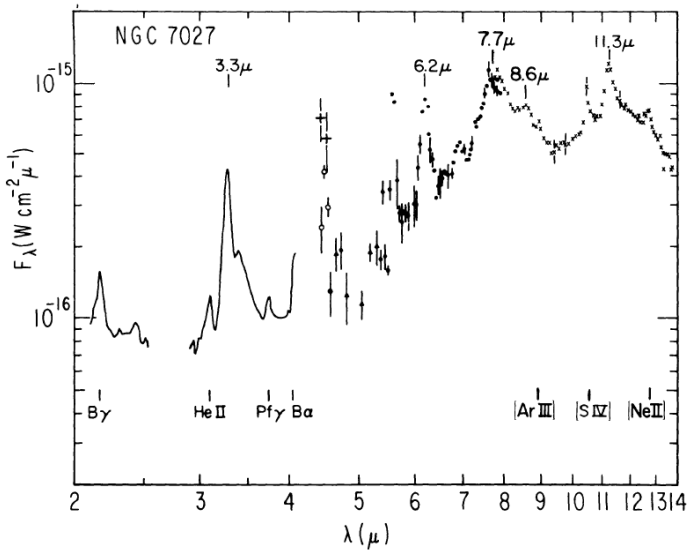

Figure 1.4: An example of the unidentified infrared emission features circa 1977. Features are seen at 3.3, 6.2, 7.7, 8.6 and 11.2 μm. Figure from Russell, Soifer, and Willner (1977), reproduced by permission of the AAS.

lens, 2005). PAH sizes are consistent with extrapolations beyond the low end of the MRN (Mathis, Rumpl, and Nordsieck, 1977) grain size distribution for interstellar dust (Sellgren, 1984).

1.2.2 Spectral appearance

Emission from PAH molecules was first observed in the 1970s at 3.3, 6.2, 7.7, 8.6 and 11.2 μm (Fig. 1.4). At the time, the origin of these bands was unknown, leading to the these features being classified as the unidentified infrared (UIR) bands. The 11.2 μm feature was the first to be recognized in a 8-13-μm study of three planetary nebulae by Gillett, Forrest, and Merrill (1973). The emission band was too broad to be atomic in origin, leading the authors to suggest it may be continuum emission from carbonates (CO_3^{2-}). A later study by Merrill, Soifer, and Russell (1975) performed 2-4 μm spectroscopy of NGC 7027. They observed the 3.3 μm feature, again too wide to be an atomic transition, suggesting a molecular origin. A follow-up analysis by Russell, Soifer, and Willner (1977) of this same planetary nebula revealed additional unknown emission features at 6.2, 7.7, and 8.6 μm in addition to the emission at 3.3 and 11.2 μm (see Fig. 1.4). Russell, Soifer, and Merrill (1977) noted that the 3.3 μm feature appears in objects that also display 11.2 μm emission. At this time the prevalence of the UIR bands was well established.

One of the key clues for identifying the carrier of the UIR emission bands was provided by Duley and Williams (1981). The authors realized that the astronomical features at 3.3 and

11.2 μm are coincident with vibrational bands of aromatic C-H bonds. This led to the suggestion of many possible carbonaceous carriers, including hydrogenated amorphous carbon (HAC; Borghesi, Bussoletti, and Colangeli 1987; Duley and Williams 1988), coal (Papoular et al., 1989), quenched carbonaceous composites (QCC; Sakata et al. 1984) and later, mixed aromatic/aliphatic nanoparticles (MAONs; Kwok and Zhang 2013), among others. The link to a carbonaceous carrier was made stark by Allamandola, Tielens, and Barker (1985), who showed that the 6.2 and 7.7 μm UIR features, which were observed toward C-rich evolved stars but not O-rich evolved stars, are very similar in appearance to the spectrum of common automobile exhaust. At one time the unidentified infrared bands were referred to as the overidentified infrared bands.

Strong constraints on the specific carrier were identified by Sellgren (1984). The author examined near-IR emission in three reflection nebulae, and found that the colour temperature of the UIR emission at 3.3 μm ($\sim$ 1000 K) was independent of distance from the central star. Furthermore, the 3.3 μm emission was observed far from the central stars, where thermal dust would be too cool to explain the emission band. Sellgren (1984) thus proposed a model of thermally fluctuating dust grains. In her model, small grains with low heat capacities must be briefly heated to high temperatures by UV photons (in a process known as stochastic heating). Afterwards, they cool radiatively by emitting infrared photons. Sellgren (1984) showed that the size of grains considered ($\sim$ 10 Å) smoothly joins the MRN size distribution of interstellar grains (Mathis, Rumpl, and Nordsieck 1977, valid for particle sizes 50 – 10000 Å). The evidence in totality pointed to UV heating of gas phase molecules, leading to IR fluorescence, as the mechanism for the UIR emission.

Léger and Puget (1984) performed theoretical calculations and showed that coronene ($C_{24}H_{12}$) at 600K can favorably reproduce the UIR emission bands, strongly linking PAHs to the astronomical features. In contrast to other proposed carriers, PAHs are: stochastically heated and consistent with inferred sizes; abundant in space; naturally present in environments where UIR bands are seen (and are stable enough to do so); have high feature-to-continuum ratios; naturally produce asymmetric band shapes due to anharmonicity; and perhaps most importantly, can reproduce the UIR bands in position and intensity from laboratory measurements and theoretical calculations. For these reasons it is generally accepted that PAHs are the carriers of the UIR emission bands.

A modern infrared spectrum displaying PAH emission is shown in Fig. 1.5, which is of an H II region in the Large Magellanic Cloud (data from *Spitzer* Space Telescope). A rising dust continuum underscores all the emission features. Strong PAH bands at 6.2, 7.7, 8.6, 11.2, 12.7 are visible, as well as a selection of weaker bands at 5.7, 12.0, $\sim$13.5, $\sim$14.2, 15.8, 16.4, 17.4

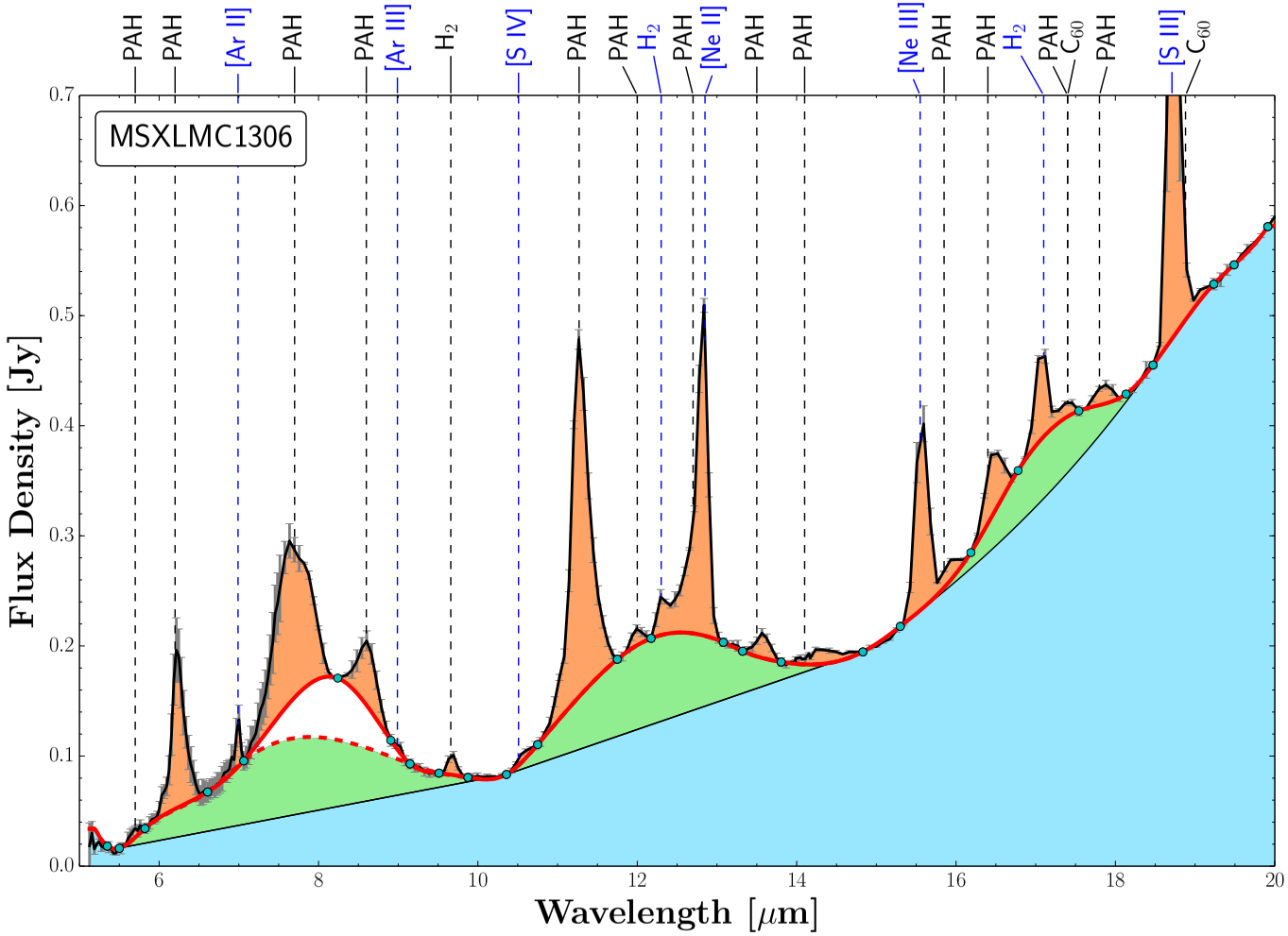

Figure 1.5: A modern mid-infrared emission spectrum is shown for an HII region in the Large Magellanic Cloud (data from *Spitzer* Space Telescope). The primary PAH emission bands are visible at 6.2, 7.7, 8.6, 11.2, and 12.7 µm. 15-20 µm emission features can be seen at 15.8, 16.4, 17.4 and 17.8 µm. Underlying plateaus, associated with PAH clusters or very small grains, are shaded in light green. The rising dust continuum is shown in (shaded) blue. The thick red line represents a fit to the local continuum. A variety of weaker PAH features are present, as well as atomic and molecular emission lines. Figure reproduced by permission of the AAS (Shannon, Stock, and Peeters, 2015).

and 17.8 μm. Commonly observed emission plateaus between 5-10, 10-15 and 15-18 μm are also present, in addition to a selection of molecular and atomic fine-structure lines.

1.2.3 The PAH emission mechanism

Dust grains ($\geq$0.0025 μm) are generally in thermal equilibrium with their environments due to their high heat capacities. In contrast, PAHs have small heat capacities, and have temperatures that vary strongly with time. The absorption of a single UV photon excites the molecule to an elevated electronic state, heating the PAH to $\sim$1000 K (Allamandola, Tielens, and Barker, 1989). The absorbed energy can be redistributed by collisional de-excitation, but in space collisions may be infrequent, depending on the environment. Other de-excitation pathways include photodissociation, ionization, or fluorescence. Which pathway is more favorable depends on the size and shape of the PAH. Internal conversion and intersystem crossing redistribute the energy to a lower electronic state but an excited vibrational state. The energy separation between the vibrational levels generally correspond to IR photons, hence why the PAH bands are clearly observed in the 3-20 μm window.

A 50-carbon atom PAH in the diffuse ISM absorbs a UV photon approximately once a year, while a similar PAH in the Orion Bar photodissociation region will absorb a photon every 10 minutes (Tielens, 2005). After absorption, the energy is redistributed to excited vibrational states in $\sim 10^{-9}$s, followed by IR photon emission due to vibrational de-excitation in $\sim$ 1 s (Tielens, 2005). Since the emission process occurs on timescales much shorter than the time between photon absorption events, the temperature of the PAH is not constant with time.

The wavelength of the emitted radiation is dependent on the structure of the PAH, as this determines which vibrational energy levels are accessible. Stretching modes, which are radial oscillations between two atoms, are observed in the astronomical spectra as the 3.3 μm band (C-H stretching) and 6.2, 7.7 μm bands (C-C stretching). Other possible vibrations include in-plane and out-of-plane bending of C-H bonds, corresponding to $\sim$8.6 μm emission and 11-14 μm emission, respectively. The C-H out-of-plane bending modes (hereafter CH_{oop}) are responsible for the 11.0, 11.2, 12.7, 13.5 and 14.2 μm emission bands. Which band is observed is determined by the number of adjacent C-H bonds around the molecule's periphery: a single C-H bond with no immediate neighbour is a "solo"; two, a duo; three, trio; and four, a quartet. Other possible vibrations are C-C-C modes, in which the entire skeleton (or a portion thereof) vibrates. Both in- and out-of-plane C-C-C modes are possible, such as elongation/compression modes, "jumping jacks" or "breathing" modes (see Ricca et al. 2010 for an overview). Vibrations involving the entire skeleton (which emit beyond 20 μm, generally)

are expected to be molecule specific, while the shorter wavelength (3-15 μm) bands are not. The former are much weaker intrinsically than the latter, and none have been observed in astronomical observations. The 15-20 μm bands are a compromise between the high emission intensities of the (nearest-neighbour) 3-15 μm modes and the molecular fingerprints of the long-wavelength vibrations. We present a summary of some of the important band assignments in Table 1.1.

Band	Assignment
3.3 μm	C-H stretch
6.2 μm	C-C stretch
7.7 μm	C-C stretch and C-H in-plane bend
8.6 μm	C-H in-plane bend
11.2 μm	C-H out-of-plane bend; solos
12.7 μm	C-H out-of-plane bend; duos and trios
15.8 μm	C-C-C in-plane bend
16.4 μm	C-C-C in-plane bend primarily
17.4 μm	C-C-C in- and out-of-plane bend
17.8 μm	C-H and C-C-C out-of-plane bend

Table 1.1: The primary emission bands and their assignments. *Stretch* modes are radial oscillations. *Bend* are "wagging" modes, and can be in or out of the plane of the molecule. *Solos*, *duos* and *trios* refer to interactions between adjacent C-H bonds on the exterior of a PAH (see Section 1.2.3).

1.2.4 PAH formation and processing

Astronomical PAHs are thought to form in two ways: through a "bottom-up" approach of increasing chemical complexity (in the outflows of evolved asymptotic giant branch stars), or through the fragmentation and destruction of large carbonaceous grains and other species in a "top-down" pathway (such as in the ISM).

Bottom-up. The outflows of carbon-rich AGB stars are sites for PAH production due to their high densities and temperatures (Latter, 1991). In general, however, PAH emission is not observed toward AGB stars. This apparent inconsistency is thought to reflect the fact that AGB stars have weak radiation fields, with few UV photons, and thus have little means to illuminate and excite PAHs (see e.g. Boersma, Hony, and Tielens 2006, in which PAHs observed toward an AGB star are thought to be illuminated by a stellar companion). PAHs *have* however been observed in the following stages of stellar evolution (i.e. the post-AGB and planetary nebula phases), which are characterized by hotter stars and higher UV fluxes, providing indirect evidence of their presence in the AGB phase. The specific chemical pathway

to PAH formation in these environments is not known, but several possibilities have been suggested. In the bottom-up approach, the formation of benzene (C_6H_6; a single aromatic cycle) is the first step. It is thought that benzene is the rate-limiting step in PAH production (Wang and Frenklach 1994). Suggested chemical reactions to form benzene typically involve acetylene (C_2H_2) or propargyl (C_3H_3). Two examples are shown below (Cherchneff 2011).

$$C_3H_3 + C_3H_3 \longrightarrow C_6H_6$$
$$1\text{-}C_4H_5 + C_2H_2 \longrightarrow C_6H_6 + H$$

Once the first ring has been formed, the question is how do additional cycles coalesce. One proposed mechanism is through H abstraction-C_2H_2 addition (HACA; Frenklach and Wang 1991). In this process, multiple acetylene sidegroups are added to a benzene molecule and hydrogen atoms are removed. The process is repeated and adjacent acetylene groups may lead to ring closure. Recent computational results however have shown that the HACA mechanism appears to terminate before three hexagonal rings (or more) can form (Kaiser, Parker, and Mebel, 2015; Kislov, Sadovnikov, and Mebel, 2013). Another possible route is through dimerisation and coalescence, suggested by Mukherjee, Sarofim, and Longwell (1994) upon studying pyrene ($C_{16}H_{10}$). This process requires a weak bond between two aromatic species (i.e. dimerisation). This may be followed by ring closure. Other processes have been proposed, but there is at present no general agreement on the pathway to aromatic hydrocarbon growth (Cherchneff, 2011).

In the context of stellar outflows, PAHs are an intermediate in the formation of more complex carbonaceous species. As illustrated in Fig. 1.6, closest to the star only small species are able to condense, such as acetylene (C_2H_2) or methane (CH_4). Further from the star more complex species can arise, such as benzene (C_6H_6) and subsequently PAHs. Further still, PAHs may be incorporated into clusters, which consist of PAHs stacked vertically and bound together by van der Waals forces (Tielens, 2008). Other structures include graphene (an aromatic "sheet", or very large PAH), graphite (vertically-stacked graphene layers), fullerenes (three-dimensional structures composed of aromatic hydrocarbon cycles, e.g. a "PAH soccer ball") or carbon nanotubes (a graphene sheet curved such that its long edges are conjoined). Additional species include diamond-like solids, amorphous particles consisting of aromatic units weakly bound together, and (solid) grains such as carbonaceous dust, which are a mixture of aromatic and non-aromatic (aliphatic) constituents.

Top-down. PAHs may also form due to the fragmentation of larger species in the inter-

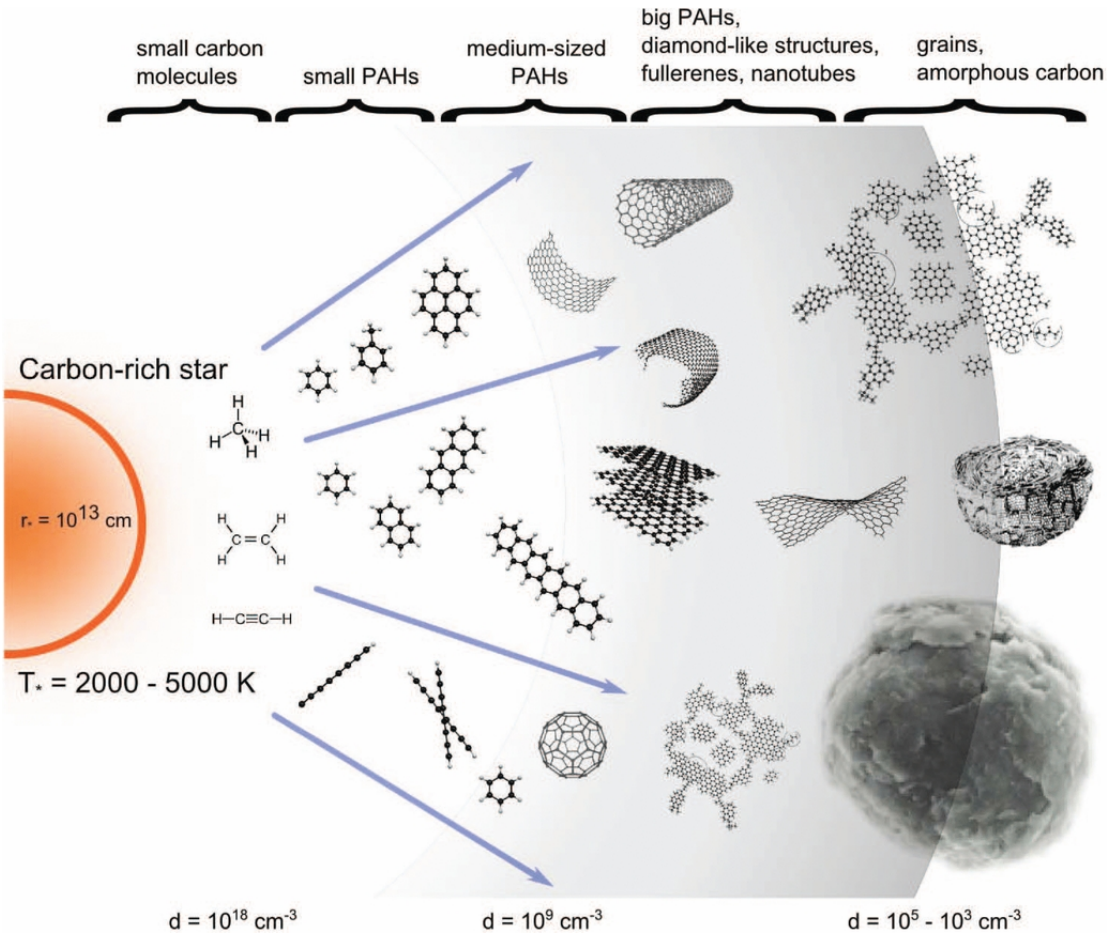

Figure 1.6: A cartoon illustrating the way in which carbonaceous species are thought to form in the stellar outflows of C-rich AGB stars. Temperatures decrease with stellar distance, allowing the formation of more complex species, and ultimately amorphous dust grains. Figure from Contreras and Salama (2013), who adapted it from Pascoli and Polleux (2000). Figure reproduced by permission of the AAS.

stellar medium. Graphitic or amorphous grains will fragment in high-velocity grain-grain collisions, producing a series of smaller carbonaceous species. These collisions are often energized by shocks in the local environment, such as an impinging shockwave from a supernova (Tielens, 2008). Laboratory experiments cannot recreate typical collision velocities, which may be on the order of 100 km/s. The analytical model of Jones, Tielens, and Hollenbach (1996) suggests that a typical interstellar shock incident upon a large grain may liberate 10% of the grain's mass, producing small carbon clusters in the process ($<$ 15 Å). This may be a possible mechanism for producing PAHs and PAH clusters in the interstellar medium (Tielens, 2008).

Once molecules and dust grains have formed, they are subject to environmental processing. These processes include: grain-grain collisions, which shatter and destroy grains, or lead to grain growth through accretion if energies are mild; the "freeze out" of molecular species onto grain surfaces, which can permit reactions such as the formation of H_2 (see Section 1.3); and additionally photoprocessing, in which small species may be radiatively dissociated. It is thought that small species (such as PAHs with $<$30 carbon atoms) are generally photodissociated or fragmented easily. Only the most stable of molecules will survive in these conditions. Grains and molecules will become part of molecular clouds, where new stars will form with different compositions. In these environments, molecules frozen onto grains may be evaporated and released back into the gas phase when pre-stellar cores form. The species formed in the atmospheres of AGB stars are thus influential beyond their nascent environments.

1.3 The importance of astronomical PAHs

PAHs are both widespread and abundant (10^{-7} relative to H, locking up $10-15\%$ of cosmic carbon; Allamandola, Tielens, and Barker 1989.) They influence many processes and environments on galactic scales: it is estimated that up to 20% of the Galactic infrared energy is emitted by PAH molecules (Smith et al., 2007). This implies significant total absorption of UV photons by PAHs, actively reshaping the spectral energy distributions of entire galaxies. PAHs are clearly seen in the spiral arms of galaxies, tracing the UV photons emitted by massive young stars. In these environments of active star formation, PAHs are important for regulating the rate at which stars form. Magnetic fields in star-forming regions tend to prevent gravitational collapse, and thus ambipolar diffusion, or the decoupling of neutral particles from charged particles is required to allow neutral species to collect gravitationally. PAHs provide important neutralization pathways, and therefore influence the efficiency of ambipolar diffusion. Examples of neutralization reactions (where M^+ is any cationic species)

include:

$$\begin{aligned} &\text{Neutralization} && \mathrm{PAH^- + M^+ \longrightarrow PAH + M} \\ &\text{Charge exchange} && \mathrm{PAH + M^+ \longrightarrow PAH^+ + M} \end{aligned}$$

PAHs are also important in determining the composition of the interstellar medium, particularly regions of H I gas. They affect the equilibrium abundances of ions, neutrals, electrons and anions through chemical reactions. These reactions include photoionization (where "γ below represents a photon), electron recombination and electron attachment, in addition to the neutralization and charge exchange reactions already introduced. Electron recombination is particularly important.

$$\begin{aligned} &\text{Photoionization} && \mathrm{PAH + \gamma \longrightarrow PAH^+ + e^-} \\ &\text{Electron recombination} && \mathrm{PAH^+ + e^- \longrightarrow PAH} \\ &\text{Electron attachment} && \mathrm{PAH + e^- \longrightarrow PAH^-} \end{aligned}$$

Gas heating in the neutral ISM and photodissociation regions is driven in large part by PAHs. This is accomplished through photoelectric heating and, to a lesser extent, gas-grain collisions. The photoelectric effect of PAHs introduces electrons into the local gas. Once released, these electrons can collide with gas-phase species, converting their kinetic energy into thermal energy, heating the gas (Bakes and Tielens, 1994). All grain sizes may partake in photoelectric heating, but small grains are more efficient than large grains due to reduced electron binding energies–only grains less than 100 Å are effective contributors (Tielens, 2008), of which PAHs are highly abundant.

PAHs are also important sites for surface chemistry. Their planar structure and high abundances results in them containing a significant fraction of the available surface area for chemical reactions. H_2, for instance, is unlikely to form in the gas phase due to low reaction rates. It is believed that accretion onto a dust grain and subsequent migration is the pathway to H_2 formation. PAHs would be important for this process due to their high abundances (Verstraete, 2011). They may also influence the ratio of gas-phase deuterium to hydrogen (D/H), as astronomical emission of deuterated PAHs has been observed (Doney et al., 2016; Peeters et al., 2004a).

Finally, as a significant fraction of the cosmic carbon abundance is locked in PAHs, they are important building blocks for the formation of complex carbonaceous species. The car-

bon in PAHs may be released by photoprocessing or collisional fragmentation. It has also been speculated that PAHs might be responsible for the 2175 Å absorption feature in the interstellar extinction curve (see e.g. Mulas et al. (2011) and references therein). They may also be ingredients in the construction of amino acids (Allamandola, 2011).

1.4 PAH emission variability

The astronomical PAH emission bands are known to exhibit high degrees of variability, in emission intensity, peak position, and profile shape (e.g. Galliano et al. 2008; Hony et al. 2001; Peeters et al. 2002; van Diedenhoven et al. 2004). We will discuss some of the key results and the general way in which these variations can be used to learn about the underlying PAH populations.

1.4.1 Intensity variations

The strengths of the PAH bands can vary significantly between sources (e.g. Boersma et al. 2010; Galliano et al. 2008; Hony et al. 2001; see review by Peeters 2011). This variability is most obvious in the brightest bands (e.g. 3.3, 6.2, 7.7, 8.6, 11.2 and 12.7 μm emission), but differences can be discerned in the (e.g.) weaker 15-20 μm bands.

Although the absolute band intensities will natural differ in different environments, the *relative* emission intensities also vary, e.g. the 6.2/11.2 flux ratio, from source to source. Flux ratios are important tools for analysis because they allow one to correct for systematic differences in a sample, such as changes in distance to the source, varying abundances of the PAH molecules, variable column densities along the line of sight, or differences in the absolute emission intensities when comparing two sources. PAH band strengths are typically normalized to the flux of a band arising from a different PAH sub-population.

The 6.2/11.2 and 7.7/11.2 flux ratios are highly correlated, with correlation coefficients typically exceeding 0.8 in inter-source studies (e.g. Galliano et al. 2008). This has been observed in studies encompassing a wide variety of objects, including H II regions, planetary nebulae, reflection nebulae, and galaxies. The 3.3 and 11.2 μm C-H bands are also correlated in intensity (Fig. 1.7), first noted by Russell, Soifer, and Willner (1977). Other correlations are present but are generally weaker (e.g. the 12.7 and 6.2 μm bands, the 7.7 and 8.6 μm bands).

Within extended sources, the intensities of individual bands can be traced spatially. For instance, in reflection nebula NGC 2023, the 15.8 and 16.4 μm PAH bands emit in different locations (Peeters et al., 2012). As well, Galliano et al. (2008) presented maps of spatially-resolved PAH emission in nearby galaxies, HII regions and photo-dissociation regions (a subset of their sample). These objects showed variations in the 6.2/11.2 ratio spatially within objects, as

well as globally from source to source. The range of the variations seen within any one object is consistent with the range in variations between sources.

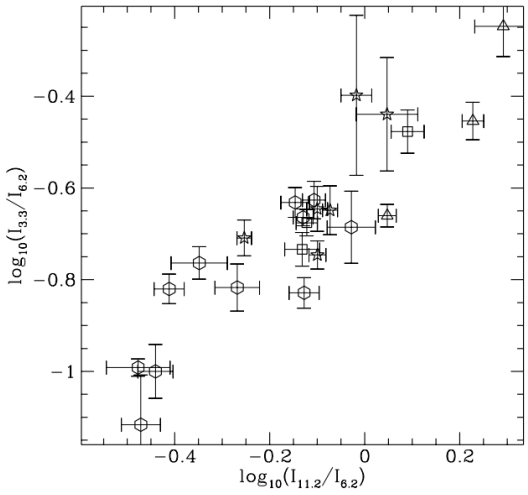

Figure 1.7: The integrated PAH emission strength of the 3.3 μm band is plotted against the strength of the 11.2 μm band for a selection of objects in the Milky Way: planetary nebulae (triangles), reflection nebulae (squares), intermediate-mass star-forming regions (stars), and HII regions (hexagons). Both bands are normalized to the strength of the 6.2 μm feature. Figure from Hony et al. (2001), used with permission.

1.4.2 Profile variations

The profiles of individual PAH features have been shown to vary as well. The largest source-to-source differences are seen in the "7.7 μm" band. The peak position of this band may shift from 7.6 μm to 8 μm and in some rare cases as far as 8.2 μm. The shape of this PAH feature also changes dramatically (see Fig. 1.8). The 7.7 μm band has two primary sub-components at 7.6 and 7.8 μm, and occasionally a blueward component at 7.35 μm and redward emission beyond 8 μm. The band shape and peak position are affected by the relative strengths of these sub-components. Variations are present in other features but to lesser degrees: the 6.2 μm band is observed to shift between 6.24 and 6.30 μm, with a weakly-varying profile (Fig. 1.8); the 3.3 and 11.2 μm bands display very little variation in comparison. The 6.2 μm band is very asymmetric, with a steep blue rise and a red tail. The 12.7 μm feature is similarly asymmetric, but in the opposite manner: it has a wing towards shorter wavelengths. The 3.3 μm band is much closer to being symmetric, while the 11.2 μm band is moderately asymmetric. The 7.7 μm band is too complex to define its symmetry due to its sub-components.

The observed profile variations led to the identification of three spectral classes (A, B, C) by Peeters et al. (2002). These are determined by the profiles of the 6.2, 7.7, and 8.6 μm bands, primarily by each's corresponding peak position. Generally, class A bands are those with

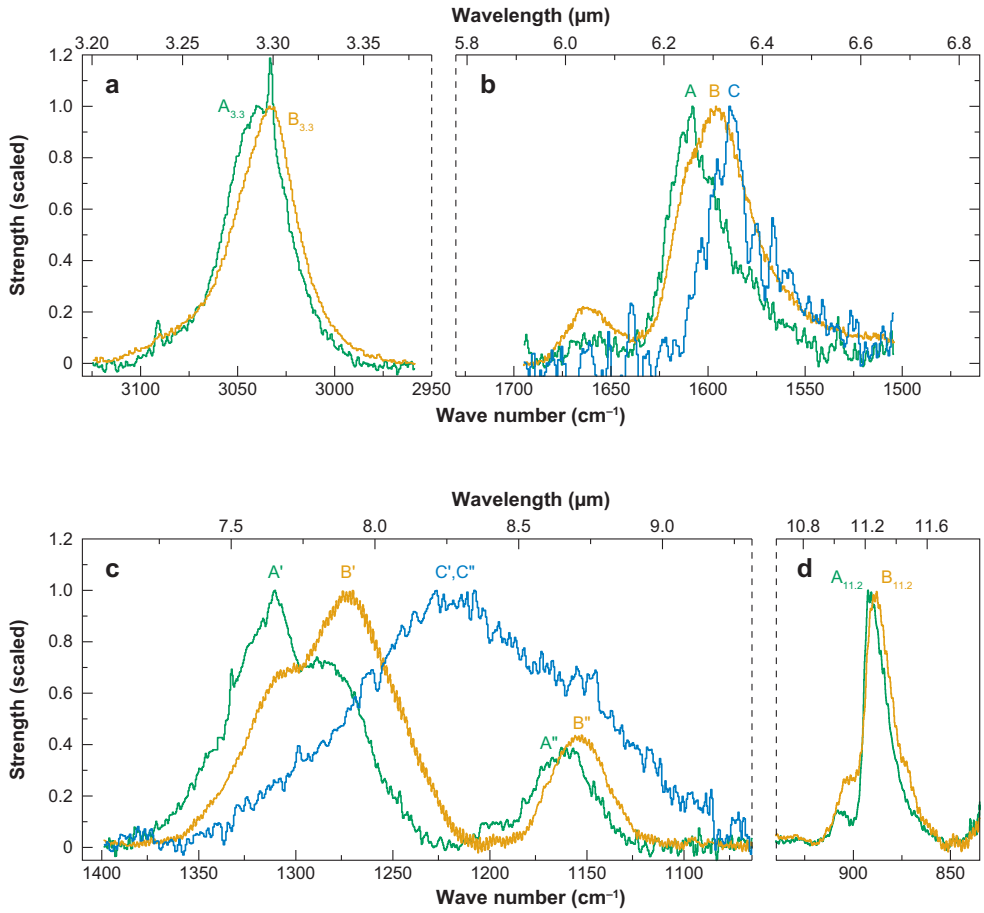

Figure 1.8: The emission profiles of classes A, B, C, defined by Peeters et al. (2002) and their range of variations. The 6.2 and 7.7 μm C-C bands show the largest variability, while the 3.3 and 11.2 μm C-H bands vary only slightly. The quantitative scheme is defined in Table 1.2. Figure from van Diedenhoven et al. (2004), reproduced by permission of the AAS.

peak positions towards shorter wavelengths, B, those shifted towards longer wavelengths, and (rare) C profiles at longer wavelengths still. For instance, the peak position of the "7.7" μm band tends toward 7.6, 8.0, or 8.2 μm for classes A, B, and C, respectively. Recently, Matsuura et al. (2014) identified a fourth class of emission: those with broad 7-9 μm emission instead of distinct 7.7 and 8.6 μm bands, which are denoted as class D sources. The specifics of the classification schemes are summarized in Table 1.2.

Class A profiles are generally associated with interstellar environments, such as H II regions, the ISM, reflection nebulae, as well as some non-isolated Herbig Be stars. Class B profiles are broadly associated with emission from circumstellar material, such as from planetary nebulae, post-AGB objects, and isolated Herbig Ae/Be stars. Note that there is some over-

Class	Characteristics						Object type
	6.2 μm band	λ_p	7.7 μm band	comp.	7.7 μm band	λ_p	
$\mathcal{A}$	A	∼6.22	A′	7.6	A″	∼8.6	H II, RN, galaxies, non-isolated Herbig Ae Be stars, PN: Hb5, pAGB‡ stars: IRAS 16279, IRAS 16594
			AB′	equal			IRAS 21282, HD97048
$\mathcal{B}$	B	6.24-6.28	B′	"7.8"	B″	8.62	isolated Herbig Ae Be stars, PNe, pAGB stars: HR4049, HD44179
$\mathcal{C}$	C	∼6.3	C′	8.22	C″	none	pAGB stars: IRAS 13416, CRL 2688
$\mathcal{D}$†		6.24		broad 7-9 μm			pAGB stars

Table 1.2: Classes $\mathcal{A}$, $\mathcal{B}$ and $\mathcal{C}$: the classification scheme defined by Peeters et al. (2002). The class is primarily determined by the peak positions of the features (λ_p): A for ISM-like sources; B for most sources with circumstellar material; and the uncommon C class, which includes certain evolved stars and pre-main sequence stars. † Class $\mathcal{D}$ was defined by Matsuura et al. (2014): these spectra exhibit broad 7-9 μm emission instead of individual 7.7 and 8.6 μm bands. ‡ post-AGB.

lap with class A by object type: some planetary nebulae and post-AGB stars display class A profiles, but these are generally minor exceptions. Class C objects are uncommon, displaying even further red-shifted features. These objects include some red giant stars, few cool carbon-rich evolved stars, and a small number of T Tauri stars (Acke, 2011; Peeters et al., 2004b; van Diedenhoven et al., 2004). The recent class D sources were identified in LMC post-AGB stars.

An interesting trend was discovered by Sloan et al. 2007 (Fig. 1.9). They observed that the central wavelength of the 7.7 μm feature is anti-correlated with effective stellar temperature in their sample of young stellar objects, evolved stars and one reflection nebula. This is also true of the 11.2 μm band. Note that a shift in peak position is linked to a change in profile class in their sample, from C (circumstellar) to B to A (interstellar). In general, class A objects do not follow this trend. However, the interpretation in this case is that photoprocessing may be responsible for class variations: the radiation fields of hotter stars are stronger and harder than those of cooler stars, thus providing more photons for PAH photoprocessing (Keller et al., 2008; Sloan et al., 2007).

1.4.3 Interpretation

Charge is known to be an important parameter in determining emission intensities for the 3-12 μm bands. Laboratory and theoretical spectra show that the 3.3 and 11.2 μm (C-H) modes are stronger in neutral species than cations, whereas the 6.2, 7.7 and 8.6 μm C-C modes dis-

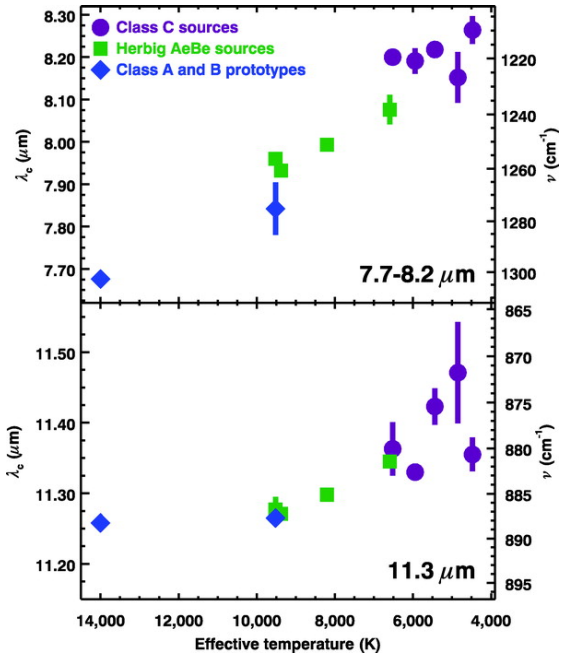

Figure 1.9: The central wavelength for the 7.7 and 11.2 μm emission features is plotted against effective stellar temperature. A distinction by object class is identified. Figure from Sloan et al. (2007), reproduced by permission of the AAS.

play opposite behaviour (e.g. Allamandola, Hudgins, and Sandford 1999; Hudgins and Allamandola 1999). The relative emission strengths of the C-H to C-C modes are therefore an indicator of the charge state of the emitting PAH populations being observed. The emission intensities can vary by one order of magnitude between charge states (for the C-C modes), meaning charge is a dominant parameter in understanding PAH variability. The charge state is determined by the local radiation field, electron density and gas temperature.

The variations in PAH band flux ratios from source to source reflect physical differences in the emitting PAH populations. For instance, the 11.2 μm band originates in a CH_{oop} mode from smooth-edged PAHs (i.e. solos, see Section 1.2.3), whereas the 12.7 μm band is associated with "irregular" edges, in which there are two and/or three CH_{oop} bonds next to each other (i.e. duos or trios). Variations in the 11.2/12.7 ratio are therefore expected to be associated with the edge structures of the PAH molecules producing the emission.

It is not yet understood what causes profile variations, though several possibilities have been proposed. One such idea is that the aromatic molecules we observe may not have strictly carbon skeletons. The substitution of an internal carbon atom for an atom of a different element (such as nitrogen) will influence the corresponding observed emission spectrum. Hudgins, Bauschlicher, and Allamandola (2005) performed theoretical calculations for the

emission spectrum of a selection of large molecules with this substitution, finding that the observational shift of the 6.2 μm peak position is tied to the internal location of the nitrogen substitution: if the nitrogen atom were closer to the center of the molecule, the feature would shift to shorter wavelengths. Thus the difference between class A and B of the 6.2 μm emission may be related to the fraction of substituted PAHs to "pure" PAHs along a particular astronomical line of sight. Other substituting species have been considered, such as silicon (which does not perturb the emission enough to explain the class variations) and oxygen (which destroys the aromaticity of the molecule).

A second possibility is that PAH clusters affect the emission profiles. Here, PAH molecules are loosely bound to each other due to induced electric dipole forces (Rapacioli, Joblin, and Boissel, 2005). These are stronger if one of the species is already ionized. They are believed to contribute to the plateau emission seen underlying the individual emission features.

A third possibility is that a mixture of PAH sizes is responsible for the profile variations. Bauschlicher, Peeters, and Allamandola (2008) performed a theoretical study of emission by large symmetric PAHs in neutral, cationic and anionic states. Their results suggest that the 7.7 μm band's two sub-components (at 7.6 and 7.8 μm) are associated with small and large PAHs, respectively. Thus the peak position (and therefore class) of the 7.7 μm band might be related to the size distribution of the PAH population.

Finally, one hypothesis concerns the aromaticity of hydrocarbons in space. Aliphatic bonds between C-C and C-H will exhibit the same stretching (and bending) modes that aromatically bonded molecules have, but due to differing bond strengths will emit at slightly different wavelengths (e.g. the aromatic C-H stretch at 3.3 μm is observed at 3.4 μm from a C-H aliphatic bond). The relative abundances of aromatic to aliphatic bonds and species might then determine the observed profiles. It is suggested the class C 7.7 μm feature may arise from aliphatics, and then the class variation of this band would result from the relative abundances of aromatics to aliphatics. Since aliphatic bonds are more easily photodissociated than aromatic bonds, the observed band class would be tied to the harshness of the environment (e.g. circumstellar to interstellar conditions; Boersma et al. 2008; Sloan et al. 2007).

1.5 Select open questions: this thesis

1.5.1 Characterizing the 15-20 μm bands

The 15-20 μm emission bands are less well studied and less well understood than the 3-12 μm bands, in part due to their weaker band intensities. However, they are tantalizing because they are expected to be molecule specific, in contrast to the 3-12 μm bands (see Sec-

tion 1.2.3). The question we wish to answer then is *what PAH sub-populations are responsible for the 15-20 μm emission*? With this information, we may be able to identify individual PAH molecules in space (not possible to date). Recent studies of the 15-20 μm bands have shown less than expected dependence on structure, but they have been limited by small sample sizes (Boersma et al., 2010; Peeters et al., 2012). A broader search is needed.

We address this by systematically studying a large sample of Galactic and extragalactic objects (57 sources in total) covering many diverse environments, presented in Chapter 2. We search for correlations between the 15-20 μm bands and the 3-15 μm bands, and interpret them from the view of charge and molecular structure. While the 6-9 μm bands are expected to be dominated by charge state, the 11-14 μm bands depend on the edge structure of the molecule, and thus may be related to the structural vibrations of the 15-20 μm features. We include spectral maps of two reflection nebulae so that we may compare the spatial morphologies of individual bands, which can help discern relationships.

1.5.2 Understanding the subtleties of PAH profile variations

Per Section 1.4.3, PAH bands are highly variable in profile shape and intensity. Charge and molecular structure are key characteristics in driving variations, but determining the exact properties of the astronomical PAH population(s) on any line of sight is a difficult if not impossible proposition due to the high spectral blending of the emission from the PAH family. One possible way of disentangling the highly blended emission is to examine in as much detail as possible the variations of individual bands. If we can better understand the exact reasons why a band varies in the way it does we can learn about the properties of the PAH populations carrying this band. Modern astronomical tools are boons for this line of inquiry: we can combine the high spectral and spatial resolutions of modern telescopes to measure profile variations on small spatial scales—which can possibly be linked to physical parameters/environmental conditions.

To this end, we present a detailed study of the 11.2 and 12.7 μm PAH bands in Chapter 3. These particular bands are interesting for a few reasons. First, they are bright (and can thus easily be detected) and are known to vary significantly. Second, the 11.2 μm PAH band, which is associated with neutral PAHs, is accompanied by a weaker band at 11.0 μm that is associated with cations—which means that we may be able to study distinct PAH populations in this analysis. And third, these bands are expected to trace molecular structure: the 11 μm emission is from solo CH_{oop} modes, while the 12.7 μm emission is from duo and/or trio CH_{oop} modes.

The important facet of this analysis is that we utilize spectral maps to trace *variations within individual sources*. The profiles of the 11.2 and 12.7 μm PAH bands vary within our chosen

reflection nebulae. We apply a Gaussian-based decomposition to quantify the changes in profile shapes, which we link to different PAH populations.

1.5.3 The nature of PAH emission towards the Galactic bulge

The PAH emission we observe in spectra is strongly dependent on what environments we observe. PAHs are commonly used to trace regions of star formation, where bright young stars provide ample exciting photons. On long sight-lines toward the Galactic bulge, outside the Galactic plane, we observe regions not typically associated with star formation. However, PAH emission was detected by Golriz et al. (2014).

To understand the origin(s) of the PAH emission, we study these lines of sight in Chapter 4. We combine mid-IR spectroscopic observations of the Galactic bulge over large spatial scales (several degrees) with far-infrared photometric imaging to deduce PAH, dust and gas properties. The observations consist of four fields, each with multiple pointings. Due to the distance to the Galactic bulge, the individual pointings also span a wide range in spatial scales ($\sim$40 pc). By being able to trace spectral variations on two different spatial scales, we will address the question, what is the source of PAH excitation on sight-lines toward the Galactic bulge?

1.6 Techniques used in this thesis

We summarize methods used in this thesis. This summary is not intended to be comprehensive, but associated references should provide sufficient details for those interested.

1.6.1 Correlations between emission bands

To test for relationships between measured quantities in our analyses, we sometimes employ correlation plots and associated correlation coefficients. Instead of directly testing for monotonic relationships between the fluxes of two PAH bands (for a variety of sources), it is important to account for variations between sources that can bias our analysis. Variations can include different distances (and thus different brightnesses), variable PAH abundances and otherwise. These systematics are accounted for by comparing flux *ratios* instead of absolute fluxes. A PAH band (e.g., the 11.2 μm emission) is chosen as a normalization factor when comparing astronomical spectra from either different environments or different positions within a single source (see, e.g., Peeters et al. 2016).

The Pearson correlation coefficient is a way to evaluate the degree of linearity between the two chosen quantities. Other methods include the Spearman correlation coefficient, which

instead tests for monotonicity; it is less sensitive to outliers than the Pearson coefficient, but it does not inform *how* two quantities are related.

1.6.2 Spectral decomposition

The spectral line profiles of PAHs show significant variation, with no single shape describing all bands. To understand the structure and variations within each profile, we at times introduce methods for decomposing the bands. A common method for decomposition is to reproduce the astronomical line with a series of Gaussian distributions. This has the form

$$f(x) = Ae^{-(x-x_0)^2/2w^2}, \tag{1.1}$$

where A, x_0 and w are the amplitude, peak position and width of the Gaussian, respectively. Depending on the number of Gaussians chosen, lesser or greater degrees of spectral complexity can be reproduced. Gaussians are chosen when the uncertainties in the emission are representative of a normal distribution, which is dependent on the physical process being described.

Another functional form that is used in decomposition is that of a Lorentzian:

$$f(x) = \frac{1}{\pi\gamma}\left[\frac{\gamma^2}{(x-x_0)^2+\gamma^2}\right]. \tag{1.2}$$

Here γ is the width and x_0 the peak position. This is employed to represent the intrinsic line profile of the emission from a single atom or molecule. It has significantly stronger wings that the Gaussian form, but is narrower (and thus weaker) at its core.

A third profile that is used in this field is that of the Drude,

$$f(x) = \left[\frac{b\gamma^2}{(x/x_r - x_r/x)^2+\gamma_r{}^2}\right], \tag{1.3}$$

which is similar to a Lorentzian profile but it is asymmetric. Here x_r is the central wavelength of the spectral line, γ_r is the fractional FWHM and b is the central intensity. These profiles are described by Smith et al. (2007).

References

Acke, B. (2011). In: *EAS Publications Series*. Ed. by C. Joblin and A. G. G. M. Tielens. Vol. 46. EAS Publications Series, pp. 259–269. DOI: 10.1051/eas/1146028.

Allamandola, L. J. (2011). In: *EAS Publications Series*. Ed. by C. Joblin and A. G. G. M. Tielens. Vol. 46. EAS Publications Series, pp. 305–317. DOI: 10.1051/eas/1146032.

Allamandola, L. J., Hudgins, D. M., and Sandford, S. A. (1999). *Astrophysical Journal, Letters* 511, pp. L115–L119. DOI: 10.1086/311843.

Allamandola, L. J., Tielens, A. G. G. M., and Barker, J. R. (1989). *Astrophysical Journal, Supplement* 71, pp. 733–775. DOI: 10.1086/191396.

– (1985). *Astrophysical Journal, Letters* 290, pp. L25–L28. DOI: 10.1086/184435.

Bakes, E. L. O. and Tielens, A. G. G. M. (1994). *Astrophysical Journal* 427, pp. 822–838. DOI: 10.1086/174188.

Bauschlicher Jr., C. W., Peeters, E., and Allamandola, L. J. (2008). *Astrophysical Journal* 678, pp. 316–327. DOI: 10.1086/533424. arXiv: 0802.1071.

Boersma, C., Hony, S., and Tielens, A. G. G. M. (2006). *Astronomy and Astrophysics* 447, pp. 213–220. DOI: 10.1051/0004-6361:20053904.

Boersma, C., Bauschlicher, C. W., Allamandola, L. J., et al. (2010). *Astronomy and Astrophysics* 511, A32, A32. DOI: 10.1051/0004-6361/200912714.

Boersma, C., Bouwman, J., Lahuis, F., et al. (2008). *Astronomy and Astrophysics* 484, pp. 241–249. DOI: 10.1051/0004-6361:20078001. arXiv: 0804.1199.

Borghesi, A., Bussoletti, E., and Colangeli, L. (1987). *Astrophysical Journal* 314, pp. 422–428. DOI: 10.1086/165074.

Cherchneff, I. (2011). In: *EAS Publications Series*. Ed. by C. Joblin and A. G. G. M. Tielens. Vol. 46. EAS Publications Series, pp. 177–189. DOI: 10.1051/eas/1146019. arXiv: 1010.2703 [astro-ph.SR].

Contreras, C. S. and Salama, F. (2013). *Astrophysical Journal, Supplement* 208, 6, p. 6. DOI: 10.1088/0067-0049/208/1/6.

Doney, K. D., Candian, A., Mori, T., et al. (2016). *Astronomy and Astrophysics* 586, A65, A65. DOI: 10.1051/0004-6361/201526809. arXiv: 1512.02874.

Duley, W. W. and Williams, D. A. (1988). *Monthly Notices of the RAS* 231, pp. 969–975.

– (1981). *Monthly Notices of the RAS* 196, pp. 269–274.

Frenklach, Michael and Wang, Hai (1991). *Symposium (International) on Combustion* 23.1. Twenty-Third Symposium (International) on Combustion, pp. 1559–1566. ISSN: 0082-0784. DOI: http://dx.doi.org/10.1016/S0082-0784(06)80426-1.

Galliano, F., Madden, S. C., Tielens, A. G. G. M., et al. (2008). *Astrophysical Journal* 679, pp. 310–345. DOI: 10.1086/587051. arXiv: 0801.4955.

Gillett, F. C., Forrest, W. J., and Merrill, K. M. (1973). *Astrophysical Journal* 183, pp. 87–93. DOI: 10.1086/152211.

Golriz, S. S., Blommaert, J. A. D. L., Vanhollebeke, E., et al. (2014). *Monthly Notices of the RAS* 443, pp. 3402–3434. DOI: 10.1093/mnras/stu1317.

Hony, S., Van Kerckhoven, C., Peeters, E., et al. (2001). *Astronomy and Astrophysics* 370, pp. 1030–1043. DOI: 10.1051/0004-6361:20010242. eprint: arXiv:astro-ph/0103035.

Hudgins, D. M. and Allamandola, L. J. (1999). *Astrophysical Journal, Letters* 516, pp. L41–L44. DOI: 10.1086/311989.

Hudgins, D. M., Bauschlicher Jr., C. W., and Allamandola, L. J. (2005). *Astrophysical Journal* 632, pp. 316–332. DOI: 10.1086/432495.

Jones, A. P., Tielens, A. G. G. M., and Hollenbach, D. J. (1996). *Astrophysical Journal* 469, p. 740. DOI: 10.1086/177823.

Kaiser, R. I., Parker, D. S. N., and Mebel, A. M. (2015). *Annual Review of Physical Chemistry* 66, pp. 43–67. DOI: 10.1146/annurev-physchem-040214-121502.

Keller, L. D., Sloan, G. C., Forrest, W. J., et al. (2008). *Astrophysical Journal* 684, pp. 411–429. DOI: 10.1086/589818. arXiv: 0809.2389.

Kislov, V. V., Sadovnikov, A. I., and Mebel, A. M. (2013). *Journal of Physical Chemistry A* 117, pp. 4794–4816. DOI: 10.1021/jp402481y.

Kwok, S. and Zhang, Y. (2013). *Astrophysical Journal* 771, 5, p. 5. DOI: 10.1088/0004-637X/771/1/5. arXiv: 1304.7629 [astro-ph.GA].

Latter, W. B. (1991). *Astrophysical Journal* 377, pp. 187–191. DOI: 10.1086/170346.

Léger, A. and Puget, J. L. (1984). *Astronomy and Astrophysics* 137, pp. L5–L8.

Mathis, J. S., Rumpl, W., and Nordsieck, K. H. (1977). *Astrophysical Journal* 217, pp. 425–433. DOI: 10.1086/155591.

Matsuura, M., Bernard-Salas, J., Lloyd Evans, T., et al. (2014). *Monthly Notices of the RAS* 439, pp. 1472–1493. DOI: 10.1093/mnras/stt2495. arXiv: 1401.0728 [astro-ph.SR].

Merrill, K. M., Soifer, B. T., and Russell, R. W. (1975). *Astrophysical Journal, Letters* 200, pp. L37–L39. DOI: 10.1086/181891.

Mukherjee, Jaideep, Sarofim, Adel F., and Longwell, John P. (1994). *Combustion and Flame* 96.3, pp. 191 –200. ISSN: 0010-2180. DOI: http://dx.doi.org/10.1016/0010-2180(94)90008-6.

Mulas, G., Malloci, G., Joblin, C., et al. (2011). In: *EAS Publications Series*. Ed. by C. Joblin and A. G. G. M. Tielens. Vol. 46. EAS Publications Series, pp. 327–340. DOI: 10.1051/eas/1146034.

Papoular, R., Conrad, J., Giuliano, M., et al. (1989). *Astronomy and Astrophysics* 217, pp. 204–208.

Pascoli, G. and Polleux, A. (2000). *Astronomy and Astrophysics* 359, pp. 799–810.

Peeters, E. (2011). In: *IAU Symposium*. Ed. by J. Cernicharo and R. Bachiller. Vol. 280. IAU Symposium, pp. 149–161. DOI: 10.1017/S174392131102494X. arXiv: 1111.3680.

Peeters, E., Allamandola, L. J., Bauschlicher Jr., C. W., et al. (2004a). *Astrophysical Journal* 604, pp. 252–257. DOI: 10.1086/381866.

Peeters, E., Tielens, A. G. G. M., Allamandola, L. J., et al. (2012). *Astrophysical Journal* 747, 44, p. 44. DOI: 10.1088/0004-637X/747/1/44. arXiv: 1112.3386 [astro-ph.GA].

Peeters, E., Hony, S., Van Kerckhoven, C., et al. (2002). *Astronomy and Astrophysics* 390, pp. 1089–1113. DOI: 10.1051/0004-6361:20020773. eprint: arXiv:astro-ph/0205400.

Peeters, E., Allamandola, L. J., Hudgins, D. M., et al. (2004b). In: *Astrophysics of Dust*. Ed. by A. N. Witt, G. C. Clayton, and B. T. Draine. Vol. 309. Astronomical Society of the Pacific Conference Series, p. 141. eprint: arXiv:astro-ph/0312184.

Peeters, E., Bauschlicher Jr., C. W., Allamandola, L. J., et al. (2016). *Astrophysical Journal*. Submitted.

Rapacioli, M., Joblin, C., and Boissel, P. (2005). *Astronomy and Astrophysics* 429, pp. 193–204. DOI: 10.1051/0004-6361:20041247.

Ricca, A., Bauschlicher Jr., C. W., Mattioda, A. L., et al. (2010). *Astrophysical Journal* 709, 42, pp. 42–52. DOI: 10.1088/0004-637X/709/1/42.

Russell, R. W., Soifer, B. T., and Merrill, K. M. (1977). *Astrophysical Journal* 213, pp. 66–70. DOI: 10.1086/155129.

Russell, R. W., Soifer, B. T., and Willner, S. P. (1977). *Astrophysical Journal, Letters* 217, pp. L149–L153. DOI: 10.1086/182559.

Sakata, A., Wada, S., Tanabe, T., et al. (1984). *Astrophysical Journal, Letters* 287, pp. L51–L54. DOI: 10.1086/184396.

Sellgren, K. (1984). *Astrophysical Journal* 277, pp. 623–633. DOI: 10.1086/161733.

Shannon, M. J., Stock, D. J., and Peeters, E. (2015). *Astrophysical Journal* 811, 153, p. 153. DOI: 10.1088/0004-637X/811/2/153. arXiv: 1508.04766.

Sloan, G. C., Jura, M., Duley, W. W., et al. (2007). *Astrophysical Journal* 664, pp. 1144–1153. DOI: 10.1086/519236. arXiv: 0705.0905.

Smith, J. D. T., Draine, B. T., Dale, D. A., et al. (2007). *Astrophysical Journal* 656, pp. 770–791. DOI: 10.1086/510549. eprint: arXiv:astro-ph/0610913.

Tielens, A. G. G. M. (2008). *Annual Review of Astron and Astrophys* 46, pp. 289–337. DOI: 10.1146/annurev.astro.46.060407.145211.

– (2005).

van Diedenhoven, B., Peeters, E., Van Kerckhoven, C., et al. (2004). *Astrophysical Journal* 611, pp. 928–939. DOI: 10.1086/422404. eprint: arXiv:astro-ph/0405098.

Verstraete, L. (2011). In: *EAS Publications Series*. Ed. by C. Joblin and A. G. G. M. Tielens. Vol. 46. EAS Publications Series, pp. 415–426. DOI: 10.1051/eas/1146043.

Wang, H. and Frenklach, M. (1994). *Journal of Physical Chemistry* 98, pp. 11465–11489.

If I read every piece of paper that landed on my desk, I'd never get out from behind it.

Jack Frost, A Touch of Frost

2

Probing the ionization states of polycyclic aromatic hydrocarbons via the 15-20 μm emission bands

M. J. Shannon, D. J. Stock, E. Peeters (2015). *Astrophysical Journal*, 811, 153.

2.1 Introduction

Polycyclic aromatic hydrocarbons (PAHs) are the most common polyatomic molecules in the universe (Tielens, 2013) and are thought to produce prominent infrared emission bands at, e.g., 3.3, 6.2, 7.7, 8.6, 11.2 and 12.7 μm. These emission bands are seen in many different environments, including H II regions, reflection nebulae (RNe), planetary nebulae (PNe), and the diffuse interstellar medium (ISM). They are attributed to infrared (IR)-active vibrational modes, generally stretching or bending modes of C-C and/or C-H bonds. Bending modes of the carbon skeleton, denoted as C-C-C modes, produce weaker but identifiable emission features at 15.8, 16.4, 17.4, and 17.8 μm, typically perched atop a broad 17 μm plateau (e.g., Moutou et al. 2000; Van Kerckhoven 2002; Van Kerckhoven et al. 2000).

PAH emission bands can be separated into three categories. The 3-15 μm bands arise from nearest-neighbour vibrations, such as the 3.3 μm C-H stretch or the 8.6 μm in-plane C-H bend. These nearest-neighbour vibrations are common to all PAHs, and their collective emission features at similar wavelengths leads to blended emission. As a result, the emission inten-

sities are high and they are readily observed in astronomical environments. In contrast, vibrations of the entire molecule (typically occurring at $> 20\mu$m, such as "drumhead" modes) are extremely molecule-dependent (e.g., Boersma et al. 2011, 2010; Ricca et al. 2010; Van Kerckhoven et al. 2000). The intensities of these bands are very low and they are difficult to detect; in fact, none to date have been identified in space. The 15-20 μm bands however represent an intermediate between the strong 3-15 μm bands and the rich but weak 20+ μm bands; they arise from vibrational modes involving a subset of the molecule (e.g., Boersma et al. 2010; Peeters et al. 2004; Van Kerckhoven et al. 2000). They are generally thought to arise in PAHs with $\sim 50 - 200$ carbon atoms (Boersma et al., 2010). The plateaus upon which the PAH bands sit are thought to arise from emission by large PAHs or PAH clusters (e.g., Allamandola, Tielens, and Barker 1989; Tielens 2008).

The 3-15 μm bands are known to have a series of correlations between the intensities of specific bands, typically attributed to common properties (primarily ionization state). The 15-20 μm PAH bands however have thus far not exhibited any correlations amongst themselves (e.g., Boersma et al. 2010; Peeters et al. 2012; Ricca et al. 2010; Smith et al. 2007b, hereafter referred to as paper I), though there are results showing the 16.4 μm band correlates with the 6.2 and 12.7 μm bands (Boersma et al. 2010, paper I). Previous studies have had limited sample sizes of moderate quality or focused on single objects. Here we investigate correlations in a large sample of objects to examine the behaviour of the 15-20 μm bands, and their relationship to the 3-15 μm emission features. The paper is organized as follows: the observations and data reduction are presented in Section 2. The methods used to analyze the spectra are summarized in Section 3. Results, including correlation plots and spatial maps, are presented in Section 4. We interpret these results in Section 5 and summarize our findings in Section 6.

2.2 Observations and Data Reduction

2.2.1 Target selection

We obtained spectra of a variety of objects from the SAGE-Spectroscopy (SAGE-Spec) Spitzer legacy program (Kemper et al., 2010) and sources from the Spitzer Infrared Nearby Galaxies Survey (SINGS, Kennicutt et al. 2003). We chose sources displaying clear PAH emission in the 15-20 μm region. Such emission can be identified by a wide 17 μm complex (or plateau) and narrower features at 15.8, 16.4, 17.4 and 17.8 μm. Sources more extended than 13.5″ in the SAGE-Spec sample were excluded, as this corresponds to the approximate size of the SL aperture at 11.2 μm (which is used for normalization when comparing band intensity ratios). Only sources with a 3σ detection of their 15-20 μm emission components (or a subset) are

included. We also applied this measurement criterion to the "MIR" (5-15 μm) PAH bands. Fifty-seven sources were identified as meeting these selection criteria, including two ISM cirrus sources. The sources in our sample are presented in Table 2.1. We also analyze a high-resolution spectral map of the RN NGC 7023 (Figure 2.1, previously analyzed by Berné and Tielens 2012; Boersma, Bregman, and Allamandola 2014, 2015; Boersma, Bregman, and Allamandola 2013; Rosenberg et al. 2011). We compare our results to that of NGC 2023 (paper I and Peeters et al. (2016), hereafter referred to as paper II). The 15-20 μm measurements of Boersma et al. (2010), comprising 15 sources, are also included for comparison. Our total sample includes carbon-rich evolved stars, young stellar objects and H II regions in the Large Magellanic Cloud, nearby galaxies, Galactic RNe, and other ISM sources.

2.2.2 Observations

The spectra we analyze were acquired with the Infrared Spectrograph (IRS; Houck et al. 2004) on board the Spitzer Space Telescope (Werner et al., 2004). The IRS instrument provides high- and low-resolution spectroscopy in the mid-IR regime (5−40 μm). Low-resolution spectra ($R \sim 60 - 130$) were obtained with the Short-Low (SL) and Long-Low (LL) modules, which provide coverage from $5 - 14$ μm and $15 - 40$ μm, respectively. We also analyze a high-resolution ($R \sim 600$) spectral map of NGC 7023 and 2 ISM objects acquired with the IRS/Short-High (SH) module, covering the wavelength range $9.9 - 19.5$ μm. These SH data were obtained from the NASA/IPAC Spitzer Heritage Archive[*] (AORkey: 3871232, PI: Giovanni Fazio). Previous studies that have examined these data are those of Boersma, Bregman, and Allamandola (2014, 2015), Boersma, Bregman, and Allamandola (2013), Rosenberg et al. (2011), and Sellgren, Uchida, and Werner (2007).

2.2.3 Reduction

The SAGE-Spec data included in this study were obtained in reduced form. The project and the data reduction process are described in detail by Kemper et al. (2010); we briefly review the reduction steps here. The Spitzer Science Center[†] (SSC) data-reduction pipeline (version S18.7) was used to produce flat-field corrected images. Background subtraction was completed using on- and off-source nod positions. Rogue pixels were removed and replaced using the `imclean` algorithm, part of `irsclean`, provided by the SSC. Spectra were extracted using the SSC pipeline modules `profile`, `ridge`, and `extract`. Extracted spectra were

[*] http://sha.ipac.caltech.edu/applications/Spitzer/SHA/
[†] http://ssc.spitzer.caltech.edu

Table 2.1: The sample

Object	Type	Resolv.[a]	SSID[b]	AOR key	Extent[c] ["]	RA [J2000]	Dec. [J2000]
HD269211	H II?[d]	Integ.	4250	19151360	9.7	05 12 30.26	-70 24 21.75
HD32364	H II?[d]	Integ.	4122	19150592	11.2	04 57 14.28	-68 26 30.55
IRAS05192-6824	UCH II[e]	Integ.	4313	19011584	6.1	05 19 06.84	-68 21 36.41
IRSX104	H II	Integ.	104	22425088	-	05 24 13.30	-68 29 58.98
IRSX4087	H II	Integ.	4087	11239168	5.3	04 55 06.47	-69 17 08.30
IRSX4713	YSO[f]	Integ.	4713	16943616	6.3	05 40 12.02	-70 10 05.83
IRSX4729	YSO[f]	Integ.	4729	16943616	5.9	05 40 46.83	-70 11 22.73
IRSX4755	YSO[f]	Integ.	4755	11239424	7.0	05 43 19.62	-69 26 27.68
MSXLMC1306	H II	Integ.	4059	10958592	6.5	04 52 58.80	-68 02 56.77
MSXLMC217	H II	Integ.	4263	10962176	5.9	05 13 24.68	-69 10 48.12
MSXLMC559	H II	Integ.	4419	10963712	-	05 25 49.23	-66 15 08.50
MSXLMC764	H II	Integ.	4538	10967040	7.6	05 32 52.62	-69 46 22.84
MSXLMC836	H II	Integ.	4527	10966528	6.4	05 32 31.95	-66 27 15.15
MSXLMC889	H II	Integ.	4621	10968576	6.7	05 38 31.64	-69 02 14.92
MSXLMC934	H II	Integ.	4652	10969088	13.4	05 39 15.83	-69 30 38.39
N159-P2	YSO	Integ.	4665	12548352	10.8	05 39 41.88	-69 46 11.94
NGC 7023	RN	Extend.	-	3871232	-	21 01 32.50	+68 10 18.0
Cirrus1b	ISM	Extend.	-	4120832	-	17 32 53.80	-33 10 01.4
Cirrus3	ISM	Extend.	-	4119296	-	16 03 38.70	-52 18 01.7

Notes. Additional sources (not listed) are from Boersma et al. (2010), Peeters et al. (2012), and Smith et al. (2007b). [a]Whether the source is resolved or not (i.e., integrated spectrum or extended); integrated sources are from Surveying the Agents of Galaxy Evolution Spectroscopy program (SAGE-Spec; Kemper et al. 2010), data release 3. [b]SAGE-Spec ID number. [c] Point sources are those with no extent listed. [d]Object type uncertain in literature. [e]Ultra-compact H II region (Beasley et al., 1996). [f]Classification from Woods et al. (in prep.).

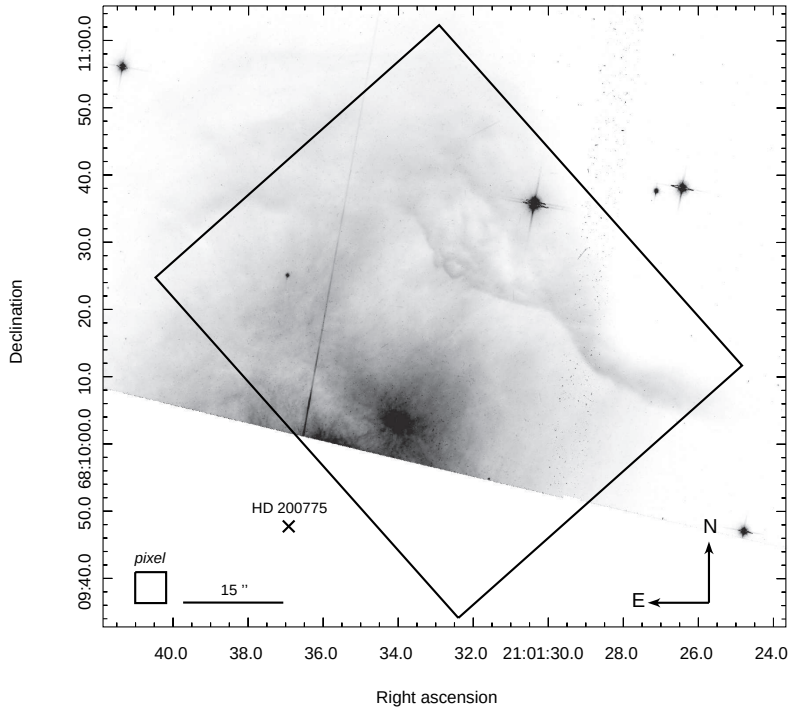

Figure 2.1: Hubble Space Telescope image of NGC 7023, with the Spitzer/IRS SH field of view outlined by the black box. This image is composed from four filters: wide-band filters at 475 and 625 nm, a long-pass filter at 850 nm, and a narrow-band filter at 658 nm. The exciting star, HD 200775, a B2.5 Ve star (Finkenzeller, 1985), is indicated by the black cross towards the lower left.

coadded to produce one spectrum per nod position, per instrument module. The products were then calibrated and stitched together to produce the final spectra.

The SINGS data were also provided in reduced form by Smith et al. (2007b). These data were processed with IRS pipeline version S14 and reduced with the `CUBISM` tool (Smith et al., 2007a), including scaling and stitching of spectral segments to construct the final low-resolution spectra.

The SH maps of NGC 7023, Cirrus 1b and Cirrus 3 were reduced in a similar manner to that of NGC 2023, which was described in paper I. The raw data were processed by the SSC, using pipeline version S18.7. The reduction process was completed using `CUBISM` (Smith et al., 2007a), including co-addition and bad pixel cleaning. The extraction for NGC 7023 was accomplished by stepping a 2 × 2-pixel aperture across the map.

2.3 Analysis

2.3.1 Spectral inventory

A typical IRS low-resolution spectrum is shown in Figure 2.2, represented by the H II region MSX LMC 1306. A rising mid-to-far-IR dust continuum is common in many objects in the sample. There are also several atomic emission lines frequently present, including [Ar II] 6.99 μm, [Ar III] 8.99 μm, [S IV] 10.51 μm, [Ne II] 12.81 μm, [Ne III] 15.56 μm, and [S III] 18.71 μm. We frequently observe the S(3) 9.7 μm, S(2) 12.3 μm and S(1) 17.0 μm rotational lines of H_2, and occasionally C_{60} fullerene emission at 17.4 and 18.9 μm (Cami et al., 2010; Sellgren et al., 2010). The PAH features at 6.2, 7.7, 8.6, 11.2, 12.7, 15.8, 16.4, 17.4, and 17.8 μm are visible in all sources. Note that the 17.4 μm band arises from both PAH and C_{60} emission (Sellgren et al., 2010). In addition to the aforementioned PAH emission bands, there are several weaker PAH bands visible at 5.25, 5.75, 6.0, 11.0, 12.0, 13.5 and 14.2 μm. Strong emission plateaus from 5-10 μm, 10-15 μm, and 15-18 μm are observed. Additionally, some spectra display a strong silicon carbide feature at 11 μm (Bernard-Salas et al., 2009; Treffers and Cohen, 1974).

2.3.2 Spectral decomposition

A local spline continuum is fit to each spectrum to isolate the PAH emission features (Figure 2.2), a method that has been used in several previous studies (e.g., Bernard-Salas et al. 2009; Boersma et al. 2010; Hony et al. 2001; Peeters et al. 2002; Stock et al. 2013, 2014). Spline anchor points are chosen to be adjacent to emission features, and are allowed to move within a predefined window. When necessary, smoothing and/or a process that locates local minima are used to improve anchor positions. In addition to the local continuum, a global contin-

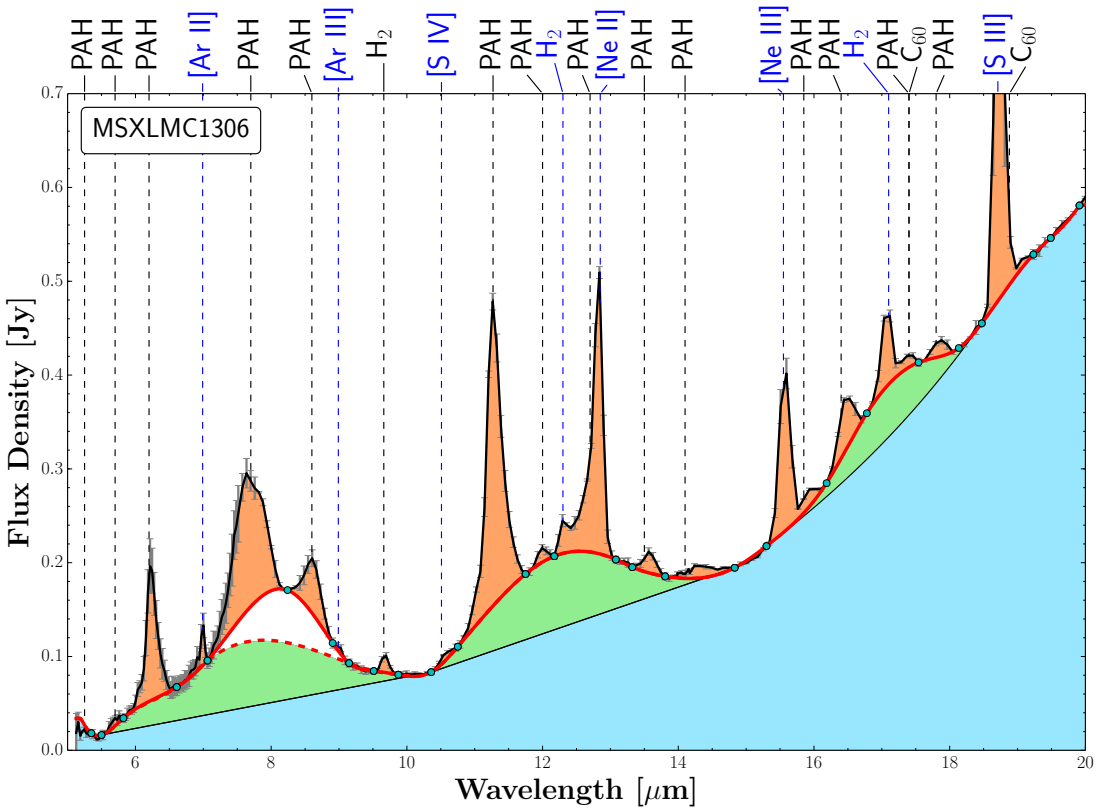

Figure 2.2: A typical IRS low-resolution spectrum from the SAGE-Spec sample is shown, that of LMC H ii region MSX 1306. Prominent PAH features and atomic/molecular emission lines are visible (see labels at top). A local continuum is identified with a spline fit (red line). The continuum in the 5-10 µm range can be fit with or without a continuum point between the 7.7 and 8.6 µm features (see dashed red line). Three plateaus are identified underneath the PAH emission bands (green shaded region).

uum is defined. This continuum underscores the emission plateaus at 5-10 μm, 10-15 μm, and 15-18 μm. The 7.7 and 8.6 μm features can be drawn with or without a spline anchor point between them, depending on the decomposition. Here, we use such an anchor point near 8.2 μm. The molecular hydrogen and atomic emission lines will be dealt with separately and are discussed in Section 3.4.

Other methods for measuring the PAH bands are possible and are considered in the literature. These include fitting Drude profiles to the individual components (the PAHFIT tool; Smith et al. 2007b) or Lorentzian profiles (Boulanger et al., 1998; Galliano et al., 2008). It has been shown that the decomposition method chosen affects the measured band intensities, but it does not affect the trends found in the correlations of band intensity ratios (Galliano et al., 2008; Smith et al., 2007b). The spline decomposition method is chosen here for comparison with previous 15-20 μm PAH studies (paper I, II, Boersma et al. 2010).

2.3.3 Measurement methods

The plateaus are measured by direct integration between the global continuum and local continuum (see Figure 2.2). After subtracting the local continuum, PAH band fluxes in the 5-15 μm range are measured by direct integration, except for the 6.0, 11.0 and 12.7 μm bands. The 6.0 and 11.0 μm bands are blended with the 6.2 and 11.2 μm bands in low-resolution spectra, respectively. Therefore, Gaussians are used to separate these subfeatures and determine their fluxes (see paper II for details). Special care is required when measuring the 12.7 μm PAH feature, as it blends with the 12.8 μm [Ne II] line and the 12.3 μm H_2 line (when present). We separate these components by scaling the average 12.7 μm PAH band profile (from Hony et al. 2001) to fit the data between 12.45 − 12.6 μm, where only PAH emission is expected (Figure 2.3). After subtracting the scaled PAH profile, the remaining lines are fit with Gaussians. This method is identical to the decomposition described by Stock et al. (2014), though we use the range 12.45 − 12.6 μm instead of 12.4 − 12.6 μm. This is because the 12.3 μm H_2 line is strong enough in some of our spectra to produce non-negligible (albeit minor) emission redward of 12.4 μm. We test for systematic effects in this decomposition by constructing an artificial spectrum. It is composed of the average 12.7 μm PAH band profile from Hony et al. (2001) plus two Gaussians, for the 12.3 H_2 line and the 12.8 [Ne II] line, and a variable amount of noise. We find that the derived PAH flux corresponds to the input artificial PAH flux within 2 to 3% when the integrated strength of the [Ne II] line is less than ten times that of the 12.7 PAH band. This is true for all our sources. The 12.3 μm H_2 line in our sample does not influence the derived PAH flux when decomposed this way.

The 15-20 μm PAH bands and the atomic/molecular lines are also measured through Gaus-

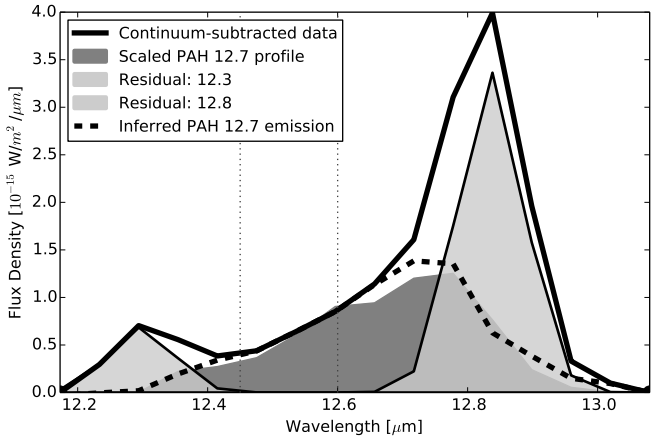

Figure 2.3: An example decomposition of the 12.7 μm complex. The continuum-subtracted spectrum (solid line) is fit with the scaled mean 12.7 μm PAH band profile (dark gray shading), as found by Hony et al. (2001). The fit is performed between 12.45 and 12.60 μm (denoted by the dotted vertical lines). The fitted PAH profile (dark gray shading) can then be subtracted from the spectrum, leaving a remainder of the 12.3 μm H_2 emission line and the 12.8 μm [Ne ii] line (light gray shading). Returning to the original continuum-subtracted data, subtracting the two atomic lines then leaves only the inferred PAH 12.7 μm emission (dashed line).

sian decomposition. The 16.4 μm band is slightly asymmetric, while the other 15-20 μm PAH bands are symmetric (paper I). There is frequent blending between the 15.55 μm [Ne III] line and the 15.8 μm PAH feature, as well as between the 17.1 μm H_2 line and the 17.4 μm PAH band in low-resolution spectra. Emission by the fullerene C_{60} is known to be present at 17.4 and 18.9 μm in some objects (Cami et al., 2010; Sellgren et al., 2010). The 17.4 μm C_{60} emission is approximately half of the intensity of the 18.9 μm band (estimated to be ∼0.4 in Sellgren et al. 2010, ∼0.6 in Cami et al. 2010 and ∼0.5 in Bernard-Salas et al. 2012; we adopt 0.5). The 18.9 μm band is observed in some of our spectra, typically blended to some degree with the 18.7 [S III] line in low-resolution spectra. We examine the presence of C_{60} emission by fitting the data with the model of C_{60} emission from TC1 (Cami et al., 2010) and an appropriate Gaussian for the [S III] 18.71 μm line. In the sample of integrated sources, we detect C_{60} emission in four objects: IRSX 4755 (with associated signal-to-noise ratio, or SNR, of 3.4), IRSX 4087 (5.6), HD 32364 (5.5) and HD 269211 (5.9). We correct our measured 17.4 μm band flux by subtracting the expected 17.4 μm C_{60} component when the 18.9 μm C_{60} band is present. The residual flux, if significant, is then attributed to the 17.4 μm PAH band.

The measured PAH and C_{60} fluxes of the SAGE-Spec sources and the two cirrus sources are presented in Table 2.2. The fluxes of the SINGS sources are shown in Table 2.3.

2.4 Results

We examine correlations between the 15-20 μm bands and the spatial distribution of the PAH emission in the extended RNe. NGC 2023S and NGC 2023N refer to the south and north maps of NGC 2023, respectively (papers I and II). Band fluxes in the correlation study are typically normalized to the 11.2 μm band. Normalization is required because PAH abundances and object distances will vary from source to source. Only band ratios with 3σ detections are included. The weighted Pearson correlation coefficients for all correlations are presented in Table 2.4.

2.4.1 Correlation plots

2.4.1.1 The 16.4, 17.4 and 17.8 μm bands

Correlation plots of the 16.4, 17.4, and 17.8 μm bands are presented in Figure 2.4. We address these in turn.

17.8 vs. 16.4 μm. These band fluxes are the strongest correlated for the integrated sources (correlation coefficient $r = 0.93$). Some segregation by object type is observed: two evolved stars sit at the lowest ratios of 16.4/11.2 and 17.8/11.2 (0.030 and 0.010, respectively), galaxies slightly higher at (0.060, 0.015), and H II regions at the highest values (centered near 0.10, 0.035). The galaxies and H II regions each span a range covering roughly a factor of two on each axis. The 17.8 and 16.4 μm bands also correlate in the RNe. NGC 7023 has a correlation coefficient of $r = 0.85$ and spans nearly the same variation in 16.4/11.2 and 17.8/11.2 as the integrated sources. NGC 7023 has a cluster of data points centered near (0.13, 0.030), which we determine to originate in the portion of the map closest to the exciting star (the upper third of the map; see Figure 2.10). NGC 2023S has a correlation coefficient of $r = 0.82$ and has a line of best fit close to that of NGC 7023, despite spanning half the range in abscissa; NGC 2023N has a similar range and correlation coefficient ($r = 0.72$). Its line of best fit is closer to the fit for the integrated sources, but it should be noted it also has far fewer pixels than those contained in the NGC 7023 or NGC 2023S maps given the SNR criterion.

17.4 vs. 16.4 μm. The 17.4 and 16.4 μm band fluxes are observed to correlate. NGC 7023 exhibits a correlation coefficient of $r = 0.80$, while NGC 2023S and 2023N have associated coefficients of $r = 0.45$ and $r = 0.57$, respectively. NGC 7023 and NGC 2023 have similar lines of best fit. The integrated sources however display a trend on a much steeper gradient, aside from two lone H II regions, and have a correlation coefficient of $r = 0.67$. The integrated sources and NGC 2023 generally span the same abscissa and ordinate ranges, but NGC 7023 is set to higher ratios of 16.4/11.2, with only modest overlap with NGC 2023 and

Table 2.2: PAH emission band fluxes: SAGE and ISM sources

Object	6.2 μm	7.7 μm	8.6 μm	11.2 μm	12.7 μm	15.8 μm	16.4 μm	17.4 μm	17.8 μm	Plateau	18.9 μm C_{60}
HD269211	-	-	3.64 (1.14)	13.09 (2.02)	22.66 (1.51)	-	1.77 (0.11)	0.42 (0.11)	0.56 (0.10)	8.81 (0.88)	1.07 (0.18)
HD32364	-	-	-	24.65 (1.68)	23.01 (1.04)	-	2.02 (0.12)	0.42 (0.08)	0.79 (0.14)	16.91 (1.69)	1.43 (0.26)
IRAS05192-6824	14.10 (0.77)	28.35 (1.85)	4.44 (0.98)	14.75 (1.70)	14.35 (1.56)	-	1.54 (0.19)	-	-	7.99 (0.80)	-
IRSX104	8.33 (1.53)	10.40 (1.15)	-	6.45 (0.71)	3.28 (0.75)	0.44 (0.12)	0.72 (0.14)	-	-	-	-
IRSX4087	9.41 (1.15)	14.48 (1.34)	3.50 (0.75)	10.60 (0.67)	10.07 (0.74)	0.63 (0.13)	1.13 (0.15)	-	0.48 (0.12)	5.27 (0.53)	1.62 (0.29)
IRSX4713	5.76 (0.64)	8.47 (0.60)	2.05 (0.20)	5.43 (0.18)	1.48 (0.18)	-	0.41 (0.10)	-	-	-	-
IRSX4729	6.95 (1.00)	10.65 (1.23)	2.17 (0.64)	5.82 (0.57)	1.92 (0.29)	-	0.41 (0.08)	-	-	2.04 (0.20)	-
IRSX4755	18.30 (2.66)	23.74 (3.48)	5.13 (0.94)	10.38 (1.17)	6.02 (0.91)	-	0.82 (0.11)	-	-	-	0.34 (0.10)
MSXLMC1306	21.60 (5.09)	38.72 (5.16)	6.76 (1.38)	20.59 (1.33)	12.46 (0.86)	0.48 (0.10)	1.64 (0.10)	-	0.46 (0.09)	8.48 (0.85)	-
MSXLMC217	27.09 (4.94)	52.02 (4.33)	7.27 (2.00)	27.14 (1.43)	24.50 (1.25)	-	2.30 (0.25)	-	-	11.70 (1.17)	-
MSXLMC222	-	-	3.10 (0.33)	6.97 (0.31)	-	-	0.82 (0.11)	-	-	-	-
MSXLMC559	31.00 (1.43)	56.55 (1.39)	7.92 (1.01)	18.46 (0.87)	17.97 (1.30)	-	1.86 (0.61)	-	-	-	-
MSXLMC764	-	76.81 (13.82)	-	39.66 (5.74)	33.30 (3.61)	1.85 (0.33)	4.40 (0.18)	0.96 (0.11)	2.09 (0.31)	-	-
MSXLMC836	22.14 (0.67)	34.98 (1.29)	5.80 (0.52)	19.88 (0.57)	9.74 (0.41)	-	1.28 (0.12)		0.52 (0.13)	7.88 (0.79)	-
MSXLMC889	61.10 (7.74)	154.46 (6.41)	20.51 (4.29)	70.84 (5.38)	80.30 (3.13)	-	8.00 (0.17)	1.47 (0.28)	2.79 (0.34)	36.50 (3.65)	-
MSXLMC934	-	-	-	50.93 (1.71)	52.89 (2.34)	-	4.88 (0.54)	0.97 (0.32)	1.94 (0.47)	23.38 (2.34)	-
N159-P2	-	-	-	32.70 (0.85)	21.82 (0.99)	-	5.01 (0.80)		1.93 (0.63)	-	-
Cirrus1b	-	-	-	52.84 (1.08)	33.84 (0.87)	1.60 (0.29)	3.60 (0.48)	1.37 (0.28)	1.30 (0.32)	-	-
Cirrus3	-	-	-	49.67 (0.94)	27.65 (0.61)	1.91 (0.18)	3.38 (0.18)	1.22 (0.23)	0.95 (0.17)	-	-

Notes. In units of 10^{-16} W/m^2, except the two extended cirrus sources, which are in units of 10^{-2} W/m^2/sr. Uncertainties are given in parentheses.

Table 2.3: PAH emission band fluxes: SINGS sources

Object	6.2 μm	7.7 μm	8.6 μm	11.2 μm	12.7 μm	15.8 μm	16.4 μm	17.4 μm	17.8 μm	Plateau
MRK33	7.82 (1.26)	13.88 (1.49)	3.33 (0.39)	5.43 (0.30)	3.72 (0.29)	-	0.45 (0.09)	0.16 (0.04)	0.16 (0.05)	-
NGC0337	-	17.62 (1.62)	3.58 (0.45)	7.84 (0.38)	3.83 (0.30)	-	0.56 (0.10)	-	-	3.47 (0.35)
NGC0628	-	-	-	3.48 (0.51)	-	-	0.25 (0.05)	-	-	-
NGC0855	-	-	-	3.50 (0.90)	-	-	0.31 (0.08)	-	-	-
NGC0925	-	-	-	4.72 (0.92)	-	-	0.27 (0.06)	-	-	-
NGC1097	73.72 (1.36)	157.03 (1.58)	24.29 (0.47)	65.07 (0.42)	38.90 (0.38)	1.07 (0.22)	3.58 (0.42)	1.56 (0.45)	-	25.74 (2.57)
NGC1482	100.70 (1.51)	230.20 (2.04)	31.10 (0.76)	74.11 (0.71)	-		4.36 (1.29)	-	-	-
NGC1512	-	-	-	9.05 (1.48)	-	-	0.47 (0.08)	-	-	3.42 (0.34)
NGC2403	7.51 (1.29)	10.42 (1.37)	-	5.13 (0.62)	-	-	0.43 (0.05)	-	-	-
NGC2798	-	-	-	47.55 (0.90)	29.26 (0.84)	0.83 (0.23)	2.07 (0.35)	1.10 (0.30)	-	-
NGC2976	-	-	-	4.56 (0.64)	-	-	0.38 (0.05)	-	-	1.83 (0.18)
NGC3049	-	-	-	5.41 (0.75)	3.25 (0.68)	-	0.28 (0.06)	-	-	-
NGC3184	-	-	-	8.38 (1.08)	5.47 (1.02)	-	0.31 (0.04)	-	-	-
NGC3265	-	-	-	8.15 (0.75)	3.89 (0.74)	-	0.46 (0.11)	-	-	-
NGC3351	16.01 (1.94)	53.97 (2.09)	5.30 (0.82)	17.63 (0.84)	11.64 (0.85)		1.04 (0.15)	-	-	12.92 (1.29)
NGC3521	13.44 (1.50)	43.05 (1.72)	6.01 (0.59)	16.56 (0.52)	-	0.33 (0.07)	1.21 (0.10)	0.36 (0.08)	0.33 (0.10)	13.29 (1.33)
NGC3621	15.28 (1.58)	-	-	12.12 (0.63)	4.96 (0.67)	-	0.74 (0.06)	0.21 (0.06)	-	4.64 (0.46)
NGC3627	16.27 (1.86)	27.32 (2.04)	4.40 (0.71)	19.59 (0.86)	-	0.44 (0.08)	0.86 (0.12)	-	-	10.66 (1.07)
NGC3773	-	-	-	4.12 (0.89)	-	-	-	-	-	-
NGC3938	-	-	-	3.00 (0.20)	1.48 (0.20)	-	0.18 (0.05)	-	-	2.18 (0.22)
NGC4254	-	-	-	23.23 (1.35)	-	-	1.61 (0.16)	-	-	8.40 (0.84)
NGC4321	33.00 (2.12)	69.04 (2.58)	10.03 (1.01)	27.13 (1.07)	14.83 (1.10)	-	1.26 (0.15)	0.54 (0.14)	-	11.56 (1.16)
NGC4536	91.38 (2.19)	192.04 (2.54)	27.99 (0.79)	66.01 (0.70)	-	1.13 (0.36)	2.86 (0.55)	-	-	29.12 (2.91)
NGC4559	-	-	-	5.29 (0.47)	2.84 (0.41)	-	0.36 (0.06)	0.12 (0.04)	-	-
NGC4569	-	-	5.89 (1.16)	24.68 (1.24)	-	0.44 (0.09)	1.23 (0.09)	-	-	14.15 (1.41)
NGC4579	-	-	-	4.76 (1.12)	-	-	0.40 (0.11)	-	-	-
NGC4631	-	-	-	30.72 (0.55)	-	0.47 (0.13)	2.09 (0.20)	-	-	-
NGC4736	34.32 (1.62)	40.69 (2.13)	9.73 (0.99)	48.69 (1.08)	-	0.89 (0.12)	2.03 (0.18)	0.47 (0.14)	0.51 (0.12)	16.99 (1.70)
NGC4826	44.40 (2.21)	108.11 (2.58)	18.10 (1.32)	42.38 (1.44)	-	0.93 (0.11)	2.30 (0.18)	0.72 (0.16)	0.72 (0.10)	19.41 (1.94)
NGC5033	19.75 (1.76)	36.88 (1.75)	6.15 (0.79)	17.27 (0.81)	8.47 (0.74)	-	0.91 (0.14)	0.33 (0.10)	0.29 (0.09)	9.01 (0.90)
NGC5055	16.65 (1.42)	44.23 (1.76)	-	21.37 (0.81)	-	-	0.97 (0.10)	0.30 (0.08)	0.30 (0.06)	10.06 (1.01)
NGC5194	27.32 (1.27)	56.63 (1.59)	10.35 (0.89)	29.35 (0.88)	-	0.48 (0.10)	1.28 (0.14)	0.43 (0.11)	0.34 (0.09)	12.83 (1.28)
NGC5195	-	32.48 (2.59)	-	36.03 (1.28)	-	-	1.93 (0.46)	-	-	15.19 (1.52)
NGC5713	36.36 (1.25)	75.25 (1.62)	11.23 (0.72)	29.04 (0.69)	-	-	1.78 (0.16)	-	-	12.49 (1.25)
NGC5866	-	-	-	8.24 (0.86)	-	0.22 (0.05)	0.34 (0.07)	-	-	-
NGC6946	90.92 (1.93)	189.33 (2.10)	29.22 (1.11)	61.51 (1.05)	-	-	4.34 (0.41)	-	-	33.86 (3.39)
NGC7331	-	-	-	15.56 (1.26)	-	0.27 (0.08)	0.83 (0.08)	-	-	7.93 (0.79)
NGC7552	81.57 (1.84)	173.99 (2.22)	26.90 (0.97)	71.78 (0.96)	47.74 (0.95)	-	4.79 (0.97)	-	-	-

Notes. In units of 10^{-14} W/m^2. Uncertainties are given in parentheses. No 3σ detections of 18.9 μm C_{60} emission were found for these data.

Table 2.4: Weighted Pearson correlation coefficients

Correlation	Integrated sources	N7023[a]	N2023N[b]	N2023S[b]
17.4 vs. 16.4	0.67	0.80	0.57	0.45
17.8 vs. 16.4	0.93	0.85	0.72	0.82
17.8 vs. 17.4	0.63	0.53	0.97	0.47
16.4 vs. 15.8	0.74	0.22	-	-0.28
17.4 vs. 15.8	0.58	0.37	-	-0.14
17.8 vs. 15.8	0.75	0.40	-	-0.08
15.8 vs. 11.2	-0.28	0.38	-	0.89
Plat. vs. 11.2	0.42	0.47	0.92	0.87
Plat. vs. 15.8	0.28	0.46	-	0.88
12.7 vs. 11.0	0.51	0.95	0.88	0.91
16.4 vs. 11.0	0.36	0.92	0.92	0.95
17.4 vs. 11.0	-0.14	0.84	0.69	0.51
17.8 vs. 11.0	-0.26	0.87	0.89	0.81
16.4 vs. 12.7	0.28 [0.68][c]	0.89	0.88	0.92
17.4 vs. 12.7	0.69	0.83	0.55	0.35
17.8 vs. 12.7	0.23 [0.66][c]	0.86	0.53	0.71

Notes. [a] See individual correlation plots for coefficients organized by region; regions defined in Figure 2.10. [b] See also paper I, II. [c] H II regions alone.

the integrated sources. This correlation was previously observed by Berné and Tielens (2012).

17.8 vs. 17.4 μm. The 17.8 and 17.4 μm bands also correlate. The integrated sources and NGC 7023 span similar ranges in abscissa and ordinate values, with associated coefficients $r = 0.63$ and $r = 0.53$, respectively. NGC 2023 spans half the range of 17.8/11.2 in comparison, though a similar extent is observed in 17.4/11.2. NGC 2023S has correlation coefficient of $r = 0.47$ and NGC 2023N of $r = 0.97$, though the latter has far fewer data points included (12 versus 52, respectively). The individual sources again fall upon a slightly different gradient, as they appear to be displaced toward higher 17.4/11.2 values. The outlying H II regions in this figure are also the outliers in the correlation plot of the 17.4 and 16.4 μm bands. Systematic problems may affect the 17.4 μm band measurement in our sample as its derived flux is dependent on an accurate measurement of the 18.9 μm C_{60} band. When the latter cannot be observed (or reliably measured) it is possible that the derived 17.4 μm PAH band flux is overestimated, as the 17.4 μm C_{60} contribution cannot be removed, if present. This issue is particularly prominent in low-resolution spectra, which comprise most of the integrated sources in this sample (apart from the two ISM cirrus sources), as the 18.9 μm C_{60} band blends with the [S III] 18.71 μm line. The RNe were observed in high resolution and are less susceptible to this type of overestimation, which may explain why the gradients observed in the correlation plots involving the 17.4 μm band differ for integrated sources versus RNe (e.g.,

Figure 2.4).

Correlations with the 12.7 μm band. The 16.4, 17.4 and 17.8 μm bands are observed to correlate with the 12.7 μm band (Figure 2.5). NGC 7023 displays a high correlation coefficient ($r = 0.89$), though there is deviation from the linear fit in our data at high abscissa values. In our data, there is a cluster of data points at 12.7/11.2=0.75, 16.4/11.2=0.13, all of which originate in the third of the map nearest the exciting star in NGC 7023. Regardless, we find a strong correlation between these band ratios in NGC 7023, peaking in the middle portion of the map ($r = 0.94$; see Figure 2.10 for map region definitions). The gradient of the NGC 7023 data is consistent with those of NGC 2023 (both north and south). The integrated sources of this study show no trend as a whole, but they do tend to cluster about a position coincident with the center of the NGC 2023 data. The subset of H II regions alone however do display a correlation ($r = 0.68$). Since the 16.4, 17.4 and 17.8 μm bands correlate (Figure 2.4), it is not surprising that we find that the 17.4 and 17.8 μm bands correlate with the 12.7 μm band in RNe. We additionally observe that H II regions display a correlation between the 17.8 and 12.7 μm bands. Nothing can be determined about H II regions amongst the 17.4 and 12.7 μm bands as there are too few sources meeting the detection criteria. The 12.7 μm band was previously observed to correlate with the 16.4 μm band in NGC 2023 (paper I; $r = 0.92$ in the southern map, $r = 0.88$ in the northern map) and in NGC 7023 (Boersma, Bregman, and Allamandola 2014; their Figure 9).

Correlation with the 6.2 μm band. We examine the flux ratios of the 16.4 and 6.2 μm bands in Figure 2.7 for the integrated sources in our sample. The 6.2 μm band cannot be measured in the SH RNe data as the wavelength coverage begins at $\sim$ 10 μm. Data from Boersma et al. (2010) are included, where we have replaced the authors' average SINGS galaxy data point with our individual SINGS sources. We observe no linear correlation ($r = 0.11$), though we note the lower-right quadrant is devoid of sources. Furthermore, we identify the H II regions as occupying the upper-left quadrant of this figure. If these are excluded from the data set, a modest correlation is observed ($r = 0.47$). A mostly linear trend ($r^2 = 0.76$) between these bands has been identified in NGC 7023 by Boersma, Bregman, and Allamandola (2014), their Figure 10, albeit with some residual curvature. Our measurements are consistent with their measurements at low abscissa/ordinate values.

Since we detect a correlation between the 16.4 and 12.7 μm bands, and essentially none between the 16.4 and 6.2 μm bands, we should expect no correlation between the 6.2 and 12.7 μm bands for consistency. We indeed detect no such correlation in our data alone. However, the 6.2 and 12.7 μm PAH bands have been observed to correlate for a sample of integrated sources of various object types (Hony et al., 2001) and within the RNe NGC 7023 (Boersma,

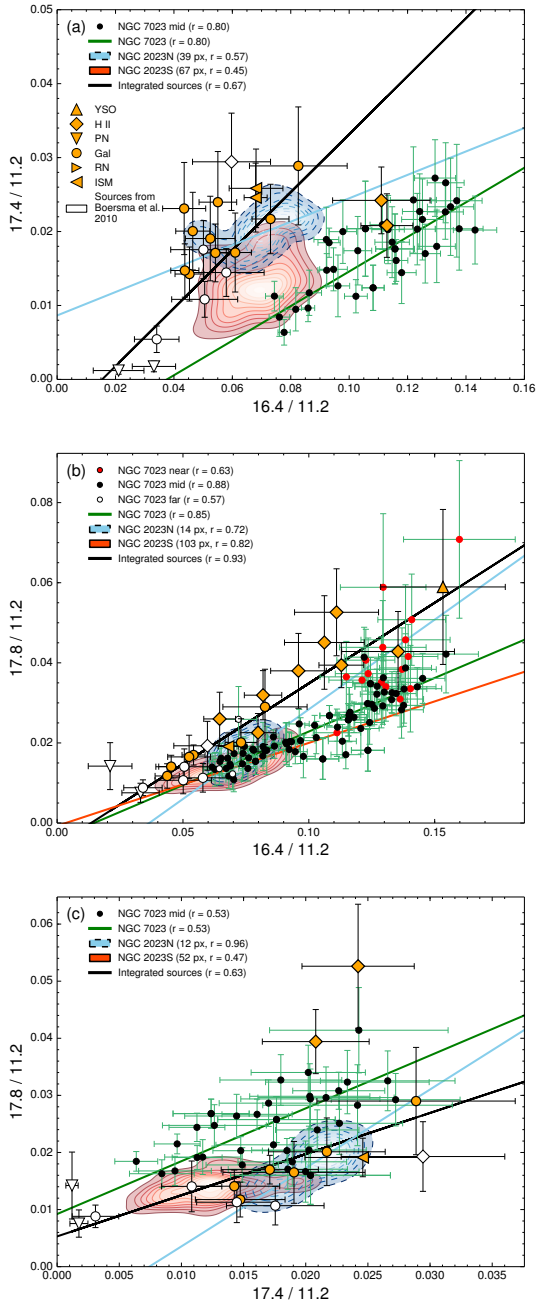

Figure 2.4: Correlation plots of flux ratios amongst the 16.4, 17.4 and 17.8 µm features. The filled blue and orange density contours represent the number densities of measurements of NGC 2023 North and South, respectively (papers I and II). Each displays ten linear contour levels, computed with a Gaussian kernel. The data points with green errorbars are from NGC 7023, separated into three regions (defined in Figure 2.10): data nearest to the exciting star (red dots); data from the center of the map, the peak PAH emission region (black dots); and data furthest from the exciting star (white dots). Each grouping is shown with an associated line of best fit when the correlation coefficient exceeds $r = 0.50$: integrated sources (black line), NGC 7023 (green line), NGC 2023N (blue line), NGC 2023S (orange line).

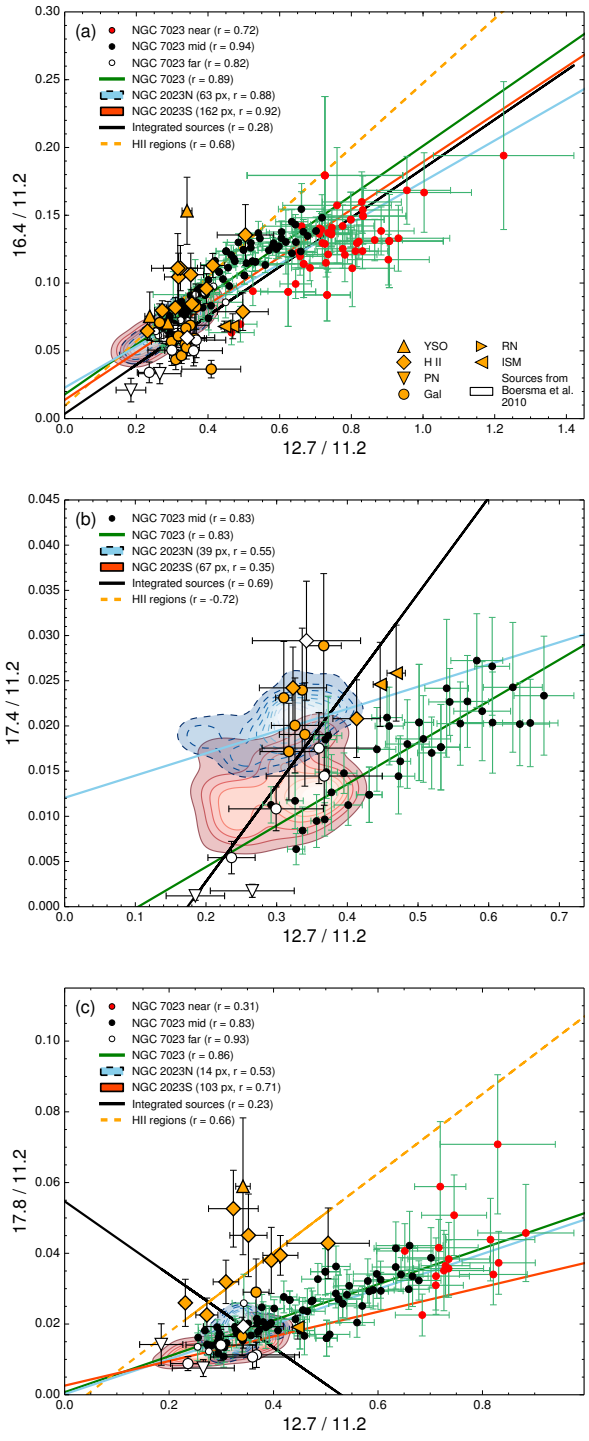

Figure 2.5: Correlation plots of the 16.4, 17.4 and 17.8 µm band fluxes versus the 12.7 µm band flux, each normalized to the 11.2 µm band flux.

Bregman, and Allamandola, 2014) and NGC 2023 (paper II). The lack of such a correlation in our sample of integrated sources is likely due to the small range of ratios probed by our data, as they span a small range of ratios relative to Hony et al. (2001).

Correlations with the 11.0 μm band. We observe that the 16.4, 17.4 and 17.8 μm bands correlate with the 11.0 μm band in NGC 2023 and NGC 7023 (Figure 2.6). The NGC 7023 pixels furthest from and nearest to the star tend to individually cluster, while the region containing the peak of the PAH emission shows linear correlations between band intensity ratios (regions defined in Figure 2.10). This clustering has been previously observed, for example in Boersma, Bregman, and Allamandola (2014). The 12.7 μm band is also included for comparison, and the RNe display strong correlations between the 12.7 and 11.0 μm bands ($r \geq 0.90$). The integrated sources show no clear correlations between the 11.0 μm band and the 12.7, 16.4, 17.4 and 17.8 μm bands, as they tend to cluster near 11.0/11.2∼0.060. They tend to be consistent with the observed RNe correlations for the 12.7 and 16.4 versus 11.0 μm bands, but they deviate for the 17.8 μm and especially the 17.4 μm band.

2.4.1.2 The 15.8 μm band

The 16.4, 17.4 and 17.8 μm bands do not appear to correlate with the 15.8 μm band (Figure 2.8). NGC 2023S shows no correlation between these bands (e.g., $r = -0.28$ when comparing the 15.8 and 16.4 μm bands) and NGC 2023N has too few detections to be represented here (papers I and II). NGC 7023 generally appears to have a similar distribution to NGC 2023S, with no overall correlation (e.g., $r = 0.22$). However, NGC 7023 does seem to exhibit a "C"-shaped distribution in the 16.4 versus 15.8 μm band intensity correlation, and to a lesser degree in the 17.8 versus 15.8 μm correlation plot. This may be indicative of a relationship present at 16.4/11.2 ratios greater than 0.12, and 17.8/11.2 ratios greater than 0.03, but it is not conclusive. The integrated sources are shown to occupy three regions of the correlation plots: the data of Boersma et al. (2010) at low abscissa values; the SINGS galaxies at an intermediate position; and H II regions or cirrus sources towards the upper-right quadrant. Together these produce a correlation (with coefficient $r = 0.74$) but this is possibly spurious. Specifically, in the previous plots (Figure 2.4), the identified correlations can be seen both individually within our sample and individually in the sample of Boersma et al. (2010). In contrast, these correlations involving the 15.8 μm band are not present in either sample in isolation. Additionally, the closeness of the [Ne III] 15.56 μm line to the 15.8 μm PAH band in low-resolution spectra affects how well the PAH band can be measured. This is compounded because the 15.8 μm PAH band is weak and is near the inflection point of the rising 15-18 μm continuum; the error on the continuum is not taken into account in the 3σ cut-off. Finally, the Pearson cor-

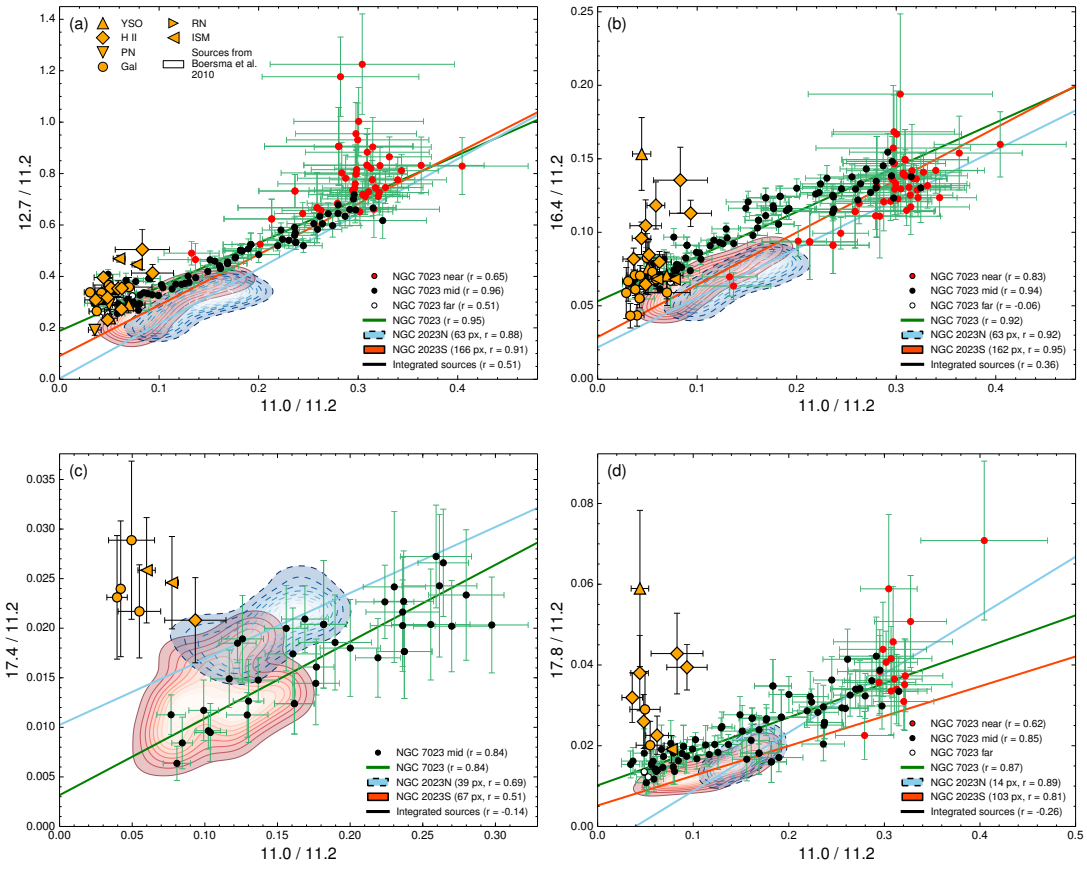

Figure 2.6: Correlation plots of the 12.7, 16.4, 17.4 and 17.8 µm bands versus the 11.0 µm band.

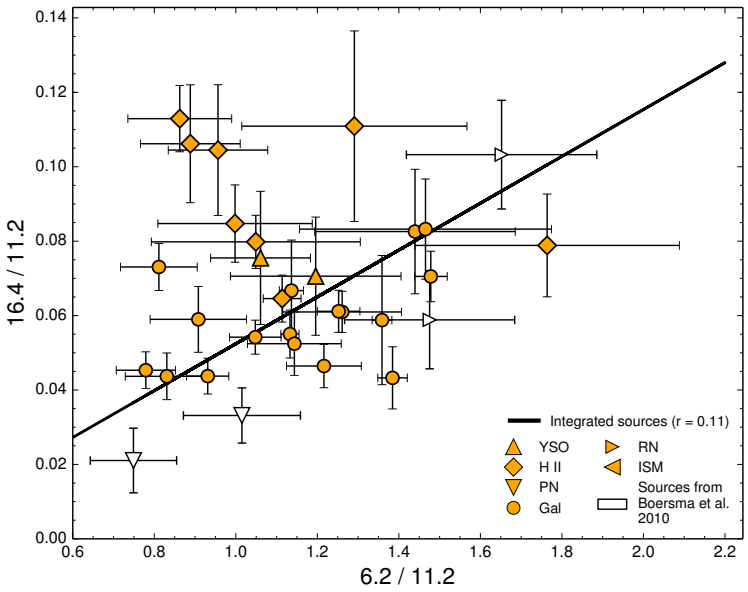

Figure 2.7: No linear relationship is observed between the 16.4 and 6.2 μm bands ($r = 0.11$); however, the lower-right quadrant is conspicuously devoid of sources, and our data span a small range of values (c.f. Boersma, Bregman, and Allamandola 2014).

relation coefficient is known to be sensitive to outlying points (Devlin, Gnanadesikan, and Kettenring, 1975), which is why the measured coefficients here are not necessarily meaningful, unlike in Figure 2.4.

The 15.8 and 11.2 μm bands were shown to correlate in NGC 2023 (paper I). We revisit this relationship in Figure 2.9(a). The data near the peak PAH emission region (i.e., in the middle of the NGC 7023 map, see Figure 2.10) are shown to correlate slightly ($r = 0.46$) and exhibit a gradient consistent with that in NGC 2023S. No correlation is identified for the integrated sources, though H II regions tend to lie at relatively high 15.8/12.7 ratios when compared to evolved stars or galaxies. The derived fluxes of the 15.8 and 12.7 μm bands are influenced by the presence of the [Ne II] 12.81 μm and [Ne III] 15.56 μm emission lines. These lines are present in H II regions and PNe and may influence or explain the observed discrepancy. Figures 2.9(b) and (c) compare the emission of the 15-18 μm plateau to those of the 11.2 and 15.8 μm bands, respectively, which were shown to correlate in NGC 2023 (paper I). We find that NGC 7023 has similar correlations within its peak emission region; the other NGC 7023 regions do not show a clear correlation by themselves but they are consistent with the correlation seen in the NGC 7023 peak ("mid") and NGC 2023. The integrated sources show no linear trend but there is significant clustering near the position (Plat./12.7, 11.2/12.7) $\sim$ (1.5, 3.5).

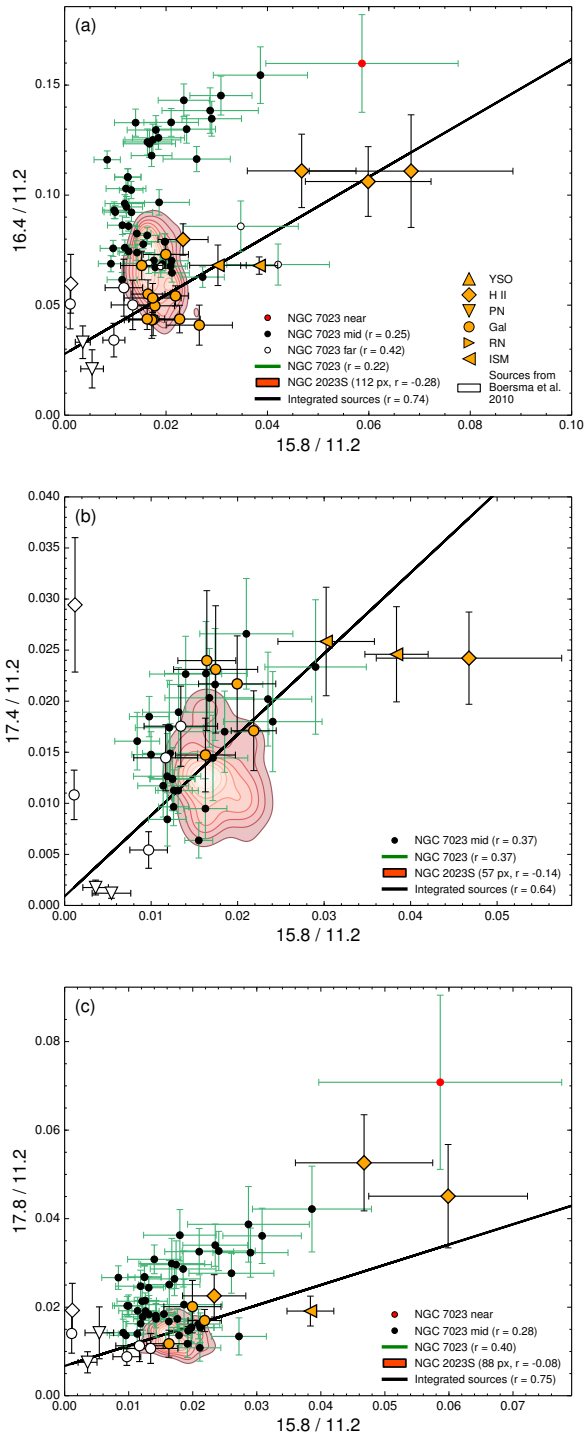

Figure 2.8: Correlation plots between the 11.2, 15.8 µm bands and the 15-18 µm plateau (panels a, b, c, respectively).

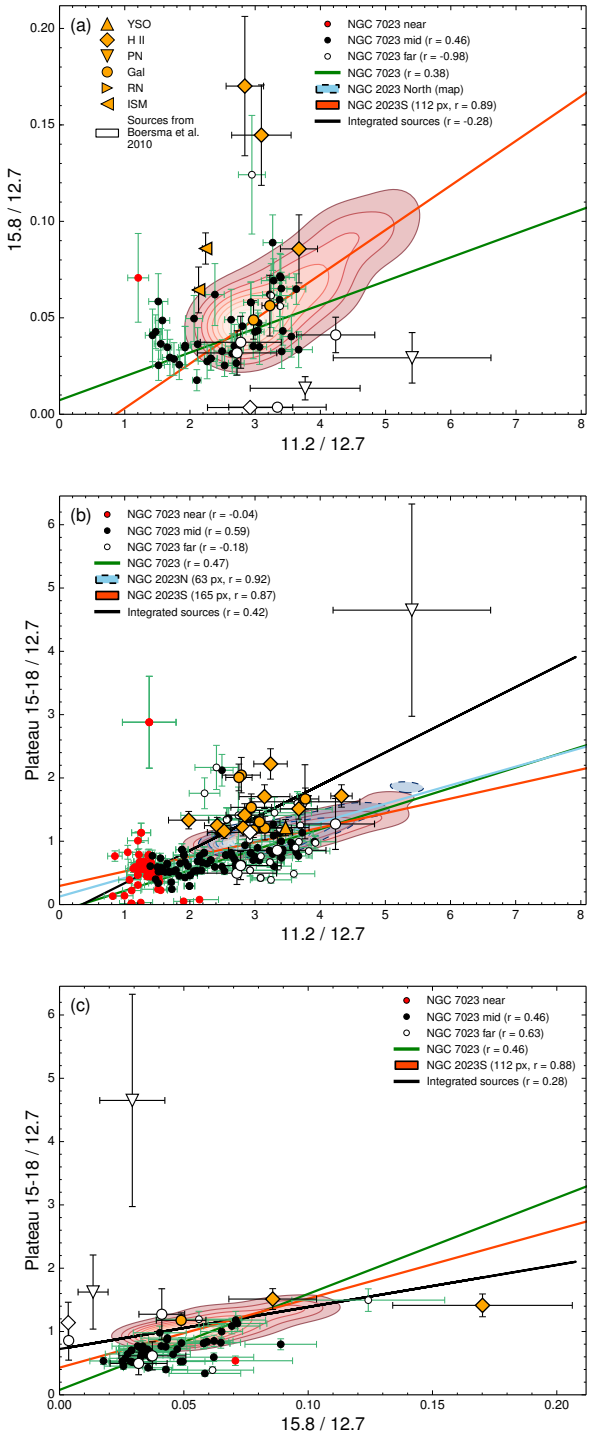

Figure 2.9: Correlation plots involving the 11.2 and 15.8 μm bands and the 15-18 μm plateau. (a) The 15.8 and 11.2 μm bands, normalized to the 12.7 μm PAH flux, correlate in RNe. (b), (c) 15-20 μm plateau correlations with the 11.2 and 15.8 μm bands in RNe.

2.4.2 Spatial distribution of 15-20 μm PAH emission

2.4.2.1 Map morphology

We have thus far focused solely on correlations between bands. Paper II finds that the tightness of a correlation between any two bands is related to their spatial coincidence. However, even two bands with different spatial distributions could retain high correlation coefficients (e.g., the 8.6 and 7.7 μm bands, with $r = 0.936$; paper II). It is therefore important to determine if the correlations we identify are corroborated by their spatial morphologies. To do this, we examine the spectral map of NGC 7023 (Figure 2.10) and compare it with the spectral map of NGC 2023 (papers I and II). The 16.4 μm data from this spectral cube has been previously examined by Sellgren, Uchida, and Werner (2007), and the 11.0, 11.2, 12.7, 16.4 μm bands and plateau emission by Boersma, Bregman, and Allamandola (2014, 2015) and Boersma, Bregman, and Allamandola (2013). Additionally, zones parallel to the PDR front have been identified by Berné and Tielens (2012) and Boersma, Bregman, and Allamandola (2014); we introduce three such zones in Figure 2.10.

The spatial distributions of the 12.7, 16.4 and 17.8 μm bands are very similar in appearance. Each of these is seen to be displaced slightly toward the irradiating star relative to the 11.2 μm band. The 17.8 μm band is slightly more compact than the 12.7 and 16.4 μm bands; we note it also has a limited SNR in comparison. In NGC 2023, the spatial distributions of the 12.7 and 16.4 μm bands are also nearly identical in appearance, and the 17.8 μm band is mildly more compact. The 17.4 μm band has some apparent differences from the 12.7, 16.4 and 17.8 μm bands in the spatial maps, despite correlating with these bands: its emission is more compact and appears to peak 10″ closer to the exciting star in both NGC 7023 and NGC 2023, though the 17.4 μm band has a limited SNR in NGC 7023. The 11.0 μm band is also displaced closer to the exciting star to a similar degree in both RNe. The 17.4 μm band appears identical to the 11.0 μm band in NGC 2023 prior to removing the C_{60} component; after correction, the 17.4 μm band is slightly more compact than the 11.0 μm band.

The 11.2 μm band and the 15-18 μm plateau have coincident peak positions in both RNe, while the 15.8 μm band peaks slightly further from the star. The 15.8 μm band is much less extended than the 11.2 μm band and the plateau in NGC 7023, but it is only reliably measured in a small portion of the map due to its low SNR. In NGC 2023, the 15.8 μm band has a higher SNR and it shows a spatial distribution extremely close to that of the 11.2 μm band. The 15-18 μm plateau in NGC 2023 is much broader in extent.

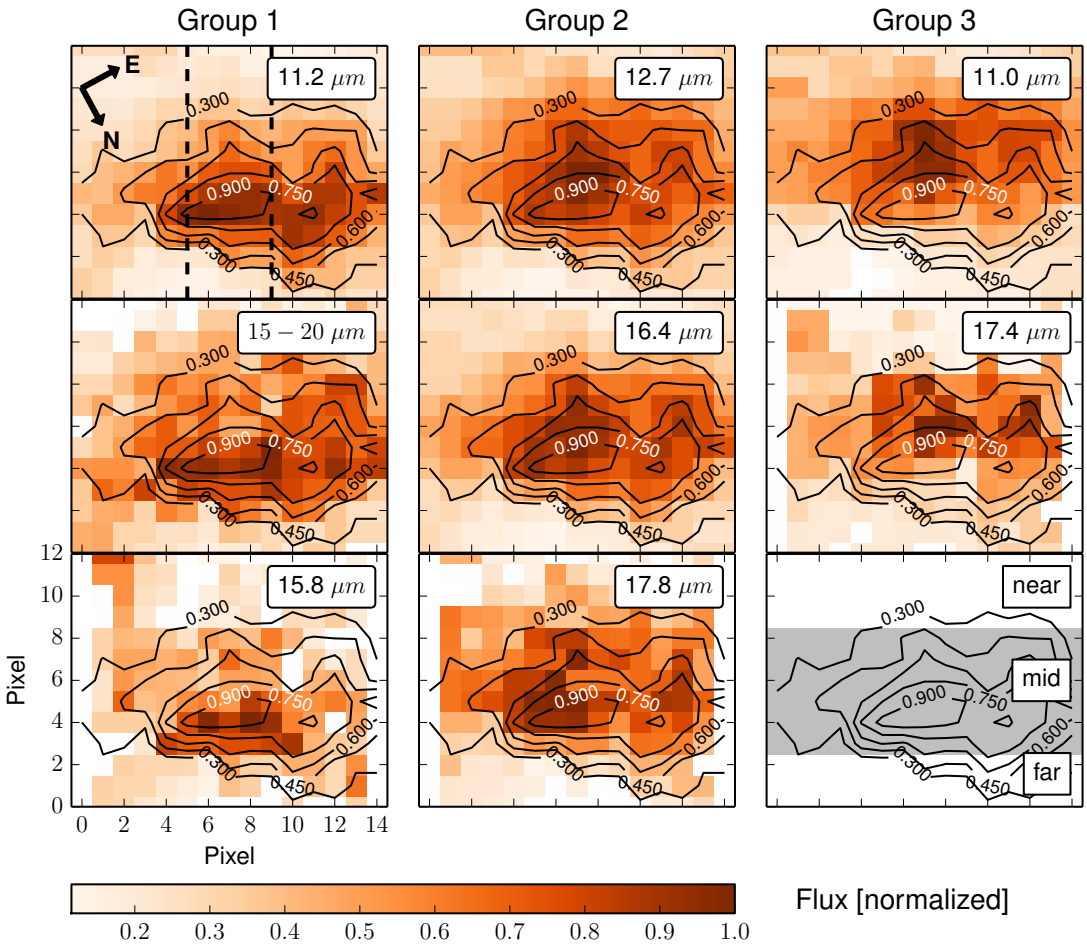

Figure 2.10: Maps of the normalized PAH band fluxes towards NGC 7023 (13 × 15 pixels). Maps have been rotated 20° such that the star is at the top of each panel in this orientation. The original field of view is as indicated in Figure 2.1. The black contours are constructed from the 11.2 µm band flux, normalized to unity. Bands are organized into vertical groupings (columns) based on similar characteristics (see text). The vertical dashed lines (shown only on the 11.2 µm map) denote the region used for the 5 pixels-wide radial cut (Figure 2.12). We introduce in the lower-right panel three simple zones to distinguish regions of NGC 7023 data present in the correlation plots.

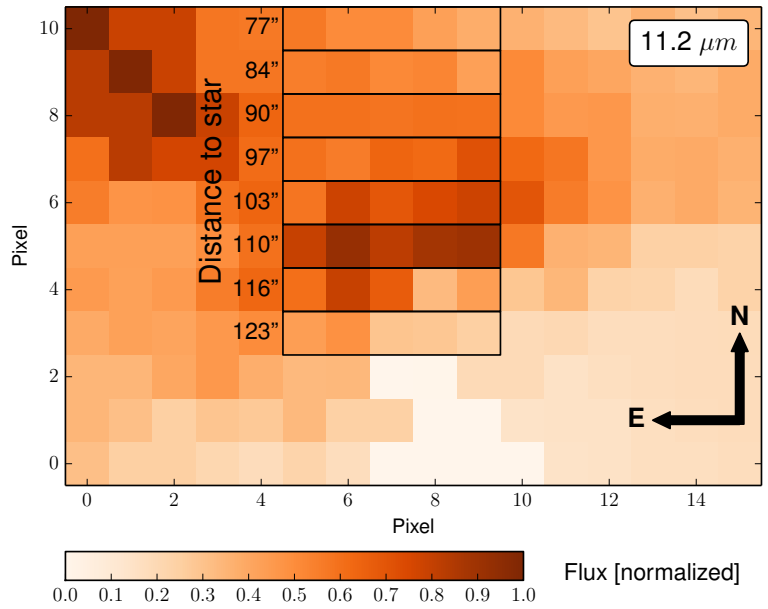

Figure 2.11: A normalized 11.2 μm PAH intensity map of NGC 2023 S (papers I and II). These data have been rotated 35 degrees counter-clockwise to be roughly perpendicular to the irradiating star's radial vector. The outlined regions identify the 5 pixels-wide apertures used to create the radial slices. The exciting star is located upward in this projection, with estimated distance to each aperture as shown.

2.4.2.2 PAH emission variability with projected distance

In order to investigate the change in PAH emission with projected distance from the illuminating star, we introduce radial slices or cuts across the maps of NGC 7023 and NGC 2023 (Figures 2.10 and 2.11) and analyze the individual band intensities as a function of the strength of the radiation field (Figures 2.12 and 2.13).

NGC 7023 is irradiated by HD 200775, a star of spectral type B2.5 Ve (Finkenzeller, 1985), of effective temperature $17000K \pm 1000K$ (Baschek et al., 1982). We find the strength of the FUV radiation field, G_o, to be 1.2×10^5 at 12″ and 1.4×10^4 at 35″ from HD 200775.[‡] This is consistent with Berné and Tielens (2012), who adopted values of $1 \pm 0.7 \times 10^5$ at 12″ and $1 \pm 0.7 \times 10^4$ at 35″.

The slices of NGC 7023 show that the 11.2 and 15.8 μm bands and the 15-18 μm plateau peak furthest from the star, at a projected distance, d, of 49″, or $G_o \sim 7.0 \times 10^3$. The 12.7, 16.4 and 17.8 μm bands peak closer to the star, at d$\sim$ 39″−44″, or $G_o \sim 11 \times 10^4 - 8.5 \times 10^3$.

[‡]G_o is the FUV flux between 6-13.6 eV, expressed in terms of the Habing field, 1.2×10^{-4} erg/s/cm^2/sr (Habing, 1968). We use the formulation of Tielens (2005): $G_o = 625 \frac{L\chi}{4\pi d^2}$, where L is the luminosity of the star, χ is the luminosity fraction between 6-13.6 eV and d is the distance from the star. χ was determined by evaluating a blackbody of effective temperature corresponding to the appropriate stellar spectral type.

The 17.4 μm band peaks at d$\sim$ 40″($G_o \sim 1.2 \times 10^4$) and the 11.0 μm band has a wide peak from d$\sim$ 30 − 39″, corresponding to $G_o \sim 1.9 \times 10^4 - 1.1 \times 10^4$. The 17.4 μm band profile is much narrower than the 11.0 μm emission, but it is aligned with the far edge of the 11.0 μm band. Slices of the 16.4 and 18.9 μm bands in NGC 7023 were presented by Sellgren, Uchida, and Werner (2007). These authors observed the 16.4 μm emission to peak at approximately 36″ distant from the star. We observe this peak to lie more distant, near 44″, but we use a different decomposition method. Overall, the spatial profiles of the 12.7, 16.4 and 17.8 μm bands are broader and more symmetric than those of the other bands. We find that we can reproduce the profiles of the 12.7 and 16.4 μm bands extremely well by adding the 11.0 and 11.2 μm profiles and renormalizing the result (see Figure 2.12).

We perform a similar analysis on NGC 2023S, whose data have higher SNR and overall intensities than NGC 2023N's (Figure 2.13). NGC 2023 is illuminated by a B1.5V star (Mookerjea et al., 2009). We derive G_o values in a similar manner as for NGC 7023. The PAH transitions occur from $G_o \sim 1.5 \times 10^3 - 3.0 \times 10^3$, in rough agreement with the estimates of $10^3 - 10^4$ in the literature, albeit on the low end (Sheffer et al. 2011, paper I). The spatial stratification seen in NGC 7023 is also present in NGC 2023S. However, the transition occurs at quite different values of G_o than NGC 7023. This suggests that our simple approximation of G_o is not accurate enough and other parameters such as density, gas temperature and/or projection effects may play a role. Specifically, the 11.0 and 17.4 μm bands peak nearest the star, with the 11.0 μm band showing a broad peak from approximately 80-95″ distant ($G_o \sim 2.9 \times 10^3 - 2.1 \times 10^3$), and the 17.4 μm band being more compact near a distance of 84″($G_o \sim 2.6 \times 10^3$). The 11.2, 15.8 μm bands and the 15-18 μm plateau all peak near d$\sim$111″($G_o \sim 1.5 \times 10^3$), but we note the plateau is slightly broader. The 12.7 and 16.4 μm bands are flat from d$\sim$80−105″ ($G_o \sim 2.9 \times 10^3 - 1.7 \times 10^3$), again broader than the other emission bands, as in NGC 7023. The 17.8 μm band is similar to the 12.7 and 16.4 μm bands but it peaks closer to the star (80-95″, $G_o \sim 2.9 \times 10^3 - 2.0 \times 10^3$), with a profile near that of the 11.0 μm band. Again, the 12.7 and 16.4 μm band profiles are well realized by summing and renormalizing the 11.0 and 11.2 μm bands, albeit with a slight overestimate near 110″.

2.5 Discussion

2.5.1 Interpretation

We first summarize the observational results, and subsequently, we discuss the implications in terms of charge and molecular structure, based on comparison with theoretical studies. The observational results consist of PAH band intensity correlations for integrated and extended

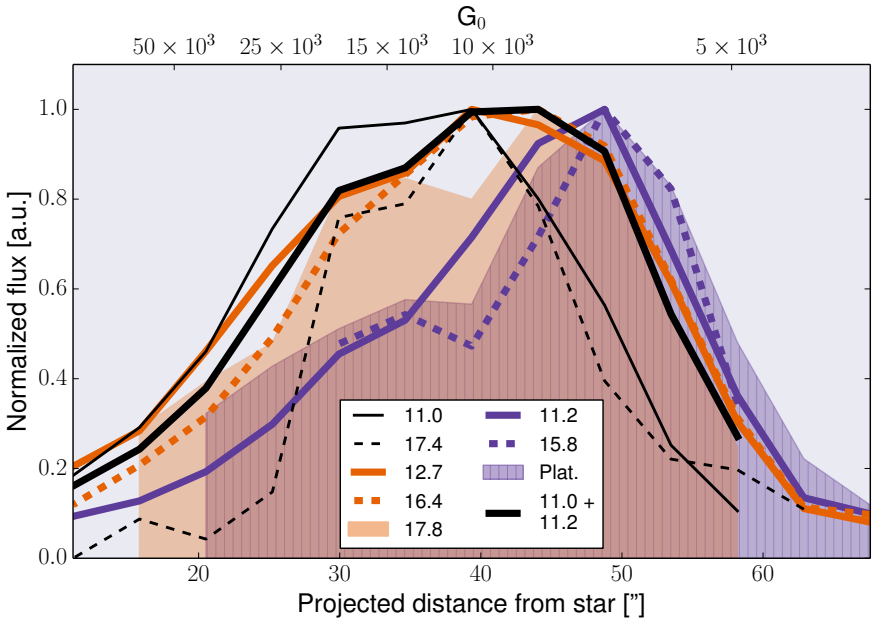

Figure 2.12: Normalized PAH intensity along a projected cut across NGC 7023 directed towards the irradiating source, extracted at 12 positions, using a 5 pixels wide extraction aperture (see Figure 2.10). The colors indicate groupings of bands with similar peak positions and/or spatial profiles along the cut.

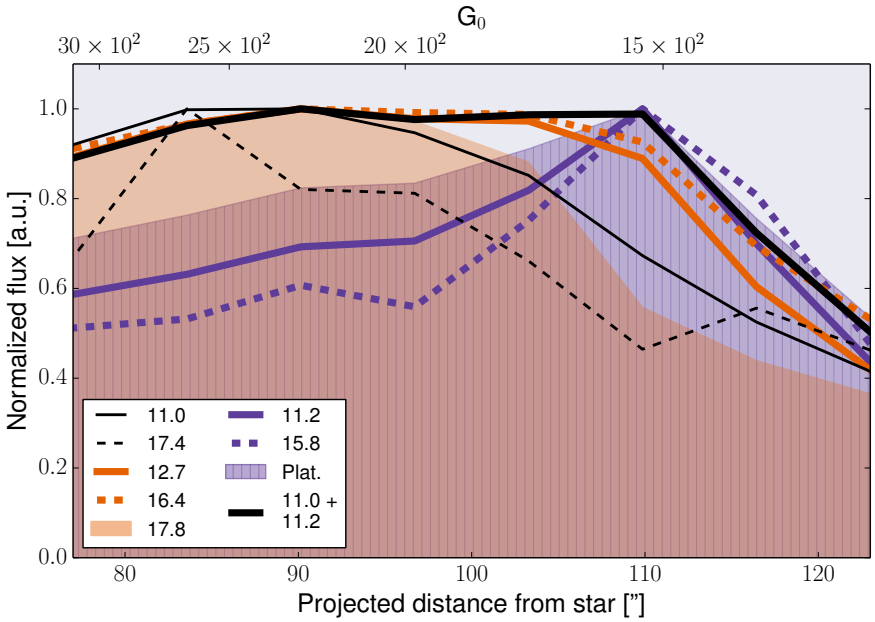

Figure 2.13: Normalized PAH intensity along a projected cut across NGC 2023S directed towards the irradiating source, extracted at 8 positions, using a 5 pixels wide extraction aperture (see Figure 2.11). The colors indicate groupings of bands with similar peak positions and/or spatial profiles along the cut.

sources, as well as spatial measurements of PAH emission in spectral maps of NGC 7023 and NGC 2023.

Correlations. The 16.4, 17.4 and 17.8 μm band fluxes are inter-correlated in all environments. Furthermore, each of these three bands correlates with the 12.7 μm band in the RNe. Amongst the sample of integrated sources, the 16.4 and 17.8 μm bands correlate with the 12.7 μm band only in H II regions. Together, these four bands (12.7, 16.4, 17.4 and 17.8 μm) correlate strongly with the 11.0 μm band in RNe. The 15.8 μm band does not correlate with any of these bands, leaving it as the odd one out. However, the 15.8 μm band is inter-correlated in RNe with the 15-18 μm plateau and the 11.2 μm band. Finally, the 16.4 and 6.2 μm bands show no overall linear correlation for the integrated sources, though if we exclude H II regions from this analysis they show a modest correlation, in line with results found in the literature (Boersma, Bregman, and Allamandola, 2014; Boersma et al., 2010). Our data are also isolated to relatively low ordinate and abscissa values, falling upon the lower end of the relationship found by Boersma, Bregman, and Allamandola (2014).

Spatial maps. The RNe spatial maps show a common morphology between the 12.7, 16.4 and 17.8 μm bands. Similarity is also observed between the 11.2 and 15.8 μm bands and the 15-18 μm plateau. Lastly, the 11.0 and 17.4 μm bands appear to peak in similar locations. We invoked radial cuts to isolate the spatial origin of each band to examine these similarities. The 11.0 and 17.4 μm bands peak closest to the star, in similar locations, though the 11.0 μm band's spatial profile is wider. The 11.2, 15.8 μm bands and 15-18 μm plateau peak furthest from the star, sharing very similar profiles. The 12.7 and 16.4 band profiles peak in an intermediate location, with very similar shapes. The 17.8 μm band follows the 12.7 and 16.4 μm bands in NGC 7023 but its profile is more similar to that of the 11.0 μm band in NGC 2023S. We observe that the profiles of the 12.7 and 16.4 μm bands bands (and the 17.8 μm band in NGC 7023) can be reproduced by averaging the spatial profiles of the 11.0 and 11.2 μm bands.

2.5.1.1 Charge

We first examine the observational results in the context of ionization states. The 11.0 and 11.2 μm PAH bands have been firmly assigned to cationic and neutral PAHs, respectively (Hony et al., 2001; Hudgins and Allamandola, 1999). The similarities of the 15.8 μm band to the 11.2 μm band in the maps, cuts, and the fact that they correlate suggest that the 15.8 μm band originates in neutral PAHs. Likewise, the observational data suggests the 17.4 μm band is coincident with the 11.0 μm emission, with which it correlates; we therefore associate the 17.4 μm band with cationic PAHs. The 12.7, 16.4 and 17.8 μm bands are self-similar in the maps and cuts, and have an extent that envelops both the 11.0 and 11.2 μm bands. In conjunction

with the correlation plots, these data suggest that the 12.7, 16.4 and 17.8 μm bands arise from both cationic and neutral PAHs.

Paper I suggested that the 17.8 μm band arises from both neutral and ionized PAHs, which we here confirm. Furthermore, paper I concluded that the 16.4 μm band is from species cospatial with the cationic portion of the emitting PAH population. This result was strongly supported by the results of Boersma, Bregman, and Allamandola (2014); the authors however noted that residual curvature in their correlations plots indicated that other population changes are at play. Here we identify two components of the 16.4 μm band: one cospatial with cationic PAHs and one cospatial with neutral PAHs. The 12.7 μm band was also shown to be coincident with PAH cations in paper I. Rosenberg et al. (2011) used blind signal separation to identify two components of the 12.7 μm band, which they associate with neutrals and cations. Boersma, Bregman, and Allamandola (2014) supported their assignment; this work also supports a combined neutral and cationic origin for the 12.7 μm band. Paper I suggested the 17.4 μm bands arises from doubly ionized PAHs and/or a subset of the cationic PAH population. We attribute the 17.4 μm bands to cations generally, and not necessarily a particular subset. The discrepancy may be due to how each paper traces cations: we use the 11.0 μm band as a tracer of cations here, whereas paper I used the 6.2 and 7.7 μm bands as tracers. Paper II finds that there are two populations contributing to the 7.7 μm band (and thus the 6.2 μm band, due to its similar morphology), and so the 7.7 μm band may not be an ideal tracer of PAH cations. Additionally, Boersma, Bregman, and Allamandola (2015) show that the 7.7 μm PAH band strength may not be a reliable tracer for PAH cations. We attribute the 15.8 μm band to neutral PAHs, in agreement with paper I.

Theoretical studies of PAH vibrational modes have given us clues about the origins of the 15-20 μm emission bands (Boersma et al., 2010; Ricca et al., 2010). These often make use of the NASA Ames PAH IR Spectroscopic Database[§] (Bauschlicher et al., 2010; Boersma et al., 2014). Specifically, the 16.4 μm band appears to arise from a mixture of out-of-plane and in-plane vibrations, particularly due to elongation and compression modes (Ricca et al., 2010). The 17.4 μm band originates in a mixture of C-C-C in-plane and out-of-plane modes and the 17.8 μm band is attributed to a mixture of C-H and C-C-C out-of-plane bending. The origin of the 15.8 μm band is unclear, though emission at 15.4 μm by C-C-C in-plane bending modes was identified by Ricca et al. (2010); this may or may not correspond to the astronomical 15.8 μm band. Using these analyses, we assert that the intrinsic intensities of the 15.8, 16.4, 17.4 or 17.8 μm bands do not vary by more than approximately a factor of 2 between

[§] http://www.astrochem.org/pahdb/

charge states (anions, neutrals, cations). This estimate is based on Figure 13 of Ricca et al. (2010), which presents average spectra for all PAHs in the Ames database containing more than 50 carbon atoms, separated by ionization state, and Figure 15 of Boersma et al. (2010), showing the intrinsic intensities for different charge states of $C_{96}H_{24}$. In general then, the 15-20 μm emission bands produce intensity variations that are much more subdued than the variations observed in the 3-12 μm range, which span approximately one order of magnitude (Allamandola, Hudgins, and Sandford, 1999). Emission by anions, neutrals and cations is expected for all four 15-20 μm bands in the database (Ricca et al., 2010). The 16.4 μm band is expected to be twice as strong for cations than for the other charge states (Bauschlicher et al., 2010; Ricca et al., 2010). The 17.8 μm band appears to have similar intensities in each charge state, while the 17.4 μm band should be strongest in anions by a factor of two (Ricca et al., 2010). These authors computed spectra for eight neutral PAHs and noted similar intensities between the 17.4 and 17.8 μm band, possibly implying a correlation; such a correlation is observed in this work. Lastly, emission was observed at 15.4 μm by (Ricca et al., 2010), with cations exceeding the intensities of neutrals and anions by a factor of two, but it is unknown if this emission corresponds to the astronomical band at 15.8 μm.

Setting aside anions due to their expected very low abundances, we note that the prediction of similar emission intensities of the 17.8 μm band between cations and neutral PAHs is consistent with our observational results. This can be seen in the spatial maps and cuts, in which the 17.8 μm band's spatial profile encompasses the 11.0 and 11.2 μm bands, centered between them. The 16.4 μm band, which is predicted to be twice as strong in cations than neutrals, is however somewhat at odds with the observational data: we observe it has the same spatial profile as the 17.8 μm band, with no preference or tendency towards the 11.0 μm emission over the 11.2 μm emission. This suggests it should arise from a similarly balanced mixture of cations and neutrals from which the 17.8 μm band originates. The 17.4 μm band is predicted by the database to have similar emission intensities between cations and neutral PAHs, which is inconsistent with our assignment solely to cations. Lastly, the database 15.4 μm band is seen to be cation-dominant, at odds with the neutral character of the 15.8 μm astronomical band from the observational data. It may simply be the case that these two bands do not correspond to the same emission feature. Other possibilities for the observed inconsistencies may include variable PAH population abundances, incompleteness and/or poor representation of these particular (sub-)populations in the database, or simply that our data are not sufficiently sensitive to probe variations at the scale of two-to-one. An examination of the radial cuts shows the latter point to be true.

2.5.1.2 Molecular structure

Molecular structure determines which vibrational modes are available to any particular PAH, but it is not known a priori how much of an influence structure will play in driving band intensity correlations on the whole. Some headway has been made in this area, in so far as particular band attributions have been suggested. The 16.4 μm band has been attributed to PAHs containing pendent rings or "pointed" edges (e.g., Boersma et al. 2010; Peeters et al. 2004; Ricca et al. 2010; Van Kerckhoven et al. 2000). The former are single cycles that attach to the carbon skeleton through two shared carbon atoms, while the latter are corners that naturally arise in parallelogram-shaped PAHs, attached through three shared carbon atoms. The 16.4 μm band correlates well with the 17.8 μm band, which appears to be somewhat structure insensitive: the 17.8 μm band was present in all eight large neutral PAHs studied by Ricca et al. (2010), despite encompassing a variety of structures, including some with pointed edges. The 12.7 μm band, which correlates well with both the 16.4 and 17.8 μm emission, is associated with a combination of duo and trio C-H out-of-plane modes (Bauschlicher, Peeters, and Allamandola, 2009; Bauschlicher et al., 2010; Hony et al., 2001). Recently, this band was suggested to specifically originate in PAHs having an armchair-like structure (Candian, Sarre, and Tielens, 2014). As pendent rings and pointed edges naturally constitute duos and trios, it is then possible that the 12.7 and 16.4 μm bands naturally correlate due to these common features. The 17.8 μm band is not known to have a dependence on duos or trios, but it has been suggested that it is a molecule-independent feature (Ricca et al., 2010), which may explain why it correlates with the 12.7 and 16.4 μm bands.

The 17.4 μm band, which correlates with the 12.7, 16.4 and 17.8 μm bands, generally appears to show the strongest emission intensities in compact PAHs (Bauschlicher et al., 2010; Ricca et al., 2010). The 15.6 μm band (which may or may not correspond to the astronomical 15.8 μm band) has been suggested to arise from vibrations of pendent rings (Boersma et al., 2010). Pendent rings are also suggested as one possible origin for the 16.4 μm band. If both the 15.8 and 16.4 μm bands are (at least in part) due to pendent rings, one would expect an intensity correlation, depending on environmental conditions (which we cannot speculate on here). In general the observational data show no such correlation between these bands, though there is a slight hint of a linear correlation when the ratio of 16.4/11.2 exceeds 0.12 (see Figure 2.8). The correlation of the 15.8 μm band with the 11.2 μm band is suggestive of large molecules, but it is known that the emission intensity of the 15.8 μm band decreases with increasing PAH size in the NASA Ames PAH IR Spectroscopic Database (Bauschlicher et al., 2010; Boersma et al., 2014; Ricca et al., 2010). Finally, Boersma et al. (2010) examined classes of PAHs, including compact, irregular, and pentagon-containing PAHs. Minor sys-

tematic trends were observed, including the fact that irregular PAHs tend to have richer and more variable spectral features when compared to compact PAHs. As molecule size increased, compact PAHs exhibited little variation in the types of C-C-C vibrational modes that were active, whereas the complex edge structure of irregular PAHs facilitated a larger variety of C-C-C vibrational modes (Boersma et al., 2010). Even with this knowledge, at the present there is no clear mapping between molecular structure and the observational data.

2.5.1.3 Summary

The exact balance between charge and molecular structure in driving the observed correlations of the 15-20 μm bands cannot be discerned. However, the maps and radial cuts appear to cleanly separate these bands into those dominated by cations (11.0, 17.4 μm), neutrals (11.2, 15.8 μm, 15-18 μm plateau), or a combination of the two (e.g., 12.7, 16.4, 17.8 μm bands). This suggests charge is the dominant factor driving these correlations, though there are indications that some bands should correlate due to structural arguments (e.g., the 12.7 and 16.4 μm bands). Ultimately, theory points towards a mixture of highly variable emission features (e.g., Boersma et al. 2010, their Figures 11-15), whereas in space we observe a relatively simple picture of four bands and one underlying plateau. This simplicity may reflect a basic commonality of the carriers, or suggest that a relatively small collection of stable molecules are responsible for the observed emission bands (Boersma et al., 2010). The latter is known as the *grandPAH* hypothesis (Andrews et al., 2015).

2.5.2 Statistics of the 15-20 μm emission

First we determine if the relative emission strengths of the 5-15 μm bands in our sample are consistent with similar measurements in the literature (Peeters et al., 2002). We accomplish this by measuring the fractional contribution of the 6.2, 7.7, 8.6 and 11.2 μm bands to the total MIR emission (which we define here as the total flux emitted by these bands) for nine H II regions and fifteen galaxies in our sample. Since Peeters et al. (2002) only had two galaxies in their sample, we use the H II regions as a direct point of comparison. Our results are presented in Figure 2.14, panel (a). We find that the H II regions are consistent with those of Peeters et al. (2002), whose data is presented in panel (b), and there is no discrepancy between H II regions and galaxies in our sample. Note that Peeters et al. (2002) included the 3.3 μm band and not the 8.6 μm band in their analysis, whereas we do the opposite (as our spectra start at 5 μm). The 3.3 and 8.6 μm bands are quite weak (less than 10% of the total MIR emission in both studies) and should therefore not strongly influence the analysis.

The same analysis is performed for the "FIR" features, i.e., the 15.8, 16.4, 17.4, 17.8 μm bands

and the 15-18 μm plateau, shown in Figure 2.14, panel (c). Due to the inconsistent detections of the 15.8, 17.4 and 17.8 μm bands, the 16.4 μm band and the 15-18 μm plateau are used together as a proxy for the total FIR PAH flux. The 15.8, 16.4 and 17.8 μm bands have fractional strengths in H II regions of $7 \pm 4\%$, $16 \pm 2\%$ and $6 \pm 1\%$, respectively. In galaxies, these are systematically lower, with values $4 \pm 1\%$, $11 \pm 3\%$ and $3 \pm 1\%$, respectively. The 17.4 μm band is observed to have similar strengths between H II regions and galaxies ($3 \pm 1\%$ in each). The plateau makes up the remainder of the measured fractional strengths. The observed inconsistency by object type may be due to underestimating the 17.4 μm PAH emission in H II regions or overestimating the 17.4 μm emission in galaxies. Neither would be surprising, as C_{60} emission at 17.4 μm is common, and it can only be removed by measuring the 18.9 μm C_{60} emission, which itself is blended with the [S III] 18.71 μm line. Recall the typical 17.4/18.9 μm C_{60} band strength ratio is approximately 0.5 (Bernard-Salas et al., 2012; Cami et al., 2010; Sellgren et al., 2010). Another possibility is that the 15.8, 16.4 and 17.8 μm bands are all overestimated in H II regions, which requires a trio of systematic errors that we deem unlikely, as the same method was applied to both H II regions and galaxies. The third possibility is that these bands truly are systematically higher in H II regions than galaxies.

As a separate analysis, we investigate whether the MIR/FIR ratio depends on object type, where the 11.2 and 16.4 μm bands are used as proxies for the MIR and FIR emission, respectively. We therefore examined 490 low-resolution spectra of the SAGE-Spec sample and used the following selection criteria: 1. PAHs must be clearly present; 2. the spectra displayed no discontinuous jumps; 3. sources were less extended than 9″(which corresponds to the approximate size of the SL aperture at 6.2 μm); and 4. the 11.2 and 16.4 μm PAH bands must have 3σ detections. We identify 10 H II regions and 22 evolved stars as meeting these criteria. The H II regions have a mean 16.4/11.2 ratio of 0.09 ± 0.02. Evolved stars exhibited a ratio of 0.12 ± 0.05, consistent with the H II regions. As such, we find no dependence on object type for the relative MIR and FIR band intensities in this analysis.

2.6 Summary & Conclusions

The 15-20 μm PAH emission bands have been investigated in fifty-seven sources, comprised of LMC point sources from the SAGE-Spectroscopy survey, nearby galaxies from SINGS, two extended cirrus sources and a spectral map of NGC 7023. We also included the sample of Boersma et al. (2010) and spectral maps of NGC 2023 (papers I and II). We investigated correlation plots of band flux ratios and examined the map morphologies of the RNe NGC 7023 and NGC 2023. We performed radial cuts across these maps to evaluate the spatial profiles of the 15-20 μm PAH emission. Our primary conclusions are as follows:

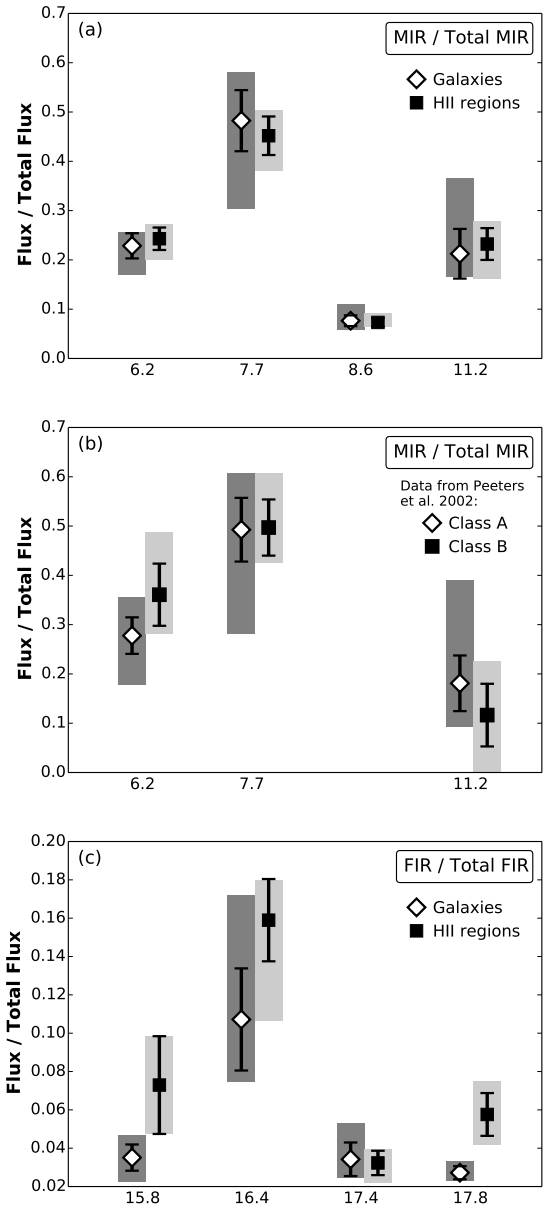

Figure 2.14: Statistical summary of the 5-15 µm and 15-20 µm PAH bands. The fraction of total flux in each band is illustrated by its mean (white diamond for galaxies, black square for H ii regions), standard deviation (black line), and minimum and maximum values (denoted by the grey rectangles). (a) The 6.2, 7.7, 8.6 and 11.2 µm emission (called "MIR" here) are normalized to their combined total emission. (b) The same analysis, for class A and B sources, as presented in Peeters et al. (2002). Note the authors included 3.3 µm emission, but did not have 8.6 µm emission. (c) The fractional emission in the "FIR" bands (15.8, 16.4, 17.4, 17.8 µm bands) are compared. The total FIR emission is considered to be the sum of the 16.4 µm and plateau emission. The plateau fraction ($\gtrsim 0.7$) is omitted for clarity.

1. Correlation plots:

    - The 16.4, 17.4 and the 17.8 μm bands are inter-correlated in all environments.
    - Within the RNe we see that the 16.4, 17.4 and 17.8 μm bands further correlate with the 11.0 and 12.7 μm bands. In H II regions, the 12.7 μm band also correlates with the 16.4 and 17.8 μm bands.
    - The 11.2 and 15.8 μm bands and the 15-18 μm plateau are inter-correlated in NGC 7023, consistent with results for NGC 2023 (paper I). The 15.8 μm band does not correlate with the 11.0, 12.7, 16.4, 17.4 or 17.8 μm bands in general. Within a sub-region of NGC 7023 the 15.8 μm band appears to show a modest correlation with the 16.4 and 17.8 μm bands.

2. Spectral maps:

    - The maps show similar morphologies between the 11.0 and 17.4 μm bands, the 12.7, 16.4 and 17.8 μm bands, and the 11.2, 15.8 μm bands with the 15-18 μm plateau.
    - The radial slices in the RNe maps show that the spatial profiles of the 12.7, 16.4 and 17.8 μm bands can be reconstructed by averaging the 11.0 and the 11.2 μm band profiles.

3. Charge dominates: we attribute the 12.7, 16.4 and 17.8 μm bands to a combination of neutral and cationic molecules. The 17.4 μm band we attribute to cations, based on similarity of its spatial distribution to the 11.0 μm emission in the maps and radial cuts. Our results support the association of the 15.8 μm band with PAHs, specifically neutral PAHs (paper I).

4. The 16.4/11.2 ratio in the general SAGE-Spec sample shows no dependence on object type. The fractional emission of the 15.8, 16.4 and 17.8 μm bands in H II regions are systematically higher than those in galaxies. The 17.4 μm band is the exception, which has similar fractional strengths in both environments.

With the significant number of sources in our sample, we were able to discover correlations between the 15-20 μm features that were not discernible in the much smaller sample studied by Boersma et al. (2010). The forthcoming JWST instrument MIRI will be an essential tool in furthering this analysis. Its large collecting area and increased spatial sensitivity will permit the construction of larger sample sizes, permitting further statistical analysis. Additionally,

its improved spectral sensitivity will also allow us to examine the PAH band profiles in detail, with less line-blending than is possible with current data sets. These key improvements, in conjunction with theoretical and laboratory analysis, may help disentangle the inter-related behaviours of the 15-20 μm bands.

Acknowledgements

We thank the anonymous referee for useful feedback. The authors thank J.D. Smith for supplying the SINGS data, as well as C. Boersma for supplying the data of their study. The authors also thank P.M. Woods for providing object classifications. The authors acknowledge support from NSERC discovery grant, NSERC acceleration grant and ERA. The IRS was a collaborative venture between Cornell University and Ball Aerospace Corporation funded by NASA through the Jet Propulsion Laboratory and Ames Research Center (Houck et al., 2004). This research has made use of NASA's Astrophysics Data System Bibliographic Services, and the SIMBAD database, operated at CDS, Strasbourg, France.

References

Allamandola, L. J., Hudgins, D. M., and Sandford, S. A. (1999). *Astrophysical Journal, Letters* 511, pp. L115–L119. DOI: 10.1086/311843.

Allamandola, L. J., Tielens, A. G. G. M., and Barker, J. R. (1989). *Astrophysical Journal, Supplement* 71, pp. 733–775. DOI: 10.1086/191396.

Andrews, H., Boersma, C., Werner, M. W., et al. (2015). *Astrophysical Journal* 807, 99, p. 99. DOI: 10.1088/0004-637X/807/1/99.

Baschek, B., Beltrametti, M., Koppen, J., et al. (1982). *Astronomy and Astrophysics* 105, p. 300.

Bauschlicher Jr., C. W., Peeters, E., and Allamandola, L. J. (2009). *Astrophysical Journal* 697, 311, pp. 311–327. DOI: 10.1088/0004-637X/697/1/311. arXiv: 0903.0412 [astro-ph.GA].

Bauschlicher Jr., C. W., Boersma, C., Ricca, A., et al. (2010). *Astrophysical Journal, Supplement* 189, 341, pp. 341–351. DOI: 10.1088/0067-0049/189/2/341.

Beasley, A. J., Ellingsen, S. P., Claussen, M. J., et al. (1996). *Astrophysical Journal* 459, p. 600. DOI: 10.1086/176924.

Bernard-Salas, J., Cami, J., Peeters, E., et al. (2012). *Astrophysical Journal* 757, 41, p. 41. DOI: 10.1088/0004-637X/757/1/41. arXiv: 1207.5794 [astro-ph.GA].

Bernard-Salas, J., Peeters, E., Sloan, G. C., et al. (2009). *Astrophysical Journal* 699, pp. 1541–1552. DOI: 10.1088/0004-637X/699/2/1541. arXiv: 0905.1124 [astro-ph.SR].

Berné, O. and Tielens, A. G. G. M. (2012). *Proceedings of the National Academy of Science* 109, pp. 401–406. DOI: 10.1073/pnas.1114207108. arXiv: 1111.0839 [astro-ph.GA].

Boersma, C., Bregman, J., and Allamandola, L. J. (2014). *Astrophysical Journal* 795, 110, p. 110. DOI: 10.1088/0004-637X/795/2/110.

– (2015). *Astrophysical Journal* 806, 121, p. 121. DOI: 10.1088/0004-637X/806/1/121.

Boersma, C., Bregman, J. D., and Allamandola, L. J. (2013). *Astrophysical Journal* 769, 117, p. 117. DOI: 10.1088/0004-637X/769/2/117.

Boersma, C., Bauschlicher Jr., C. W., Ricca, A., et al. (2011). *Astrophysical Journal* 729, 64, p. 64. DOI: 10.1088/0004-637X/729/1/64.

Boersma, C., Bauschlicher, C. W., Allamandola, L. J., et al. (2010). *Astronomy and Astrophysics* 511, A32, A32. DOI: 10.1051/0004-6361/200912714.

Boersma, C., Bauschlicher Jr., C. W., Ricca, A., et al. (2014). *Astrophysical Journal, Supplement* 211, 8, p. 8. DOI: 10.1088/0067-0049/211/1/8.

Boulanger, F., Abergel, A., Bernard, J. P., et al. (1998). In: *Star Formation with the Infrared Space Observatory*. Ed. by J. Yun and L. Liseau. Vol. 132. Astronomical Society of the Pacific Conference Series, p. 15.

Cami, J., Bernard-Salas, J., Peeters, E., et al. (2010). *Science* 329, pp. 1180–. DOI: 10.1126/science.1192035.

Candian, A., Sarre, P. J., and Tielens, A. G. G. M. (2014). *Astrophysical Journal, Letters* 791, L10, p. L10. DOI: 10.1088/2041-8205/791/1/L10. arXiv: 1407.2010.

Devlin, Susan J., Gnanadesikan, R., and Kettenring, J. R. (1975). *Biometrika* 62.3, pp. 531–545. DOI: 10.1093/biomet/62.3.531.

Finkenzeller, U. (1985). *Astronomy and Astrophysics* 151, pp. 340–348.

Galliano, F., Madden, S. C., Tielens, A. G. G. M., et al. (2008). *Astrophysical Journal* 679, pp. 310–345. DOI: 10.1086/587051. arXiv: 0801.4955.

Habing, H. J. (1968). *Bulletin Astronomical Institute of the Netherlands* 19, p. 421.

Hony, S., Van Kerckhoven, C., Peeters, E., et al. (2001). *Astronomy and Astrophysics* 370, pp. 1030–1043. DOI: 10.1051/0004-6361:20010242. eprint: arXiv:astro-ph/0103035.

Houck, J. R., Roellig, T. L., van Cleve, J., et al. (2004). *Astrophysical Journal, Supplement* 154, pp. 18–24. DOI: 10.1086/423134. eprint: arXiv:astro-ph/0406167.

Hudgins, D. M. and Allamandola, L. J. (1999). *Astrophysical Journal, Letters* 516, pp. L41–L44. DOI: 10.1086/311989.

Kemper, F., Woods, P. M., Antoniou, V., et al. (2010). *Publications of the ASP* 122, pp. 683–700. DOI: 10.1086/653438. arXiv: 1004.1142 [astro-ph.GA].

Kennicutt Jr., R. C., Armus, L., Bendo, G., et al. (2003). *Publications of the ASP* 115, pp. 928–952. DOI: 10.1086/376941. eprint: astro-ph/0305437.

Mookerjea, B., Sandell, G., Jarrett, T. H., et al. (2009). *Astronomy and Astrophysics* 507, pp. 1485–1502. DOI: 10.1051/0004-6361/200912550. arXiv: 0909.2614 [astro-ph.GA].

Moutou, C., Verstraete, L., Léger, A., et al. (2000). *Astronomy and Astrophysics* 354, pp. L17–L20. eprint: arXiv:astro-ph/9912559.

Peeters, E., Mattioda, A. L., Hudgins, D. M., et al. (2004). *Astrophysical Journal, Letters* 617, pp. L65–L68. DOI: 10.1086/427186.

Peeters, E., Tielens, A. G. G. M., Allamandola, L. J., et al. (2012). *Astrophysical Journal* 747, 44, p. 44. DOI: 10.1088/0004-637X/747/1/44. arXiv: 1112.3386 [astro-ph.GA].

Peeters, E., Hony, S., Van Kerckhoven, C., et al. (2002). *Astronomy and Astrophysics* 390, pp. 1089–1113. DOI: 10.1051/0004-6361:20020773. eprint: arXiv:astro-ph/0205400.

Peeters, E., Bauschlicher Jr., C. W., Allamandola, L. J., et al. (2016). *Astrophysical Journal*. Submitted.

Ricca, A., Bauschlicher Jr., C. W., Mattioda, A. L., et al. (2010). *Astrophysical Journal* 709, 42, pp. 42–52. DOI: 10.1088/0004-637X/709/1/42.

Rosenberg, M. J. F., Berné, O., Boersma, C., et al. (2011). *Astronomy and Astrophysics* 532, A128, A128. DOI: 10.1051/0004-6361/201016340. arXiv: 1106.5899 [astro-ph.GA].

Sellgren, K., Uchida, K. I., and Werner, M. W. (2007). *Astrophysical Journal* 659, pp. 1338–1351. DOI: 10.1086/511805. eprint: astro-ph/0612544.

Sellgren, K., Werner, M. W., Ingalls, J. G., et al. (2010). *Astrophysical Journal, Letters* 722, pp. L54–L57. DOI: 10.1088/2041-8205/722/1/L54. arXiv: 1009.0539 [astro-ph.GA].

Sheffer, Y., Wolfire, M. G., Hollenbach, D. J., et al. (2011). *Astrophysical Journal* 741, 45, p. 45. DOI: 10.1088/0004-637X/741/1/45. arXiv: 1110.4614 [astro-ph.GA].

Smith, J. D. T., Armus, L., Dale, D. A., et al. (2007a). *Publications of the ASP* 119, pp. 1133–1144. DOI: 10.1086/522634. arXiv: 0708.3745.

Smith, J. D. T., Draine, B. T., Dale, D. A., et al. (2007b). *Astrophysical Journal* 656, pp. 770–791. DOI: 10.1086/510549. eprint: arXiv:astro-ph/0610913.

Stock, D. J., Peeters, E., Tielens, A. G. G. M., et al. (2013). *Astrophysical Journal* 771, 72, p. 72. DOI: 10.1088/0004-637X/771/1/72. arXiv: 1305.5258 [astro-ph.GA].

Stock, D. J., Peeters, E., Choi, W. D.-Y., et al. (2014). *Astrophysical Journal* 791, 99, p. 99. DOI: 10.1088/0004-637X/791/2/99. arXiv: 1407.0702.

Tielens, A. G. G. M. (2008). *Annual Review of Astron and Astrophys* 46, pp. 289–337. DOI: 10.1146/annurev.astro.46.060407.145211.

– (2013). *Reviews of Modern Physics* 85, pp. 1021–1081. DOI: 10.1103/RevModPhys.85.1021.

Tielens, A. G. G. M. (2005).

Treffers, R. and Cohen, M. (1974). *Astrophysical Journal* 188, pp. 545–552. DOI: 10.1086/152746.

Van Kerckhoven, C. (2002). PhD thesis. Institute of Astronomy, Katholieke Universiteit Leuven, Belgium.

Van Kerckhoven, C., Hony, S., Peeters, E., et al. (2000). *Astronomy and Astrophysics* 357, pp. 1013–1019.

Werner, M. W., Roellig, T. L., Low, F. J., et al. (2004). *Astrophysical Journal, Supplement* 154, pp. 1–9. DOI: 10.1086/422992. eprint: arXiv:astro-ph/0406223.

You must pardon me, by the way, for speaking to you in this vague way.

Isaac Asimov, Foundation

3

Interpreting the subtle spectral variations of the 11 and 12.7 μm polycyclic aromatic hydrocarbon bands

M. J. Shannon, D. J. Stock, E. Peeters (2016). *Astrophysical Journal*, 824, 111.

3.1 Introduction

Prominent infrared (IR) emission bands between 3 and 20 μm are observed in many astronomical environments. These spectral features are attributed to the vibrational fluorescence of polycyclic aromatic hydrocarbons (PAHs), which are electronically excited by ultraviolet (UV) photons. PAH molecules are composed of a hexagonal honeycomb carbon lattice, typically containing 50-100 carbon atoms, with a dusting of hydrogen atoms about the periphery. Compact structures are generally the most stable, but a variety of PAH shapes and sizes are expected to exist in space (Allamandola, Tielens, and Barker, 1989; Jochims et al., 1994; van der Zwet and Allamandola, 1985).

The strongest PAH emission bands are observed at 3.3, 6.2, 7.7, 8.6, 11.2, and 12.7 μm. A variety of weaker bands are also seen in the observational spectra (at, e.g., 11.0, 12.0 and 13.5, 14.2, 16.4 μm). The PAH bands can be associated with the following vibrations: C-H stretching (3.3 μm); C-C stretching (6.2 μm); C-C stretching and C-H in-plane bending (7.7, 8.6 μm); and C-H out-of-plane bending (hereafter CH_{oop}—PAH bands in the 10-15 μm region). It is

the number of adjacent C-H groups that determines the wavelength of the emission in the 10-15 μm region, i.e. solo, duo, trio and quartet C-H groups.

The relative emission intensities in these bands are known to be highly variable between sources and within individual resolved objects (e.g. Galliano et al. 2008; Hony et al. 2001; Shannon, Stock, and Peeters 2015; Stock et al. 2014). The charge state of the PAH population has been identified in laboratory studies as the most important parameter in driving variations in the relative emission intensities, sometimes reaching one order of magnitude between charge states (Allamandola, Hudgins, and Sandford, 1999; Galliano et al., 2008). Likewise, the profiles are known to vary in shape and peak position, which have been linked to object type (e.g. Peeters et al. 2002; van Diedenhoven et al. 2004). The variability of the PAH profiles is thought to represent differences in PAH sub-populations, possibly in, e.g., size or structure (e.g. Candian et al. 2012; Hudgins, Bauschlicher, and Allamandola 2005; Sloan et al. 2014, 2007; see Peeters 2011 for a detailed overview).

Decomposing the PAH emission bands with a mixture of functions (e.g. Gaussians, Lorentzians, Drude profiles) is one way to investigate the origins of the observed spectral variability (Boersma, Rubin, and Allamandola, 2012; Galliano et al., 2008; Peeters et al., 2002; Smith et al., 2007b). A recent result by Peeters et al. (2016) showed that the 7.7 and 8.6 μm emission bands can be decomposed into four Gaussian components, revealing that at least two PAH sub-populations contributed to this emission. Motivated by this result, we apply here a similar approach to the 11 μm emission complex (i.e., both the 11.0 and 11.2 μm bands) and the 12.7 μm emission complex. Since the variations of the 11 and 12.7 μm complexes are relatively minor when compared to the 7.7 and 8.6 μm emission bands, it is critical to examine high spectral resolution observations. In addition, if band substructure indeed traces PAH sub-populations, the astronomical data considered must span a sufficiently wide swath of physical conditions, such that any intrinsic differences are reflected in the observational band profiles.

We present here new decompositions of the 11 and 12.7 μm emission complexes in high-resolution *Spitzer*/IRS maps of reflection nebulae (RNe) and a star-forming region in order to understand the PAH sub-populations that produce the blended emission bands. We organize the paper as follows: the targets, observations, and continuum determination are presented in Section 4.2. The spectral variability in the spectra prior to any further analysis are examined in Section 3.3. We introduce new methods for decomposing the 11 and 12.7 μm PAH emission bands in Section 3.4. Results are presented in Section 4.4 and we discuss the implications of these results in Section 4.5. We present a brief summary in Section 4.6.

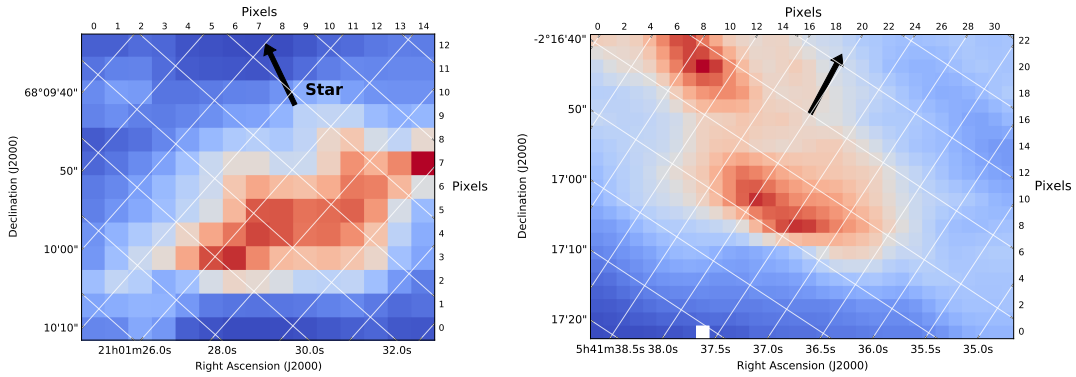

Figure 3.1: Astrometry for NGC 7023 (left) and NGC 2023 South (right). The normalized flux of the traditional 11.2 μm band is shown in each map (cf. Figs. 3.7 and 3.8). The illuminating star for NGC 7023 is HD 200775, 11″ beyond the boundary of the image along the indicated radial vector (black arrow). For NGC 2023 South, the illuminating star is HD 37903, and it is approximately 42″ from the boundary of the image.

3.2 Observations and data

3.2.1 Target selection and observations

We chose targets with *Spitzer*/IRS-SH maps that exhibit strong emission in the 11 and 12.7 μm PAH complexes. The chosen sources were the RNe NGC 7023, NGC 2023 (two pointings—North and South), and the star-forming region M17.

Spectroscopic maps were obtained using the Infrared Spectrograph (IRS; Houck et al. 2004) on-board the *Spitzer* Space Telescope (Werner et al., 2004). These data, spanning 10-20 μm at resolving power R∼600, were obtained from the NASA/IPAC *Spitzer* Heritage Archive*. The spectral maps included in this work are summarized in Table 3.1. Astrometry for NGC 7023 and NGC 2023 South is presented in Fig. 3.1, and for NGC 2023 North and M17 in Fig. 3.2.

3.2.2 Data reduction

The NGC 2023 North and South SH maps were previously presented by Peeters et al. (2012) and Shannon, Stock, and Peeters (2015). These data were processed by the *Spitzer* Science Center (pipeline version S18.7). Further processing was accomplished with the `CUBISM` tool (Smith et al., 2007a), including coaddition and bad pixel cleaning. For the purpose of spectral extraction, a 2 × 2-pixel aperture was stepped across each map. This ensured that the extraction apertures matched the point-spread function, removing non-independent pixels.

*http://sha.ipac.caltech.edu/applications/Spitzer/SHA/

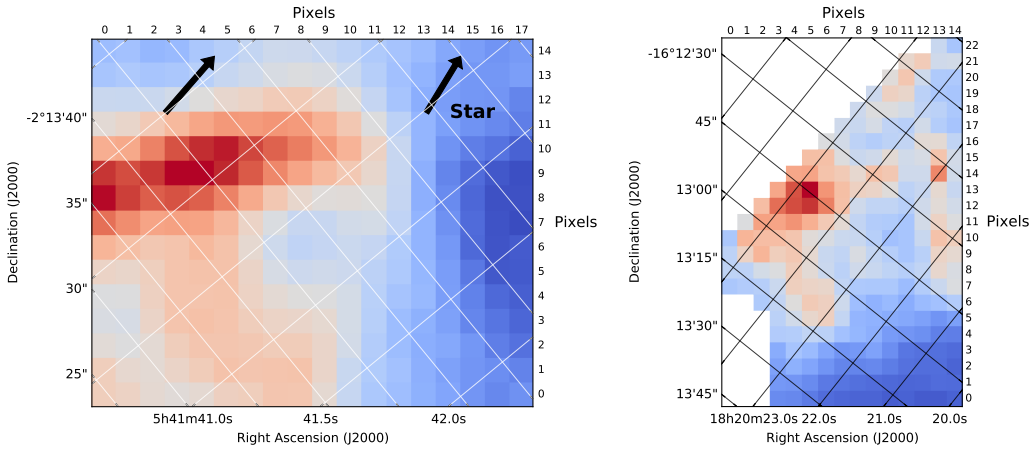

Figure 3.2: Astrometry for NGC 2023 North (left) and M17 (right). The normalized flux of the traditional 11.2 µm band is shown in each map (cf. Figs. A.1 and A.2). The illuminating star for NGC 2023 North is HD 37903, 83″ beyond the boundary of the image along the indicated radial vectors (black arrows; two are displayed to illustrate the distance). M17 is more complex, and no arrow is displayed. See Sheffer and Wolfire (2013) for details.

Table 3.1: Target properties & observation log

Object	Distance [kpc]	Exciting Star spectral type	Field of view[a] $' \times '$	Field of view[a] pc × pc	AORkey[b]	Ref.[d]
NGC 7023	0.43	B2.5	1.13 × 0.94	0.14 × 0.12	3871232	1,2
NGC 2023 South	0.35	B1.5	1.24 × 0.86	0.13 × 0.09	14033920	3
NGC 2023 North	0.35	B1.5	0.72 × 0.56	0.07 × 0.06	26337024	3
M17-SW	1.98	O4[c]	3.27 × 1.67	1.90 × 0.96	11543296	4,5,6,7

[a] Field of view of the SH maps. [b] The AORkey uniquely identifies *Spitzer* Space Telescope observations. [c] The major exciting star is thought to be CEN 1, a double O4-type star (Chini, Elsaesser, and Neckel, 1980; Hoffmeister et al., 2008). [d] References: (1) Sellgren, Uchida, and Werner (2007); (2) Rosenberg et al. (2011); (3) Peeters et al. (2012); (4) Xu et al. (2011); (5) Hoffmeister et al. (2008); (6) Chini, Elsaesser, and Neckel (1980); (7) Sheffer and Wolfire (2013).

Further details of the reduction process can be found in Peeters et al. (2012). A similar approach was applied in the reduction of the SH maps of NGC 7023 and M17. The map of NGC 7023 has been previously analyzed by Berné and Tielens (2012), Boersma, Bregman, and Allamandola (2013), Rosenberg et al. (2011), and Shannon, Stock, and Peeters (2015) and Sellgren, Uchida, and Werner (2007). *Spitzer*/IRS observations of M17-SW have been previously examined by Povich et al. (2007) and Sheffer and Wolfire (2013).

Extinction is small in NGC 2023, as are the variations in extinction, as concluded by Peeters et al. (2016) and Stock et al. (2016), with A_k values on the order of 0.1. We thus do not correct for it in this source. The extinction in NGC 7023 and M17 was investigated by Stock et al. (2016). These authors computed the extinction with the iterative Spoon method (Spoon et al., 2007; Stock et al., 2013) using *Spitzer*/IRS-SL data. Regarding NGC 7023, Stock et al. (2016) found significant extinction ($A_k \sim 2$) in the lower left corner of the map, as also reported by Boersma, Bregman, and Allamandola (2013). The small amount of extinction in the rest of the map, combined with the fact that the gradients of the extinction curve in the 11.0-11.6 and 12.3-13 μm regions are small, leads to a change in profile shapes of the 11.2 and 12.7 μm features at approximately the 4% level towards NGC 7023. In contrast, the extinction towards M17 reaches a maximum A_k value of 1.48 in our field, with typical values near unity. Therefore, we dereddened our spectra using the Chiar & Tielens (2006) extinction law. Further discussion and analysis on this topic is presented in Section 3.6.5, including its effect on the 12.7/11.2 band strength ratio.

3.2.3 Continuum estimation

A local spline continuum was chosen to isolate the PAH emission features. A series of anchor points were chosen between 10-20 μm (Fig. 3.3) to define the spline. This type of continuum determination has been performed several times in the literature and is chosen here for the purposes of comparison (e.g., Galliano et al. 2008; Hony et al. 2001; Peeters et al. 2002; Van Kerckhoven et al. 2000). The PAH band profiles and fluxes derived from the spline method are not very sensitive to the precise position of the anchor points, depending on the apparent smoothness of the underlying continuum (i.e. spectra with, e.g., undulating continua will lead to less precise PAH band flux measurements). We estimate the influence of the continuum choice on our 11.2 and 12.7 μm band fluxes to be at the 5% level.

3.3 Spectral profiles

We focus here specifically on the PAH emission bands at 11.0, 11.2 and 12.7 μm. The former two bands we will generally refer to as the "11 μm" emission complex, and the latter as the

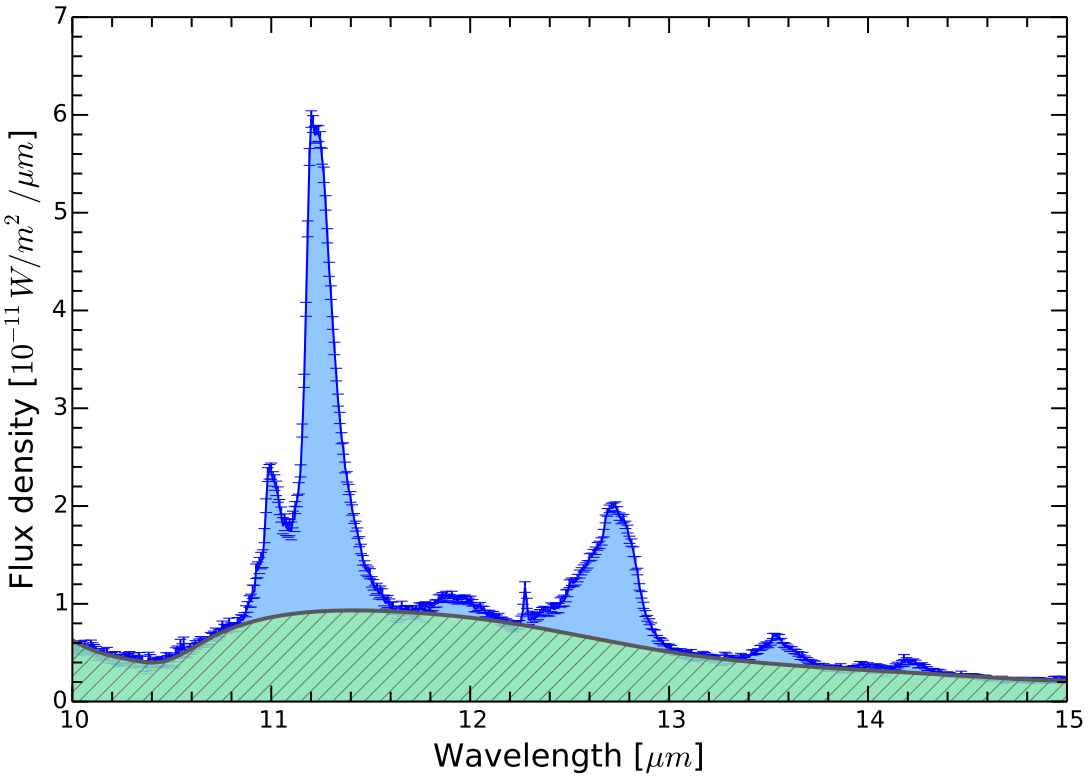

Figure 3.3: Sample spectrum from NGC 7023. A spline continuum is defined by the green hatched area. The prominent 11 and 12.7 µm emission complexes are visible, in addition to a variety of smaller features at (e.g.,) 12.0, 13.5, 14.2 µm and molecular hydrogen emission at 12.3 µm.

12.7 μm emission complex. The 12.0 μm PAH band is excluded as it does not exhibit spectral blending with the 12.7 μm emission.

The variability of the 11 μm and 12.7 μm emission complexes in NGC 7023 is examined in Fig. 3.4. A representative set of pixels are chosen from the map such that each position is a different distance from the illuminating source.

The relative strengths of the 11.0 and 11.2 μm emission bands show significant variations across the map (upper panel). As stellar distance decreases, four effects are simultaneously visible: the 11.0 μm band strength relative to the 11.2 μm emission increases monotonically; the peak position of the 11.2 μm band moves to shorter wavelengths (from class A(B) to class A; see also Boersma, Bregman, and Allamandola 2013; Boersma, Rubin, and Allamandola 2012); a small, narrow feature at 11.20 μm appears; and the red wing of the 11 μm complex either shifts towards shorter wavelengths or decreases in intensity (also reported by Boersma, Bregman, and Allamandola (2013) and Boersma, Rubin, and Allamandola (2012) for Orion and NGC 7023, respectively).

For these same positions, we inspect the behaviour of the 12.7 μm complex (Fig. 3.4, lower panel). As stellar distance decreases, there is a clear transition of the 12.7 μm peak position towards shorter wavelengths—from approximately 12.77 to 12.71 μm. The red wing also decreases in intensity (or shifts to shorter wavelengths) during this transition. In addition, there is a difference in the blue wing of the 12.7 μm complex between the map positions: in the range 12.5 - 12.7 μm, positions closer to the star display greater emission intensities than those further away. It does not appear that the entire emission complex is shifting, as the offsets of the red wing, peak position and blue wing are not consistent. Likewise, the emission blueward of 12.5 μm are identical in each position.

The other sources exhibit only minor variations. M17 displays a similar peak transition in the 11.2 μm band, while NGC 2023 North and South show little peak variation in the 11 μm complex. At 12.7 μm, NGC 2023 South and M17 have small variations in the peak profile and red wing, but not as clearly as for NGC 7023. The North map of NGC 2023 has no discernible 12.7 μm variations.

The observed sub-structure of the emission complexes in NGC 7023 suggests that subtle and possibly important clues about PAH sub-populations may be accessible.

3.4 Methods for analyzing the PAH bands

We now discuss traditional methods and a newly proposed method for analyzing the 11 and 12.7 μm PAH bands.

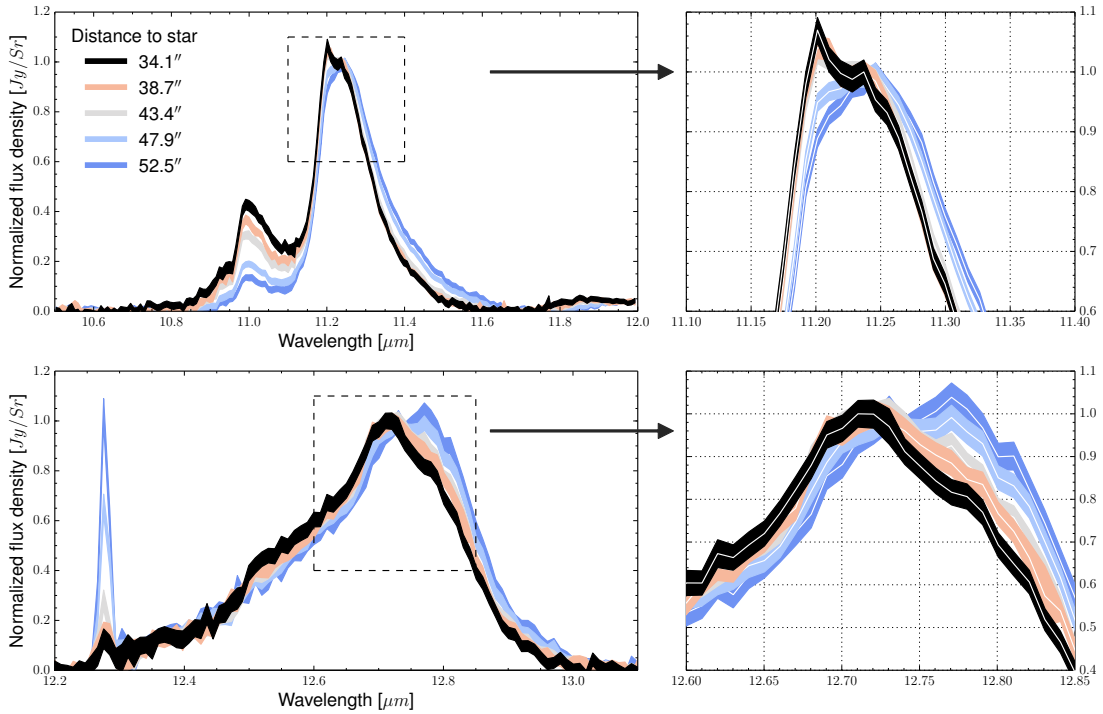

Figure 3.4: The continuum-subtracted emission in NGC 7023 of the 11 µm emission complex (top) and the 12.7 µm emission complex (bottom). The colour-coding represents different stellar distances. On the right is an expanded view of the emission peak, identified by the dashed rectangle. The width of each line represents the $\pm 1\sigma$ uncertainty on the flux density measurements.

3.4.1 The traditional approach

The 11 μm emission complex consists of two components: a strong, broad feature near 11.2 μm and a weaker band near 11.0 μm. They are generally blended together near 11.1 μm. There are multiple ways in which to measure the fluxes in these two emission bands. The simplest method is to integrate the 11 μm complex shortward of 11.1 μm (representing the 11.0 μm band) and longward of 11.1 μm (representing the 11.2 μm band). A more complex method involves using Gaussian components to help disentangle the spectral blend (see, e.g., Peeters et al. 2016; Stock et al. 2014). In this case, one simultaneously fits a Gaussian to the 11.0 μm band and a Gaussian to the blue wing of the 11.2 μm complex. The 11.0 μm flux is then the flux contained within the fitted Gaussian at 11.0 μm. The 11.2 μm band flux is measured by subtracting the 11.0 μm Gaussian from the original spectrum and integrating the remainder. A good single Gaussian fit to the 11.2 μm band is not possible due to the asymmetric red wing (Pech, Joblin, and Boissel 2002; van Diedenhoven et al. 2004). A third method to separate the 11.0 and 11.2 μm emission was introduced by Boersma, Rubin, and Allamandola (2012). The authors used a five-component Gaussian decomposition in which one component was responsible for the 11.0 μm emission. The sum of the remaining components then represented the 11.2 μm emission. A fourth possibility is to fit the 11 μm emission with two Drude profiles, an approach used by the PAHFIT tool (Smith et al., 2007b).

For the 12.7 μm band, one measurement method (besides direct integration) was presented by Stock et al. (2014). Their approach uses the average 12.7 μm emission profile from Hony et al. (2001) as a template. This template is scaled to the data in the range 12.4-12.7 μm, where only PAH emission is expected. There is frequently an adjacent [Ne II] 12.81 μm atomic line and H_2 emission at 12.3 μm, which prevents scaling beyond this spectral window. After fitting the PAH template and subtracting its profile, only atomic and/or molecular emission lines remain. These are fit with Gaussian functions in accordance with the instrumental spectral resolution of the data. Afterwards, the atomic and molecular lines are subtracted from the original 12.7 μm emission complex, leaving only the 12.7 μm PAH emission. As with the 11 μm emission, another possible 12.7 μm decomposition is to fit the band with two Drude profiles (the PAHFIT approach).

To account for the diversity of the profile variations (see Section 3.3), we have introduced a new decomposition method which we will explore in detail.

3.4.2 A new decomposition

We attempted to fit the 11 and 12.7 μm complexes with a variety of Gaussians and Lorentzians. We used the non-linear least squares fitting tool MPFIT (Markwardt, 2009), which is an im-

plementation of the Levenberg-Marquardt algorithm (Moré, 1978). We compute the reduced-χ^2 of the fit for each pixel in our spectral cubes. A histogram of all pixels in each cube is prepared, which is used to evaluate the overall fit. The best reduced-χ^2 values resulted from fitting the 11 μm complex with five Gaussians and the 12.7 μm complex with four. To determine their nominal parameters we applied an iteration method. Initially, the components were permitted to move, as long as they did not overlap. Their widths were also allowed to vary. After allowing several "free runs" we observed that some of the parameters were converging on particular values (those areas of the spectrum with less complex structure). We fixed these converging parameters and recomputed our fits. The process was iterated in this manner until all parameters had converged. The final fits are thus obtained with fixed peak positions and full-width at half-maximum (FWHM) values while only the peak intensity of each component was allowed to vary.

It is important to emphasize that *the decompositions we adopt are arbitrary*. We do not suggest that they reflect a "true decomposition" or any a priori knowledge. Rather, this method is applied to understand what (if anything) may be learned about the PAH bands through simple fitting.

The 11 μm complex The best fits resulted from a five-component Gaussian fit. The Gaussians were fixed to the following positions: 11.021 μm (FWHM: 0.066 μm), 11.000 μm (0.021 μm), 11.199 μm (0.021 μm), 11.320 μm (0.118 μm) and 11.245 μm (0.055 μm). An example of the decomposition we adopted is shown in Fig. 3.5. We see that the 11.0 μm emission is determined by two components, and the 11.2 μm emission by three components. The two components of the 11.0 μm emission can be qualitatively interpreted as an underlying broad component (centered near 11.0 μm) and a narrower symmetric feature placed upon it. The 11.2 μm profile displays a strong Gaussian feature centered near 11.25 μm with an accompanying red wing (out to 11.6 μm). The slight asymmetry of the 11.2 μm peak, namely on the short-wavelength edge (near 11.20 μm), is coincident with the fifth component.

The 12.7 μm complex We applied the same methodology to the 12.7 μm emission complex and found that the best statistics resulted from a four-component decomposition. A sample decomposition is presented in Fig. 3.6. One component of the fit is linked to the broad blue wing, upon which a weaker, narrower component is placed. The other two components compete to fit the peak position of the band and the spectral profile of its long-wavelength wing. The adopted central wavelengths of our components are as follows: 12.55 μm (FWHM: 0.160 μm), 12.54 μm (0.035 μm), 12.72 μm (0.090 μm) and 12.78 μm (0.080 μm).

3.5 Results

3.5.1 Spectral characteristics of the fit

We present our decompositions of the 11 and 12.7 μm emission complex in Figs. 3.5 and 3.6, respectively, for a choice of three locations in NGC 7023. These positions are chosen along a radial vector emanating outward from the central star. The positions are 34″, 43″ and 53″ distant from the star, respectively.

3.5.1.1 The 11 μm emission

Considering the 11 μm emission first, we see that at the closest location the 11-G1 component dominates the 11.0 μm emission (Fig. 3.5, upper panel). Here, the 11-G2 component contributes weakly. At further distances, however, the flux of the 11-G1 component decreases significantly, while the flux of the 11-G2 component is relatively unchanged. At the furthest distance, the peak flux density of the 11-G2 component slightly exceeds that of the 11-G1 component. The 11.2 μm emission profile varies across the three map positions. Near the star, the 11.2 μm peak is asymmetric and centered near 11.20 μm. Far from the star, we see that the peak of the 11.2 μm emission has shifted to ∼11.25 μm and it is now more symmetric. Note that the fit has a slight mismatch on the peak emission at the closer positions.

The 11-G3 component decreases in intensity with distance, similar to that of the 11-G1 emission. The 11-G3 component appears to be at least partially responsible for the asymmetry of the peak 11.2 μm emission at positions near the star. The other two components, 11-G4 (which traces the red-shaded wing) and 11-G5 (which contains the bulk of the flux at the traditional position of 11.2 μm) increase in flux density with increasing distance.

3.5.1.2 The 12.7 μm emission

In Fig. 3.6 we see that at the position nearest the star the peak of the 12.7 μm complex lies blueward of 12.75 μm (which we use as a reference). At this location, the flux of 12-G3 is clearly greater than that of 12-G4. We observe strong asymmetry of the 12.7 μm peak at this position. Note the fit cannot completely reproduce the peak shape observed. At the position furthest from the central star (lower panel), however, the peak is now located redward of 12.75 μm. The flux of the 12-G4 component now exceeds that of the 12-G3 component considerably, indicating that it is the relative strengths of the 12-G3 and 12-G4 components that determines the peak position of the 12.7 μm emission. At an intermediate distance from the central star in NGC 7023 (middle panel), we see that 12-G3 and 12-G4 are of roughly equal strength, and that the 12.7 μm emission has a peak position that is intermediate between the extremes of

the upper and lower panels. The broad component in this decomposition, 12-G1, is generally unchanged across the three map positions. The 12-G2 component however decreases in relative intensity as one moves to further distances from the central star.

3.5.2 Spatial morphology

3.5.2.1 The 11 μm decomposition

Starting with NGC 7023, we present spectral maps of the five components of the 11 μm decomposition in Fig. 3.7. We have included maps of the traditional 11.0 and 11.2 μm decomposition, defined here as direct integration, for comparison (see Section 3.4.1). We observe that the distribution of the 11-G1 component is extremely similar to that of the 11.0 μm band. Recall that the 11-G1 component is the broad underlying feature centered near 11.0 μm. The 11-G2 component, which is the smaller feature perched on top of the 11-G1 plateau, shows a spatial distribution that is intermediate between that of the 11.0 and 11.2 μm emission. This is also true for the 11-G3 component, which appears to be intermediate in morphology between the 11.0 and 11.2 μm bands. The 11-G4 and 11-G5 components are both coincident with the 11.2 μm emission.

Similar results are found in NGC 2023 South (Fig. 3.8). The map of the 11-G1 component's flux is an extremely good match to that of the traditional 11.0 μm component. The 11-G2 and 11-G3 components are also intermediate in morphology between that of the 11.0 and 11.2 μm bands. However, it is clear that in NGC 2023 South the 11-G3 component is closer in spatial distribution to that of the 11.0 μm emission and the 11-G2 component is closer in spatial distribution to that of the 11.2 μm emission. The 11-G4 and 11-G5 components again match the 11.2 μm emission, though the 11-G4 component is less extended in comparison.

The spectral maps of NGC 2023 North are presented in Fig. A.1. We observe that the 11.0 μm band and the 11-G1 components are similar, each peaking along a vertical slice in the map. Additionally, the 11-G3, 11-G4 and 11-G5 components exhibit similar morphologies, each peaking along a common horizontal strip. The 11-G2 component appears to share the peak positions of these two groups, forming an "L" shape from the horizontal and vertical peak PAH zones.

In M17 (Fig. A.2), there is generally very little variation between the traditional 11.0 and 11.2 μm emission maps. They appear to peak in the same position in the map. However, there is one apparent difference: there is 11.2 μm emission in the upper corner, forming a small ridge along the boundary of the field of view. We will hereafter refer to this feature as the M17 "spur." Using this as a distinguishing characteristic, we observe that the 11.2 μm band, the 11-G4 component and the 11-G5 component all have emission in this region. Conversely,

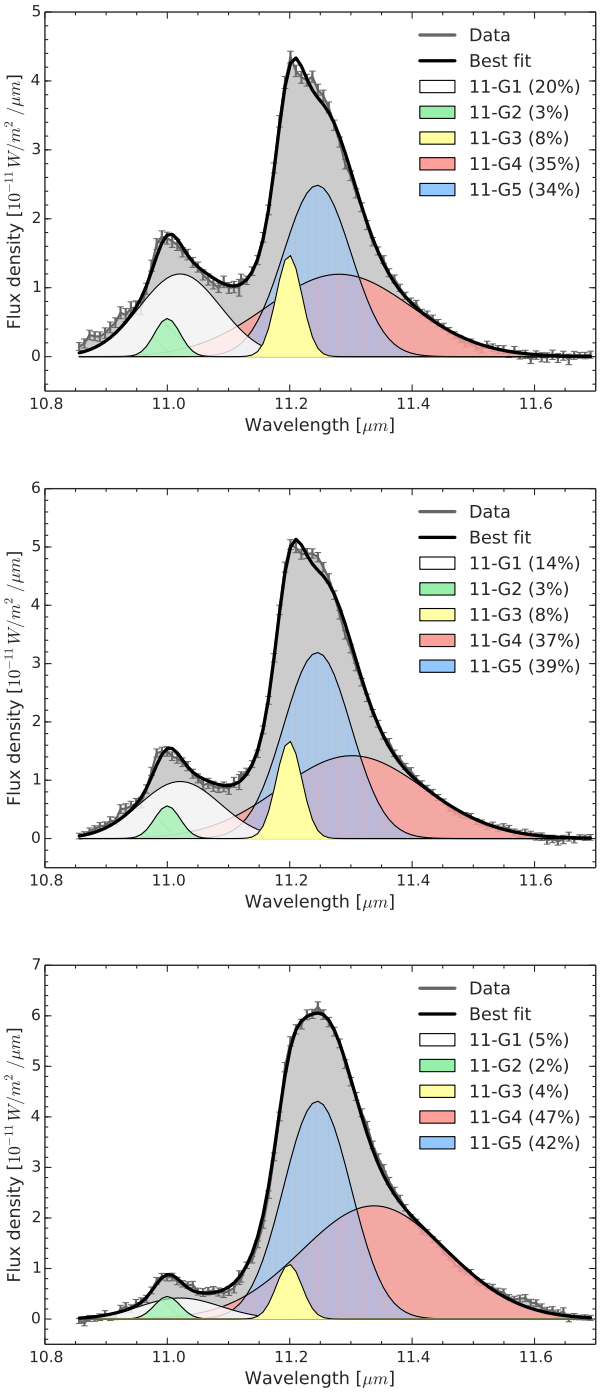

Figure 3.5: The 11 µm decomposition in NGC 7023 for three positions at varying distances from the central star (34″ in the upper panel, 43″ in the middle panel, and 53″ in the lower panel). These positions correspond to the closest, furthest, and intermediate positions in Fig. 3.4. The percentages in parentheses indicate the fraction of total flux carried by each component.

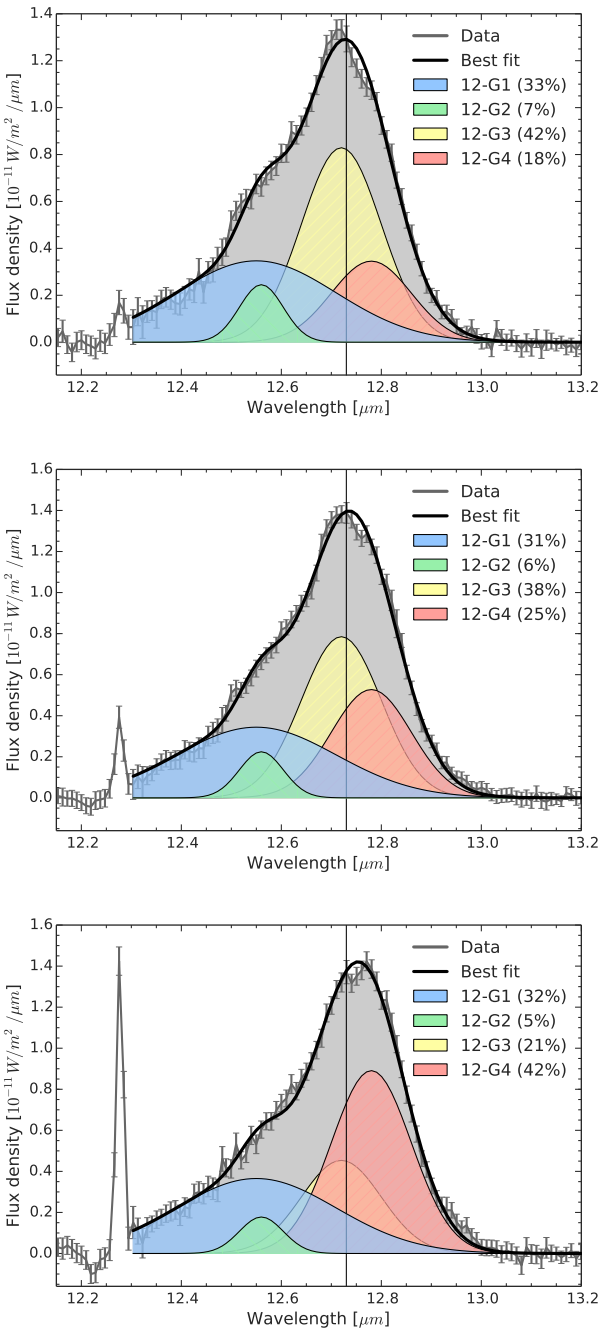

Figure 3.6: The 12.7 μm decomposition in NGC 7023 for three positions at varying distances from the central star (34″ in the upper panel, 43″ in the middle panel, and 53″ in the lower panel). These positions correspond to the closest, furthest, and intermediate positions in Fig. 3.4. The percentages in parentheses indicate the fraction of total flux carried by each component. The vertical line at 12.73 μm is to guide the eye.

the 11.0 μm band and the 11-G1, 11-G2 and 11-G3 components all have very little emission in comparison. We also observe that the 11-G2 component is more extended than the 11-G1 and 11-G3 emission, and is closer in morphology to that of the 11-G4 and 11-G5 bands. This suggests that the 11-G1 and 11-G3 bands are more closely related to the 11.0 μm emission than the 11-G2 component.

In brief summary, the emission of the 11-G1 component closely spatially matches the 11.0 μm band. The maps of the 11-G2 and 11-G3 components are a mixture of the 11.0 and 11.2 μm maps, while the 11-G4 and 11-G5 distributions are well-matched to that of the traditional 11.2 μm band.

3.5.2.2 The 12 μm decomposition

In Fig. 3.7 we present maps of the four components of the 12.7 μm decomposition. We again include maps of the 11.0 and 11.2 μm emission bands as measured with the traditional decomposition (see Section 3.4.1). As shown in Fig. 3.6, it is the 12-G3 and 12-G4 components whose relative strengths determine the position of the 12.7 μm peak. The 12-G3 component of the 12.7 μm decomposition has a very similar spatial distribution to that of the 11.0 μm emission, peaking in generally the same location. The morphologies of the 12-G4 component and the 11.2 μm emission are likewise very similar. There is generally very little overlap between the 12-G3 and 12-G4 components in these maps. The 12-G2 component generally peaks where the 11.0 μm emission does, and therefore also the 12-G3 component, but it is clearly more extended than either of these features. The 12-G1 component is the most extended, with emission at both the 11.0 and 11.2 μm peaks. This is consistent with the findings in Fig. 3.6, in which the 12-G1 component showed little variation in flux density for three chosen positions in the NGC 7023 map and the 12-G2 component increased in strength when approaching the star.

We perform a similar analysis on the map of NGC 2023 South (Fig. 3.8). We also observe strong similarities between the spatial distributions 11.0 μm and 12-G3 fluxes, and the 11.2 μm and 12-G4 fluxes. The 12-G1 and 12-G2 components both appear to involve a mixture of the spatial emission of the 11.0 and 11.2 μm bands, which is generally consistent with what was observed in NGC 7023.

The spatial distributions of the emission bands in NGC 2023 North (Fig. A.1 in the appendix) are difficult to interpret. Very broadly, the peak of the 11.2 μm emission is coincident with the peak of the 12-G4 component's emission. The 11.0 μm emission peaks along a vertical line in the map; the 12-G3 component also has strong emission in this region, but there appears to also be significant emission in the same location as that of the 11.2 μm band (spanning a horizontal zone). The 12-G1 and 12-G2 components are broad and generally overlap

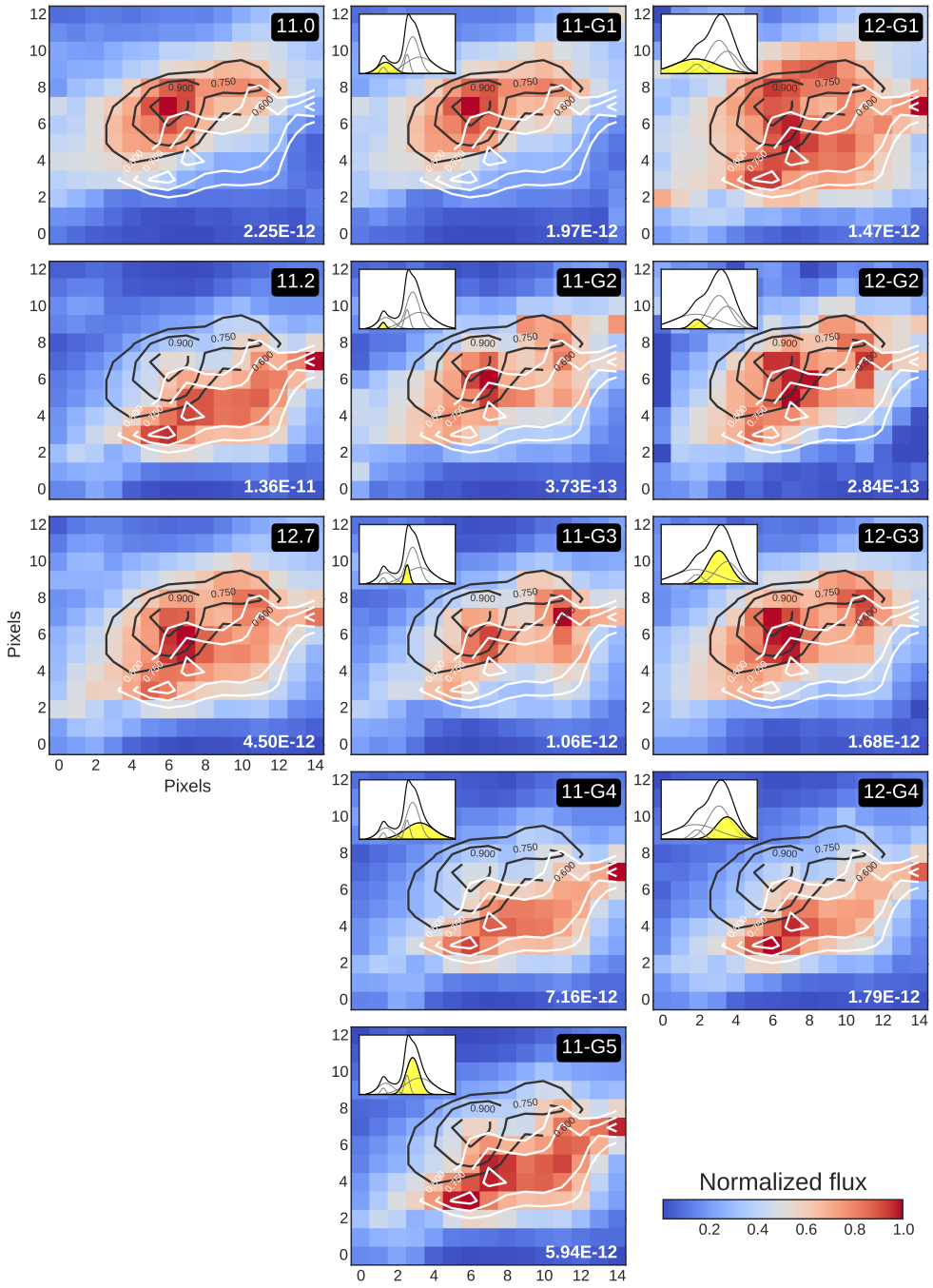

Figure 3.7: PAH emission in NGC 7023. The left column displays the 11.0, 11.2 and 12.7 µm emission measured using the traditional methods. The middle column displays the flux of each component in the 11 µm decomposition, and the right column displays the emission for the 12.7 µm decomposition. Each map is normalized, with the normalization constant given in the lower-right corner. The name of each band is identified by the black rectangle and the inset figures identify which component is being plotted (highlighted in yellow). The black and white contours trace the traditional 11.0 and 11.2 µm emission, respectively.

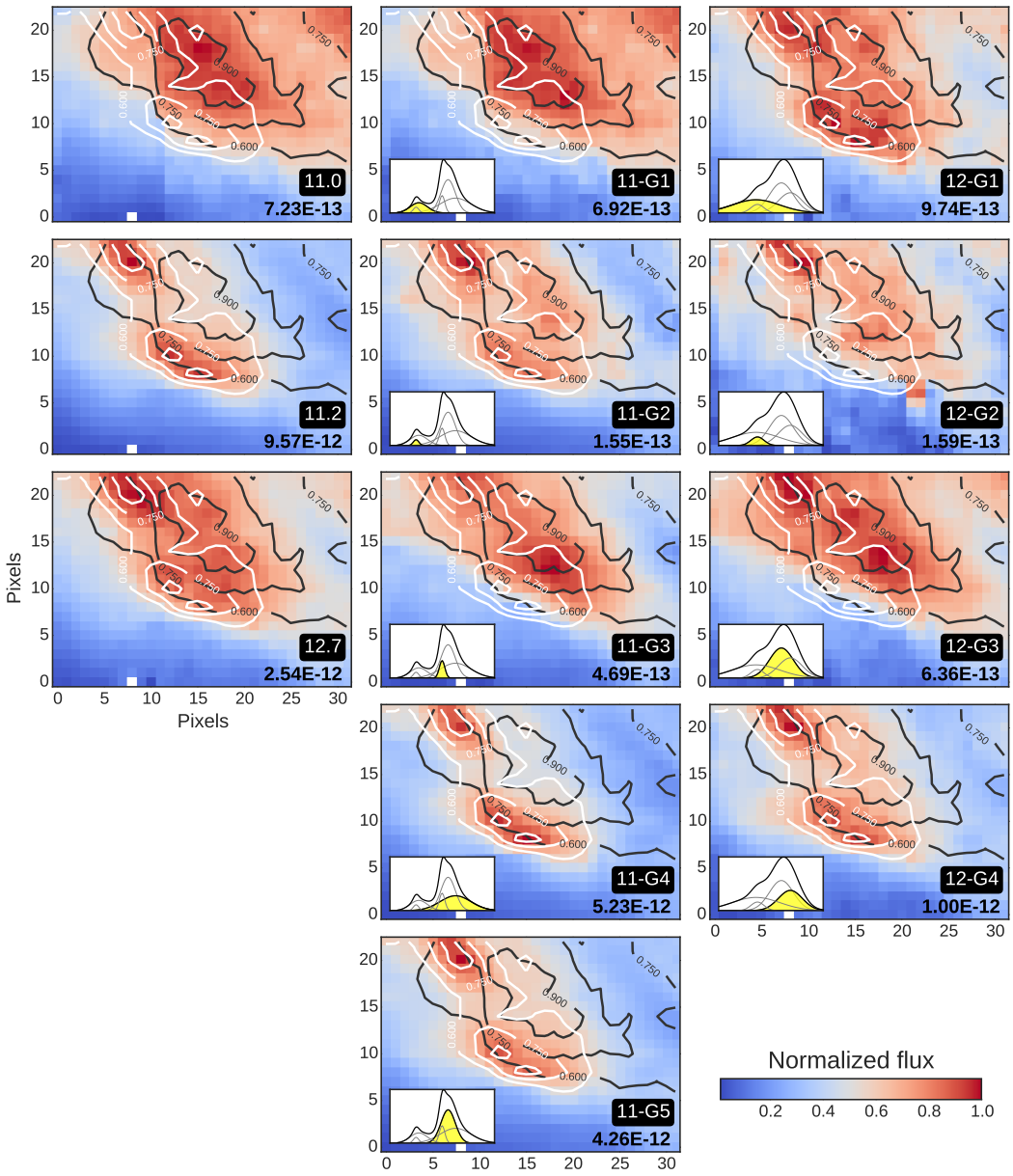

Figure 3.8: PAH emission in NGC 2023 South. The conventions are the same as those used in Fig. 3.7.

the locations in which the 11.0 and 11.2 μm emission originates. The 12-G1 component has the most extended emission in this map. Spectral maps of the emission in M17 are presented in the appendix in Fig. A.2. M17 is also difficult to disentangle, but there is roughly a commonality between the 11.2 μm emission, 12-G4, and 12-G1 components. Likewise, a grouping of the 11.0 μm emission, 12-G3 and 12-G2 components is observed, as found in NGC 7023.

Summarizing, the 12-G3 emission spatially matches that of the 11.0 μm band, while the 12-G4 emission component is a close spatial match to the 11.2 μm emission. The spatial distributions of the 12-G1 and 12-G2 emission maps are clearly a mixture of the 11.0 and 11.2 μm emission maps.

3.6 Discussion

The profile variability of the 11 and 12.7 μm PAH complexes can be explained within the framework of our adopted decompositions. The asymmetry of the 11.2 μm peak is determined by the strength of the 11-G3 component, and the asymmetry of the 12.7 μm peak is determined by the competition between the 12-G3 and 12-G4 components. The spectral maps reveal that some components are spatially coincident while others display distinct spatial morphologies.

3.6.1 Structural similarities

To quantify the morphological similarities of the spectral maps we introduce the structural similarity algorithm of Wang et al. (2004). This is an image processing method to evaluate the similarities between images based on local luminance, contrast and structure. The method produces a structural similarity index (SSIM) to quantify how alike two images are. The SSIM value ranges from -1 to 1, where values approaching 1 represent very similar images (only identical images have an SSIM index of unity). The SSIM index is computed by first comparing sub-regions, or windows, of the two images. The windows are used to compare each portion of the corresponding images, before producing a single number to encapsulate the similarity between the images as a whole. The SSIM index between two images x and y of common size $N \times M$ is defined as follows:

$$\mathrm{SSIM}(x, y) = \frac{(2\mu_x\mu_y + C_1)(2\sigma_{xy} + C_2)}{(\mu_x^2 + \mu_y^2 + C_1)(\sigma_x^2 + \sigma_y^2 + C_2)}$$

where μ and σ are the mean and variance of each window, respectively. The constants C_1 and C_2 are variables for preventing instability when the denominator would otherwise approach zero. They are defined as $C_1 = (K_1 R)^2$ and $C_2 = (K_2 R)^2$, in which R is the dynamic range

of the image, and K_1 and K_2 are canonically 0.01 and 0.03, respectively (Wang et al., 2004). We use the structural_similarity subpackage of the scikit-image Python package (Walt et al., 2014) to compute the SSIM values. The default window size of 7 pixels is used, as are the canonical K_1 and K_2 values.

We present the SSIM values comparing the maps from our decomposition in Table 3.2. SSIM indices exceeding 0.90 are presented in red. Due to the NaNs in the M17 map and the SSIM requirement for rectangular windows we could not analyze the M17 map in this manner.

We find the same results as were determined from visual inspection: the morphologies of the 11-G1 and 12-G3 emission components are well-matched with that of the 11.0 μm emission; the 11-G4, 11-G5 and 12-G4 emission components are spatially well-matched with the 11.2 μm emission; and the 11-G2, 11-G3, 12-G1 and 12-G2 emission components are spatially a mixture of the two. Similar conclusions about the 12.7 μm components are reached when examining correlation plots of band flux ratios (Fig. A.3).

3.6.2 The 11.0 and 11.2 μm bands: assignments

Since early on, astronomical observations of extended sources have revealed that the major PAH bands exhibit spatially different behaviour. In particular, the 8.6 and 11.0 μm bands peak closer to the exciting star than the 3.3 and 11.2 μm bands, which peak further away (e.g. Joblin et al. 1996; Sloan et al. 1999). The behaviour has been attributed to the PAH charge state, as laboratory experiments have shown that the 8.6 and 11.0 μm emission are dominated by cations, and the 11.2 μm emission by neutral PAHs (Allamandola, Hudgins, and Sandford, 1999; Hudgins and Allamandola, 1999). A comparison of astronomical spectra to laboratory and theoretically calculated spectra by Hony et al. (2001) reinforced the assignment of the 11.0 and 11.2 μm bands to solo CH_{oop} bending in cations and neutrals, respectively. More recently, computed spectra of (very) large PAHs by Bauschlicher, Peeters, and Allamandola (2008) and Ricca et al. (2012) showed that the solo CH_{oop} emission from PAH neutrals becomes blueshifted upon ionization, supporting the same assignment. Using blind signal separation, Rosenberg et al. (2011) also identified the 11.0 μm band as cationic and the 11.2 μm band as neutral.

Recently, however, there have been suggestions of further complexity in the assignments of the 11.0 and 11.2 μm bands, which we address here. For one, Candian and Sarre (2015) showed that *neutral* acenes produce emission near 11.0 μm. At present it is not clear how significant their contribution will be to the astronomical 11.0 μm emission band, as they con-

Table 3.2: Structural similarity indices

NGC 7023

11.0											
11.2	0.30										
11-G1	0.99	0.30									
11-G2	0.75	0.73	0.74								
11-G3	0.69	0.78	0.69	0.93							
11-G4	0.24	0.98	0.24	0.66	0.71						
11-G5	0.32	0.99	0.32	0.75	0.79	0.96					
12-G1	0.63	0.68	0.64	0.74	0.71	0.67	0.69				
12-G2	0.75	0.71	0.75	0.93	0.90	0.64	0.74	0.74			
12-G3	0.88	0.60	0.88	0.94	0.91	0.52	0.63	0.75	0.94		
12-G4	0.22	0.96	0.22	0.65	0.69	0.96	0.95	0.60	0.64	0.51	
	11.0	11.2	11-G1	11-G2	11-G3	11-G4	11-G5	12-G1	12-G2	12-G3	12-G4

NGC 2023 South

11.0											
11.2	0.52										
11-G1	0.97	0.50									
11-G2	0.66	0.86	0.60								
11-G3	0.81	0.60	0.80	0.70							
11-G4	0.47	0.99	0.44	0.81	0.53						
11-G5	0.55	0.99	0.53	0.87	0.63	0.97					
12-G1	0.66	0.87	0.63	0.83	0.70	0.83	0.87				
12-G2	0.68	0.61	0.65	0.72	0.77	0.56	0.63	0.55			
12-G3	0.84	0.53	0.83	0.70	0.92	0.46	0.57	0.61	0.82		
12-G4	0.55	0.95	0.52	0.86	0.60	0.93	0.96	0.87	0.64	0.53	
	11.0	11.2	11-G1	11-G2	11-G3	11-G4	11-G5	12-G1	12-G2	12-G3	12-G4

NGC 2023 North

11.0											
11.2	0.61										
11-G1	0.99	0.63									
11-G2	0.76	0.89	0.75								
11-G3	0.66	0.93	0.68	0.91							
11-G4	0.56	0.99	0.57	0.85	0.90						
11-G5	0.68	0.98	0.70	0.92	0.93	0.94					
12-G1	0.64	0.76	0.64	0.78	0.77	0.75	0.76				
12-G2	0.64	0.64	0.65	0.69	0.75	0.60	0.68	0.43			
12-G3	0.87	0.76	0.88	0.88	0.83	0.70	0.82	0.64	0.78		
12-G4	0.77	0.76	0.76	0.83	0.79	0.71	0.83	0.74	0.70	0.80	
	11.0	11.2	11-G1	11-G2	11-G3	11-G4	11-G5	12-G1	12-G2	12-G3	12-G4

stitute a small set of the PAH family. The NASA Ames PAH IR Spectroscopic Database[†] (Bauschlicher et al., 2010; Boersma et al., 2014), hereafter referred to as PAHdb, has few included acenes at this time. Using PAHdb, Boersma, Bregman, and Allamandola (2013) showed that *cationic* nitrogen-substituted PAHs, or PANHs, were required to fit the 11.0 μm astronomical emission in NGC 7023. Another possibility is that $[SiPAH]^+$ complexes may contribute to the 11.0 μm band, as shown by quantum chemical calculations by Joalland et al. (2009). The resulting IR emission intensities of such complexes are expected to be similar to those of pure PAH cations. To confirm this assignment further laboratory and theoretical work are required (Joalland et al., 2009). Regarding the 11.2 μm emission, it has been proposed that its red wing (out to 11.4-11.6 μm) is due to the emission from very small grains (VSGs; Berné et al. 2007; Rosenberg et al. 2011). If VSG abundances are sufficiently high, they may influence the peak position of the 11.2 μm complex.

Apart from neutral acenes, all assignments of the 11.0 μm band point towards a cationic carrier. Similarly, apart from VSGs, all assignments of the 11.2 μm band point towards neutral PAHs. We adopt such charge assignments, leading to the following conclusions:

1. The 11 μm complex:

    11-G1 — dominated by cations
    11-G2 — mixed charge
    11-G3 — mixed charge
    11-G4 — dominated by neutrals
    11-G5 — dominated by neutrals

2. The 12.7 μm complex:

    12-G1 — mixed charge
    12-G2 — mixed charge
    12-G3 — dominated by cations
    12-G4 — dominated by neutrals

3.6.3 Neutral emission at 11.0 μm

The mixed behaviour of the 11-G2 component indicates that the traditional 11.0 μm band is not purely cationic. The 11-G1 component however dominates the 11.0 μm flux, meaning that the emission is still primarily cationic. We estimate the contributions of these two components to the traditional 11.0 μm emission in Fig. 3.9. The 11-G1 component in general carries

[†] http://www.astrochem.org/pahdb/

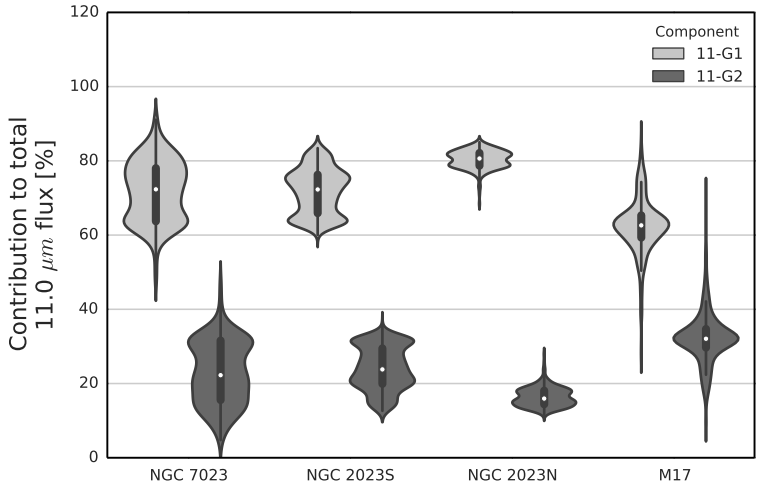

Figure 3.9: Breakdown of the fractional contributions to the traditional 11.0 μm flux from the 11-G1 and 11-G2 components for each object. The violin shape is a histogram of all pixels in each data cube, shown per object. The violin width corresponds to the number of pixels contributing at a given percent level. The total histogram is fitted with a kernel density estimate (which leads to the violin shape). The mean values are indicated by the white dots and the standard deviation by the thick dark line. The thin dark line (running vertically through each shape) represents the total data range.

60-80% of the flux: $72 \pm 8\%$ (NGC 7023), $72 \pm 6\%$ (NGC 2023 South), $80 \pm 3\%$ (NGC 2023 North) and $62 \pm 7\%$ (M17). The 11-G2 component generally is the complement to these values: $23 \pm 8\%$ (NGC 7023), $24 \pm 6\%$ (NGC 2023 South), $16 \pm 3\%$ (NGC 2023 North) and $32 \pm 7\%$ (M17). In some instances there is a minor contribution (less than 5%) from either the 11-G3 or 11-G4 component.

We use the structural similarity indices (Table 3.2) to quantify the mixed behaviour of the 11-G2 component. To do so, we must make the assumption here that the traditional 11.2 μm component traces neutral PAHs and the 11-G1 component traces pure cations. We can reach the same conclusions if we instead use the traditional 11.0 μm band as a tracer of pure cations, though with greater uncertainty (since the 11-G2 component is a minor contributor to the 11.0 μm emission). The similarity indices show that in NGC 7023, the 11-G2 component is equally similar to the 11.2 μm emission (SSIM = 0.73) as it is to the 11-G1 emission (SSIM = 0.74). In NGC 2023 South and North, however, the 11-G2 component is more similar to the 11.2 μm band than the 11-G1 emission (SSIM = 0.86 versus 0.60 in the southern map and SSIM = 0.89 versus 0.75 in the northern map). This implies that at minimum 50% of the flux of the 11-G2 component is from neutral PAHs. In turn, this then implies that *the traditional 11.0 μm band is roughly 8 – 16% neutral and 78 – 88% cationic, with uncertainties approaching ten percentage points.*

Recently, Candian and Sarre (2015) reported that the solo CH_{oop} mode of neutral acenes falls near 11.03 μm and argues for a possible contribution from neutral acenes to the 11.0 μm band. The results reported here, that there is a small neutral contribution to the 11.0 μm band in our sample, provide the first observational evidence in support of a partial origin in a neutral carrier.

Rosenberg et al. (2011) applied blind signal separation to NGC 7023 and identified three basis vectors: PAH^0, PAH^+ and VSGs. One interesting result of their analysis is that the PAH^0 signal, which is associated with neutral PAHs, showed a local emission peak at 11.0 μm. The authors suggest this is an artifact of the applied method, and may be compensated for by a local minimum in their VSG signal. However, since we have identified a component of the traditional 11.0 μm band that is linked to neutral PAHs, we suggest that it may be due to the non-cationic component that we have found.

In the traditional assignment of the 11.0 and 11.2 μm bands, i.e. originating from solo CH_{oop} modes in cations and neutrals, respectively, the 11.0/11.2 ratio traces the PAH charge fraction (Boersma, Rubin, and Allamandola, 2012). To examine this, one must determine the intrinsic 11.0/11.2 flux ratio of a PAH after a single photon excitation event. The authors chose circumcoronene as being representative of a typical PAH, which then relates the observed 11.0/11.2 flux ratio to an implied neutral-to-cation fraction. The neutral fraction was shown to decrease in Orion from 80% to 65% when moving away from the star, before returning to 80% at further distances. The unexpected diminution of the neutral fraction with increasing distance may reflect dehydrogenation, which would affect the measured 11.0/11.2 μm ratio, or it may indicate that circumcoronene is not a reasonable proxy for the total PAH population (Boersma, Rubin, and Allamandola, 2012). Our results show that neutral PAHs contribute to the 11.0 μm band, at approximately the 8-16% level. This may be an additional contributing factor to the unusual 11.0/11.2 behaviour observed by Boersma, Rubin, and Allamandola (2012).

Mean spectra of species in PAHdb were presented by Boersma, Bregman, and Allamandola (2013), binned by size and charge state (their Fig. 9). There does not appear to be neutral emission at 11.0 μm. This may reflect biases or limitations of the database (see Bauschlicher et al. 2010; Boersma et al. 2011). The neutral emission we deduce to exist at 11.0 μm is a small fraction of the cationic emission at 11.0 μm, and thus it may be hidden (if present in the PAHdb spectra) by averaging over all species.

3.6.4 Profile asymmetries

3.6.4.1 The 11 μm emission

The 11.2 μm band displays two asymmetries: a prominent red wing in the range 11.4-11.6 μm and a narrow peak near 11.20 μm that appears only when sufficiently close to the illuminating source (c.f. Fig. 3.4). We exclude the 11.0 μm band from consideration here as it is understood to be a separate band.

In our decomposition, the 11-G3, 11-G4 and 11-G5 components all emit significantly at 11.20 μm (Fig. 3.5). However, the 11-G3 component is much narrower than the others and it is located at exactly 11.20 μm, meaning that it might provide some clues about the origin of the peak asymmetry. With the caveats in mind, the results show that the spatial distribution of the 11-G3 component is a mixture of the traditional 11.0 and 11.2 μm emission. The 11-G3 component has almost no spectroscopic overlap with the traditional 11.0 μm emission, and the 11-G3 component is strongly blended at 11.2 μm with the neutral-carrying 11-G4 and 11-G5 bands, which dominate the 11.2 μm flux. This implies that *we identify a cationic contribution to the 11.2 μm emission.*

Furthermore, the strength of the 11-G1 and 11-G3 components both increase when approaching the star (as shown in Fig. 3.5). This is complemented by a transition of the 11.2 μm peak position from class A(B) (near 11.24 μm) to class A (near 11.20 μm) as reported by Boersma, Bregman, and Allamandola (2013) and Boersma, Rubin, and Allamandola (2012) (see Peeters et al. 2002; van Diedenhoven et al. 2004 for classification details). Since the 11-G3 component is coincident with the nominal class A position, it suggests that it is the relative intensity of the 11-G3 component to that of 11.2 μm emission peak that determines the PAH class. Knowing also that the 11-G3 component has a cationic contribution, this implies that the PAH classification of the 11.2 μm band is partially moderated by the relative fraction of emission from PAH cations to neutrals. This effect is likely in addition to that reported by Candian and Sarre (2015), who studied neutral PAHs and identified that the class variations, from A to A(B), result from changes in the distribution of PAH masses.

During the class transition from A(B) to A, the flux in the red wing decreases significantly in NGC 7023 (c.f. Fig. 3.4), and less so in NGC 2023 South. The spectral asymmetry due to the variable red wing is well known in the literature (Hony et al., 2001; Hudgins and Allamandola, 1999; van Diedenhoven et al., 2004). Many PAH bands display a red wing due to anharmonicity, but the magnitude of variations seen in the observations cannot be reconciled with the expected degree of asymmetry from this effect (van Diedenhoven et al., 2004). Possible explanations have been presented in the literature but its origin has not yet been es-

tablished. Suggestions include emission from VSGs (Berné et al., 2007; Rapacioli et al., 2006; Rosenberg et al., 2011), PAH clusters (Boersma, Bregman, and Allamandola, 2014), PAH anions (Bauschlicher, Peeters, and Allamandola, 2009), low-mass PAHs (Candian and Sarre, 2015) and superhydrogenated PAHs (Boersma, Bregman, and Allamandola, 2014; Knorke et al., 2009).

Rosenberg et al. (2011) found a spatial separation between neutral PAHs and very small grains in NGC 7023 based on blind signal separation. In our decomposition, the flux of the red wing is carried by the 11-G4 component, while the "symmetric" 11.2 μm emission is carried primarily by the 11-G5 component. As introduced in Section 3.5.2, the spectral maps of the 11-G4 and 11-G5 components are similar but have subtle differences. We observe in NGC 7023 and 2023 South that the 11-G4 (red wing) emission is less extended than the 11-G5 emission, despite peaking in the same map position. The discrepancy with the results of Rosenberg et al. (2011) is likely a consequence of the large width of our 11-G4 component, which has significant contributions at 11.1 μm and greater.

We conclude that the entire 11 μm complex traces the following (not necessarily unique) populations: at 11.0 μm, PAH cations and a small fraction of neutrals; and at 11.2 μm, PAH neutrals and a small fraction of PAH cations. With our decomposition we are unable to deduce the carrier of the red wing.

3.6.4.2 The 12.7 μm emission

The 12.7 μm band is quite asymmetric, exhibiting a blue-shaded wing (Hony et al., 2001). Our decomposition accounts for the blue wing primarily through the flux of the 12-G1 component, which is broad and centered at 12.55 μm. In NGC 7023, the 12-G1 component is very extended, easily encompassing the regions containing strong 11.0 and 11.2 μm emission. This suggests that the broad component, as defined here, has no charge preference. In NGC 2023 South, it is also quite extended, though to a lesser extent than in NGC 7023. The structural similarity indices show that the map of the 12-G1 component is equal parts 11.0 and 11.2 μm emission in NGC 7023. The 12-G1 component is slightly more similar to the 11.2 μm emission than the 11.0 μm emission in NGC 2023 South. Similar results to NGC 2023 South are found in the northern map, suggesting only a weak dependence on charge. This likely originates in the broadness of the component and reflects that the proposed decomposition does not completely disentangle all PAH sub-populations.

Bauschlicher, Peeters, and Allamandola (2008, 2009) used density functional theory (DFT) to compute the absorption spectra of large symmetric PAHs and large irregular PAHs. Near 12.7 μm, these authors found that the mean emission from PAH cations is blueshifted from

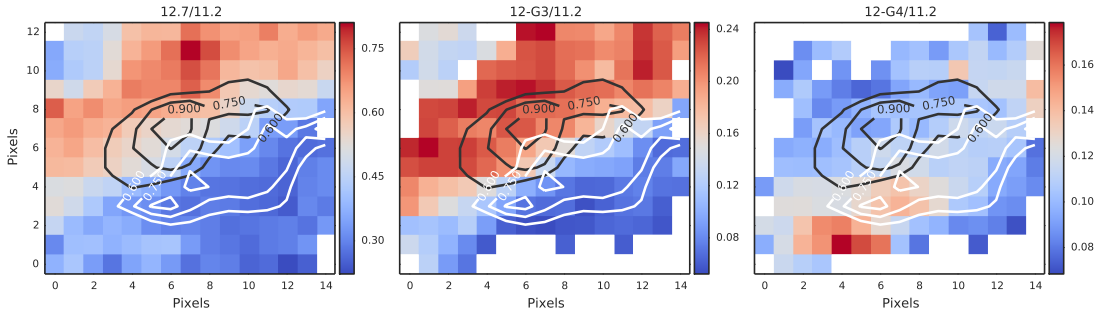

Figure 3.10: The 12.7/11.2 ratio in NGC 7023 is compared to the 12-G3/11.2 and 12-G4/11.2 ratios (left, middle and right panels, respectively). The black contours are constructed from the traditional 11.0 μm emission and the white contours from the 11.2 μm emission.

the neutral position. In our decomposition, we find the same relationship: the 12-G3 component at 12.72 μm is cationic, while the 12-G4 component at 12.78 μm is neutral. Hence, the intrinsic spectra and observations are consistent with each other.

Boersma, Bregman, and Allamandola (2013) decomposed the PAH emission in NGC 7023 with PAHdb. In fitting the 12.7 μm emission the authors find that, in the dense region, neutrals are responsible for the majority of the total intensity. In the diffuse region(s), the cations instead carry most of the intensity[‡]. We observe that the ratio of the cationic 12-G3 emission to the neutral 12-G4 emission is higher in the diffuse region than the dense region, consistent with their result. Boersma, Bregman, and Allamandola (2013) also found that the dense region was characterized by small PAHs (those with fewer than 50 carbon atoms) and the diffuse region was dominated by large PAHs (those with more than 50 carbon atoms). Within this framework, the 12-G3 component then originates in large PAHs preferentially. The 12-G4 component corresponds to emission that was comparable between small and large PAHs in the PAHdb fit (Boersma, Bregman, and Allamandola, 2013), suggesting an equal mixture of sizes.

It has been noted in the literature that some PAH correlation plots involving the 12.7 μm band display a bifurcation (Boersma, Bregman, and Allamandola, 2014; Stock et al., 2014). As our results show that the profile of the 12.7 μm band can be strongly dependent on ionization, perhaps the bifurcated correlations simply trace the two different charge states of the 12.7 μm emission.

3.6.5 The 12.7/11.2 intensity ratio

The 12.7/11.2 ratio has long been understood as probing hydrogen adjacency, as the 11.2 μm band is associated with solo CH_{oop} bending modes and the 12.7 μm band with duo and trio CH_{oop} bending modes (Bauschlicher, Peeters, and Allamandola, 2008; Hony et al., 2001). The astronomical range of 12.7/11.2 intensity ratios has been shown to be consistent with computed spectra of irregular PAHs, which have solos, duos, trios and quartets (Bauschlicher, Peeters, and Allamandola, 2009; Ricca et al., 2012). PAHs with only solos and duos, such as those from the coronene family, lead to 12.7/11.2 ratios that lie at the low end of the astronomical range (Ricca et al., 2012). In addition, this ratio can be further enhanced due to the coupling between the CH_{oop} modes and the C-C ring deformation mode in (elongated) armchair PAHs contributing to the 12.7 μm emission (Candian and Sarre, 2015).

Through the use of PAHdb, Boersma, Bregman, and Allamandola (2015) showed that the spatial variation of the 12.7/11.2 ratio in NGC 7023 seems to primarily trace ionization rather than edge structure. Based on their database fits, the authors observed that the ionization fraction increases by 200% across NGC 7023, whereas the hydrogen adjacency only drops by 25%. Since we have presented a way of generally disentangling ions from neutrals in the 11 and 12.7 μm complexes, we can probe the dependence of the 11.2/12.7 ratio on charge and molecular edge structure.[§] We found that the ionization fraction (defined as the flux from cations divided by the flux from both cations and neutrals) spans a factor of of 3.1 ± 1.4 across the NGC 7023 map. Although the uncertainty is large, the derived ionization fraction is very similar to the 200% increase (i.e. a factor of 3) determined by Boersma, Bregman, and Allamandola (2015). To study hydrogen adjacency, we measured the 12.7/11.2 ratio separately for cations and neutrals. For cations, hydrogen adjacency varies across the map by approximately 30%, while for neutrals it varies by about 10%. These results are generally consistent with the 25% value presented by Boersma, Bregman, and Allamandola (2015). We also applied this analysis to NGC 2023 South and found that the ionization fraction spans a range of 1.9

[‡]The "diffuse region" of Boersma, Bregman, and Allamandola (2013) refers to the region between the star and PDR front. The "dense region" refers to the region beyond that.

[§]To probe charge and hydrogen adjacency, we first use our decompositions to isolate the neutral and cationic contribution to the 11 and 12.7 μm complexes. To do this, we use the charge breakdown adopted in Section 3.6.2. For the mixed charge bands (e.g. 11-G2, 11-G3), we use the spatial maps and structural similarity indices to discern if one charge state appears to be dominant. The 11-G2 and 12-G2 components are found to be on average equally similar to the cationic- and neutral-dominated bands. Thus, we assume half of their flux contributes to the total cationic emission, and half to the neutral emission. For the other mixed charge bands (11-G3, 12-G1), we tested a series of different charge fractions (25%, 50%, or 75% cationic). The fluxes of these components relative to the other fluxes in the calculation are sufficiently low that they do not affect our conclusions. Since the 11 μm emission is thought to trace solo CH_{oop} structures, and the 12.7 μm emission duo and trio CH_{oop} structures, we finally measure the solo/duo+trio ratio for cations, and separately for neutrals.

$\pm$ 0.8 (or a 100% increase across the map). The hydrogen adjacency varied by approximately 25% for cations, but only 7 or 8% for neutrals. This analysis shows that the 12.7/11.2 ratio depends largely on the ionization fraction and to a lesser extent on molecular edge structure. However, when charge state is taken into account (by only considering neutral PAHs or only PAH ions), we can trace molecular edge structure of the PAH population.

The spatial morphology of the 12.7/11.2 emission was compared against the spatial distribution of the 6.2/(6.2 + 11.2 μm) fraction and the PAHdb-derived fractional emission in PAH cations (Boersma, Bregman, and Allamandola, 2014). The latter two both display smooth gradations across the PDR, whereas the 12.7/11.2 map shows pockets of enhanced ratios. The authors interpreted this as a consequence of the mixed-charge behaviour of the 12.7 μm band. We re-examine this relationship in Fig. 3.10. We now include two additional maps: the 12-G3/11.2 and 12-G4/11.2 ratios. We find a stark increase in the contrast between the diffuse and dense regions when examining 12-G3/11.2 instead of 12.7/11.2. This originates in the fact that, to first order, the neutral dependence is removed. The 12-G4/11.2 ratio shows little emission in the diffuse region and relatively little variation across the region of peak 11.2 μm emission. One maximum is observed in the dense region. Clearly the 12-G3/11.2 and 12-G4/11.2 ratios are tracing different PAH populations. Taking these effects into account, it is apparent that the 12.7/11.2 ratio probes both ionization and molecule structure, which both depend on the local physical conditions (c.f. Boersma, Bregman, and Allamandola 2015).

It's worth noting that the 12.7/11.2 ratio can be greatly affected by extinction. To illustrate this, we quantify this effect by comparing the 12.7/11.2 ratio before and after correcting for extinction in M17 (Fig. 3.11) and two H II regions from Hony et al. (2001). Using the interstellar extinction curves of Chiar and Tielens (2006), we corrected for extinction. In M17, the 12.7/11.2 ratio decreases from a range of 0.37-0.72 (before correction) to 0.35-0.52 (after correction). Some pixels exhibit a greater than 30% decrease in the 12.7/11.2 ratio. We also examined two H II regions from the sample of Hony et al. (2001), using the extinction measurements of Martín-Hernández et al. (2002): IRAS 15384-5348 ($A_k = 1.3$) and IRAS 18317-0757 ($A_k = 2.0$). The latter source exhibits the largest 12.7/11.2 ratio in the study of Hony et al. (2001) before extinction correction (1.49), but this value is near unity after correction (1.03). Extinction correction thus significantly reduces the large range in 12.7/11.2 ratios observed in H II regions.

With regards to the 12.7/11.2 ratio in NGC 7023, only three pixels in the map meeting the signal-to-noise criterion are affected by extinction to any substantial degree (approximately 10-15% flux difference in the 12.7 μm band). These pixels are on the lower edge of the map and do not affect the map or our conclusions.

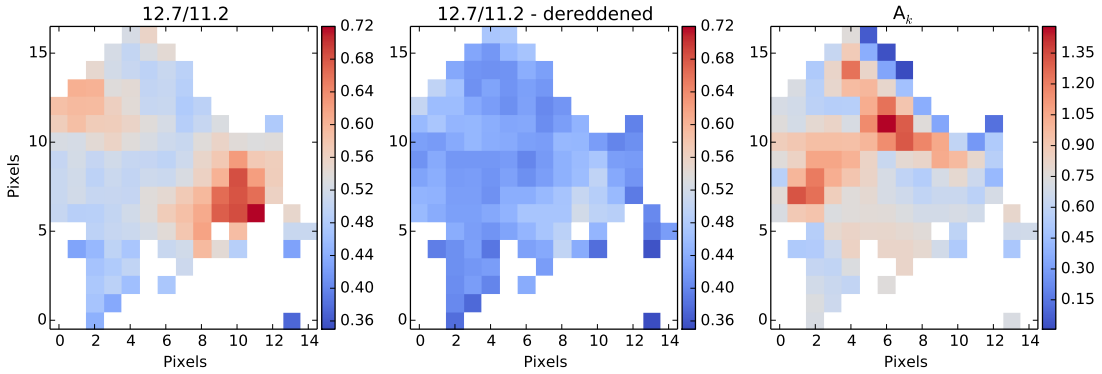

Figure 3.11: The effect of extinction on the 12.7/11.2 ratio in M17 is examined. Left panel: the 12.7/11.2 ratio with no correction. Middle panel: the extinction corrected 12.7/11.2 ratio. Right panel: the extinction map used for the correction.

3.7 Conclusions

We have examined the spatial and spectral behavior of the 11 and 12.7 μm PAH emission complexes in high-resolution *Spitzer*/IRS maps of NGC 7023, NGC 2023 South and North and M17. We have introduced a five-component Gaussian decomposition of the 11 μm emission and a four-component decomposition of the 12.7 μm emission. At 11 μm, two components are centered near 11.0 μm, one of which is relatively broad and the other relatively narrow. A narrow, weak Gaussian component is located near the peak of the 11.2 μm complex, slightly offset towards the blue. A strong band carries most of the peak 11.2 μm emission, and a final broad emission component is responsible for the red wing of the 11.2 μm band. The 12.7 μm decomposition consists of one broad feature on the blue wing, two components near 12.75 μm, and a narrow feature that appears on the blue wing in some positions.

We investigated the spatial distributions of these components in our spectral maps and quantified their similarities with the structural similarity index, in addition to flux correlation plots. We have arrived at the following conclusions:

1. The traditional 11.0 μm emission band has a contribution from neutral PAHs. We identify a broad cationic feature at 11.00 μm and a weaker, narrower mixed-charge state band at 11.00 μm. In total, 78-88% of the traditional 11.0 μm flux is carried by cations, and 8-16% of the flux is carried by neutral PAHs. This may be supporting evidence for the contribution of neutral acenes to the 11.0 μm band (Candian and Sarre, 2015).

2. The traditional broad 11.2 μm emission band has a small cationic contribution at 11.20 μm. The relative strength of this cationic feature to the broad 11.2 μm emission determines the overall peak position of the 11.2 μm complex. This implies that the PAH

classification of the 11.2 μm emission is partially determined by the fraction of PAH cations to neutrals, in addition to the varying distribution of PAH masses reported by Candian and Sarre (2015).

3. The variable peak position of the 12.7 μm complex can be explained by the relative strengths of two competing Gaussian components at 12.72 and 12.78 μm. The features are spectroscopically blended, yet they distinctly trace cations and neutrals, respectively, in the spectral maps.

4. The component responsible for the bulk of the blue-shaded wing of the 12.7 μm band appears to be only weakly dependent on charge. This may indicate that the proposed decomposition does not completely disentangle all PAH sub-populations.

5. The observed contribution of both cation and neutral PAHs to the 12.7 μm band supports the use of the 12.7/11.2 intensity ratio as a charge proxy (Boersma, Bregman, and Allamandola, 2015). However, after accounting for PAH charge, structural variations are still probed by the 12.7/11.2 ratio.

These results illustrate the power of spectral maps for understanding the complicated spectral profiles of PAHs, wherein blended spectral components can be understood as independent spatial components. The next step is to apply this technique to other high-resolution spectral maps as well as integrated spectra of individual objects. This will help improve the quantification of the non-cationic emission at 11.0 μm and understand the behaviour of the broad blue 12.7 μm wing, which appears to be insensitive to charge based on the applied decomposition. This work and the interpretation of the PAH emission bands will strongly benefit from the heightened spectral resolution and sensitivity of the forthcoming James Webb Space Telescope mission.

Acknowledgments

The authors acknowledge support from an NSERC discovery grant, NSERC acceleration grant and ERA. MJS acknowledges support from a QEII-GSST scholarship. The IRS was a collaborative venture between Cornell University and Ball Aerospace Corporation funded by NASA through the Jet Propulsion Laboratory and Ames Research Center (Houck et al., 2004). This research has made use of NASA's Astrophysics Data System Bibliographic Services, and the SIMBAD database, operated at CDS, Strasbourg, France. This work has also

made use of the Matplotlib Python plotting library (Hunter, 2007) and the Seaborn Python visualization library.[¶]

References

Allamandola, L. J., Hudgins, D. M., and Sandford, S. A. (1999). *Astrophysical Journal, Letters* 511, pp. L115–L119. DOI: 10.1086/311843.

Allamandola, L. J., Tielens, A. G. G. M., and Barker, J. R. (1989). *Astrophysical Journal, Supplement* 71, pp. 733–775. DOI: 10.1086/191396.

Bauschlicher Jr., C. W., Peeters, E., and Allamandola, L. J. (2008). *Astrophysical Journal* 678, pp. 316–327. DOI: 10.1086/533424. arXiv: 0802.1071.

– (2009). *Astrophysical Journal* 697, 311, pp. 311–327. DOI: 10.1088/0004-637X/697/1/311. arXiv: 0903.0412 [astro-ph.GA].

Bauschlicher Jr., C. W., Boersma, C., Ricca, A., et al. (2010). *Astrophysical Journal, Supplement* 189, 341, pp. 341–351. DOI: 10.1088/0067-0049/189/2/341.

Berné, O. and Tielens, A. G. G. M. (2012). *Proceedings of the National Academy of Science* 109, pp. 401–406. DOI: 10.1073/pnas.1114207108. arXiv: 1111.0839 [astro-ph.GA].

Berné, O., Joblin, C., Deville, Y., et al. (2007). *Astronomy and Astrophysics* 469, pp. 575–586. DOI: 10.1051/0004-6361:20066282. eprint: astro-ph/0703072.

Boersma, C., Bregman, J., and Allamandola, L. J. (2014). *Astrophysical Journal* 795, 110, p. 110. DOI: 10.1088/0004-637X/795/2/110.

– (2015). *Astrophysical Journal* 806, 121, p. 121. DOI: 10.1088/0004-637X/806/1/121.

Boersma, C., Bregman, J. D., and Allamandola, L. J. (2013). *Astrophysical Journal* 769, 117, p. 117. DOI: 10.1088/0004-637X/769/2/117.

Boersma, C., Rubin, R. H., and Allamandola, L. J. (2012). *Astrophysical Journal* 753, 168, p. 168. DOI: 10.1088/0004-637X/753/2/168.

Boersma, C., Bauschlicher Jr., C. W., Ricca, A., et al. (2011). *Astrophysical Journal* 729, 64, p. 64. DOI: 10.1088/0004-637X/729/1/64.

Boersma, C., Bauschlicher Jr., C. W., Ricca, A., et al. (2014). *Astrophysical Journal, Supplement* 211, 8, p. 8. DOI: 10.1088/0067-0049/211/1/8.

Candian, A. and Sarre, P. J. (2015). *Monthly Notices of the RAS* 448, pp. 2960–2970. DOI: 10.1093/mnras/stv192. arXiv: 1501.06811.

Candian, A., Kerr, T. H., Song, I.-O., et al. (2012). *Monthly Notices of the RAS* 426, pp. 389–397. DOI: 10.1111/j.1365-2966.2012.21760.x. arXiv: 1207.6990 [astro-ph.GA].

[¶] http://dx.doi.org/10.5281/zenodo.19108

Chiar, J. E. and Tielens, A. G. G. M. (2006). *Astrophysical Journal* 637, pp. 774–785. DOI: 10.1086/498406. eprint: astro-ph/0510156.

Chini, R., Elsaesser, H., and Neckel, T. (1980). *Astronomy and Astrophysics* 91, pp. 186–193.

Galliano, F., Madden, S. C., Tielens, A. G. G. M., et al. (2008). *Astrophysical Journal* 679, pp. 310–345. DOI: 10.1086/587051. arXiv: 0801.4955.

Hoffmeister, V. H., Chini, R., Scheyda, C. M., et al. (2008). *Astrophysical Journal* 686, pp. 310–324. DOI: 10.1086/591070.

Hony, S., Van Kerckhoven, C., Peeters, E., et al. (2001). *Astronomy and Astrophysics* 370, pp. 1030–1043. DOI: 10.1051/0004-6361:20010242. eprint: arXiv:astro-ph/0103035.

Houck, J. R., Roellig, T. L., van Cleve, J., et al. (2004). *Astrophysical Journal, Supplement* 154, pp. 18–24. DOI: 10.1086/423134. eprint: arXiv:astro-ph/0406167.

Hudgins, D. M. and Allamandola, L. J. (1999). *Astrophysical Journal, Letters* 516, pp. L41–L44. DOI: 10.1086/311989.

Hudgins, D. M., Bauschlicher Jr., C. W., and Allamandola, L. J. (2005). *Astrophysical Journal* 632, pp. 316–332. DOI: 10.1086/432495.

Hunter, J. D. (2007). *Computing In Science & Engineering* 9.3, pp. 90–95.

Joalland, B., Simon, A., Marsden, C. J., et al. (2009). *Astronomy and Astrophysics* 494, pp. 969–976. DOI: 10.1051/0004-6361:200810863. arXiv: 0811.2949.

Joblin, C., Tielens, A. G. G. M., Geballe, T. R., et al. (1996). *Astrophysical Journal, Letters* 460, p. L119. DOI: 10.1086/309986.

Jochims, H. W., Ruhl, E., Baumgartel, H., et al. (1994). *Astrophysical Journal* 420, pp. 307–317. DOI: 10.1086/173560.

Knorke, H., Langer, J., Oomens, J., et al. (2009). *Astrophysical Journal, Letters* 706, pp. L66–L70. DOI: 10.1088/0004-637X/706/1/L66.

Markwardt, C. B. (2009). In: *Astronomical Data Analysis Software and Systems XVIII*. Ed. by D. A. Bohlender, D. Durand, and P. Dowler. Vol. 411. Astronomical Society of the Pacific Conference Series, p. 251. arXiv: 0902.2850 [astro-ph.IM].

Martín-Hernández, N. L., Peeters, E., Morisset, C., et al. (2002). *Astronomy and Astrophysics* 381, pp. 606–627. DOI: 10.1051/0004-6361:20011504. eprint: astro-ph/0110653.

Moré, Jorge J. (1978). English. In: *Numerical Analysis*. Ed. by G.A. Watson. Vol. 630. Lecture Notes in Mathematics. Springer Berlin Heidelberg, pp. 105–116. ISBN: 978-3-540-08538-6. DOI: 10.1007/BFb0067700.

Pech, C., Joblin, C., and Boissel, P. (2002). *Astronomy and Astrophysics* 388, pp. 639–651. DOI: 10.1051/0004-6361:20020416.

Peeters, E. (2011). In: *IAU Symposium*. Ed. by J. Cernicharo and R. Bachiller. Vol. 280. IAU Symposium, pp. 149–161. DOI: 10.1017/S174392131102494X. arXiv: 1111.3680.

Peeters, E., Tielens, A. G. G. M., Allamandola, L. J., et al. (2012). *Astrophysical Journal* 747, 44, p. 44. DOI: 10.1088/0004-637X/747/1/44. arXiv: 1112.3386 [astro-ph.GA].

Peeters, E., Hony, S., Van Kerckhoven, C., et al. (2002). *Astronomy and Astrophysics* 390, pp. 1089–1113. DOI: 10.1051/0004-6361:20020773. eprint: arXiv:astro-ph/0205400.

Peeters, E., Bauschlicher Jr., C. W., Allamandola, L. J., et al. (2016). *Astrophysical Journal*. Submitted.

Povich, M. S., Stone, J. M., Churchwell, E., et al. (2007). *Astrophysical Journal* 660, pp. 346–362. DOI: 10.1086/513073.

Rapacioli, M., Calvo, F., Joblin, C., et al. (2006). *Astronomy and Astrophysics* 460, pp. 519–531. DOI: 10.1051/0004-6361:20065412. eprint: astro-ph/0609186.

Ricca, A., Bauschlicher Jr., C. W., Boersma, C., et al. (2012). *Astrophysical Journal* 754, 75, p. 75. DOI: 10.1088/0004-637X/754/1/75.

Rosenberg, M. J. F., Berné, O., Boersma, C., et al. (2011). *Astronomy and Astrophysics* 532, A128, A128. DOI: 10.1051/0004-6361/201016340. arXiv: 1106.5899 [astro-ph.GA].

Sellgren, K., Uchida, K. I., and Werner, M. W. (2007). *Astrophysical Journal* 659, pp. 1338–1351. DOI: 10.1086/511805. eprint: astro-ph/0612544.

Shannon, M. J., Stock, D. J., and Peeters, E. (2015). *Astrophysical Journal* 811, 153, p. 153. DOI: 10.1088/0004-637X/811/2/153. arXiv: 1508.04766.

Sheffer, Y. and Wolfire, M. G. (2013). *Astrophysical Journal, Letters* 774, L14, p. L14. DOI: 10.1088/2041-8205/774/1/L14. arXiv: 1309.3181 [astro-ph.GA].

Sloan, G. C., Lagadec, E., Zijlstra, A. A., et al. (2014). *Astrophysical Journal* 791, 28, p. 28. DOI: 10.1088/0004-637X/791/1/28. arXiv: 1406.7034 [astro-ph.SR].

Sloan, G. C., Hayward, T. L., Allamandola, L. J., et al. (1999). *Astrophysical Journal, Letters* 513, pp. L65–L68. DOI: 10.1086/311906. eprint: astro-ph/9902077.

Sloan, G. C., Jura, M., Duley, W. W., et al. (2007). *Astrophysical Journal* 664, pp. 1144–1153. DOI: 10.1086/519236. arXiv: 0705.0905.

Smith, J. D. T., Armus, L., Dale, D. A., et al. (2007a). *Publications of the ASP* 119, pp. 1133–1144. DOI: 10.1086/522634. arXiv: 0708.3745.

Smith, J. D. T., Draine, B. T., Dale, D. A., et al. (2007b). *Astrophysical Journal* 656, pp. 770–791. DOI: 10.1086/510549. eprint: arXiv:astro-ph/0610913.

Spoon, H. W. W., Marshall, J. A., Houck, J. R., et al. (2007). *Astrophysical Journal, Letters* 654, pp. L49–L52. DOI: 10.1086/511268. eprint: astro-ph/0611918.

Stock, D. J., Peeters, E., Tielens, A. G. G. M., et al. (2013). *Astrophysical Journal* 771, 72, p. 72. DOI: 10.1088/0004-637X/771/1/72. arXiv: 1305.5258 [astro-ph.GA].

Stock, D. J., Choi, W. D.-Y., Moya, L. G. V., et al. (2016). *Astrophysical Journal* 819, 65, p. 65. DOI: 10.3847/0004-637X/819/1/65. arXiv: 1601.07906.

Stock, D. J., Peeters, E., Choi, W. D.-Y., et al. (2014). *Astrophysical Journal* 791, 99, p. 99. DOI: 10.1088/0004-637X/791/2/99. arXiv: 1407.0702.

van der Zwet, G. P. and Allamandola, L. J. (1985). *Astronomy and Astrophysics* 146, pp. 76–80.

van Diedenhoven, B., Peeters, E., Van Kerckhoven, C., et al. (2004). *Astrophysical Journal* 611, pp. 928–939. DOI: 10.1086/422404. eprint: arXiv:astro-ph/0405098.

Van Kerckhoven, C., Hony, S., Peeters, E., et al. (2000). *Astronomy and Astrophysics* 357, pp. 1013–1019.

Walt, Stéfan van der, Schönberger, Johannes L., Nunez-Iglesias, Juan, et al. (2014). *PeerJ* 2, e453. ISSN: 2167-8359. DOI: 10.7717/peerj.453.

Wang, Z., Bovik, A. C., Sheikh, H. R., et al. (2004). *IEEE Transactions on Image Processing* 13, pp. 600–612. DOI: 10.1109/TIP.2003.819861.

Werner, M. W., Roellig, T. L., Low, F. J., et al. (2004). *Astrophysical Journal, Supplement* 154, pp. 1–9. DOI: 10.1086/422992. eprint: arXiv:astro-ph/0406223.

Xu, Y., Moscadelli, L., Reid, M. J., et al. (2011). *Astrophysical Journal* 733, 25, p. 25. DOI: 10.1088/0004-637X/733/1/25. arXiv: 1103.3139.

I made the last bit up.

DI Robert Lewis, Inspector Morse

4

Kicking up dust: peering into the Galactic bulge

M. J. Shannon, E. Peeters, J. Cami (2016). In preparation/to be submitted.

4.1 Introduction

PAHs are an extremely common family of astronomical molecules producing a variety of infrared emission features, most prominently between 3-20 μm, at (e.g.) 3.3, 6.2, 7.7, 8.6, 11.2, 12.7 and 16.4 μm. They are common in the interstellar medium and circumstellar environments, and as such most lines of sight are populated with PAH emission features (for a review see Tielens 2008 and references therein). Their emission characteristics are highly variable, changing in profile shape, absolute strength and *relative* strength between bands. These variations are linked to the physical conditions of their environments by the local radiation field, density of species, temperature, etc. (which determine PAH charge and structure, for example). By carefully studying the emission characteristics of the PAH bands we can infer properties of their surrounding environments.

PAH emission is weak in sight-lines with no illuminating source and thus hard to detect. Golriz et al. (2014) studied AGB stars in the Galactic bulge and identified PAH emission in background positions of their observations. The Galactic bulge consists mostly of an old (10 ± 2.5 Gyr) population of stars (Ortolani et al., 1995; Zoccali et al., 2003). Many of these stars are in the asymptotic giant branch (AGB) phase, or at the tip of the red giant branch (RGB) phase (e.g. Ojha et al. 2003; Omont et al. 1999 for the latitudes we observe) and have evolved

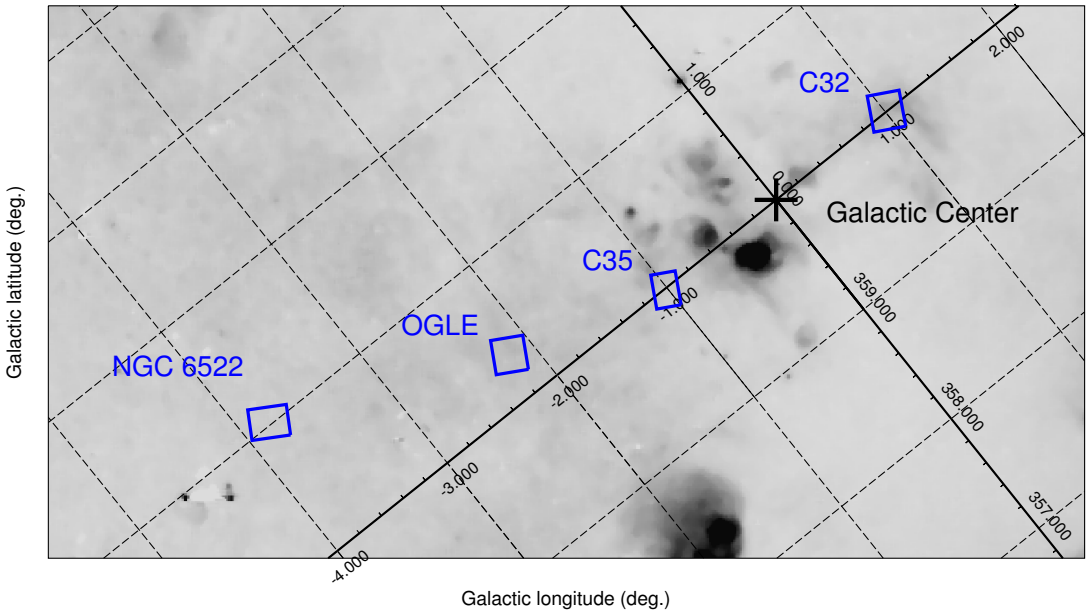

Figure 4.1: An overview of the Spitzer/IRS fields (labelled rectangles) overlaid on an Hα map from the Southern Hα Sky Survey Atlas (SHASSA; Gaustad et al. 2001). The tilt of the rectangles are determined by the spatial extent of the observations towards each field. The Galactic center is indicated by the black cross.

from a population of 1.5 - 2 $M_{\odot}$ stars (Blommaert et al., 2006; Groenewegen and Blommaert, 2005). To understand the origin(s) of the PAH emission, we present a mid- and far-infrared study of emission towards the Galactic bulge in four fields. In addition to characterizing the PAH emission, we study dust properties on these lines of sight by examining the FIR spectral energy distributions (SEDs). We also examine the molecular and atomic fine-structure lines to trace (e.g.) properties of the radiation field with a goal of determining the nature of emission toward the bulge. Our paper is organized in the following way: the observations and data reduction steps are presented in Sec. 4.2. Methods we employ to analyze our spectra are explained in Sec. 4.3.1. We present our results in Sec. 4.4 and discuss their implications in Sec. 4.5. A summary of our conclusions can be found in Sec. 4.6.

4.2 Observations and Data Reduction

4.2.1 Target selection and observations

Golriz et al. (2014) reported strong background emission, including PAH emission, towards the Galactic bulge in four fields (C32, C35, OGLE, NGC 6522), each containing multiple pointings. These fields lie at different projected distances to the Galactic bulge (Fig. 4.1). We will study the properties of these fields to understand the origin of the emission features.

The spectroscopic observations were acquired with the Infrared Spectrograph (IRS; Houck et al. 2004) on the *Spitzer* Space Telescope (Werner et al., 2004). These data were obtained from the NASA/IPAC *Spitzer* Heritage Archive.* The low-resolution ($R \sim 100$) data span approximately 5-40 μm, using the short low (SL) and long low (LL) modules. These data were previously analyzed by Golriz et al. (2014) for the purpose of studying bulge asymptotic giant branch (AGB) stars, which lie at the center of each aperture. However, we are only interested in the off-source emission. A summary of our observations is presented in Table 4.1, which is based on the sample of Golriz et al. (2014), their Table 1. Each field consists of multiple spectral maps, with corresponding unique identifiers, as illustrated in Figs. 4.2, 4.3, 4.4 and 4.5, for the fields of C32, C35, OGLE and NGC 6522, respectively. Our sample contains a total of 47 separate positions across these fields.

Photometric observations between 12 and 500 μm are included from three sources: first, from the *Herschel* Space Observatory (Pilbratt et al., 2010) infrared Galactic plane survey (Hi-GAL; Molinari et al. 2010), which observed the Galactic plane with the Photoconductor Array Camera and Spectrometer (PACS; Poglitsch et al. 2010) and Spectral and Photometric Imaging REceiver (SPIRE; Griffin et al. 2010). Second, we include photometric observations taken by the *AKARI* Space Telescope (Murakami et al., 2007) with its Far-Infrared Surveyor (FIS) instrument (Kawada et al., 2007), released as part of the *AKARI* all-sky survey maps (Doi et al., 2015). And third, we analyze images obtained by the Infrared Astronomical Satellite (IRAS), which were released via Improved Reprocessing of the IRAS Survey (IRIS; Miville-Deschênes and Lagache 2005). The photometric observations are summarized in Table 4.2. Measurements of the Hα emission toward the Galactic bulge were acquired from the Southern Hα Sky Survey Atlas (SHASSA; Gaustad et al. 2001).

Photometric calibration errors of the Hi-GAL photometric observations were estimated to be 5% for Herschel/PACS and 4% for Herschel/SPIRE (Molinari et al., 2016). For the IRIS sample of IRAS observations, the errors are approximately 15%, 18%, 11% and 20% for the 12, 25, 60 and 100 μm bands, respectively (Miville-Deschênes and Lagache, 2005). The AKARI photometric errors can be up to 20%, 30%, 40% and 40% for the 60, 90, 140 and 160 μm filters (Kawada et al., 2007).

4.2.2 Data reduction

The Spitzer/IRS data were reduced using the `CUBISM` tool (Smith et al., 2007a), starting with the basic calibrated data processed by the *Spitzer* Science Center (pipeline version S18.18). The `CUBISM` tool handles coaddition and bad pixel cleaning, creating full spectral cubes. Since we

*http://sha.ipac.caltech.edu/applications/Spitzer/SHA/

Table 4.1: Spitzer/IRS observations

ID	Object[a]	RA (J2000)	Dec. (J2000)	b (deg.)	l (deg.)	AOR key[b]
C32-1	J174117.5-282957	17:41:17.50	-28:29:57.5	1.037	359.874	10421504
C32-2	J174122.7-283146	17:41:22.70	-28:31:47.0	1.005	359.858	10421504
C32-3	J174123.6-282723	17:41:23.56	-28:27:24.2	1.041	359.922	10422784
C32-4	J174126.6-282702	17:41:26.60	-28:27:02.2	1.034	359.933	10421504
C32-5	J174127.3-282851	17:41:27.26	-28:28:52.1	1.016	359.908	10421504
C32-6	J174127.9-282816	17:41:27.88	-28:28:17.1	1.019	359.918	10421504
C32-7	J174128.5-282733	17:41:28.51	-28:27:33.8	1.024	359.929	10421504
C32-8	J174130.2-282801	17:41:30.15	-28:28:01.3	1.015	359.926	10422784
C32-9	J174134.6-282431	17:41:34.60	-28:24:31.4	1.032	359.984	10421504
C32-10	J174139.5-282428	17:41:39.48	-28:24:28.2	1.017	359.994	10421504
C32-11	J174140.0-282521	17:41:39.94	-28:25:21.2	1.008	359.982	10421504
C32-12	J174155.3-281638	17:41:55.27	-28:16:38.7	1.037	0.135	10421504
C32-13	J174157.6-282237	17:41:57.53	-28:22:37.7	0.977	0.055	10421504
C32-14	J174158.8-281849	17:41:58.73	-28:18:49.2	1.007	0.111	10421504
C32-15	J174203.7-281729	17:42:03.69	-28:17:29.9	1.003	0.139	10421504
C32-16	J174206.85-281832	17:42:06.86	-28:18:32.4	0.984	0.131	10421504
C35-1	J174917.0-293502	17:49:16.96	-29:35:02.7	-1.019	359.859	10421248
C35-2	J174924.1-293522	17:49:23.99	-29:35:22.2	-1.044	359.868	10421248
C35-3	J174943.7-292154	17:49:43.65	-29:21:54.5	-0.989	0.097	10421248
C35-4	J174948.1-292104	17:49:48.05	-29:21:04.8	-0.996	0.117	10421248
C35-5	J174951.7-292108	17:49:51.65	-29:21:08.7	-1.008	0.122	10421248
OGLE-1	J175432.0-295326	17:54:31.94	-29:53:26.5	-2.156	0.176	10422528
OGLE-2	J175456.8-294157	17:54:56.80	-29:41:57.4	-2.137	0.387	10422528
OGLE-3	J175459.0-294701	17:54:58.98	-29:47:01.4	-2.186	0.318	10422528
OGLE-4	J175511.9-294027	17:55:11.90	-29:40:27.8	-2.171	0.436	10423040
OGLE-5	J175515.4-294122	17:55:15.41	-29:41:22.8	-2.190	0.429	10423040
OGLE-6	J175517.0-294131	17:55:16.97	-29:41:31.9	-2.196	0.43	10423040
OGLE-7	J175521.7-293912	17:55:21.70	-29:39:13.0	-2.192	0.472	10423040
NGC 6522-1	J180234.8-295958	18:02:34.78	-29:59:58.9	-3.722	0.95	10421760
NGC 6522-2	J180238.8-295954	18:02:38.72	-29:59:54.6	-3.734	0.958	10421760
NGC 6522-3	J180248.9-295430	18:02:48.90	-29:54:31.0	-3.722	1.054	10422016
NGC 6522-4	J180249.5-295853	18:02:49.44	-29:58:53.4	-3.759	0.992	10422272
NGC 6522-5	J180259.6-300254	18:02:59.51	-30:02:54.3	-3.824	0.951	10421760
NGC 6522-6	J180301.6-300001	18:03:01.60	-30:00:01.1	-3.807	0.997	10422272
NGC 6522-7	J180304.8-295258	18:03:04.80	-29:52:59.3	-3.760	1.105	10422272
NGC 6522-8	J180305.3-295515	18:03:05.25	-29:55:15.9	-3.780	1.072	10421760
NGC 6522-9	J180305.4-295527	18:03:05.33	-29:55:27.8	-3.782	1.07	10422016
NGC 6522-10	J180308.2-295747	18:03:08.11	-29:57:48.0	-3.809	1.04	10422016
NGC 6522-11	J180308.6-300526	18:03:08.52	-30:05:26.5	-3.873	0.93	10421760
NGC 6522-12	J180308.7-295220	18:03:08.69	-29:52:20.4	-3.767	1.121	10421760
NGC 6522-13	J180311.5-295747	18:03:11.47	-29:57:47.2	-3.820	1.047	10421760
NGC 6522-14	J180313.9-295621	18:03:13.88	-29:56:20.9	-3.816	1.072	10422016
NGC 6522-15	J180316.1-295538	18:03:15.99	-29:55:38.3	-3.817	1.086	10422272
NGC 6522-16	J180323.9-295410	18:03:23.84	-29:54:10.7	-3.830	1.121	10422016
NGC 6522-17	J180328.4-295545	18:03:28.36	-29:55:45.4	-3.856	1.106	10421760
NGC 6522-18	J180333.3-295911	18:03:33.26	-29:59:11.5	-3.900	1.065	10422016
NGC 6522-19	J180334.1-295958	18:03:34.07	-29:59:58.8	-3.909	1.055	10421760

This table from (Golriz et al., 2014), their Table 1 (adapted). [a]References: Omont et al. (2003); Ojha et al. (2003); Blommaert et al. (2006). [b]The AORkey uniquely identifies *Spitzer* Space Telescope observations.

Table 4.2: Photometric observations

Observatory	Instrument	Nominal filters	Data origin	Data references
Herschel Space Observatory	PACS, SPIRE	70, 160, 250, 350, 500 μm	Hi-GAL	1
AKARI	FIS	60, 90, 140, 160 μm	All-sky survey maps	2
Infrared Astronomical Satellite (IRAS)		12, 25, 50, 100 μm	IRIS	3
Cerro Tololo Inter-American Observatory		656 nm	SHASSA	4

References: (1) Hi-GAL: The *Herschel* Infrared Galactic Plane Survey (Molinari et al., 2010); (2) *AKARI* Far-Infrared All-Sky Survey Maps (Doi et al., 2015); (3) IRIS: Improved Reprocessing of the *IRAS* Survey (Miville-Deschênes and Lagache, 2005); (4) SHASSA: Southern Hα Sky Survey Atlas (Gaustad et al., 2001).

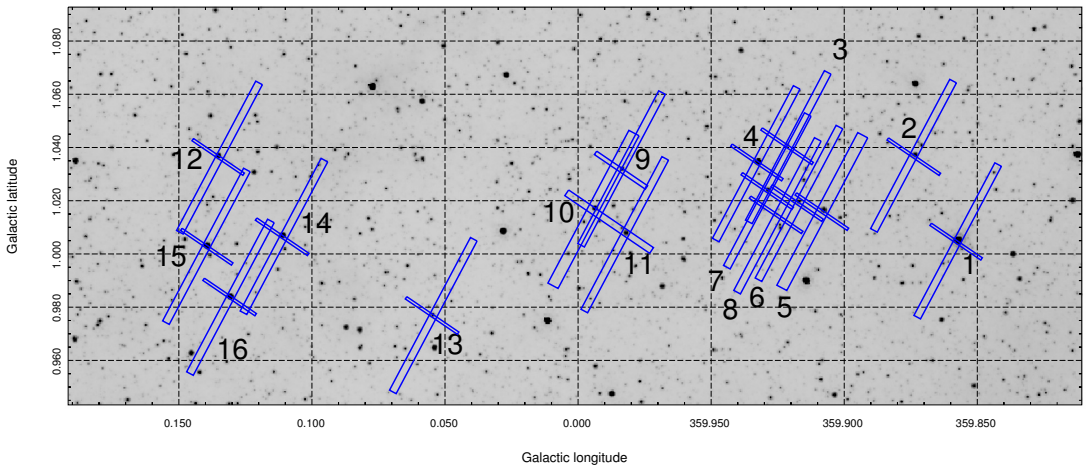

Figure 4.2: The IRS apertures for C32 are overlaid on an IRAC 8 μm image. The numbered labels correspond to the overlapping SL and LL apertures (the short and long blue rectangles, respectively), e.g. C32-1 (c.f. Table 4.1).

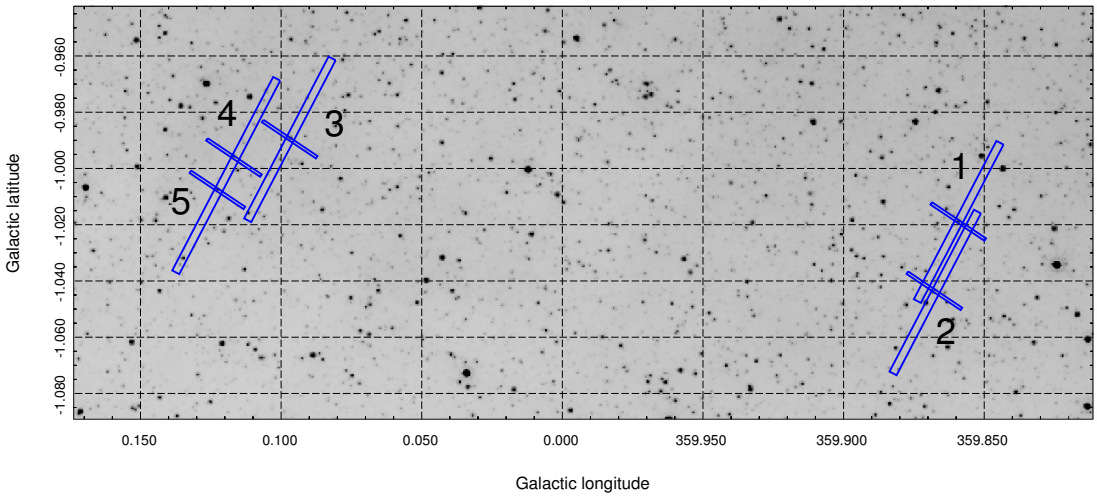

Figure 4.3: The IRS apertures for C35 are overlaid on an IRAC 8 µm image. The numbered labels correspond to the overlapping SL and LL apertures (the short and long blue rectangles, respectively), e.g. C35-3 (c.f. Table 4.1).

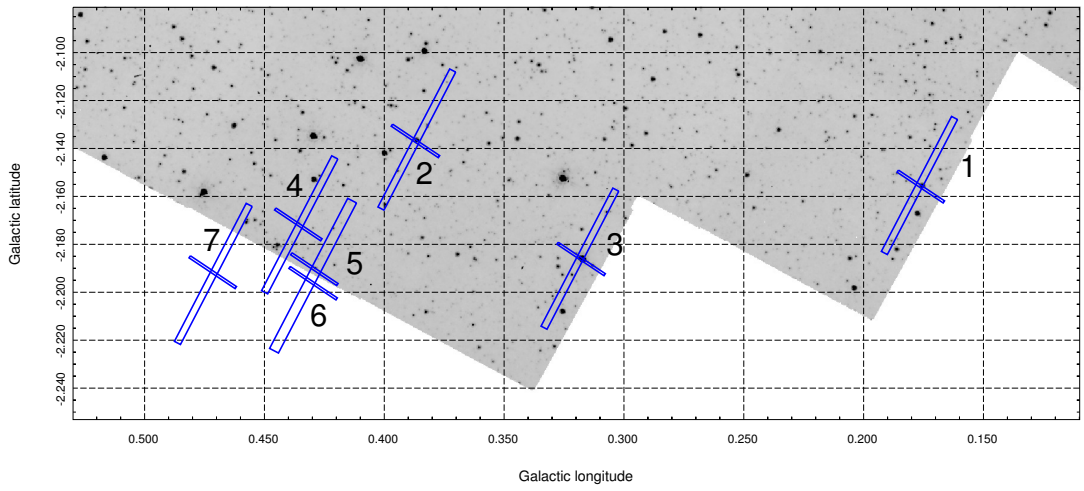

Figure 4.4: The IRS apertures for OGLE overlaid on an IRAC 8 µm image.The numbered labels correspond to the overlapping SL and LL apertures (the short and long blue rectangles, respectively), e.g. OGLE-3 (c.f. Table 4.1).

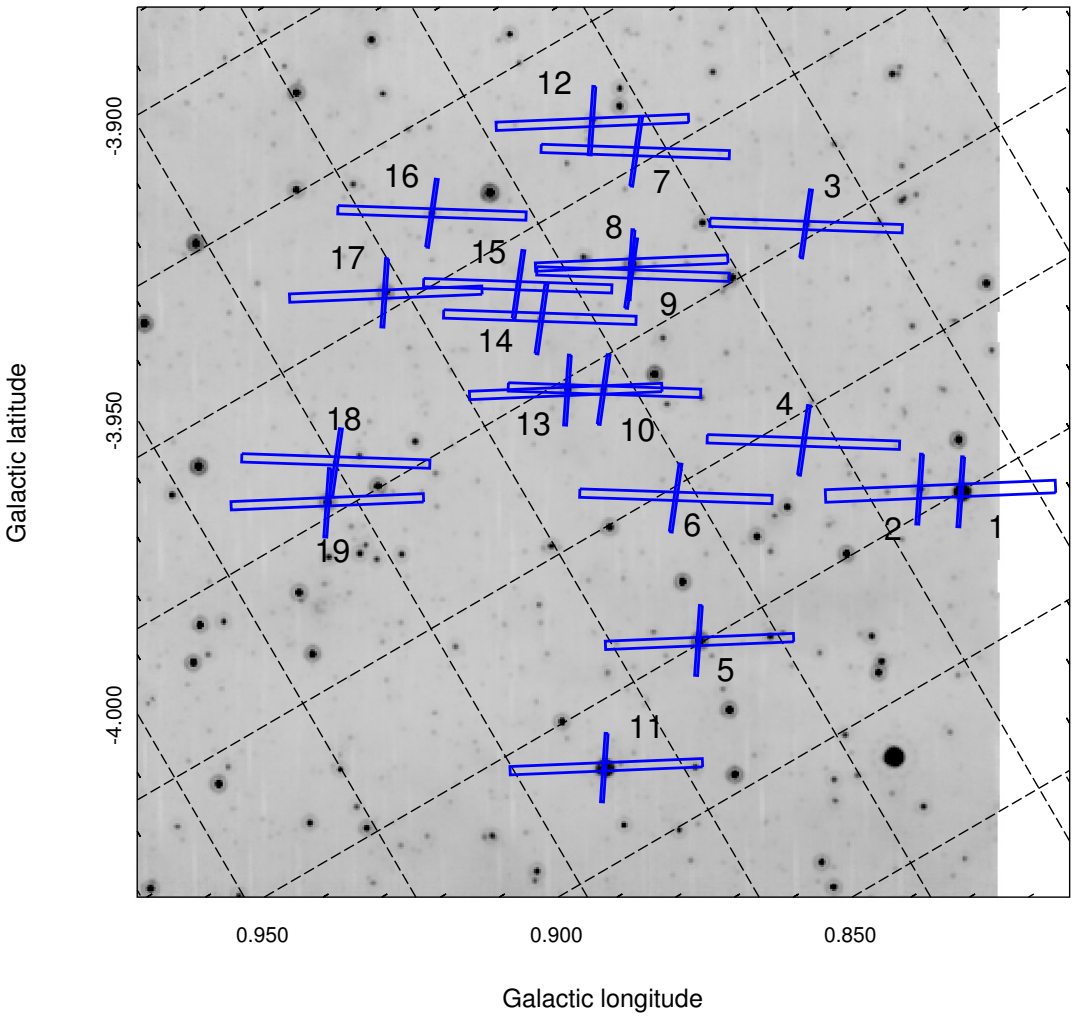

Figure 4.5: The IRS apertures for NGC 6522 overlaid on a 24 µm *Spitzer* image acquired with the Multiband Imaging Photometer for Spitzer (MIPS; Rieke et al. 2004). The numbered labels correspond to the overlapping SL and LL apertures (the short and long blue rectangles, respectively), e.g. NGC 6522-1 (c.f. Table 4.1).

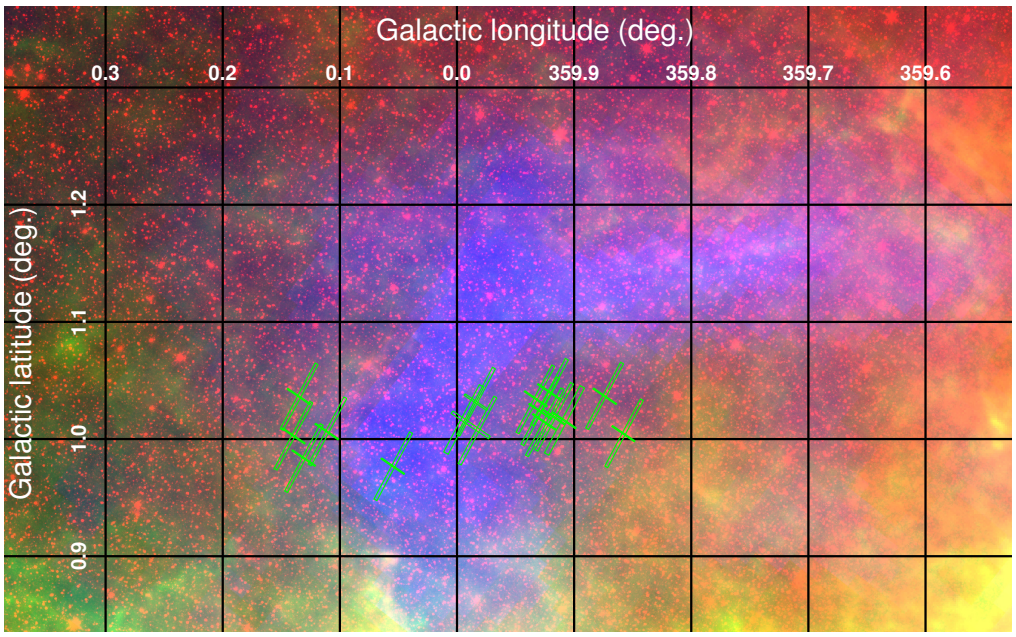

Figure 4.6: A composite image of C32, constructed with images from Spitzer/IRAC 8 µm (red), Herschel/SPIRE 250 µm (green) and 656 nm Hα emission (blue). The green rectangles identify the SL and LL apertures (less elongated and more elongated, respectively; c.f. Fig. 4.2 and Table 4.1 for identifications). An elevated Hα emission zone (or channel) that bisects the IRS apertures is visible.

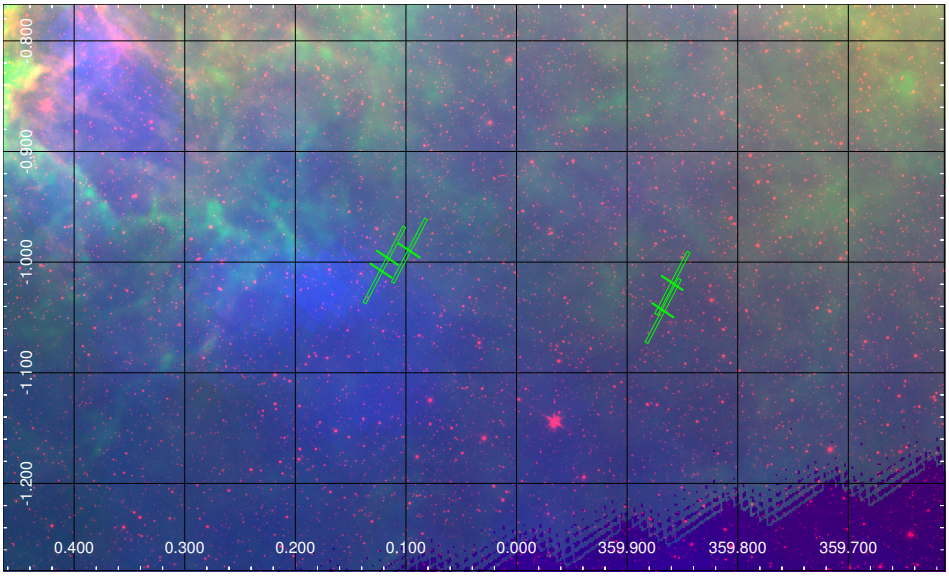

Figure 4.7: A composite image of C35, with Galactic longitude (in degrees) on the x axis and Galactic latitude (in degrees) on the y axis. The image is composed of emission from Spitzer/IRAC 8 µm (red), Herschel/SPIRE 250 µm (green) and 656 nm Hα (blue). The leftmost C35 pointings (corresponding to positions C35-3, C35-4 and C35-5) are coincident with elevated an Hα emission region or channel (c.f. Fig 4.3).

were interested in the background (off-star) emission, no further reduction was done, apart from identifying cosmic ray spikes or bad pixels not previously identified. The slits were rebinned with a 2 × 2-pixel aperture to match the point-spread function of IRS and thus remove non-independent (adjacent) pixels. Additional details of this approach are described by Peeters et al. (2012). The photometric data were retrieved fully processed and no further reduction was necessary.

4.2.3 Aperture overlap

The IRS/SL and IRS/LL apertures are oriented such that they are perpendicular to each other on the sky, and thus the intended astronomical target would lie at their intersection. Since we are interested in the background emission in the IRS observations, we cannot measure the SL and LL spectra at the same spatial position, and so there must be an offset. After combining nod positions, each SL aperture in our observations typically spans 83″, while the LL apertures cover 233″. The maximum separation between SL and LL pointings is thus approximately 118″, with mean separations near 59″. We thus analyzed our spectra in two ways: first, we measured the median spectra in each module (avoiding the stellar emission zone), and stitched the median components together to produce a single full spectrum from 5-38 μm; and second, we analyzed the SL and LL spectra entirely independently. No systematics were identified when comparing the separate spectra to the fully stitched median spectra, and thus we use the latter to represent the astronomical background emission for each pointing. It should be noted that some of the positions in each field are close enough to their neighbors such that the (e.g.) SL aperture of one position may overlap the LL aperture of another. However, we are interested in the general behaviour of the spectra in the fields, rather than small position-to-position variations. Instead we use apertures that are tightly clustered to verify consistency in our results. In C32 and C35, calibration offset between the SL and LL modules (and its sub-orders SL1, SL2, LL1 and LL2) are within the calibration uncertainties of the instrument. In the OGLE and NGC 6522 fields, however, a large jump is observed between the SL and LL modules in most of the positions. In all positions, the individual LL1 and LL2 orders are well matched, but the SL1 and SL2 orders generally are not. Because of this, we do not scale the SL and LL modules in OGLE and NGC 6522, and therefore treat the < 15 μm emission in these fields as unreliable in most of the pointings.

4.3 Spectral properties and analysis

Many PAH emission features are present in the spectra, including bands at 6.2, 7.7, 8.6, 11.2, 12.7, 16.4, 17.4 and 17.8 μm (see Fig. 4.8). Weaker PAH emission at 12.0 μm, 15.8 μm and

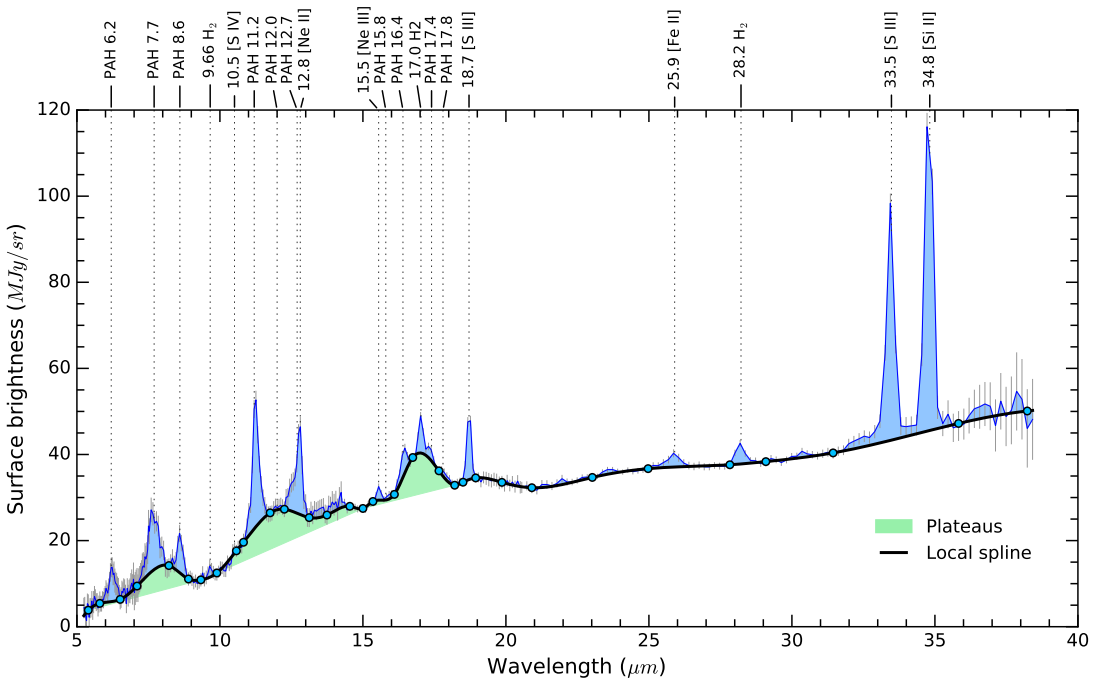

Figure 4.8: The median spectrum of C32-1. The thick black curve is the local spline continuum. The separation between the spline continuum and the thin gray (quasi-linear) curve defines the 5-10, 10-15 and 15-18 μm plateaus (shaded green; see Section 4.3.1). The prominent emission features are identified with dotted vertical lines.

possibly 14.0 μm may also be present. A smoothly increasing dust continuum is apparent below the individual emission bands, as are broad plateaus between 5-10 μm, 10-15 μm and 15-18 μm. Atomic emission lines are present, such as 12.8 μm [Ne II], 15.5 μm [Ne III], 18.7 μm [S III], 25.9 μm [Fe II], 33.5 μm [S III] and the 34.8 μm [Si II] line. H_2 emission is also identified at 17.0 μm and 28.2 μm.

4.3.1 Analysis methods

To measure the band and line fluxes, the emission features in each spectrum were isolated from the underlying continuum by fitting a local spline continuum (Fig. 4.8). The spline is constructed by fitting a series of anchor positions at locations where only continuum emission is expected. This is a common approach in the literature for measuring the strengths of the PAH emission features (e.g. Galliano et al. 2008; Hony et al. 2001; Peeters et al. 2002; Van Kerckhoven et al. 2000). Other possible analysis methods include fitting Drude profiles (PAHFIT; Smith et al. (2007b)) or Lorentzian profiles (Boulanger et al., 1998; Galliano et al., 2008; Smith et al., 2007b). Galliano et al. (2008) showed that the inferred PAH fluxes vary with method, but the overall trends are consistent.

The continuum-subtracted spectra are analyzed in a few ways: the PAH features are directly integrated, except for the 11.0 and 12.7 μm bands, which are blended with the 11.2 μm emission and the 12.8 μm [Ne II] line, respectively. There may also be 12.3 μm H_2 emission blended with the PAH emission. The H_2 emission, 12.7 μm PAH band and the 12.8 μm [Ne II] line are separated by fitting a template for the PAH emission (for details see Stock et al. 2014 and Shannon, Stock, and Peeters 2015). The 11.0 μm emission is fit with a gaussian while fixing the overlapping shape of the 11.2 μm band profile. The other atomic and molecular lines are fit with Gaussians whose widths are fixed to the instrument's spectral resolution.

A common method for estimating the plateau strengths is to fit straight lines between the continuum emission at 5, 10, 15 and 18 μm (Peeters et al., 2012). The difference between this curve and the local spline defines the plateau regions, which are then directly integrated (Fig. 4.8).

4.4 Results

4.4.1 Composite images

We constructed composite 3-color images of C32 and C35 (Figs. 4.6 and 4.7, respectively). Each composite is constructed of images from *Spitzer*/IRAC (8 μm), *Herschel*/SPIRE (250 μm) and the SHASSA Hα survey (656 nm). In C32, there appears to be a region of elevated Hα emission (or "channel") that bisects the IRS apertures. The 8 μm and 250 μm emission appears to peak on either side of this region. A similar elevated Hα region/channel is apparent in C35 (Fig. 4.7), coincident with positions 3, 4 and 5, and with accompanying inhomogeneities in the 8 and 350 μm emission. There was insufficient coverage to prepare similar figures for OGLE and NGC 6522.

4.4.2 The spectra

Median spectra for each position in the four fields (C32, C35, OGLE, NGC 6522) are shown in Fig. 4.9. C32 (Fig. 4.9a) displays remarkably similar spectra across the sixteen apertures, both in overall continuum shape and individual emission features. Continuum deviations between positions are typically less than 5 MJy/sr on ∼20-40 MJy/sr continua. The PAH features and plateaus appear to be similar in strength and shape across all positions. Only the atomic fine-structure lines show significant variations in C32, as the 18.7 μm [S III], 33.5 μm [S III] and 34.8 μm [Si II] emission lines vary by a factor of approximately two in peak intensity. The 25.9 μm [Fe II] line is also visible, which is typically a tracer of shocked gas (van den Ancker et al., 1999).

The C35 spectra (Fig. 4.9b) are very similar in appearance to the spectra of C32. The only spectral differences within the C35 field are variations in their continuum shape past $\sim$ 25 μm, with position 2 being slightly flatter than the other positions. The 25.9 μm [Fe II] line is again present.

The OGLE spectra (Fig. 4.9c) display a strong jump between modules SL and LL (near $\sim$ 14.5 μm) in some positions (see Section 4.2.3). Beyond 15 μm all spectra within the field have comparable continua, typically of surface brightness ∼24 MJy/sr. The overall shapes of the OGLE spectra are quite distinct from those of the C32 and C35 fields however: these spectra are essentially flat past 20 μm, whereas the C32 and C35 continua were still rising, suggesting different dust properties between the fields. In the OGLE spectra, the PAH features are still visible, though some are weak and/or difficult to detect above the noise (e.g. the 12.7 μm feature in C35-6). There is clear 11.2 μm emission in several of the C35 positions. The 15-20 PAH emission is also distinct from that seen towards the C32 and C35 fields. Such emission has been observed before by Van Kerckhoven et al. (2000) and Peeters et al. (2006).The 25.9 μm [Fe II] emission line is also detected in this field, along with the other previously discussed H_2, neon and sulphur emission lines.

The overall shape of the NGC 6522 spectra (Fig. 4.9d) is significantly different from those of other fields. Though the continuum reaches a peak surface brightness of $\sim$ 25 MJy/sr (similar to the OGLE continua), the continuum declines past 25 μm, by as much as 20% by 38 μm. The spectra are very noisy and show almost no PAH emission features, apart from possibly very weak 7.7 and 11.2 μm bands in some positions. However, the 15-20 μm plateau is present and very strong in NGC 6522. The 33.5 μm [S III] and 34.8 μm [Si II] lines are also present.

We compare all four fields, overlaid, in Fig. 4.10, with a single median spectrum being constructed from all positions in each field. The C32 and C35 spectra (which are at 1°N and 1°S Galactic latitude, respectively) are extremely similar, differing only in the strength of their atomic fine-structure lines and possibly the continuum near 12-14 μm. The NGC 6522 and OGLE fields are also well-matched, with the NGC 6522 emission being slightly brighter in the 20-25 μm range, and declining towards 38 μm.

4.4.3 Variability of the emission features

We measured all of the emission features in the median spectra and tabulated the results (Section AB.1 in the Appendix). We present the full set of corresponding spectral maps for C32 and C35 in the Appendix (Figs. B.1, B.2, B.3 and B.4). Due to the limited number of reliable measurements in the OGLE and NGC 6522 fields (c.f. Tables B.1 and B.2) no such figures are

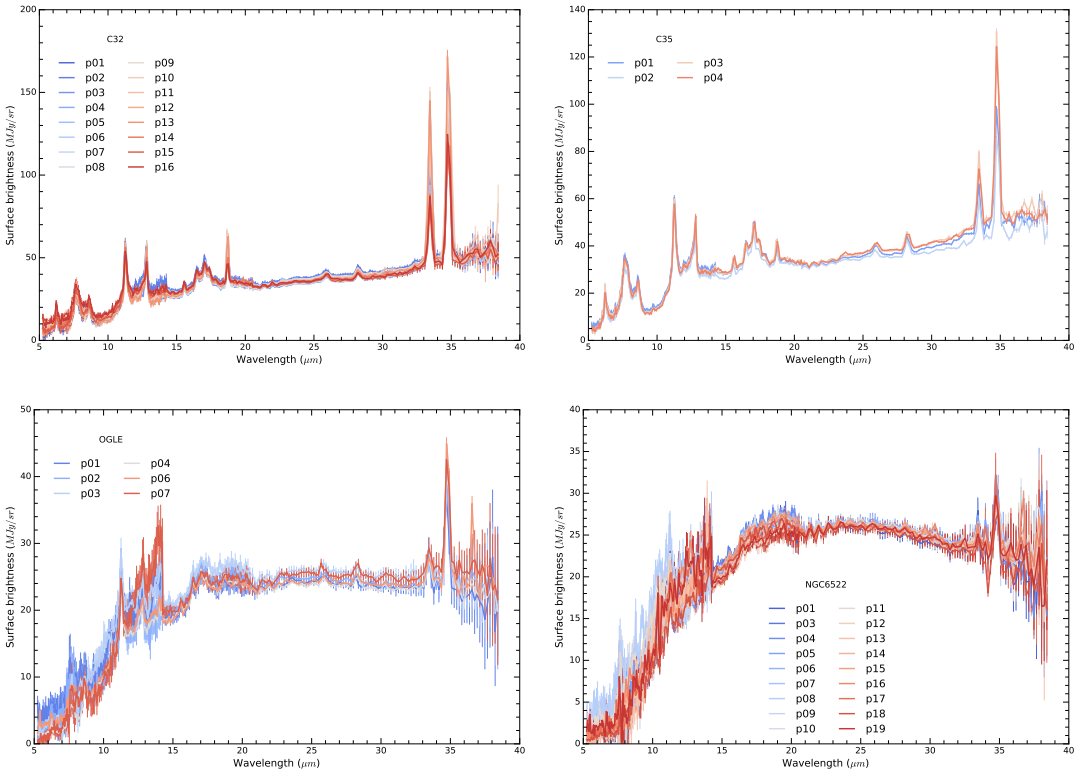

Figure 4.9: Spectra for C32, C35, OGLE and NGC6522 are shown in panels (a), (b), (c) and (d), respectively. These spectra were created by stitching the emission from the SL and LL modules, which are not necessarily spatially coincident (see Section 4.2.3), and taking a median over all positions in each field. The colors and inset labels indicate individual positions (see Table 1 of Golriz et al. 2014).

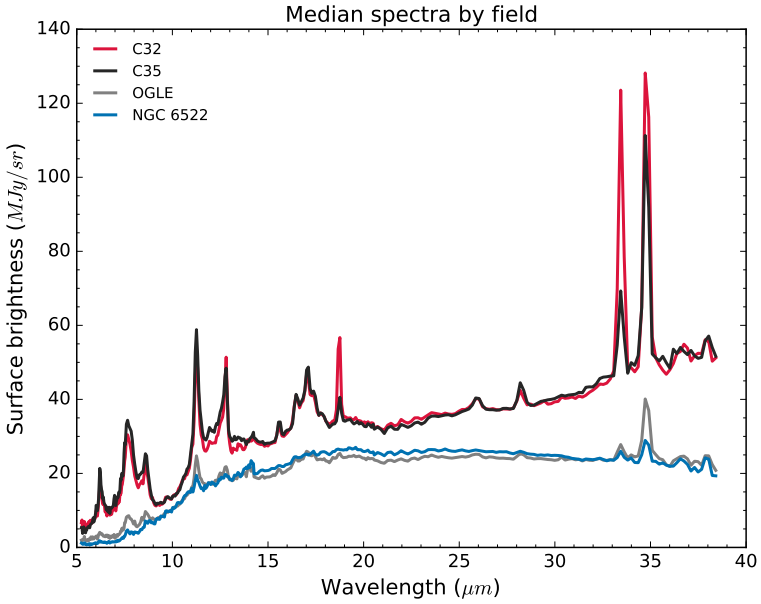

Figure 4.10: A comparison of the median spectra in each field. The C32 and C35 spectra are exceedingly similar in all but the atomic fine-structure lines, as is the OGLE/NGC 6522 pair.

prepared for these sources.

We examine select emission features in C32 in Fig. 4.11. The 7.7 and 11.2 μm PAH bands are weakest in the central part of the C32 field (near the apertures of C32-9, C32-10 and C32-11), and peak towards the outer regions (corresponding to C32-2 and C32-12, roughly; c.f. Fig. 4.2). Conversely, the fine-structure lines all peak in the central part of the map, suggesting an anti-correspondence (e.g. the 18.7 μm [S III] emission). Taking into account the RGB image of C32 (Fig. 4.6), there is a correspondence with the elevated Hα emission region: where the Hα emission is strong, the atomic lines are brightest and PAH bands are weakest. The 25.9 μm [Fe II] emission has no 3σ detection where the Hα emission is strong, but instead it peaks strongly on either side of the Hα channel (in this projection). The 12.8 μm [Ne II] line is detected throughout C32, with extremely strong variations near the Hα channel: the emission is three times brighter in the Hα channel than it is in the neighbouring cluster on the left (positions 12, 14, 15 and 16). The 15.5 μm [Ne III] line is much less variable, and is only detected in the central part of the field (in five positions). The [Ne III]/[Ne II] flux ratio shows no monotonic trend, suggesting systematic issues with the measurements of one or both of these lines may be present in our analysis. Turning to the 17.0 μm H_2 emission, the line is weakest in the Hα channel and strongest in the far right part of the field (near C32-1), furthest from the channel.

We prepare a similar figure for C35 (Fig. 4.12), with the full set of maps located in the Ap-

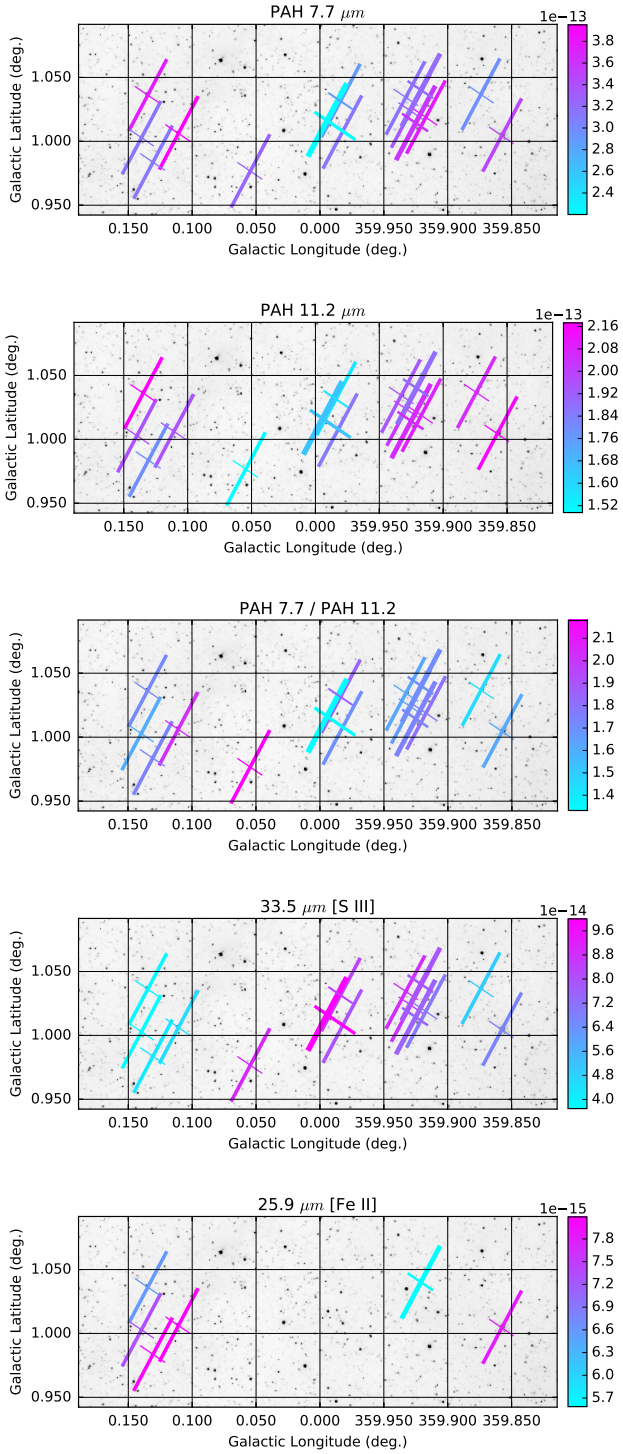

Figure 4.11: Maps of select emission band fluxes in the C32 fields, averaged over each position and in units of $\mathrm{MWm^{-2}/sr}$. From top to bottom: the 7.7 µm PAH band, the 11.2 µm PAH band, the PAH 7.7/11.2 flux ratio, the 33.5 µm [S iii] line, and the 25.9 µm [Fe ii] line. The sulphur fine-structure line peaks in the central part of the map, where the PAH emission is generally weakest (roughly coincident with the elevated Hα emission; see Figs. 4.2 and 4.6). Similar figures for the other PAH bands and atomic/molecular lines are found in Figs. B.1 and B.2, respectively.

pendix (Figs. B.3 and B.4). This field has only five positions, so our ability to trace smooth variations is limited. What is clear however is that positions 3, 4 and 5, which are coincident with the elevated Hα emission (Fig. 4.3), have elevated fine-structure line emission relative to positions 1 and 2. The PAH emission is relatively flat across the field, though perhaps slightly higher in the Hα channel (positions 3, 4 and 5). The channel positions also display a $\sim$10% higher PAH 7.7/11.2 μm flux ratio. The 17.0 μm H_2 emission is also generally greater towards positions 3, 4 and 5, which is opposite behaviour from that of C32.

The OGLE and NGC 6522 spectra are generally too noisy for this type of analysis, though the 34.8 μm [Si II] emission is well detected. In OGLE, its emission peaks strongly at position OGLE-7. In NGC 6522 the silicon emission is essentially flat across the field, apart from NGC 6522-1, though uncertainties are quite high.

4.4.4 PAH flux ratio correlations

A common method for identifying systematic variations in PAH populations is to evaluate band flux ratios (e.g. Galliano et al. 2008). In Fig. A.3 we examine the emission strengths of the 6.2 and 7.7 μm PAH bands, using the 11.2 μm band as a normalization factor. A weak correlation is observed (with weighted Pearson correlation coefficient $r = 0.47$ in C32). The data generally span a range in 6.2/11.2 of 0.5-1.2 in C32, 0.9-1.0 in C35, and 0.4-0.6 in OGLE. Peeters et al. (2016) analyzed spectral maps of the reflection nebula NGC 2023 and found a high correlation coefficient between the 6.2 and 7.7 μm bands ($r > 0.97$). We plot their line of best fit for comparison (Fig. A.3). Our data generally exhibit lower 6.2/11.2 flux ratios than in NGC 2023, with the C32 and C35 measurements roughly consistent with an extrapolation of the best fit line towards lower values. We perform a similar comparison with best fits for W49A, a large star-forming region (Stock et al., 2014). We include best fit lines for their ultra-compact H II regions, as well as their entire sample (which includes diffuse sight-lines; see their paper for details), both of which have correlation coefficients $r > 0.8$. The W49A 6.2/11.2 flux ratios reach the low values that we observe in our sample ($\sim$0.6), a factor of two smaller than the lowest ratios observed in NGC 2023. The generally weak correlation of the 6.2 and 7.7 μm bands in our fields toward the Galactic bulge suggests that we are not probing a wide variety of environmental conditions, particularly in C32 which has many positions and bright PAH features.

4.4.5 Correlations in the entire sample

We also investigate correlations between all measured PAH bands, plateaus, atomic and molecular emission lines and continuum strengths (measured near 10 and 15 μm). We apply a hier-

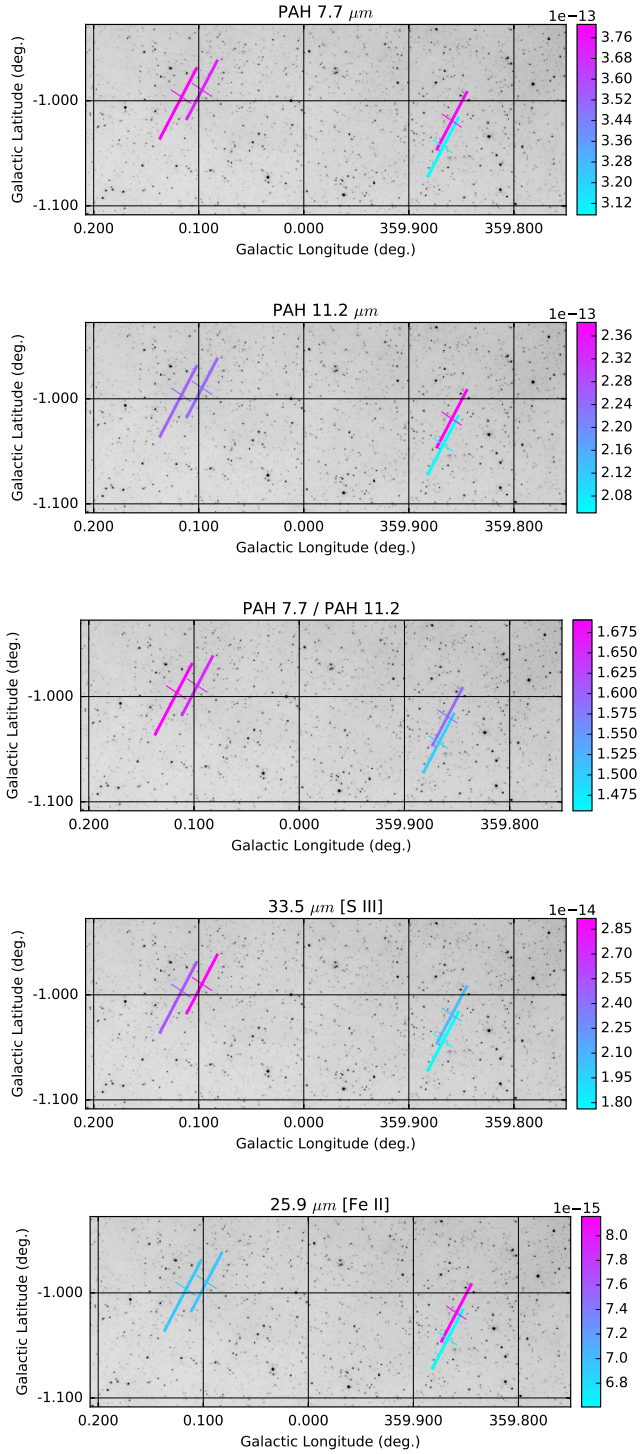

Figure 4.12: Maps of select emission band fluxes in the C35 fields, averaged over each position and in units of $\mathrm{MWm}^{-2}/\mathrm{sr}$. From top to bottom: the 7.7 µm PAH band, the 11.2 µm PAH band, the PAH 7.7/11.2 flux ratio, the 33.5 µm [S iii] line, and the 25.9 µm [Fe ii] line. The PAH emission varies weakly across the field, while the fine-structure lines are significantly stronger towards the left in this orientation–where elevated Hα emission is present (positions 3, 4 and 5; see Figs. 4.3 and 4.7). We present similar figures for the other PAH bands and atomic/molecular lines in Figs. B.3 and B.4, respectively.

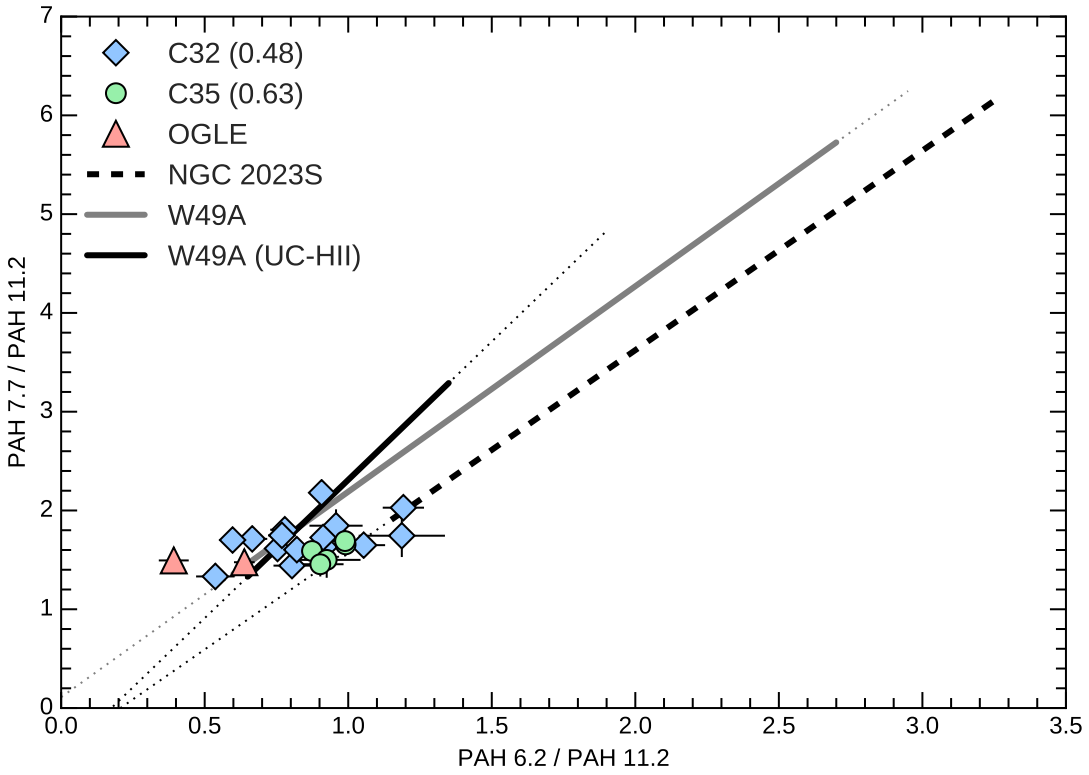

Figure 4.13: Flux correlations between the 6.2 and 7.7 μm PAH bands, normalized to the 11.2 μm PAH emission, for C32 (blue diamonds), C35 (green circles) and OGLE (red triangles). In parentheses is the weighted Pearson correlation coefficient for each field (omitted if fewer than 3 data points). The lines shown are lines of best fit from *different* data sets: the dashed black line for NGC 2023 (Peeters et al. 2016), the solid gray line for W49A (Stock et al., 2014), and the solid black line for ultracompact HII regions in W49A (Stock et al., 2014). The extents of the solid lines indicate the range in the data from which they were originally determined. Extrapolations of these best fits are shown with the light dotted lines.

archical clustering algorithm to our measurements and present five groupings. Note the 16.4 μm band is an outlier and does not fall within any grouping. The quantities listed below are in the same order as in the correlation matrix (Fig. 4.14) for easy comparison:

- Group 1 - 18.7 μm [S III], 33.5 μm [S III], 12.8 μm [Ne II], 34.8 μm [Si II]
- Group 2 - 17.0 and 28.2 μm H_2, 5-10 μm plateau, PAH 11.2 μm, 10-15 μm plateau
- Group 3 - 10 and 15 μm continua, 15-18 μm plateau, 15.5 μm [Ne III], 25.9 μm [Fe II]
- Group 4 - PAH 17.4, 17.8
- Group 5 - PAH 12.7, 8.6, 6.2 and 7.7 μm
- Outlier - PAH 16.4 μm

The members of group 1 are highly correlated and are all fine-structure lines originating in ionized gas with comparable ionization potentials (∼16-23 eV). These lines do not correlate with any other measured quantity in our analysis.

Group 2 consists of features that generally correlate well with each other and are anti-correlated with group 1. The 11.2 μm band is typically associated with large PAHs, which may explain its inclusion (see, e.g. Peeters et al. (2012)).

Group 3 is somewhat peculiar. It contains the continuum strengths at 10 and 15 μm, the 15-18 μm plateau and the 25.9 μm [Fe II] and 15.5 μm [Ne III] lines. Ne II requires ∼41 eV to become doubly ionized, so the presence of the [Ne III] line here is unexpected.

Group 4 only contains the 17.4 and 17.8 μm PAH emission. They are both subject to systematic errors based on how the 15-18 μm continuum is drawn, so their pairing is expected. The lack of the 16.4 μm band in this group is perplexing. The 16.4 μm emission only displays a very weak correlation (r∼0.3) with the 15 μm continuum and 25.9 μm [Fe II] line.

Finally, group 5 consists of the 6.2, 7.7, 8.6 and 12.7 μm PAH bands. These can be understood as ionized PAH bands, particularly the 6-9 μm emission, while the 12.7 μm band is associated with a mixture of neutral and cationic states (see, e.g., Boersma, Bregman, and Allamandola 2014; Shannon, Stock, and Peeters 2016). The 12.7 μm band has the weakest correlation with the other members of this group.

4.4.6 Spectral energy distributions

Using our photometric images, we constructed spectral energy distributions (SEDs) for each of our fields. This was accomplished by sampling the surface brightness of the photometric

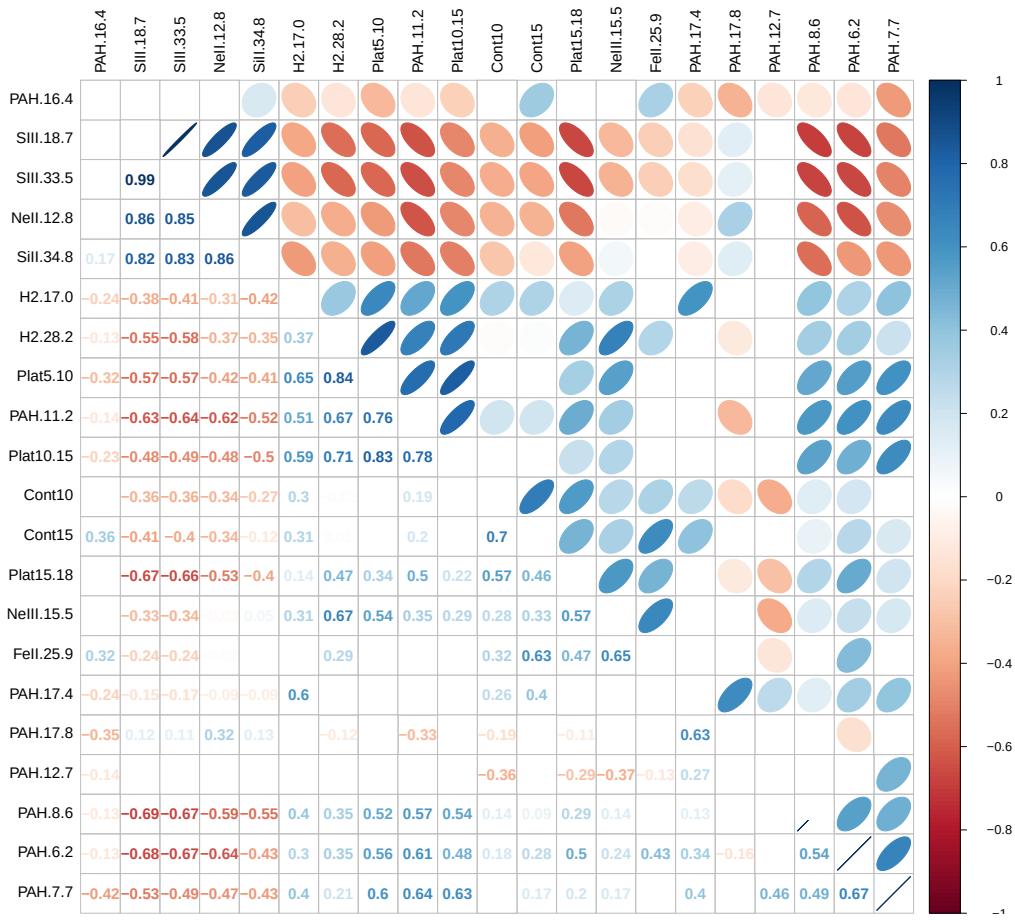

Figure 4.14: Correlation matrix for all quantities measured in the spectra of C32 and C35: PAH band fluxes, atomic and molecular emission line fluxes, plateau strengths, and continuum strengths (see Section 4.4.5 for details). The matrix is symmetric, with the Pearson R correlation coefficient presented in the lower half. The upper half is a representation of the correlation coefficient with color-coded ellipses: positive correlations are blue and oriented 45° clockwise of vertical, negative correlations are red and oriented 45° counter-clockwise of vertical. The linear eccentricity of each ellipse is proportional to its corresponding correlation coefficient, i.e. ellipses with coefficients closer to 1 or -1 are closer to lines than circles. Insignificant correlations ($\sigma = 0.2$) are blank. The quantities are ordered based on groupings via a hierarchical clustering algorithm (see Sec. 4.4.5).

observations at each pixel in our *Spitzer*/IRS apertures in the following way: if the IRS pixels were entirely contained within a larger pixel of the photometric images, the corresponding surface brightness was adopted; if any IRS pixel overlapped multiple photometric pixels, the mean surface brightness was measured. In no cases were the IRS pixels larger than the spatial resolution of the photometric images.

Fig. 4.15 displays the resulting SEDs for the 16 pointings toward C32 and the four pointings toward C35. With no *Herschel* Hi-GAL photometric measurements of OGLE and NGC 6522, we exclude these sources, since we lack > 200 μm photometry.

Most of the C32 photometric measurements are consistent (particularly with the neighboring measurements, e.g. *AKARI* 60 μm and *Herschel* 70 μm), with the stark exception of the measurements near 160 μm. Specifically, the *AKARI* photometry at 140 and 160 μm are (approximately) twice the surface brightness of the *Herschel*/PACS 160 μm measurement. The origin of the discrepancy is likely due to the greater calibration uncertainty on the *AKARI* measurements. The *IRAS*, *AKARI* and *Herschel* measurements all agree at the shorter wavelengths (< 100 μm). For the purpose of this analysis, we constructed each SED in two ways: first, with the *AKARI*/FIS measurements at 140 and 160 μm; and second, with the *Herschel*/PACS measurement at 160 μm. All other measurements are uncontroversial and included to construct the SED.

There is little variation in the C32 photometric measurements between different positions at short wavelengths (< 60 μm) and at long wavelengths (350, 500 μm; note however that the coverage of the 350 μm image is limited, and thus the 350 μm emission could not be measured at all positions). In the $60 - 250$ μm range, surface brightnesses vary between individual C32 positions, sometimes as much as 50%. The *Herschel* and *AKARI* measurements (except for the 160 μm filter) show that the C32-1 position is consistently the brightest in the field. This is also true in the *IRAS* measurements, though there is less variation between positions in these data (possibly due to its larger spatial resolution, relative to *AKARI* and *Herschel*).

In general, C35 shows the same trends as C32: consistent measurements between the three observatories, apart from the $\sim$160 μm discrepancy, and variations in surface brightness within the field in the $60 - 250$ μm range. Perhaps the most striking feature is that positions C35-1 and C35-2 tend to cluster together in surface brightness, while positions C35-3 and C35-4 do the same but at higher overall brightnesses. Positions 3 and 4 are coincident with elevated Hα emission (Fig. 4.3), which suggests that environmental conditions vary across the C35 field. We already observed such a clustering in the spectral maps (Fig. 4.12).

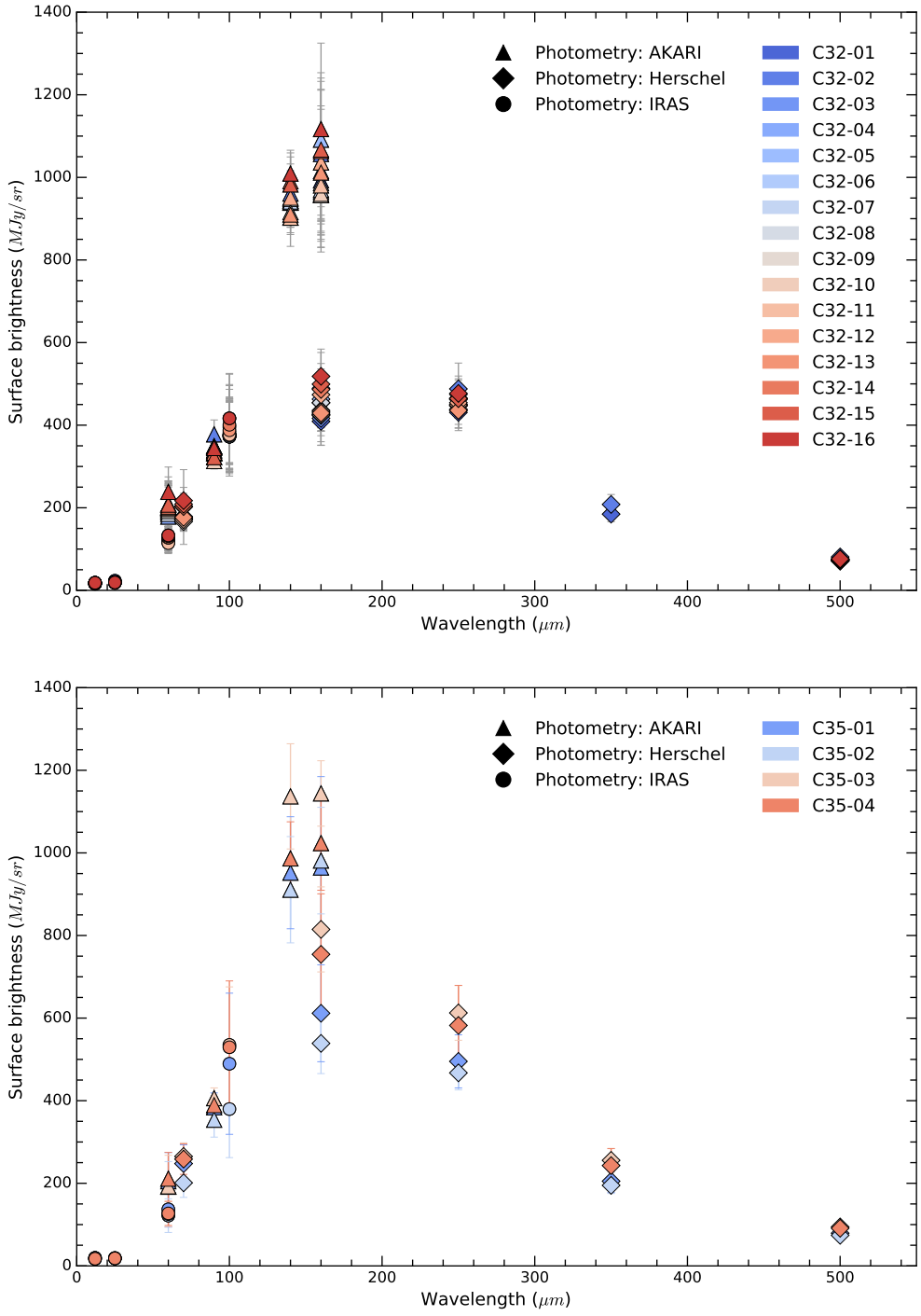

Figure 4.15: Spectral energy distributions for C32 (top) and C35 (bottom), constructed with photometric observations from *Herschel* Space Observatory, *Infrared Astronomical Satellite* and *AKARI* (see Table 4.2). A clear separation between individual positions is present at 160 µm, 250 µm and 350 µm, particularly in C35.

4.4.7 Summary

The median spectra of all the positions in C32 look very similar, as do the spectra of C35. However, when examining the individual emission features, spatial variations are clearly present. We use the composite image (Fig. 4.6) of C32 to identify an elevated Hα emission region (or channel). This Hα channel is linked to weak PAH emission and strong fine-structure emission. The 25.9 μm [Fe II] line, which is a tracer of shocked gas, is strong outside the Hα channel and is undetected (at 3σ) inside the channel. SEDs show that there are significant surface brightness variations across the field, sometimes by as much as 50%, which indicates that the dust properties are not constant.

We examine fewer positions in C35, but there are similar characteristics: the median spectra in C35 are similar, but the composite image shows significant Hα emission near positions 3, 4 and 5 (Fig. 4.7). The fine-structure lines peak in this region, as in C32. The 25.9 μm [Fe II] line is also observed across the field, but no clear variation is apparent between on-channel and off-channel regions, in contrast to the field of C32. The SEDs show that the C35 positions coincident with the Hα channel are systematically brighter than the other positions (1, 2). The PAH emission in C35 does not vary as much as it does in C32, but it is linked with the Hα structure to some degree: (e.g.) the 7.7/11.2 PAH ratio is $\sim$10% higher here.

A relatively weak correlation is identified between the 6.2 and 7.7 μm PAH band fluxes, which is normally one of the strongest PAH correlations measured. This is because we are probing a small range in flux ratios. It is very remarkable though that our ratios are similar to those in ultra-compact H II regions (Stock et al., 2014) and do not coincide with those of reflection nebulae and the more diffuse ISM. In this respect, we note that the observed fine-structure line emission is not similar to those observed toward these ultra-compact H II regions with similar PAH ratios. Ultra-compact H II regions exhibit higher degrees of ionization, with strong 10.5 μm [S IV] emission and much stronger 12.8 μm [Ne II] emission than we see in our spectra (Stock et al., 2014).

In general, these lines of sight are complex but we have the following tools: known Hα emission structure, 25.9 μm [Fe II] emission possibly tracing shocked gas, strongly varying dust surface brightnesses, PAH variations which are anti-correlated with the Hα emission, fine-structure line emission and H_2 emission. To understand what environments we are observing along these sight-lines we need to discern whether or not these emission features are simply coincident or linked to the same physical conditions/environments.

4.5 Discussion

The key questions in this analysis are: what environments are we probing on these sightlines, and how do these environments contribute to the observed spectra? To answer this, we examine the similarities between our spectra and representative spectra for different environments.

4.5.1 SED fitting approach

To quantify the dust properties of our observations, and observations typical of other environments, we use the radiative transfer code DUSTY (Elitzur and Ivezić, 2001; Ivezic and Elitzur, 1997; Ivezic, Nenkova, and Elitzur, 1999). DUSTY solves the radiative transfer equation for dusty media by applying scaling relations to reduce the number of parameters that must be solved for simultaneously. The key to this approach is that the radiative flux incident on a slab boundary, with dust temperature T, is singly-defined when the properties of the region are prescribed (e.g, composition, grain size distribution; Ivezic, Nenkova, and Elitzur 1999).

Our approach is to produce model SEDS with DUSTY and perform least-squares fitting of the photometric observations to these models with MPFIT (Markwardt, 2009), which utilizes the Levenberg-Marquardt algorithm (Moré, 1978). DUSTY permits variable dust compositions, dust size distributions, radiation fields, geometry, optical depths, and depending on which configuration is utilized, density distributions. In general, when the slab or shell is optically thick, increasing τ_0 has the effect of shifting the SED as a whole to longer wavelengths and roughly retains its shape (Ivezic, Nenkova, and Elitzur, 1999). The dust composition can influence the near- and mid-infrared SED, as (e.g.) a higher fraction of silicates will produce stronger silicate absorption near 9.7 μm. The output SED is only weakly dependent on the exact shape of the external radiation field, in general, and only when the optical depth is less than or comparable to unity. For the assumed dust sublimation temperature (1500 K), there is no influence on the resulting model SED at wavelengths shorter than 2 μm. At longer wavelengths, only the scale of the SED is affected, not its shape. Grain sizes smaller than 0.05 μm in radius only affect the SED at wavelengths shorter than visible in this model. For larger grains, increasing grain sizes increases the far-IR optical depths for a given τ_0 (Ivezic, Nenkova, and Elitzur, 1999).

For our models, we assume plane-parallel slab geometry, with an impinging isotropic radiation field defined by the interstellar radiation field (ISRF) of Mathis, Mezger, and Panagia (1983) applied to the left slab boundary. No external radiation is assumed to be incident on the

right side of the slab (where the observer is located). The dust composition is the code-default mixture of 53% silicates and 47% graphitic grains, with properties defined by Draine and Lee (1984), typical for the ISM. Grain sizes are defined by the Mathis, Rumpl and Nordsieck distribution (MRN; Mathis, Rumpl, and Nordsieck 1977), which assumes minimum and maximum grain sizes of 0.005 μm and 0.25 μm, respectively, and a power-law index $q = 3.5$. We produced models spanning $\tau_\circ = 0.001$ to $\tau_\circ = 30$, with the optical depth measured at 550 nm. The dust temperature at the incident (left) slab face was computed in the range 10-100 K, which is a boundary condition that sets the incident luminosity of the radiation field.

We fit only the photometric observations past 50 μm, which characterizes the emission of "big" grains in thermal equilibrium (i.e. we do not account for the emission of stochastically heated PAHs and very small grains). One fit is performed for each position in the C32 and C35 fields. Per the discrepancy between the Herschel/PACS 140 μm and AKARI 140 and 160 μm observations, we perform fits with each separately. For the C32 photometry across all positions, if we assume the Herschel photometric datum at 160 μm we find reduced-$\chi^2 = 2.0 \pm 0.7$, whereas the AKARI data lead to reduced-$\chi^2 = 4.5 \pm 1.0$. In C35, with Herschel we find reduced-$\chi^2 = 1.1 \pm 0.3$, and with AKARI reduced-$\chi^2 = 2.1 \pm 0.9$. Due to the consistently better statistics of the former we only present results assuming the Herschel emission at 160 μm instead of the two AKARI measurements at 140 and 160 μm.

4.5.2 Comparison with the diffuse interstellar medium

We examine an SED of the diffuse cirrus emission presented by Boulanger (1999). It is composed of a 5-16 μm ISOCAM spectrum (Boulanger et al., 1996a) and *COBE* satellite measurements of high latitude cirrus emission (Bernard et al., 1994; Boulanger et al., 1996b). The latter were acquired with the Diffuse Infrared Background Experiment (DIRBE) and the Far Infrared Absolute Spectrometer (FIRAS; Boggess et al. 1992).

We compare the cirrus emission to the *Spitzer*/IRS low-resolution spectra and photometric measurements of C32 and C35 in Fig. 4.16. The flux of the cirrus SED, which was originally presented in units of flux per hydrogen atom, is divided by an arbitrary constant (7×10^{-8}) for a qualitative comparison with our data.

The FIR cirrus emission peaks at $>$ 150 μm, whereas the FIR emission of C32 and C35 peak near 100 μm (Fig. 4.16, top), indicating warmer dust temperatures toward the Galactic bulge than towards cirrus clouds. In each SED, the peak intensity of the MIR emission is comparable to the peak intensity of the FIR emission. The cirrus SED does not appear to exhibit 12.8 μm [Ne II] emission, while C32 and C35 both clearly do.

We derive model dust temperatures of 30-33 K in C32 and 28-32 K in C35. Both environ-

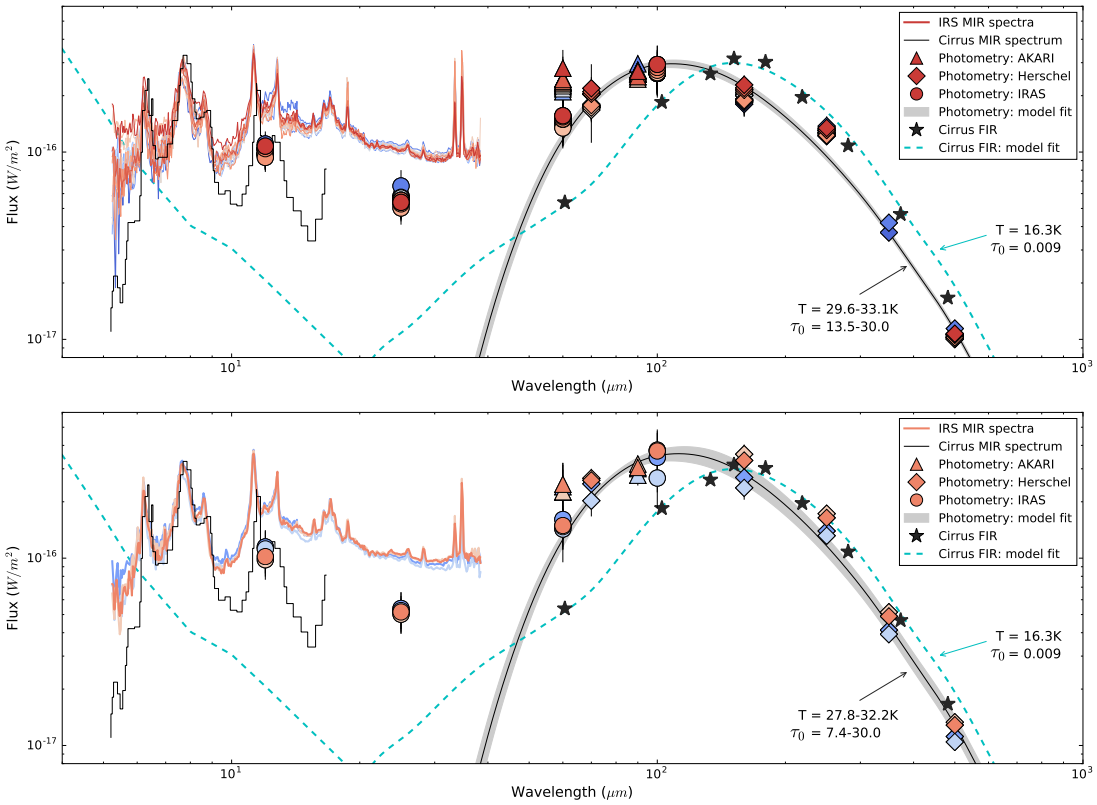

Figure 4.16: A comparison between the diffuse cirrus emission and the emission in our fields of C32 (top) and C35 (bottom). The colors of the IRS spectra and photometry represent the different pointings within each field (c.f. Figs. 4.9 and 4.15). The cirrus emission is shown in the stepped black line (MIR) and black stars (FIR). *The cirrus emission is arbitrarily scaled in flux for the sake of comparison* (see Section 4.5.2). Model fits to the $>$ 50 μm photometry are shown: C32 and C35 (black line with shaded gray to indicate the 1σ deviation) and the cirrus emission (dashed cyan line). The Galactic bulge emission is consistent with enshrouded warm dust (T$\sim$ 30K, $\tau_o \sim>$ 10), and the cirrus with cold exposed dust ($T = 16.3K$, $\tau_o = 0.009$). Note that for the sake of clarity, this view is zoomed in: two additional cirrus data points at low flux levels (at $\sim$672 and 918 μm) are below the horizontal in this figure (see Fig. 4.17 for an expanded view that includes these data).

ments are optically thick ($\tau_o = 13 - 30$ in C32, $\tau_o = 7 - 30$ in C35). In contrast, the cirrus emission is consistent with 16 K dust on optically thin lines of sight ($\tau_o = 0.009$). The fit of the cirrus emission is strongly dependent on the 60 μm flux, which was important for constraining the optical depth. The obtained cirrus temperature is close to that found by Boulanger et al. (1996b) for these data, 17.5 K.

Despite the similarity of the PAH features observed toward the Galactic bulge and cirrus clouds, their sight-lines are very different: the bulge has (relatively) warm dust seen through an optically thick medium (i.e. the Galactic plane), while the cirrus emission is consistent with cold grains in diffuse media (where there is less heating and less extinction).

4.5.3 Comparison with Orion Bar

The Orion Bar is a well-studied photodissociation region, known for its edge-on view of the transition from H II region to molecular cloud (Tielens et al., 1993). We have modelled the FIR emission of *Herschel* PACS and SPIRE observations of three positions in Orion (Arab et al. 2012, their Fig. 4): on the bar itself, 30″ahead of the bar (closer to the illuminating source), and 38 ″further behind the bar (further distant from the illuminating source). We compare the SEDs and model fits for C32, C35 and the cirrus emission to Orion in Fig. 4.17. Note that, as in Section 4.5.2, the cirrus emission is arbitrarily scaled in flux–here we present it offset from the Galactic bulge positions in peak flux for the sake of comparison (by dividing the SED by 8×10^{-8}).

The emission in Orion is very bright, dwarfing the C32 and C35 emission by as much as $\sim$ three orders of magnitude at $\sim$ 70 μm. The Orion FIR continuum is monotonically decreasing beyond 70 μm, indicating hotter (large) grains in Orion. Our model fits show that grain temperatures in front of, on and behind the bar are approximately 74 K, 70 K and 41 K, respectively. Arab et al. (2012) report for the same positions dust temperatures of 70.6 ± 10.5 K, 48.8 ± 4.0 K and 37.1 ± 2.5 K, respectively. The off-bar positions are in good agreement, but the bar dust temperature we infer is significantly hotter than what they find, suggesting issues with our models. The optical depths associated with the positions in front of, on and behind the bar in our models are $\tau_\circ = 7.7$, 11.6 and 0.2, respectively, as measured at 0.55 μm. The low optical depth of the emission behind the bar may also be emblematic of issues with our model approach.

4.5.4 Model limitations

It is clear that our chosen model geometry is not correct. We have thus far assumed a plane-parallel slab geometry, whereas in reality the dust is likely illuminated at a significant angle from the angle at which we view the dust. The strong near- to mid-infrared emission in our models, generally inconsistent with the observed mid-infrared emission, likely originates in our assumed interstellar radiation field propagating through the column into our line of sight. Despite this, as a proof of concept we can generally replicate reasonable temperatures (such as those consistent with two of three positions in Orion Bar, and the cirrus). Moving forward, we will introduce new model geometry and possibly resolve the discrepancies.

4.5.5 Prevalence of PAHs

With model SEDs, we are now able to tabulate the total far-infrared flux, as well as the mid-infrared flux from PAHs. Using the formulation of Tielens (2005), we measured the fraction

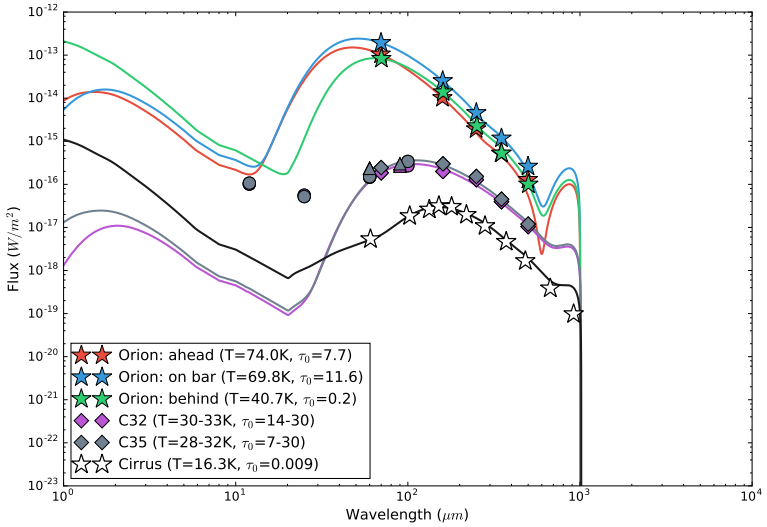

Figure 4.17: A comparison of the FIR photometry of the Galactic bulge fields C32 and C35 with the diffuse cirrus emission (Boulanger, 1999) and three Orion positions (Arab et al., 2012): $\sim 30''$ in front of the bar, on, and $\sim 38''$ behind the bar. The dust in orion is significantly hotter (and brighter) than the dust we observe toward the Galactic bulge. *Note that the cirrus SED is scaled in flux by an arbitrary scale factor for comparison* (see Section 4.5.2).

of carbon locked in PAHs. The percentage of carbon locked in PAHs along our sight-lines toward C32 and C35 is approximately 5.0 ± 0.6%. These values are somewhat high relative to values typical for the ISM (∼3.5%, Tielens 2005). In C32, this fraction is at a minimum in the strong Hα "channel" at position C32-10 (∼4%), and reaches a maximum to the left of the channel at positions C32-12 and C32-14 (∼6%). No systematic variation across the C35 field is detected.

4.6 Conclusions

We have analyzed the background emission in *Spitzer*/IRS observations toward the Galactic bulge. Combined with mid- and far-infrared photometry, we have investigated the spectral characteristics of our observations in the context of disentangling the contributors and contributions to our lines-of-sight. Our primary conclusions are as follows:

1. The background emission in the fields of C32 and C35, at 1° N and 1° S Galactic latitude, have exceedingly similar spectra, with strong PAH emission, fine-structure lines, plateaus, and molecular emission. The background emission toward OGLE and NGC 6522, at 2° S, and 3° S Galactic latitude, have much weaker emission, with flat or declining continua, barely detectable PAH bands and few fine-structure lines.

2. The strength of the PAH and fine-structure features are related to a region of elevated

Hα emission: where the Hα emission is bright, the fine-structure lines are bright and the PAH bands are weaker, generally.

3. In contrast, the 25.9 μm [Fe II] line peaks on either side of the Hα channel in C32. This line is thought to be a tracer of shocked gas, suggesting that there may be a bubble impacting the surrounding gas in this region.

4. SED modelling indicates that the temperatures of thermal dust grains in C32 and C35 are $\sim$30 K, with optical depths $\tau_0 \gtrsim 10$. In comparison, cirrus grains are $\sim$16 K and dust in Orion Bar is approximately 40-70 K. Our models need to be iterated with more realistic geometries.

5. We infer that $5.0 \pm 0.6\%$ of the total carbon along the sight-lines to C32 and C35 are locked in PAHs. This is somewhat high compared to typical expectations of 3.5%.

The extreme similarity between the spectra towards C32 and C35, which are diametrically opposed from the Galactic center, is quite peculiar. Not only are their dust continua comparable, but the plateaus, PAH bands, H_2 lines and 25.9 μm [Fe II] emission strengths are also very similar. Only the atomic fine-structure lines appear to differ significantly between them. Why there are so many shared spectral characteristics between fields vastly separated opens the door to many questions, such as: is this emission typical of all Bulge sight-lines? OGLE and NGC 6522 have different spectra, but they are also further away from the Galactic center. Is there a systematic dependence on Galactocentric distance?

To understand the strong variations within the C32 field, further comparisons with other environments are needed. There is clearly a relationship between the elevated Hα emission region that we see in imaging and the strengths of the emission bands, as some are correlated and some are anti-correlated with this region. The further inclusion of multi-wavelength imaging and, in particular, an understanding the origin of the shock-tracing 25.9 μm [Fe II] line will help complete the picture.

Acknowledgments

The authors acknowledge support from an NSERC discovery grant. MJS acknowledges support from a QEII-GSST scholarship. The IRS was a collaborative venture between Cornell University and Ball Aerospace Corporation funded by NASA through the Jet Propulsion Laboratory and Ames Research Center (Houck et al., 2004). The Southern Hα Sky Survey Atlas (SHASSA) (Gaustad et al., 2001) was produced with support from the National Science Foundation. This research is based on observations with AKARI, a JAXA project with the

participation of ESA. This research has made use of NASA's Astrophysics Data System Bibliographic Services, and the SIMBAD database, operated at CDS, Strasbourg, France. This work has also made use of the Matplotlib Python plotting library (Hunter, 2007) and the Seaborn Python visualization library[†].

References

Arab, H., Abergel, A., Habart, E., et al. (2012). *Astronomy and Astrophysics* 541, A19, A19. DOI: 10.1051/0004-6361/201118537. arXiv: 1202.1624.

Bernard, J. P., Boulanger, F., Desert, F. X., et al. (1994). *Astronomy and Astrophysics* 291, pp. L5–L8.

Blommaert, J. A. D. L., Groenewegen, M. A. T., Okumura, K., et al. (2006). *Astronomy and Astrophysics* 460, pp. 555–563. DOI: 10.1051/0004-6361:20066145. eprint: astro-ph/0609230.

Boersma, C., Bregman, J., and Allamandola, L. J. (2014). *Astrophysical Journal* 795, 110, p. 110. DOI: 10.1088/0004-637X/795/2/110.

Boggess, N. W., Mather, J. C., Weiss, R., et al. (1992). *Astrophysical Journal* 397, pp. 420–429. DOI: 10.1086/171797.

Boulanger, F. (1999). In: *New Perspectives on the Interstellar Medium*. Ed. by A. R. Taylor, T. L. Landecker, and G. Joncas. Vol. 168. Astronomical Society of the Pacific Conference Series, p. 173.

Boulanger, F., Reach, W. T., Abergel, A., et al. (1996a). *Astronomy and Astrophysics* 315, pp. L325–L328.

Boulanger, F., Abergel, A., Bernard, J.-P., et al. (1996b). *Astronomy and Astrophysics* 312, pp. 256–262.

Boulanger, F., Abergel, A., Bernard, J. P., et al. (1998). In: *Star Formation with the Infrared Space Observatory*. Ed. by J. Yun and L. Liseau. Vol. 132. Astronomical Society of the Pacific Conference Series, p. 15.

Doi, Y., Takita, S., Ootsubo, T., et al. (2015). *Publications of the ASJ* 67, 50, p. 50. DOI: 10.1093/pasj/psv022. arXiv: 1503.06421.

Draine, B. T. and Lee, H. M. (1984). *Astrophysical Journal* 285, pp. 89–108. DOI: 10.1086/162480.

Elitzur, M. and Ivezić, Ž. (2001). *Monthly Notices of the RAS* 327, pp. 403–421. DOI: 10.1046/j.1365-8711.2001.04706.x. eprint: astro-ph/0106096.

[†] http://dx.doi.org/10.5281/zenodo.19108

Galliano, F., Madden, S. C., Tielens, A. G. G. M., et al. (2008). *Astrophysical Journal* 679, pp. 310–345. DOI: 10.1086/587051. arXiv: 0801.4955.

Gaustad, J. E., McCullough, P. R., Rosing, W., et al. (2001). *Publications of the ASP* 113, pp. 1326–1348. DOI: 10.1086/323969. eprint: astro-ph/0108518.

Golriz, S. S., Blommaert, J. A. D. L., Vanhollebeke, E., et al. (2014). *Monthly Notices of the RAS* 443, pp. 3402–3434. DOI: 10.1093/mnras/stu1317.

Griffin, M. J., Abergel, A., Abreu, A., et al. (2010). *Astronomy and Astrophysics* 518, L3, p. L3. DOI: 10.1051/0004-6361/201014519. arXiv: 1005.5123 [astro-ph.IM].

Groenewegen, M. A. T. and Blommaert, J. A. D. L. (2005). *Astronomy and Astrophysics* 443, pp. 143–156. DOI: 10.1051/0004-6361:20053131. eprint: astro-ph/0506338.

Hony, S., Van Kerckhoven, C., Peeters, E., et al. (2001). *Astronomy and Astrophysics* 370, pp. 1030–1043. DOI: 10.1051/0004-6361:20010242. eprint: arXiv:astro-ph/0103035.

Houck, J. R., Roellig, T. L., van Cleve, J., et al. (2004). *Astrophysical Journal, Supplement* 154, pp. 18–24. DOI: 10.1086/423134. eprint: arXiv:astro-ph/0406167.

Hunter, J. D. (2007). *Computing In Science & Engineering* 9.3, pp. 90–95.

Ivezic, Z. and Elitzur, M. (1997). *Monthly Notices of the RAS* 287, pp. 799–811. DOI: 10.1093/mnras/287.4.799. eprint: astro-ph/9612164.

Ivezic, Z., Nenkova, M., and Elitzur, M. (1999). *ArXiv Astrophysics e-prints*. eprint: astro-ph/9910475.

Kawada, M., Baba, H., Barthel, P. D., et al. (2007). *Publications of the ASJ* 59, S389. DOI: 10.1093/pasj/59.sp2.S389. arXiv: 0708.3004.

Markwardt, C. B. (2009). In: *Astronomical Data Analysis Software and Systems XVIII*. Ed. by D. A. Bohlender, D. Durand, and P. Dowler. Vol. 411. Astronomical Society of the Pacific Conference Series, p. 251. arXiv: 0902.2850 [astro-ph.IM].

Mathis, J. S., Mezger, P. G., and Panagia, N. (1983). *Astronomy and Astrophysics* 128, pp. 212–229.

Mathis, J. S., Rumpl, W., and Nordsieck, K. H. (1977). *Astrophysical Journal* 217, pp. 425–433. DOI: 10.1086/155591.

Miville-Deschênes, M.-A. and Lagache, G. (2005). *Astrophysical Journal, Supplement* 157, pp. 302–323. DOI: 10.1086/427938. eprint: astro-ph/0412216.

Molinari, S., Swinyard, B., Bally, J., et al. (2010). *Publications of the ASP* 122, pp. 314–325. DOI: 10.1086/651314. arXiv: 1001.2106.

Molinari, S., Schisano, E., Elia, D., et al. (2016). *Astronomy and Astrophysics* 591, A149, A149. DOI: 10.1051/0004-6361/201526380. arXiv: 1604.05911.

Moré, Jorge J. (1978). English. In: *Numerical Analysis*. Ed. by G.A. Watson. Vol. 630. Lecture Notes in Mathematics. Springer Berlin Heidelberg, pp. 105–116. ISBN: 978-3-540-08538-6. DOI: 10.1007/BFb0067700.

Murakami, H., Baba, H., Barthel, P., et al. (2007). *Publications of the ASJ* 59, S369. DOI: 10.1093/pasj/59.sp2.S369. arXiv: 0708.1796.

Ojha, D. K., Omont, A., Schuller, F., et al. (2003). *Astronomy and Astrophysics* 403, pp. 141–154. DOI: 10.1051/0004-6361:20030208. eprint: astro-ph/0303137.

Omont, A., Ganesh, S., Alard, C., et al. (1999). *Astronomy and Astrophysics* 348, pp. 755–767. eprint: astro-ph/9906489.

Ortolani, S., Renzini, A., Gilmozzi, R., et al. (1995). *Nature* 377, pp. 701–704. DOI: 10.1038/377701a0.

Peeters, E., Tielens, A. G. G. M., Allamandola, L. J., et al. (2012). *Astrophysical Journal* 747, 44, p. 44. DOI: 10.1088/0004-637X/747/1/44. arXiv: 1112.3386 [astro-ph.GA].

Peeters, E., Mattioda, A. L., Kemper, F., et al. (2006). In: *Astronomical Society of the Pacific Conference Series*. Ed. by L. Armus and W. T. Reach. Vol. 357. Astronomical Society of the Pacific Conference Series, p. 95. eprint: astro-ph/0507008.

Peeters, E., Hony, S., Van Kerckhoven, C., et al. (2002). *Astronomy and Astrophysics* 390, pp. 1089–1113. DOI: 10.1051/0004-6361:20020773. eprint: arXiv:astro-ph/0205400.

Pilbratt, G. L., Riedinger, J. R., Passvogel, T., et al. (2010). *Astronomy and Astrophysics* 518, L1, p. L1. DOI: 10.1051/0004-6361/201014759. arXiv: 1005.5331 [astro-ph.IM].

Poglitsch, A., Waelkens, C., Geis, N., et al. (2010). *Astronomy and Astrophysics* 518, L2, p. L2. DOI: 10.1051/0004-6361/201014535. arXiv: 1005.1487 [astro-ph.IM].

Rieke, G. H., Young, E. T., Engelbracht, C. W., et al. (2004). *Astrophysical Journal, Supplement* 154, pp. 25–29. DOI: 10.1086/422717.

Shannon, M. J., Stock, D. J., and Peeters, E. (2016). *Astrophysical Journal* 824, 111, p. 111. DOI: 10.3847/0004-637X/824/2/111. arXiv: 1604.08589.

– (2015). *Astrophysical Journal* 811, 153, p. 153. DOI: 10.1088/0004-637X/811/2/153. arXiv: 1508.04766.

Smith, J. D. T., Armus, L., Dale, D. A., et al. (2007a). *Publications of the ASP* 119, pp. 1133–1144. DOI: 10.1086/522634. arXiv: 0708.3745.

Smith, J. D. T., Draine, B. T., Dale, D. A., et al. (2007b). *Astrophysical Journal* 656, pp. 770–791. DOI: 10.1086/510549. eprint: arXiv:astro-ph/0610913.

Stock, D. J., Peeters, E., Choi, W. D.-Y., et al. (2014). *Astrophysical Journal* 791, 99, p. 99. DOI: 10.1088/0004-637X/791/2/99. arXiv: 1407.0702.

Tielens, A. G. G. M. (2008). *Annual Review of Astron and Astrophys* 46, pp. 289–337. DOI: 10.1146/annurev.astro.46.060407.145211.

– (2005).

Tielens, A. G. G. M., Meixner, M. M., van der Werf, P. P., et al. (1993). *Science* 262, pp. 86–89. DOI: 10.1126/science.262.5130.86.

van den Ancker, M. E., Wesselius, P. R., Tielens, A. G. G. M., et al. (1999). *Astronomy and Astrophysics* 348, pp. 877–887.

Van Kerckhoven, C., Hony, S., Peeters, E., et al. (2000). *Astronomy and Astrophysics* 357, pp. 1013–1019.

Werner, M. W., Roellig, T. L., Low, F. J., et al. (2004). *Astrophysical Journal, Supplement* 154, pp. 1–9. DOI: 10.1086/422992. eprint: arXiv:astro-ph/0406223.

Zoccali, M., Renzini, A., Ortolani, S., et al. (2003). *Astronomy and Astrophysics* 399, pp. 931–956. DOI: 10.1051/0004-6361:20021604. eprint: astro-ph/0210660.

It's just an excuse for more beer.

Endeavour Morse, Inspector Morse

5 Conclusions

In this thesis we analyzed the nature and variability of the PAH emission bands in several environments. The questions we wished to answer were:

Can we explain *why* the shapes of the 11.2 and 12.7 μm PAH bands vary in the way they do?

We addressed this question in Chapter 2. Our method of approach was to exploit the high utility of spectral mapping techniques. We examined observations from the *Spitzer* Space Telescope of the reflection nebulae NGC 7023 and NGC 2023 (north and south) and the star-forming region M17. We applied a Gaussian-based decomposition technique to recreate the observed PAH band profiles in different regions of the maps. Most of the Gaussian components we deduce are shown to have independent spatial distributions, suggesting that we are tracing distinct PAH populations. We determined that the 11.2 and 12.7 μm bands both have contributions from cationic and neutral PAHs.

The 11.0 and 11.2 μm bands are traditionally understood as originating from cationic and neutral PAHs with solo CH_{oop} bending modes, respectively. Our analysis shows that the traditional 11.0 μm band consists of a spectrally-broad cationic component that dominates the flux at 11.0 μm, but there is a non-negligible contribution (∼8-16%) from neutral PAHs. Likewise, we find that the broad 11.2 μm emission has a cationic sub-component near 11.20 μm. The relative strength of this cationic component to the otherwise neutral 11.2 μm band determines the peak position of the overall band, and thus the PAH class of the 11.2 μm band.

The variations we observe of the 12.7 μm band in profile and peak position are in some

ways more interesting. We find that the peak position of the band is explained in our decomposition by the relative strengths of two competing components, one at 12.72 μm and one at 12.78 μm. Our spectral maps indicate that they have independent spatial morphologies and trace PAH cations and neutrals, respectively, despite being highly blended spectroscopically.

We also examined the 12.7/11.2 ratio, which is expected to trace molecular structure. Based on our results, we find that in our sample of sources we are primarily probing charge variations.

Our decompositions were arbitrary, and thus we do not posit that they are necessarily *correct*. However, the fact that the components in our decomposition are *spatially independent, and ordered by distance to the exciting star* suggests that our decomposition is meaningful for understanding the astronomical PAH populations. The takeaway is that the relative contribution of neutral and cationic PAHs determines the exact spectral profiles of the 11.2 and 12.7 μm bands in the objects we studied.

What are the carriers (and/or their properties) of the 15-20 μm bands?

Despite what we know about PAHs, no single astronomical PAH has been identified. The difficulty lies in the fact that the typical PAH bands originate from vibrational modes common to the family of PAHs. In contrast, >20 μm emission corresponds to vibrations that are molecule-specific, but they have been too weak for us to detect in space thus far. The 15-20 μm bands are expected to be dependent on molecular structure yet are bright enough to be studied observationally. There are few studies on these bands in the literature, and each has been limited to a small number of sources.

The premise of our study in Chapter 3 was to accumulate as large a sample as possible of spectra exhibiting 15-20 μm emission, totalling 57 Galactic and extragalactic sources, including two spectral maps of reflection nebulae. By searching for relationships between the 15-20 μm bands and the better studied 5-15 μm bands, we use our knowledge of the latter to infer characteristics of the former.

Using the results of our correlation plots, spectral maps and radial cuts, we determined the following groupings of similar bands:

- Group 1 - The 12.7, 16.4 and 17.8 μm bands
- Group 2 - The 11.2, 15.8 μm bands and the 15-18 μm plateau
- Group 3 - The 11.0 and 17.4 μm bands

The results of our detailed study of the 11.2 and 12.7 μm bands in Chapter 2 show that the 11.0 μm band is dominated by cations and the 11.2 μm band is dominated by neutrals, as is

traditionally understood. Based on this fact, we infer the following charge properties of our groupings:

- Group 1 - A roughly equal mixture of cations and neutrals
- Group 2 - Dominated by neutrals
- Group 3 - Dominated by cations

Molecular structure may still be important, but in the environments we studied we conclude that charge dominates the intensity variations of the 15-20 μm bands.

What is the source of excitation for PAH emission toward the Galactic bulge?

In Chapter 4 we examined PAH emission in lines of sight toward the Galactic bulge. To understand the origin of the PAH excitation, we have analyzed mid-infrared spectroscopic observations acquired with the *Spitzer* Space Telescope, far-infrared photometric observations and Hα observations to interpret our results. Our observations contain multiple pointings toward four positions: at approximately 1°, -1°, -2° and -3° Galactic latitude.

One of the most surprising results is that the spectra toward the fields at 1° and -1° latitude (C32 and C35) have *almost identical spectra, down to the PAH features and overall continuum shape*. The only difference between these spectra is the strength of the fine-structure lines. This suggests there may be a "typical" spectrum for sight-lines toward the Galactic bulge, and warrants further investigation.

We identify a region (or channel) of elevated Hα emission in C32. The fine-structure lines are strongest in this channel, whereas the PAH features are generally weakest. We also identify the 25.9 μm [Fe II] emission line, which is thought to be a typical tracer of shocked gas. The [Fe II] line is not detected in the Hα channel, but is present outside the channel.

To better understand our lines of sight, we have modelled the far-infrared dust emission with a radiative transfer code. We generally find that the emission in C32 and C35 are consistent with $\sim$30 K gas. We compare our observations to an SED of diffuse cirrus emission, which we find to contain much colder dust ($\sim$16 K). Comparisons with the bright photodissociation region Orion Bar show that positions in and around the bar are consistent with approximately 40-70 K dust, warmer than the dust we observe towards the Galactic bulge. The model SEDs allow us to estimate the fraction of carbon locked in PAHs on our lines of sight. We find a mean value of 5.0$\pm$0.6%, which is slightly high compared to typical expected values for the ISM of 3.5%.

Returning to the question of what is exciting the PAHs, we note that the fields at -2° and -3° Galactic latitude show very weak PAH emission. This suggests the PAH emission may be correlated with Galactocentric distance. It is unlikely that the bulge population itself is exciting the PAHs, as these are expected to be old, low-mass stars. While these stars can excite PAHs, they are much less efficient compared to higher energy sources and cannot explain the ionized gas fine-structure lines and the 25.9 μm [Fe II] line we observe. These hint towards a more complicated origin of the emission towards these line of sights. To answer this question, the next step is to analyze similar spectroscopic observations towards a different part of the Galactic bulge to see what variations are present, if any.

Future directions

For future work, I believe the following lines of inquiry are worthwhile:

- Apply our Gaussian-based decomposition of the 11.2 and 12.7 μm bands to as many high-resolution infrared spectra as possible to:

    1. Validate the applied Gaussian decomposition of the 11.2 and 12.7 PAH bands (Chapter 2) by applying it to a larger sample with different types of environments. First to see if the observed profile changes can be fit and second to see if the conclusions are general (applicable to all sources) or solely to reflection nebulae or even just these 2 sources.
    2. Test if the decomposition fails in environments with extreme spectral profiles.

- See if the decomposition can be successfully applied to low-resolution spectra. This opens the door to comparisons with other decompositions, such as a 4-component decomposition of the 7.7 and 8.6 μm bands (Peeters et al., 2016). Another possibility is to re-examine the 15-20 μm emission bands and determine if they are linked to the components of our 11.2 and 12.7 μm decompositions.

- Examine in further scrutiny PAH emission toward the Galactic bulge. It is remarkable that of the four fields we study (which are widely separated spatially) that we observe basically two distinct SEDs. Are these spectra typical of particular environments? To answer this, we need to better understand the environments of our observations. What is the nature of the Hα emission regions (or channels) in our C32 and C35 observations? We can examine CO maps to search for velocity gradients and X-ray maps to search for shocked gas. The 25.9 μm [Fe II] shock tracer is present outside the channels, so what dynamical process are we observing?

- Improve our radiative transfer modelling (Chapter 4) by including more realistic geometry and modelling the complete SED instead of being limited to the far-emission photometry. Also, the inclusion of a grain component to mimic the PAH emission may be useful. We will also compare our SEDs to those of other environments (e.g., the ISM of galaxies) to complement our observations of cirrus clouds and Orion Bar.

On the future of the field, the launch of *James Webb* Space Telescope (JWST) will strongly impact studies of PAH emission. The basic question of how and why the PAH bands vary becomes an ever-more tractable problem with each generation of instrument and telescope. The sole reason why we could decompose the 11.2 and 12.7 μm bands is because the *Spitzer* Space Telescope and its Infrared Spectrograph have sufficient spectral resolution to see the profile variations, in conjunction with sufficient spatial resolution to *probe* the variations over their corresponding spatial scales. Whereas *Spitzer* only had high-resolution spectroscopy beyond 10 μm, *JWST* will offer several to ∼ten times the spectral resolution of *Spitzer* across the whole 5-27 μm range. This is critical because we can observe all of the primary PAH bands in high-resolution spectral maps simultaneously. *JWST* also has significantly improved sensitivity (e.g. at 3-5 μm , the near-infrared camera can detect objects one hundred times fainter than *Spitzer*). The spatial resolution is also somewhat astounding, with pixel sizes between 0.20-0.27″, many times improved from *Spitzer*.

The cumulation of all these improvements is that the spectral maps upon which much of our analysis has hinged will be vastly improved with *JWST*. With this, we can more accurately determine the spectral shapes of the PAH bands and sample them at finer spatial intervals, meaning we can better understand how precisely they vary. These variations can in turn be linked to variations of the physical conditions in the surrounding environment, e.g., properties of the radiation field. The biggest problem with understanding PAH variations is dealing with how *blended* they are. *JWST* is poised to blow the problem open and our understanding of the astronomical PAH populations with it.

References

Peeters, E., Bauschlicher Jr., C. W., Allamandola, L. J., et al. (2016). *Astrophysical Journal*. Submitted.

A

Additional content for Chapter 3

A.1 Spatial Maps of NGC 2023 North and M17

The maps of NGC 2023 North and M17 are presented in Figs. A.1 and A.2, respectively. These are discussed in the main text in Sections 3.5.2.1 and 3.5.2.2. Here we give a brief summary.

In general, NGC 2023 North displays a much more complex morphology than NGC 2023 South or NGC 7023. The peak PAH emission appears to be oriented either vertically in this map (e.g. 11.0 μm, 11-G1 emission) or horizontally (e.g. 11.2 μm, 11-G3, 11-G4, 11-G5, 12-G4 emission), with significant overlap. However, the similarities between bands found in NGC 2023 North are generally consistent with those found for NGC 2023 South and NGC 7023 (see main text). Likewise, M17 is a complicated environment for analysis. In Fig. A.2, we observe that the peak 11.0 and 11.2 μm emission regions are nearly coincident. However, the key distinguishing feature seems to be the M17 "spur" emission in the upper right corner of the map, which is stronger in the 11.2 μm band. Based only on this distinguishing feature, key results from studying NGC 7023 and NGC 2023 South are also present here. The most robust trends—that the 11.0 μm and 12-G3 emission are well-matched, as are the 11.2 μm and 12-G4 emission—are both observed in M17 when examining the spur, despite its complexity.

A.2 Flux correlation plots

We examine ratios of band fluxes to probe for the presence of correlations between emission features (Fig. A.3). We compare first the 12-G3 and 12-G4 band fluxes to that of the 11.0 μm emission (all normalized to the 11.2 μm band). We also plot the 12-G3 and 12-G4 band

fluxes against that of the 11.2 μm band (then normalized to the 11.0 μm emission). We identify a strong correlation between the 12-G4 and 11.2 μm bands in NGC 7023 and NGC 2023 South and a mild correlation in NGC 2023 North (with associated weighted Pearson correlation coefficients of 0.98, 0.97 and 0.58, respectively). Another strong correlation is identified between the 12-G3 and 11.0 μm bands in these same sources, with coefficients 0.96, 0.89 and 0.87, respectively. The "cross terms" of these correlations, i.e. the 12-G3 band versus the 11.0 μm band, and the 12-G3 versus the 11.2 μm emission, reveal some residual structure and/or mild correlations. There is clearly some "cross-contamination", but the strongest relationships are nevertheless between the 12-G3 and 11.0 μm bands, and between the 12-G4 and the 11.2 μm bands. Similar correlation plots for the 12-G1 and 12-G2 components are presented in the lower panels of Fig. A.3. In general, both the 12-G1 and 12-G2 components correlate with the 11.0 and 11.2 μm bands, implying a mixed charge origin. M17 is an unusual case, as the only distinction between the traditional 11.0 and 11.2 μm emission in the spectral maps was the M17 spur. The correlation plots involving M17 are also outlying cases, as the 11.0/11.2 ratio is constant.

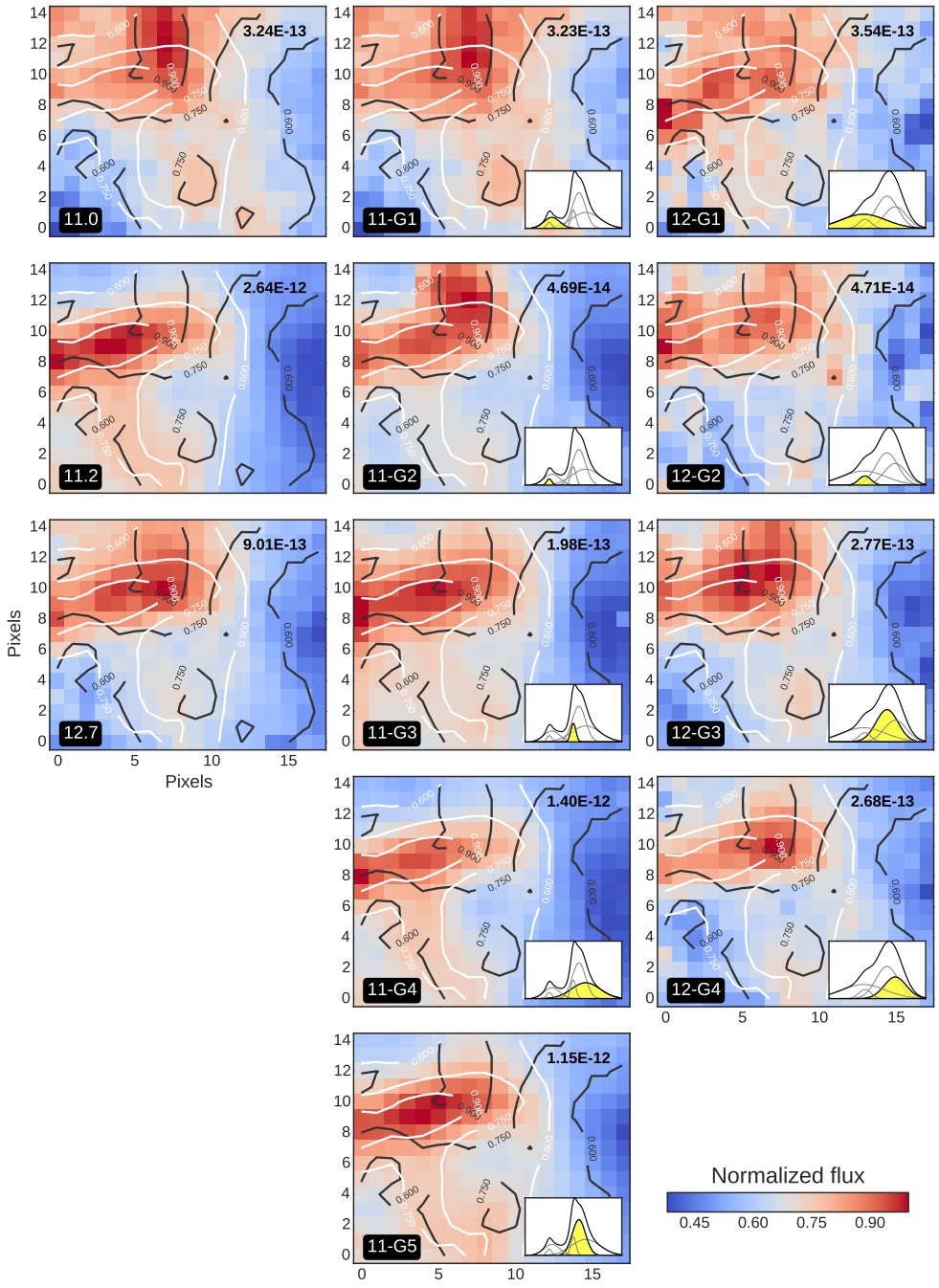

Figure A.1: PAH emission in NGC 2023 North. The conventions are the same as those used in Fig. 3.7.

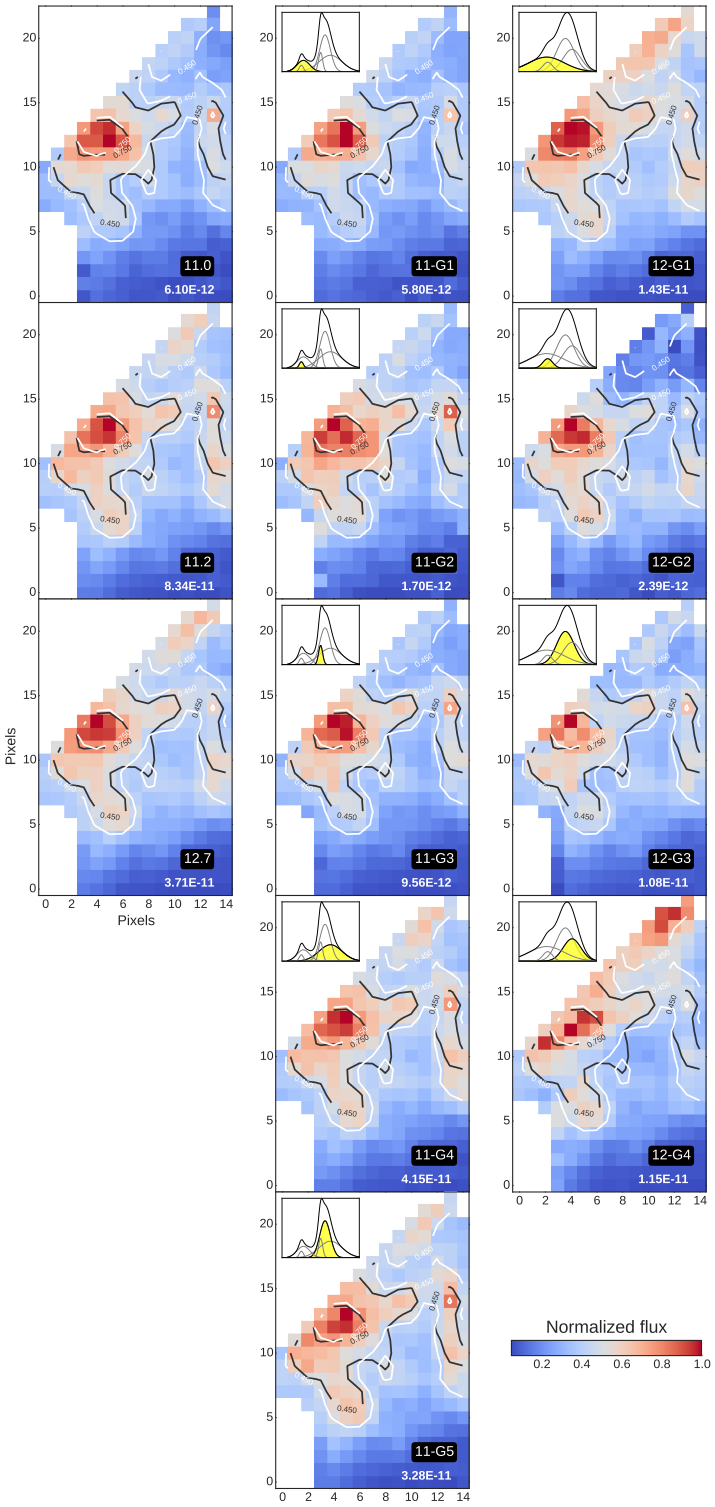

Figure A.2: PAH emission in M17. The conventions are the same as those used in Fig. 3.7.

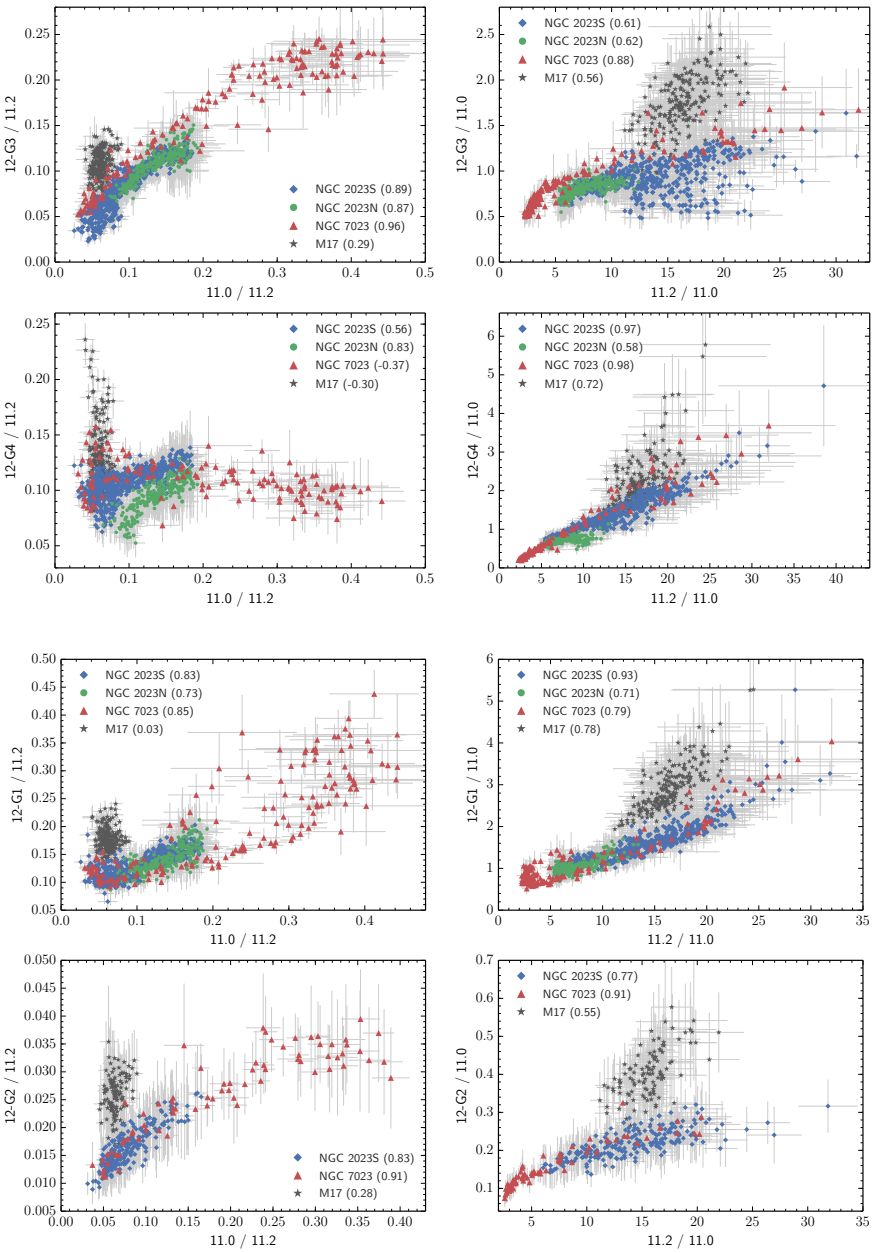

Figure A.3: Correlation plots comparing the intensities of the 12-G1, 12-G2, 12-G3 and 12-G4 components of the 12.7 µm decomposition to the traditional 11.0 and 11.2 µm emission intensities. The number in parentheses is the weighted Pearson correlation coefficient for each source. Each figure is normalized to either the 11.0 or 11.2 µm band, as appropriate.

B

Additional content for Chapter 4

B.1 Band and line fluxes

We include here tables of all measured quantities and maps of emission in C32 and C35. These were discussed in the text in Section 4.4.3.

Table B.1: PAH band fluxes

Object	Feature							
	6.2 μm	7.7 μm	8.6 μm	11.2 μm	12.7 μm	16.4 μm	17.4 μm	17.8 μm
C32-1	16.5 (0.7)	29.7 (0.9)	9.3 (1.2)	20.6 (1.4)	9.5 (1.3)	1.6 (0.2)	0.5 (0.1)	
C32-2	16.3 (0.5)	34.8 (0.7)	7.8 (0.8)	21.6 (1.0)	9.4 (0.9)	1.7 (0.2)	1.0 (0.2)	
C32-3	12.5 (0.6)	32.3 (0.8)	6.4 (1.0)	18.8 (1.1)		1.2 (0.2)	0.7 (0.1)	
C32-4	17.8 (0.5)	31.7 (0.6)	6.0 (0.8)	19.4 (0.9)	8.6 (0.9)	0.8 (0.1)	0.7 (0.1)	
C32-6	16.2 (0.6)	37.6 (0.8)	7.7 (1.0)	20.9 (1.1)	8.9 (1.1)			
C32-7	21.4 (0.7)	33.4 (0.9)	6.3 (1.1)	20.3 (1.3)	9.7 (1.2)	1.3 (0.2)	0.8 (0.2)	
C32-8	15.8 (0.6)	36.0 (0.7)	7.5 (0.9)	20.6 (1.1)	8.1 (1.0)	1.2 (0.2)	0.8 (0.2)	
C32-9	15.0 (0.7)	28.9 (0.9)	7.5 (1.2)	15.6 (1.3)	8.6 (1.3)	1.1 (0.2)	1.0 (0.1)	0.9 (0.1)
C32-10	8.9 (0.8)	22.0 (1.0)	6.3 (1.3)	16.5 (1.5)	6.7 (1.4)	1.5 (0.4)		
C32-11	11.1 (0.6)	31.5 (0.7)	4.5 (0.9)	18.5 (1.1)	8.3 (1.1)	1.2 (0.2)	0.9 (0.1)	0.6 (0.2)
C32-12	19.8 (0.4)	37.5 (0.5)	9.9 (0.7)	21.7 (0.8)	9.2 (0.8)	1.1 (0.2)	0.8 (0.2)	
C32-13	13.6 (0.3)	32.6 (0.4)	6.2 (0.5)	15.0 (0.5)	8.6 (0.5)	1.3 (0.2)	0.6 (0.1)	0.5 (0.2)
C32-14	23.2 (0.6)	39.5 (0.7)	7.9 (0.9)	19.5 (1.1)	9.2 (1.0)	1.4 (0.3)	1.0 (0.3)	
C32-15	16.1 (0.6)	31.4 (0.8)	7.3 (1.0)	19.6 (1.1)	8.9 (1.1)	1.5 (0.3)	1.0 (0.2)	
C32-16	21.3 (1.1)	31.3 (1.4)	6.6 (1.8)	17.9 (2.1)	7.1 (2.0)	1.5 (0.4)	1.0 (0.3)	
C35-1	20.8 (0.7)	37.9 (0.9)	7.8 (1.1)	23.8 (1.3)	8.4 (1.2)	1.0 (0.2)	0.8 (0.1)	0.5 (0.2)
C35-2	19.0 (1.2)	30.8 (1.5)	7.7 (2.0)	20.5 (2.3)	6.7 (2.2)	1.6 (0.2)	0.4 (0.1)	
C35-3	22.3 (0.8)	37.2 (1.0)	9.4 (1.3)	22.5 (1.5)	8.2 (1.4)	1.3 (0.2)	0.8 (0.2)	
C35-4	22.3 (1.0)	38.1 (1.3)	9.7 (1.7)	22.6 (1.9)	8.4 (1.9)	0.7 (0.2)	1.0 (0.1)	0.7 (0.2)
C35-5	19.5 (0.9)	31.5 (1.1)	6.8 (1.5)	21.6 (1.7)	8.4 (1.6)	1.6 (0.3)		
OGLE-2				5.8 (0.8)				
OGLE-4	2.1 (0.2)	8.0 (0.3)		5.4 (0.4)	2.5 (0.4)	0.4 (0.1)		
OGLE-6	2.7 (0.3)			5.0 (0.6)	3.1 (0.6)			

Notes. In units of 10^{-14} MWm^{-2}/sr. Uncertainties are given in parentheses. A 3σ signal-to-noise criterion is applied to our measurements; fields or positions with no bands meeting this criterion are omitted from the table.

Table B.2: Atomic and molecular line fluxes

Object	Feature							
	[Ne II] 12.8 μm	[Ne III] 15.5 μm	H_2 17.0 μm	[S III] 18.7 μm	[Fe II] 25.9 μm	H_2 28.2 μm	[S III] 33.5 μm	[Si II] 34.8 μm
C32-1	2.2 (0.4)		1.7 (0.4)	2.6 (0.3)			4.9 (0.3)	6.8 (0.3)
C32-2	4.2 (0.3)		2.5 (0.4)	3.7 (0.4)	0.8 (0.2)		6.7 (0.3)	9.0 (0.4)
C32-3	5.6 (0.3)	0.8 (0.2)	1.5 (0.2)	4.5 (0.3)	0.6 (0.1)	0.6 (0.1)	7.9 (0.1)	8.7 (0.2)
C32-4	4.4 (0.2)	0.8 (0.2)	1.7 (0.4)	4.8 (0.3)			8.9 (0.3)	10.0 (0.4)
C32-6	2.4 (0.3)		1.6 (0.5)	3.4 (0.5)			7.0 (0.4)	8.4 (0.6)
C32-7	3.5 (0.3)		1.8 (0.4)	4.9 (0.4)			8.7 (0.4)	9.8 (0.5)
C32-8	3.9 (0.3)	0.8 (0.2)	1.9 (0.3)	4.4 (0.3)			7.6 (0.3)	8.5 (0.3)
C32-9	5.0 (0.4)		1.9 (0.3)	4.7 (0.3)			8.4 (0.3)	9.3 (0.4)
C32-10	6.0 (0.4)			5.7 (0.6)			10.0 (0.6)	12.0 (0.9)
C32-11	5.0 (0.3)	0.9 (0.3)	2.0 (0.4)	4.5 (0.4)			8.0 (0.3)	9.1 (0.3)
C32-12	2.4 (0.2)		1.8 (0.4)	1.7 (0.4)	0.7 (0.2)		3.9 (0.4)	7.0 (0.3)
C32-13	5.8 (0.1)	0.9 (0.3)	1.4 (0.5)	4.7 (0.4)			9.0 (0.4)	12.0 (0.5)
C32-14	3.1 (0.3)		1.6 (0.5)	2.4 (0.5)	0.8 (0.2)		4.6 (0.3)	7.8 (0.4)
C32-15	1.8 (0.3)		1.8 (0.5)	2.1 (0.5)	0.7 (0.2)		3.7 (0.3)	7.0 (0.4)
C32-16	2.5 (0.6)		1.8 (0.6)	2.3 (0.6)	0.8 (0.2)		4.3 (0.3)	8.1 (0.4)
C35-1	1.3 (0.3)	1.3 (0.2)	2.2 (0.3)	1.0 (0.2)	0.8 (0.2)	1.0 (0.2)	2.1 (0.2)	5.0 (0.2)
C35-2		0.9 (0.2)	1.6 (0.2)	0.9 (0.2)	0.7 (0.2)	1.0 (0.2)	1.8 (0.2)	4.3 (0.2)
C35-3	2.4 (0.4)	1.2 (0.2)	2.3 (0.3)	1.5 (0.3)	0.7 (0.1)	1.0 (0.2)	2.9 (0.2)	7.3 (0.2)
C35-4	3.2 (0.5)	1.3 (0.3)	2.4 (0.3)	1.2 (0.2)	0.7 (0.2)	1.0 (0.2)	2.5 (0.2)	6.9 (0.2)
C35-5	5.2 (0.4)	1.3 (0.3)	1.4 (0.4)	4.0 (0.4)	1.0 (0.2)	0.9 (0.2)	7.0 (0.3)	13.3 (0.3)
OGLE-1								2.0 (0.6)
OGLE-2								1.4 (0.3)
OGLE-3								2.5 (0.4)
OGLE-4	0.4 (0.1)						0.6 (0.2)	1.9 (0.2)
OGLE-6							0.6 (0.2)	2.3 (0.2)
OGLE-7								6.7 (0.9)
NGC6522-1							0.8 (0.3)	1.7 (0.4)
NGC6522-3								0.8 (0.2)
NGC6522-5								0.9 (0.3)
NGC6522-6								0.8 (0.1)
NGC6522-7								0.6 (0.1)
NGC6522-9							0.3 (0.1)	0.6 (0.2)
NGC6522-10								0.8 (0.2)
NGC6522-14								0.8 (0.2)
NGC6522-15								0.7 (0.1)
NGC6522-16							0.3 (0.1)	0.8 (0.1)
NGC6522-18								0.6 (0.1)

Notes. In units of 10^{-14} MWm^{-2}/sr. Uncertainties are given in parentheses. A 3σ signal-to-noise criterion is applied to our measurements; fields or positions with no bands meeting this criterion are omitted from the table.

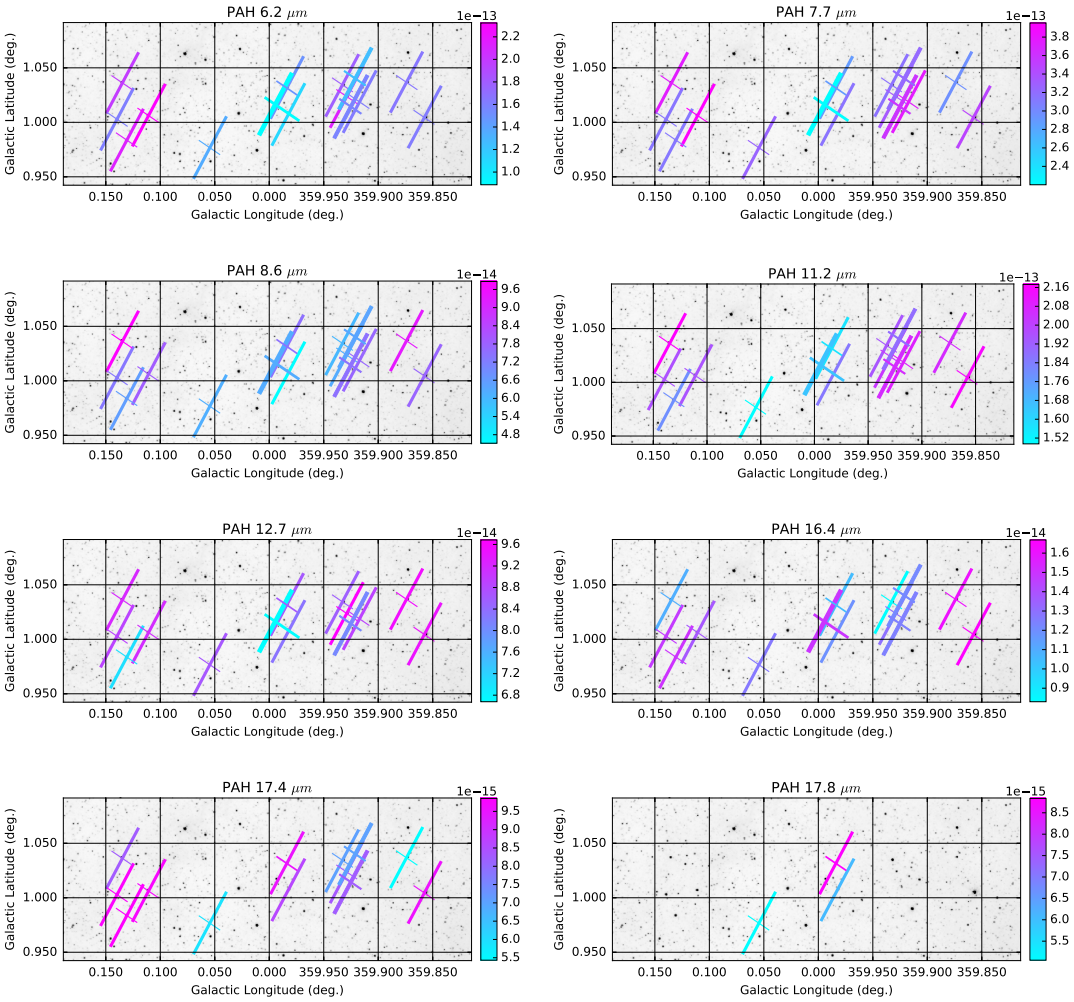

Figure B.1: The PAH emission band fluxes in the C32 fields, in $\mathrm{MWm}^{-2}/\mathrm{sr}$. A 3σ signal-to-noise criterion has been applied to these data.

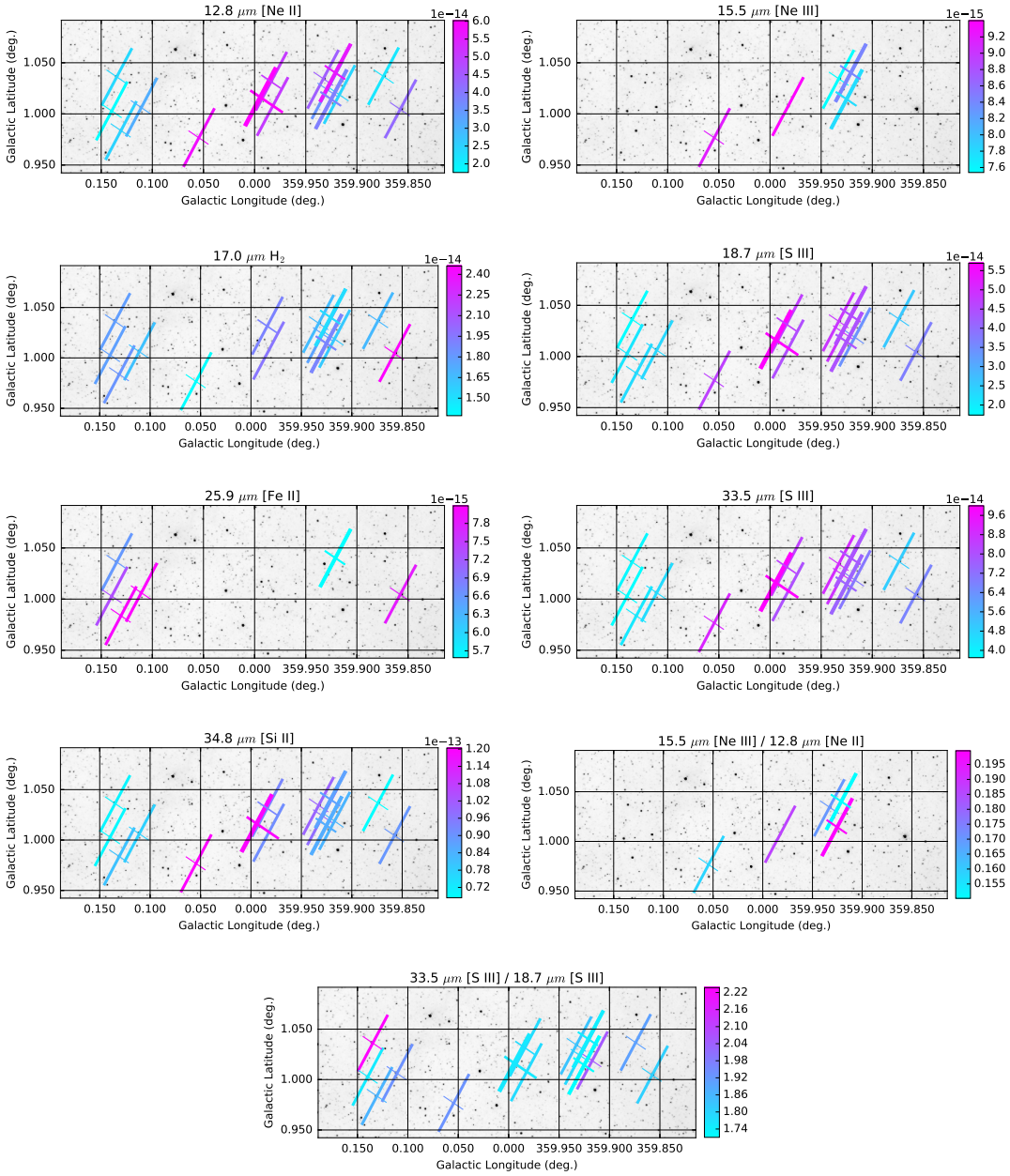

Figure B.2: The atomic and molecular emission line fluxes in the C32 fields, in $\mathrm{MWm}^{-2}/\mathrm{sr}$. A 3σ signal-to-noise criterion has been applied to these data.

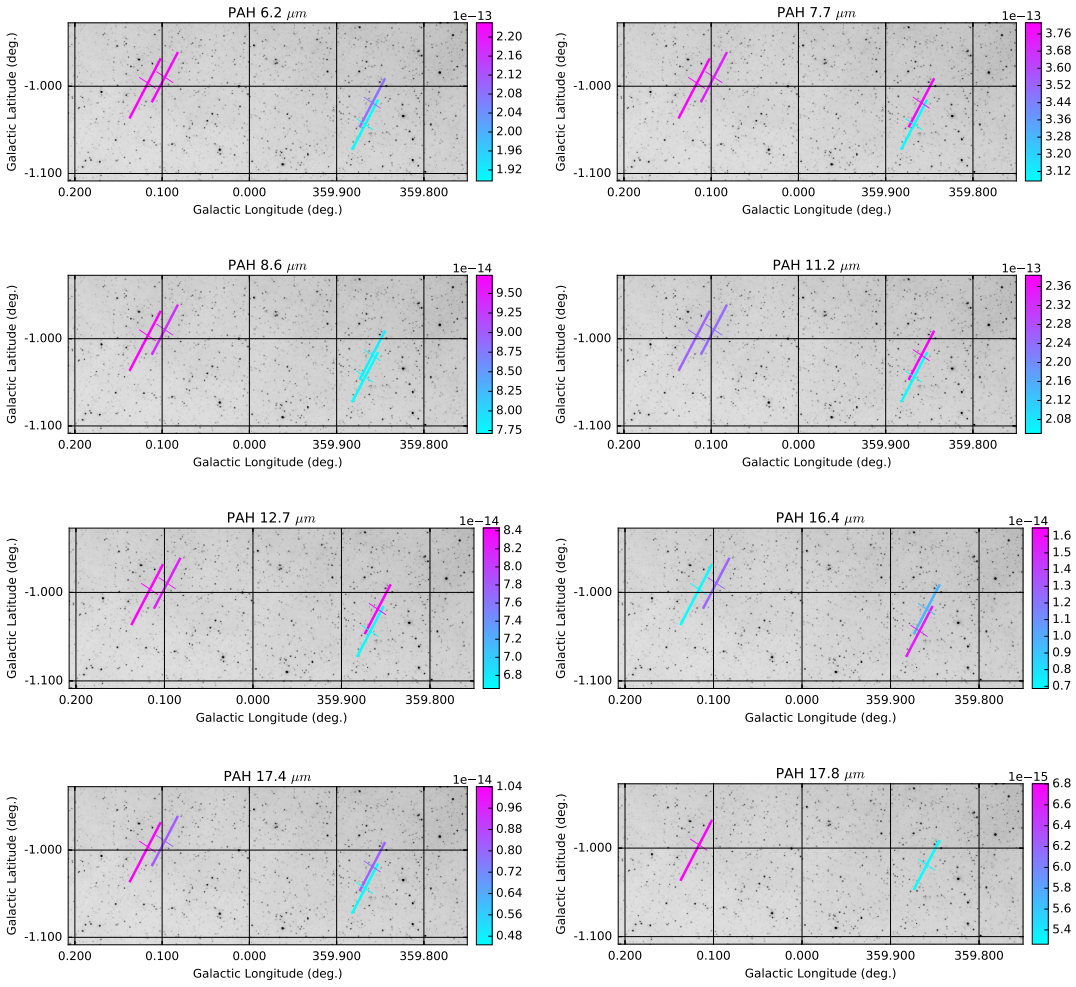

Figure B.3: The PAH emission band fluxes in the C35 fields, in $\mathrm{MWm}^{-2}/\mathrm{sr}$. A 3σ signal-to-noise criterion has been applied to these data.

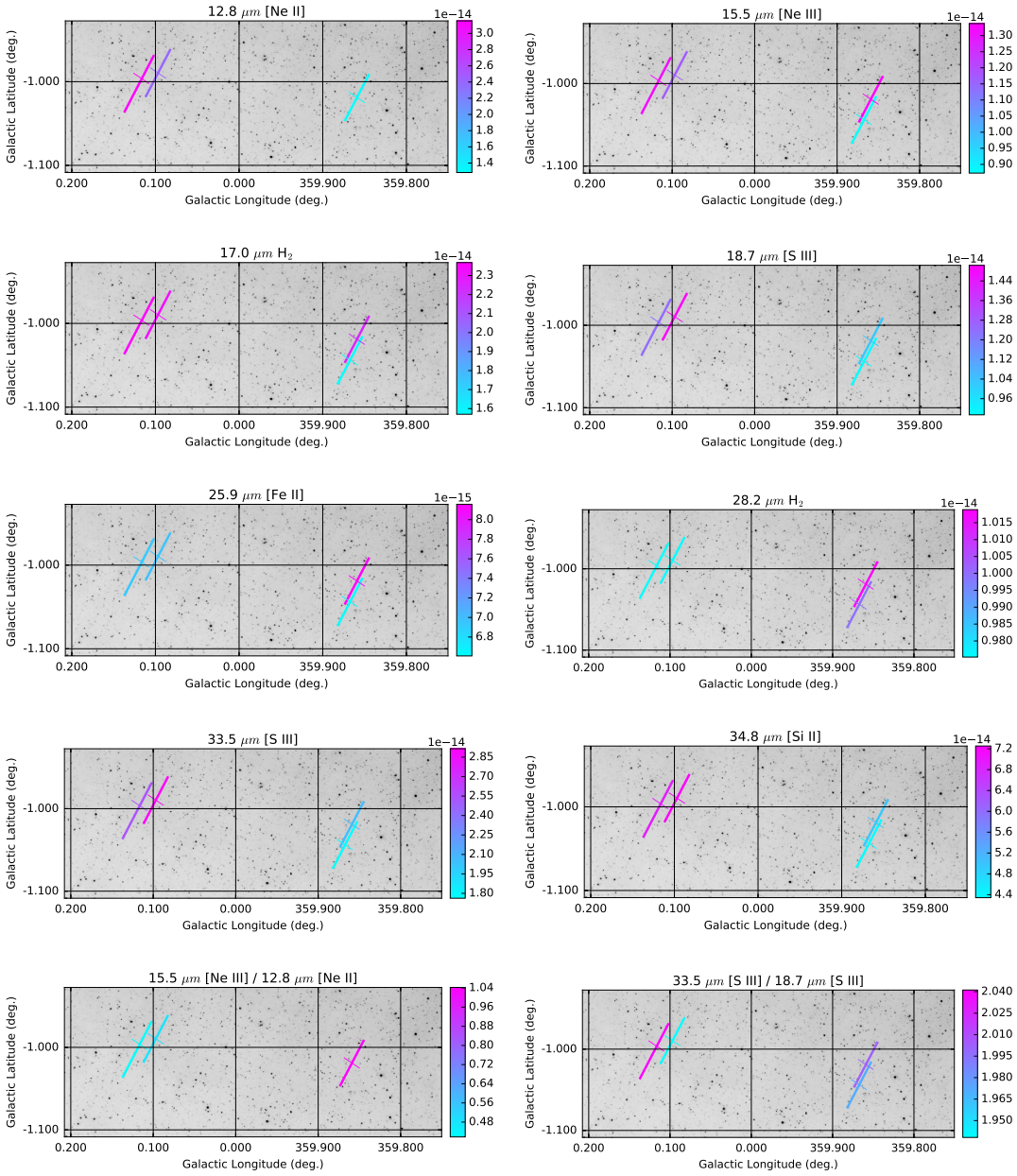

Figure B.4: The atomic and molecular emission line fluxes in the C35 fields, in $\mathrm{MWm}^{-2}/\mathrm{sr}$. A 3σ signal-to-noise criterion has been applied to these data.

Matthew J. Shannon

Education

Ph.D. Astronomy, University of Western Ontario, 2016

Dissertation: "The spectral variability of astronomical PAHs"

Advisor: Prof. Els Peeters

M.Sc. Astronomy, University of Western Ontario, 2012

Thesis: "Polycyclic aromatic hydrocarbon emission in evolved stars"

Advisor: Prof. Els Peeters

B.Sc. Honours Physics & Astronomy, University of Victoria, 2011

Honours project: "Analyzing n-body simulations of galaxy mergers"

Advisor: Prof. Arif Babul

Grants, Fellowships, & Awards

2016 — Faculty of Science Graduate Student Teaching Award

2015 — Queen Elizabeth II Graduate Scholarship in Science and Technology

2014 — Ontario Graduate Scholarship

2012 — Queen Elizabeth II Graduate Scholarship in Science and Technology

2010 — Miranda Ward Physics Scholarship

2010 — University of Victoria Physics and Astronomy Co-op Student of the Year

2008 — Don Ingham Memorial Scholarship

Peer-Reviewed Journal Articles

1. **M. J. Shannon**, D. J. Stock, E. Peeters, 2016, ApJ, 824, 111 –
"Interpreting the subtle spectral variations of the 11.2 and 12.7 μm polycyclic aromatic hydrocarbon bands." [ADS]
2. **M. J. Shannon**, D. J. Stock, E. Peeters, 2015, ApJ, 811, 153 –
"Probing the ionization states of polycyclic aromatic hydrocarbons via the 15–20 μm emission bands." [ADS]
3. D. J. Stock, E. Peeters, W. D.-Y. Choi, **M. J. Shannon**, 2014, ApJ, 791, 99 –
"The mid-infrared appearance of the Galactic mini-starburst W49A." [ADS]

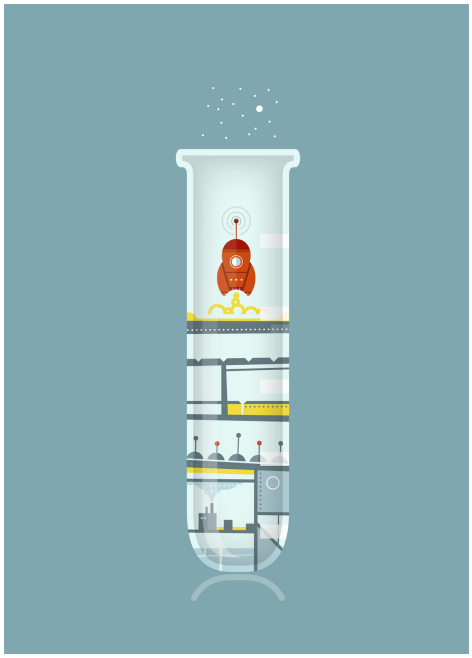

This thesis was typeset using LaTeX, originally developed by Leslie Lamport and based on Donald Knuth's TeX. The body text is set in 11 point Egenolff-Berner Garamond, a revival of Claude Garamont's humanist typeface. The above illustration, *Science Experiment 02*, was created by Ben Schlitter and released under CC BY-NC-ND 3.0. A template that can be used to format a PhD dissertation with this look & feel has been released under the permissive AGPL license, and can be found online at github.com/suchow/Dissertate or from its lead author, Jordan Suchow, at suchow@post.harvard.edu.